Kinematic and Thermodynamic Effects on Particle Clustering in Turbulent Flows

by

Ahmed Saieed

A thesis
presented to the University of Waterloo
in fulfillment of the
thesis requirement for the degree of
Doctor of Philosophy
in
Mechanical and Mechatronics Engineering

Waterloo, Ontario, Canada, 2025

© Ahmed Saieed 2025

Examining Committee Membership

The following served on the Examining Committee for this thesis. The decision of the Examining Committee is by majority vote.

External Examiner:	Andrew Bragg Associate Professor Dept. of Civil & Environmental Engineering, Duke University
Supervisor(s):	Jean-Pierre Hickey Associate Professor Dept. of Mechanical Engineering, University of Waterloo
Internal Member:	Cecile Devaud Professor Dept. of Mechanical Engineering, University of Waterloo
Internal Member:	Xianguo Li Professor Dept. of Mechanical Engineering, University of Waterloo
Internal-External Member:	Marek Stastna Professor Dept. of Applied Mathematics, University of Waterloo

Author's Declaration

This thesis consists of material all of which I authored or co-authored: see Statement of Contributions included in the thesis. This is a true copy of the thesis, including any required final revisions, as accepted by my examiners.

I understand that my thesis may be made electronically available to the public.

Statement of Contributions

This thesis is a compilation of the following publications:

Chapter 2: A. Saieed, M. M. Rahman, and J. P. Hickey. Role of viscosity in the preferential concentration of heated, bidispersed particles. *International Journal of Multiphase Flow*, 155:104185, 2022, DOI.

Chapter 3: A. Saieed, and J. P. Hickey. Viscosity-modulated clustering of heated bidispersed particles in a turbulent gas. *Journal of Fluid Mechanics*, 979:A46, 2024, DOI.

Chapter 4: A. Saieed, and J. P. Hickey. Viscosity-driven clustering of heated polydispersed particles in subsonic jet flows. *International Journal of Heat and Fluid Flow*, 112:109754, 2025, DOI.

Chapter 5: A. Saieed, and J. P. Hickey. Particle dispersion in supersonic particle-laden jets. *Journal of Fluid Mechanics*. [Under Revision]

This format will result in some repetition of concepts and discussion. However, since the findings of one publication were used as a foundation for the next analysis, this structure will aid the understanding of the results.

The research presented in this thesis is the result of my own study, where I was the primary researcher and author, while my supervisor reviewed and supervised my research. In the article reported in Chapter 2, M. M. Rahman contributed to some minor aspects of the analysis and review of the paper.

I also co-authored two articles during this research that are:

1. M. M. Rahman, A. Saieed, and J. P. Hickey. Turbulence-induced electrical discharges in charged particle-laden Martian boundary layers. *Flow*, 3:E34, 2023. DOI
2. M. M. Rahman, A. Saieed, M. F. Khan, and J. P. Hickey. Group combustion of dispersed spherical core–shell nanothermite particles. *Thermo*, 2(3):209-231, 2022. DOI

Abstract

Particle-laden flows are ubiquitous in numerous state-of-the-art engineering applications such as dispersed metallic particle combustion, particle solar collectors, and cold spray manufacturing. In such thermal applications, ensuring a uniform distribution of particles within a carrier fluid is critical, yet inertial particles intrinsically cluster in turbulent flows. In past investigations, particle clustering was treated as a purely kinematic problem, and typically, the variable temperature effects of both the particles and the gas were neglected. This is perplexing, as the increase in carrier gas temperature increases viscosity, which concomitantly enhances the coupling force between the fluid and the particles. Thus, it is plausible that particle clustering is influenced not only by kinematics but also by local thermodynamics. This line of thinking has motivated the scientific questions that underpin the present work.

To understand the role of thermodynamics on particle clustering, Direct Numerical Simulations (DNS) were carried out to analyze the clustering behavior of heated dispersed particles in Homogeneous Isotropic Turbulence (HIT) and subsonic jet flows; the study was then extended to explore particle-laden supersonic jet flows. In these analyses, the continuum and particulate phases were modeled with the Eulerian and Lagrangian point-particle approaches, respectively. The fluid-particle energy was coupled with Two-Way Coupling (TWC), while momentum exchange between the two phases was modeled with One-Way Coupling (OWC) and TWC. The analysis of the simulations led to the discovery of a novel particle clustering mechanism called Viscous Capturing (VC), in which preformed particle clusters create hot spots. The higher temperature of the gas in these hot spots led to regions with higher local viscosity, termed *viscous clouds*. The increased drag on the particles in the viscous clouds makes it hard for the clustered particles to leave the clusters, and it also aids in *capturing* more particles passing through the viscous clouds. This ultimately enhances particle clustering. An opposite particle clustering behavior was observed in a carrier phase with liquid-like viscosity (viscosity decreases with temperature rise), where particle heating resulted in superior particle dispersion.

Furthermore, the VC effect was found to increase with the rise in particle loading density. This is because, at higher particle loading density, the two prerequisites of VC are satisfied: (1) particles should be clustered before particle heating is initiated, and (2) these clusters should be large and unevenly distributed in the flow. In these viscous clouds, the fluid-particle and particle-particle slip velocities were found to be well-correlated, which further aids in keeping particles clustered. Apart from these conditions, particles should be uniformly heated for VC to take effect.

The HIT helps to isolate the effect of turbulence on particle clustering but lacks generalizability or the mean shear of more relevant particle-laden flow configurations, such as a jet flow. In subsonic jets, even a moderate rise in local gas viscosity can initiate VC, which results in higher clustering of heated particles as compared to unheated particles. This is because the introduction of particles within the jet core, which causes particles to be close to each other, also satisfies the two prerequisites of VC and retains particles within the jet. Thus, instead of individual viscous clouds compared to the HIT case, the entire central region of the jet acts as a viscous cloud. Even the particles with a higher radial velocity component remained within the jet, as they were unable to cross the sharp temperature gradient at the outer edge of the jet due to their propensity to collect at the location of a sharp scalar gradient. Thus, heated particles are essentially restrained within the jet.

On the other hand, in supersonic jet flows, it was determined that particles of different inertia have a distinct axial location where they start dispersing radially (x_r). This x_r is marked with a local Stokes number of $St^* \approx 0.6$. A new metric was also introduced to estimate x_r for practical applications. Particle dispersion was also influenced by the compressibility effects, where larger particles were found to have a higher propensity to settle in high-density gradient and dilatation regions of the flow.

Acknowledgements

This academic journey is beyond words can ever express. There are so many people who supported me in this endeavor and enabled me to achieve this dream. I greatly thank my supervisor Dr. Jean-Pierre Hickey for his extraordinary support, mentorship and encouragement. He introduced me to numerous academic and professional avenues, which became the highlights of my PhD. I cannot thank you enough for your support.

I thank Dr. Cecile Devaud, whose exceptional classes sparked a deeper understanding and my passion for turbulent flows. She played a huge role in my PhD. I am also deeply grateful to Dr. Filippo Colleti for hosting my research visit at ETH Zurich, Switzerland. I not only gained significant knowledge of particle-laden turbulence from him, but collaborating with his experimental research group also gave me a wealth of knowledge about different research tools. I am profoundly grateful to my committee members for assessing my research and providing valuable feedback.

Lastly, I cannot thank my parents, my beloved, enough for their unconditional support and love. This would simply be impossible without you. I am eternally thankful to you!

Dedication

This thesis is dedicated to my parents, my beloved. You made it possible!

Table of Contents

Examining Committee Membership ii

Author's Declaration iii

Statement of Contributions iv

Abstract v

Acknowledgements vii

Dedication viii

List of Figures xiv

List of Tables xxii

List of Abbreviations xxiii

1 Introduction 1

1.1 Fluid-Particle Interaction 3

1.2 Particle Clustering 9
1.3 Research Motivation 12
1.4 Problem Statement 14
1.5 Objectives 15

2 Role of Viscosity in the Preferential Concentration of Heated, Bidispersed Particles 18

Abstract 18
2.1 Introduction 19
2.2 Methodology 24
2.2.1 Carrier Phase 28
2.2.2 Particulate Phase 29
2.2.3 Heating Module 30
2.2.4 Radial Distribution Function 31
2.3 Results 32
2.3.1 Evolution of Timescales 33
2.3.2 Evolution of Stokes Number 35
2.3.3 Quantification of Particle Clustering 36
2.3.4 Viscous Capturing 41
2.3.5 Particle Distribution and Heating 44
2.3.6 Strain Rate and Vorticity 47
2.4 Summary 53

3 Viscosity-Modulated Clustering of Heated Bidispersed Particles in a Turbulent Gas **57**

Abstract . . . 57

3.1 Introduction . . . 58

3.2 Methodology . . . 64

3.2.1 Continuum Phase . . . 68

3.2.2 Particulate Phase . . . 69

3.2.3 Particle Heating Model . . . 70

3.3 Results . . . 71

3.3.1 Re_λ Independence . . . 71

3.3.2 Particle Heating . . . 71

3.3.3 Turbulence Modulation . . . 74

3.3.4 Timescales and Stokes Number . . . 75

3.3.5 Clustering Quantification . . . 76

3.3.6 Viscous Capturing . . . 81

3.3.7 Fluid-Particle Acceleration . . . 83

3.3.8 Particle Distribution . . . 86

3.3.9 Mathematical Interpretation of Viscous Capturing . . . 92

3.4 Summary . . . 96

4 Viscosity-Driven Clustering of Heated Polydispersed Particles in Subsonic Jet Flows **99**

Abstract . . . 99

4.1 Introduction . . . 100

4.2 Methodology . . . 104
4.2.1 Simulation Methodology . . . 104
4.2.2 Governing Equations . . . 110
4.3 Results . . . 112
4.4 Summary . . . 126

5 Particle Dispersion in Supersonic Particle-Laden Jets 128

Abstract . . . 128
5.1 Introduction . . . 129
5.1.1 Particle Clustering . . . 129
5.1.2 Particle Transport . . . 130
5.1.3 Particle-Turbulence Interaction . . . 132
5.2 Methodology . . . 134
5.2.1 Simulation Setup . . . 135
5.2.2 Continuum Phase . . . 138
5.2.3 Particulate Phase . . . 139
5.2.4 Validation . . . 141
5.3 Results . . . 145
5.3.1 Fractal Dimension Analysis . . . 147
5.3.2 Finite-Time Lyapunov Exponent . . . 150
5.3.3 Local Particle Characteristics . . . 153
5.3.4 Local Eddy Characteristics . . . 156
5.3.5 Particle-Jet Interaction . . . 161

5.3.6 Effect of Compressibility on Dispersion 169
5.4 Discussion 171
5.5 Summary 172

6 Conclusions **174**

6.1 Future Recommendations 177

References **178**

APPENDICES **204**

A Non-Dimensional Governing Equations **205**

A.1 Units 205
A.2 Non-Dimensionalization 206
A.2.1 Continuity Equation 207
A.2.2 Momentum Equation 208
A.2.3 Energy Equation 209
A.2.4 Entropy Equation 210
A.2.5 Lagrangian Equations 213

List of Figures

2.1 Comparison between the evolution of the particle and fluid temperatures normalized with temperature at $t = 0$ of heating. 32

2.2 Evolution of normalized τ_l (left) and τ_η (right) with the flow time. 34

2.3 Variation in normalized TKE with respect to the flow time. The shaded area represents the boundaries of TKE (solid black lines) as the viscosity increases from 0.6 to 1.7. Here only Gas 1 and Liquid 1 cases are shown as all gas and liquid cases overlapped due to OWC. 35

2.4 Evolution of St_l (left), large particles, and St_η (right), small particles, with time. 36

2.5 RDF of the small (left column) and large (right column) particles at $t = 1$, half TKE and $t = 10$. 38

2.6 RDF of the small and large particles of base case 2 at even timesteps under different conditions. 42

2.7 Effect of heating on discrete particle drag force in a gas. Arrows present fluid-particle drift velocity: the longer the arrow, the higher the drift velocity. 44

2.8 PDF of fluid-particle drift velocity normalized with Kolmogorov velocity ($u_\eta = \eta/\tau_\eta$) in heated gas and liquid at even timesteps. 45

2.9 Trend-lines of the peak values of normalized fluid-particle drift velocity PDF at each timestep. 46

2.10 Temperature contours of gas with particle distribution, in a $2\pi \times 2\pi$ slide, at three different time snaps. The temperature is normalized by its maximum value at each timestep. 47

2.11 Temperature contours of liquid with particle distribution, in a $2\pi \times 2\pi$ slide, at three different time snaps. The temperature is normalized by its maximum value at each timestep. 48

2.12 Distribution of particles in gas and liquid with strain rate at $t = 1$, half TKE and $t = 10$. 49

2.13 Distribution of particles in gas and liquid with vorticity at $t = 1$, half TKE and $t = 10$. 51

2.14 The difference between the number of small and large particles (ΔN) in different strain rate regions. 52

2.15 The difference between the number of smaller and larger particles (ΔN) in different vorticity regions. 53

2.16 Distribution of (A) small particles and vortical structures, (B) large particles and vortical structures, and (C) small and large particles in the 3D domain of Gas 2 at $t = 10$. Here, small and large particles are represented by black and red colors, respectively, while vortices are shown with teal blue structures. 54

3.1 The dependence of particle clustering (RDF) on Re_λ. 72

3.2 The average difference between particle (T_p) and fluid (T_f) temperatures (left), and the variance (σ^2) of this temperature difference (right), normalized with the temperature at $t = 0$ of heating (T_0). 73

3.3 The evolution of normalized Taylor micro-length scale (λ). Here, H and NH in the legend represent simulations with heated and non-heated particles. . 75

3.4 The temporal evolution of normalized TKE in H and NH cases. 76

3.5 The mean energy spectrum ($\overline{E(k)}$) of the test cases at $t = 0$ of H simulations, normalized with its initial value. The $L_{5,OWC}$ is identical to present L_5, except with momentum OWC. 77

3.6 The evolution of integral (τ_l) and Kolmogorov (τ_η) timescales normalized with their initial values. 78

3.7 The temporal evolution St_l and St_η in the heating regime. 78

3.8 The RDF of small and large particles at even timesteps. 79

3.9 PDF of normalized particle-particle relative velocity at $t = 0$ of heating. Here, n present the n^{th} particle. 80

3.10 The temporal evolution of fluid-particle mean drift velocity ($\overline{|u_p - u_f(x_p)|}$) in the hot regions, normalized with the Kolmogorov velocity ($u_\eta = \eta/\tau_\eta$). . 81

3.11 The temporal evolution of fluid-particle velocity distance correlation coefficient ($\mathbf{R}_{u_p,u_f(x_p)}$) in the hot zones. 82

3.12 The temporal evolution of mean small and large particle acceleration magnitude. The local fluid acceleration at small ($\overline{a_f(x_\eta)}$) and large ($\overline{a_f(x_l)}$) particle location is also provided for comparison. Note that these curves are non-normalized. 84

3.13 The behavior of mean particle drag coefficient (C_D) with respect to the normalized dynamic viscosity. 84

3.14 The temporal evolution of normalized difference in mean TKE at the position of small (x_η) and large (x_l) particles. 86

3.15 The normalized difference in the number of small (N_η) and large (N_l) particles in different strain rate, S, (left column) and vorticity, Ω, (right column) regions at even timesteps. 87

3.16 Clusters identification using DBSCAN method at $t = 2$ of heating. These 3D snapshots represent the overall distribution of clusters in the domain, whereas the 2D slices show the normalized temperature ($\acute{T_f} = T_f/T_{f,max}|_{t=2}$, where $T_{f,max}|_{t=2}$ is the maximum fluid temperature at $t = 2$) and clusters distribution in 2D slice of depth= 5η computed at the center ($x = 0$) of the box domain. Here, each particle cluster is identified with a different color, and unclustered particles are removed. 91

3.17 PDF of normalized particle velocity (u_p) and clustered particle velocity ($u_{p,c}$). 92

3.18 The PDF of normalized particle temperature in the entire domain (T_p) and in clusters ($T_{p,c}$) at $t = 2$ of heating. Where, T_{max} is 600. Only one timestep is shown as a similar distribution is obtained at other timesteps. 93

3.19 The average number of particles in a cluster per cluster characteristic length (L_c). Here, $N_{p,c}$ and N_c are the number of clustered particles and the number of clusters in the domain, respectively. 94

3.20 PDF of $\varphi_c - \overline{\varphi_{uc}}$ at $t = 2$. 95

4.1 Schematic of the present simulation setup. 105

4.2 Jet axial velocity, u_x (left) and axial turbulent intensity, $U' = (\overline{u'^2})^{1/2}$ (right), at five downstream locations, shown as a multiple of d_j. Here u_x and U' are normalized with the centerline velocity (u_c) and jet mean velocity ($\overline{u}$), respectively. The present radial profiles of U' are compared with the experimental data of Hussein et al. [1], shown as a dotted line. 108

4.3 Temporally averaged evolution of the H and NH particles' St along the jet centerline. 109

4.4 PDF of normalized Voronoï cell volume (V) compared with the random Poisson distribution (dotted line). Here $\overline{V}$ is the mean volume of all the cells, while V is computed by temporally averaging Voronoï cell volume over 3 FTT. 113

4.5 2D Voronoï tessellation diagram of the H and NH particles at the center of the domain. The thickness of each slice is $5\delta n_z$, where δn_z is the cell size in the z-direction. The length (x) and height (y) of these plots are $10d_j$ and $9d_j$ respectively. 114

4.6 Temporally and azimuthally averaged radial concentration of H and NH particles (θ) normalized with the mean centerline particle concentration ($\overline{\theta_c}$). 116

4.7 Temporally and azimuthally averaged radial evaluation of the magnitude of vorticity ($||\Omega||$) at five downstream locations. 117

4.8 Average radial particle-fluid slip velocity ($\overline{u_{pf}}$) in the streamwise direction, normalized with its initial value ($u_{pf,0}$). 118

4.9 Contours of the high viscosity region of the jet overlaid with particles, in a thin slice of thickness $5\delta n_z$ at the center of the domain of the H case. The fluid viscosity is normalized with the maximum dynamic viscosity of the fluid, $\mu_{f,max}$. The length (x) and height (y) of these plots are $10d_j$ and $9d_j$ respectively. 119

4.10 Normalized number of particles ($N_p(||\nabla_r T(x_p)||)^*$) binned based on the magnitude of the radial component of the temperature gradient ($||\nabla_r T||$) at the location of the particles. 120

4.11 Contours of the normalized vorticity overlaid with particles, in a thin slice of thickness $5\delta n_z$ at the center of the domain of the H case. Here, $\overline{\Omega}$ is the spatially averaged vorticity. The length (x) and height (y) of these plots are $10d_j$ and $9d_j$ respectively. 121

4.12 The PDF of vorticity (Ω) and strain-rate (S) at the particle location, normalized with their mean values, respectively. 122

4.13 Normalized second order structure function ($S^2_{u_f(x_p)}$) of fluid velocity at the location of H and NH particles. Here, $S^2_{u_f(x_p),0}$ is the value of the first bin of $S^2_{u_f(x_p)}$. 123

4.14 The PDF of temporally averaged inter-particle slip velocity (u_{pp}) of the considered four particle species, normalized with the jet inlet velocity (u_j). 124

4.15 Number of clustered particles (N_{cl}) versus the inter-particle distance (D), normalized with the total number of particles of each species (N_p). 125

5.1 Simulation setup depicting three sub-simulations. 136

5.2 Normalized axial component of the jet centerline velocity (u_{c_x}), and azimuthally average TKE at $x = 8$ of the $512 \times 256 \times 256$ and $768 \times 384 \times 384$ meshes. 142

5.3 Axial fluid-particle slip velocity (u_{pg}) of the $512\times256\times256$ and $768\times384\times384$ grids, normalized with the initial value at $x = 0$ ($u_{pg,0}$). 143

5.4 Radial evolution of temporal and azimuthal mean axial velocity, u_x (left), and root-mean-square gas velocity, u_{rms} (right), of the single-phase jet flow at five axial locations. In the left plot, TM represent Troutt and McLaughlin [2], particularly the solution of Equation (5.12). 144

5.5 Fluid vortices shown with $\mathcal{Q}$-criterion (top), overlaid with particles (bottom) of the considered four species as titled. The vortices in the top image and particles in the bottom four images are colored with the local gas velocity (u_g). Recall that the particle size increases from P1 to P4. 146

5.6 Logarithmic correlation integral, $\log(C_l)$ (left), with respect to the inter-particle distance, l, normalized with the initial inter-particle distance, l_0. The correlation dimension (D_2) of each curve is shown in the legend. The variation in D_2 with normalized cluster volume (V_c) is shown in the plot on the right. The gray-shaded area highlights the region containing inflection points. 147

5.7 Evolution of temporally and spatially averaged turbulent kinetic energy (TKE) and eddy-length scale (L_{eddy}). Here L_{eddy} is normalized with jet diameter d_j. The dotted vertical lines mark the location of respective particle initial radial dispersion, where St^* is the local Stokes number of the particles at that location (discussed in Section 5.3.3). 151

5.8 FTLE ($\lambda(x)$) computed along the streamwise direction, where $\lambda(x)$ is averaged over all pairs of a particle species on the given y-z plane along x-axis to obtain a single curve. The red dotted line shows the axial location (x_r) of peak particle dispersion. 152

5.9 Contour of FTLE ($\lambda(x)$) in a thin slice at the center of the domain. Here, only positive (dispersion) values of FTLE are shown. The dotted red color line depicts the x_r of the corresponding particle species. 154

5.10 Particle axial acceleration ($a_{p,x}$) normalized with the initial value ($a_{p,x,0}$). The dotted lines represent the x_r of the corresponding particle species. . . 156

5.11 Magnitude of the local gas velocity gradient at the particle position in the radial direction, $||\partial u_{g,x}(x_p)/\partial r|| = \sqrt{(\partial u_{g,x}(x_p)/\partial y)^2 + (\partial u_{g,x}(x_p)/\partial z)^2}$, non-dimensionlized with the respective particle aerodynamic timescale (τ_p). Here, $||\cdot||$ represents the magnitude, and ϑ in the legend shows the exponential decay constant of the corresponding particle species. 157

5.12 Contour of temporally averaged $\mathcal{Q}(y,z)$ on a 2D thin slice in y-z plane at x_r = 3.3, 5.5, 6.8 and 7.5 for P1, P2, P3 and P4 particles, respectively. Where, $\mathcal{Q}_{max}(y,z)$ is the maximum value of $\mathcal{Q}(y,z)$ at each x_r plane. . . . 158

5.13 Mean 1D energy spectrum computed at the y-z planes at x_r = 3.3, 5.5, 6.8 and 7.5 of the P1, P2, P3 and P4 particles, respectively. 159

5.14 Second-order structure function of the local gas velocity ($S^2_{u_g(x_p)}(\Delta r)$) at the particle position, evaluated at the y-z planes at $x_r = 3.3$, 5.5, 6.8 and 7.5 of the P1, P2, P3 and P4 particles, respectively. The second-order structure function is normalized with its first non-zero value $S^2_{u_g(x_p)}(\Delta r)_0$. 160

5.15 Joint PDF of the particle (u_p) and local gas ($u_g(x_p)$) velocities. 162

5.16 Turbulent kinetic energy (TKE(x_p)) and dissipation rate ($\varepsilon(x_p)$) at the location of particles. 163

5.17 Relative kinetic energy of the particles, ΔKE (left), and axial component of particle-gas slip velocity, u_{pg} (right). 164

5.18 Second-order neighboring particle slip velocity function ($\chi^2_{u_{pg}}(x)$). The dotted lines on the plot show the slope. 166

5.19 Comparison of the averaged product of particle fluctuating velocity components and mean Reynolds stresses ($\overline{u'_i u'_j}$) local gas velocity fluctuations ($u'_p(x_p)$). Note that due to the symmetry of the jet, $\overline{u'_y u'_y} \approx \overline{u'_z u'_z}$ and $\overline{u'_x u'_y} \approx \overline{u'_x u'_z}$. Therefore, we have only shown $\overline{u'_y u'_y}$ (top-right) and $\overline{u'_x u'_y}$ (bottom-left) curves in this plot. 167

5.20 PDF of the magnitude of gas density gradient (left) and dilatation (right) computed at the position of particles. We preserved the sign of each component before taking the magnitude and multiplied these signs to the final magnitude value, which gave us a negative sign for the magnitude. The dotted red line presents the Gaussian curve. 169

5.21 Number of particles (n_s) normalized with the total number of particles of a given species (n_p) in the entire domain, sampled in the regions where $\rho_g(x_p) > ||\rho_g + \sigma(\rho_g)||^*$ (left), $\nabla \cdot \rho_g(x_p) > ||\nabla \cdot \rho_g + \sigma(\nabla \cdot \rho_g)||^*$ (middle), $\nabla \cdot u_g(x_p) > ||\nabla \cdot u_g + \sigma(\nabla \cdot u_g)||^*$ (right). Here, σ is the standard deviation and the superscript $*$ represents that the curves are normalized with their maximum value. 170

List of Tables

2.1 The characteristics of the fully developed HIT. 26

2.2 Combinations of small and large particle radii and the corresponding St_l and St_η at $t = 0$ of the gas and liquid simulations with heating. 27

3.1 Characteristics of the fully developed HIT. 67

3.2 Particle St_l and St_η values at the start of heating simulations. 68

3.3 Particle species specific values of ϵ for cluster identification in 3D snapshots. 89

4.1 Particle diameter and initial Stokes number (St_0) in the present simulations. 109

4.2 Stokes number ($St_{x=10}$) of H and NH particles at $x = 10$ 110

5.1 Diameters (d_p) and Stokes number (St) at the jet inlet, of the four particle species (denoted P1 to P4). 135

5.2 Turbulence characteristics of the supersonic jet flow. 140

A.1 The selected reference variables. 207

List of Abbreviations

CIC Cloud-in-Cell 5

CSA Canadian Space Agency 12

CV Constant Viscosity 33, 34, 36, 40

DBSCAN Density Based Spatial Clustering of Application with Noise xvii, 88–91, 97, 125, 148, 149

DNS Direct Numerical Simulations v, 15, 18, 23, 24, 53, 57, 60, 64, 65, 96, 99, 104, 126, 128, 133–135, 172, 174, 175, 177

FTLE Finite-Time Lyapunov Exponent xx, 151–154, 158

FTT Flows Through Time xvii, 107, 113, 137, 138, 141, 142

FWC Four-Way Coupling 3, 4, 177

H Heated xv–xviii, xxii, 71, 75–77, 81, 107, 109, 110, 112–119, 121–125, 127

HIT Homogeneous Isotropic Turbulence v, vi, xxii, 10, 11, 15, 16, 25, 26, 28, 32, 33, 60, 65–67, 75, 96, 103, 104, 106, 110, 113, 118, 120, 126, 130, 133, 135, 136, 140, 143, 172, 174–176

ISRU In-Situ Resource Utilization 12

MPI Message Passing Interface 24

NASA National Aeronautics and Space Administration 12

NGP Nearest Grid Point 5

NH Non-Heated xv, xvii, xviii, xxii, 71, 74–77, 81, 107, 109, 110, 112–118, 122–125, 127

NSCBC Navier-Stokes Characteristics Boundary Condition 106, 127, 137

OWC One-Way Coupling v, xiv, xvi, 3, 5, 15, 16, 25, 26, 33, 35, 62, 64, 77, 86, 138

PC Preferential Concentration 9, 10, 18–21, 23, 24, 31, 53, 55, 60, 88, 100, 130, 133, 138, 155, 170

PDF Probability Density Function xiv, xvi–xix, xxi, 11, 12, 43, 45–47, 80, 90, 92, 93, 95, 96, 113, 122, 124, 161, 162, 169

RDF Radial Distribution Function xiv–xvi, 11, 31, 36–39, 42, 44, 66, 71, 72, 77, 79–82, 88, 89, 96

TSC Triangular Shaped Cloud 5, 140, 141

TWC Two-Way Coupling v, 3–5, 7, 8, 15, 16, 25, 52, 57, 61, 62, 64, 66, 67, 69, 74, 75, 86, 96, 99, 102, 103, 108, 115, 126, 128, 129, 134, 138, 140–142, 165, 175, 210

VC Viscous Capturing v, vi, 16, 19, 39, 40, 43, 52, 55, 57, 58, 62, 63, 71, 81–83, 85, 86, 88–90, 93, 95–97, 102, 103, 124–127, 174–177

Chapter 1

Introduction

Turbulent flows perfectly exemplify *harmony within chaos*. A deeper look into such flows reveals a complex realm of length scales in which energy is passed down from the integral (large), inertial, and Kolmogorov (small) scales [3], akin to a waterfall. The integral scale is the energy-containing scale, defined by large turbulent eddies. These eddies break down into smaller eddies and form the inertial scale, which is an intermediate scale that transfers energy from the integral scale to the Taylor microscale. At the Taylor microscale, the fluid viscous effects become noticeable; however, they are not dominant at this scale. The turbulent energy in the flow is then passed down to the Kolmogorov scale, where it is dissipated into heat due to viscous dissipation. Hence, despite the randomness of turbulence, there is a statistical organization of turbulence.

A widely studied sub-domain of turbulence is particle-laden turbulent flows, which we unknowingly witness in our daily lives by mixing sugar in coffee, or in the form of rain and snowfall. In the literature of particle-laden flows, the word *particles* inclusively refers to any particulate phase in a multiphase flow, where particles can be liquid droplets within a gas or solid matter in a gas or liquid [4]. The seemingly simple presence of particles substantially complicates the underlying convoluted turbulence due to the phenomena of turbulence modulation and particle clustering. Having particles in a turbulent flow also

introduces additional length and timescales, along with some other critical parameters such as fluid-particle slip velocity and particle volume fraction, etc.

Consequently, particle-laden turbulent flows, especially with a focus on inertial particle clustering, have garnered scientific scrutiny for decades. Here, efforts range from answering some of the most fundamental questions in nature such as how planets form due to the clustering of dust particles [5, 6] and clustering and coalescence of water droplets in clouds leading to precipitation [7, 8]. Likewise, numerous advanced engineering applications deal with particle-laden flows. These include the combustion of dispersed nanothermites for propulsion [9, 10], cold spray additive manufacturing methods [11], precision drug delivery [12, 13, 14], and metallurgy [15], among others. In some applications, particle clustering is desired, such as aerosol control in industrial filters [16], food and chemical processing [17]. But, in most thermal applications, a homogeneous distribution of particles is required as particle clustering can impede combustion [18], drop inter-particle heat transfer, and result in uneven gas expansion [19]. Therefore, understanding the fundamental concepts of particle clustering in such flows is critical.

To predict particle dispersion in such applications, for the past four decades, a dimensionless parameter called *Stokes number* (St) [20] has been extensively utilized. The St is the ratio of particle momentum τ_p to a turbulent τ_f timescale. Although St is used as a measure to quantify the propensity of particles to cluster, it mainly depends on the particle and fluid dynamics properties. The subscripts p and f represent particles and fluid characteristics. Thus, it is a reliable metric to estimate particle dispersion provided that there are no thermodynamic changes (mainly density and viscosity) in the flow. However, this is not the case in thermal applications. In past studies, the effect of temperature-driven fluid density on particle clustering has been well-characterized (see [21, 22]). But the influence of temperature-dependent fluid viscosity on clustering is greatly overlooked, as in most studies, fluid viscosity is modeled as a constant for simplicity. Before delving into this issue, it is critical to understand the fundamentals of fluid-particle interaction and the particle clustering phenomenon, which are discussed in the following sections.

1.1 Fluid-Particle Interaction

The presence of particles can have various implications on a turbulent flow. The most critical among these is the turbulent attenuation or enhancement, due to the momentum and energy exchange between the carrier and particulate phases. These fluid-particle interactions are strongly dependent on particle volume (Φ_v) and mass (Φ_m) fractions [23], where these are the ratios of particle-to-fluid volume and mass, respectively. It has been reported that particles do not affect local turbulence if the particle diameter is smaller than the smallest turbulence length scales, and Φ_m and Φ_v are minimal. To simplify this problem, if Φ_v is much smaller than the fluid-particle density ratio (ρ_f/ρ_p) such that $\rho_f/\rho_p \ll 1$, then Φ_m can be approximated as $\Phi_v\rho_p/\rho_f$ [24]. In incompressible particle-laden flows, ρ_p/ρ_f is typically constant. Thus, it can be assumed that $\Phi_m \propto \Phi_v$. As a result, the strength of particles' influence on the local turbulence is estimated with particle volume fraction. Moreover, as a whole, the fluid-particle interaction can be characterized with three critical ratios: particle diameter to a turbulent length scale (d_p/l_f); particle-to-fluid density ratio (ρ_p/ρ_f); and particle momentum to a turbulence timescales (τ_p/τ_f), which is essentially particle Stokes number, St [24]. The St will be discussed later in this chapter.

In numerical simulations, the effect of particles on turbulence is classified into three regimes that are momentum One-Way Coupling (OWC), Two-Way Coupling (TWC), and Four-Way Coupling (FWC). In momentum OWC, $\Phi_v \leq 10^{-6}$, which implies that only particles are influenced by the fluid and the back-reaction force from the particles on the fluid is negligible [25]. Between $10^{-6} < \Phi_v \leq 10^{-3}$, the back-reaction drag force becomes significant enough to influence turbulence structures, which results in turbulence modulation. This regime is called TWC. It is essential to model particle reaction force on the fluid in this regime for accurate modeling and this adds another layer of complexity to the flow physics. For example, in this case, small inertial particles dissipate turbulent kinetic energy (TKE) as the fluid drags them. Moreover, turbulence modulation is the result of particles and fluid exchanging energy and momentum, such that particles deplete the energy of the larger scales [26] and feed it to the smaller scales [27]. This effect is also a

function of particle inertia [28]. In this case, even at moderate mass loading, particles can deplete the TKE by up to 85% [29]. Thus, turbulence modulation is relevant when Φ_v falls in TWC, and has attracted a great deal of scientific investigations in this domain. On the other hand, $\Phi_v > 10^{-3}$ marks the starting limit of FWC in which particle-particle collisions are also nontrivial. The inter-particle collisions also attenuate fluid energy, and this effect increases with particle St [30]. It was observed that between TWC and FWC the energy dissipation drops by up to 7%, as TWC affects particle clustering, which in return alters the gradient of the local fluid velocity. This ultimately influences fluid particle energy exchange.

Over the years different numerical schemes have been introduced to model particle-laden flows: from the *Dusty Gas* (low cost) approach in which, due to low particle concentration and uniform particle distribution, both phases are modeled as a single phase [31]; to fully particle resolved scheme (most expensive) where particle size is equal to or greater than the smallest turbulent eddies such that boundary layer effects on the particles and all the turbulent scales created by particle motion also have to be resolved [32, 33]. The two most common approaches for numerically assessing particle-laden flows are the *Eulerian-Eulerian* and *Lagrangian-Eulerian* schemes. In the Eulerian-Eulerian approach, which is also known as *two-fluid* method, the carrier and particulate phases are dealt with as intermixing fluids [34, 35]. In practice, the velocity field of the particles with higher inertia deviates from the flow field, and particle spatial distributions can also be non-uniform as the particle inertia increases. While the Eulerian method assumes a distinct velocity field for the particles, which limits the inertia of the particles that can be studied with this approach unless [36], a probabilistic method is employed. The Lagrangian point-particle method, on the other hand, tracks individual particles without any limitation on particle inertia and polydispersity (flow containing particles of different sizes). Hence, in the Eulerian-Lagrangian approach, the fluid equation set is solved with the Eulerian approach, whereas particle governing equations are solved with a Lagrangian description, along with interphase coupling. In the Lagrangian point-particle assumption for particles, it is assumed that the particle size is smaller than the Kolmogorov scale. Thus, although

this approach focuses on scales equal to or greater than particle size, it is computationally very expensive, due to the tracking of individual particles.

The fluid-particle interaction is modeled with different coupling schemes such as Nearest Grid Point (NGP), Cloud-in-Cell (CIC), Triangular Shaped Cloud (TSC) methods [37, 38]. The NGP scheme maps the particle properties to the nearest point on the computational grid. This method is computationally inexpensive; however, it introduces noise as fluid-particle mapping is discontinuous (not smooth). The CIC method attenuates the noise experienced in NGP by interpolating the particle's attributes to eight $(2 \times 2 \times 2)$ nearest grid points in a 3D mesh. The TSC scheme projects the particle's attributes to twenty-seven $(3 \times 3 \times 3)$ neighboring mesh points in a 3D grid. This is the most accurate scheme, which delivers smooth fluid-particle interaction, but intuitively, it is the most expensive among these methods.

In the Eulerian-Lagrangian approach, the particle trajectories are computed based on the fluid velocity field employing the equation of particle motion. In momentum TWC, the particle reaction drag force is incorporated into the momentum equation of the fluid, which is the Navier-Stokes equation. In the Eulerian description of the fluid, the continuity equation is:

$$\frac{D\rho_f}{Dt} = 0 \tag{1.1}$$

here D/Dt is the substantial derivative following the fluid motion. The subscript f represents the fluid parameters. The transport equation for fluid momentum is defined as:

$$\frac{D\,\rho_f\,\mathbf{u}_f}{Dt} = -\frac{\partial P_f}{\partial x_i} + \nabla \cdot \boldsymbol{\tau} \tag{1.2}$$

where $\boldsymbol{\tau}$, $\mathbf{u}$ and P_f are the viscous stress tensor, velocity vector, and fluid pressure, respectively. In the present form, Equation (1.2) depicts OWC and in TWC particle reaction drag force ($\mathbf{F}_p$) must be added on the right-hand side of this equation. The term $\mathbf{F}_p$ is expressed as:

$$\mathbf{F}_p = \sum_x m_p C_D \frac{\mathbf{u}_p - \mathbf{u}_f(x_p)}{\tau_p} \tag{1.3}$$

here C_D and m are the coefficient of drag force and mass, respectively. The subscripts p and f depict the particle and fluid parameters. The symbol $\sum_x$ represents the sum over all the particles at a particular x position. Note that Equation (1.2) governs the fluid's momentum transport, and the particle movement establishes a group of boundary conditions that are arduous to solve. This issue is addressed by taking into account the drag on the particles. But this is an oversimplification of the problem at hand, as the drag law can only provide a reasonable estimate of the fluid-particle interaction.

The particle equation of motion can be expressed as [39]:

$$m_p \frac{d\mathbf{u}_p}{dt} = \mathbf{F}_a + \mathbf{F}_G + \mathbf{F}_D + \mathbf{F}_B + \mathbf{F}_m \tag{1.4}$$

In Equation (1.4), $\mathbf{F}_a$, $\mathbf{F}_G$, $\mathbf{F}_D$, $\mathbf{F}_B$ and $\mathbf{F}_m$ are fluid acceleration, gravitational, Stokes drag force, Basset history and added mass forces, respectively. The $\mathbf{F}_a$ is given as:

$$\mathbf{F}_a = m_f \frac{D\mathbf{u}_f}{Dt} \tag{1.5}$$

here m_f is the mass of the fluid displaced by the spherical particles. The other forces are mathematically defined as:

$$\mathbf{F}_G = (m_p - m_f)\,\mathbf{G} \tag{1.6}$$

$$\mathbf{F}_D = -3\pi\mu_f d_p C_D\,(\mathbf{u}_p - \mathbf{u}_f) \tag{1.7}$$

$$\mathbf{F}_B = -\frac{3}{2}\pi d_p^2 \mu_f \int_0^t \frac{\frac{d}{d\Gamma}\left(\mathbf{u}_p - \mathbf{u}_f - \frac{1}{24} d_p^2 \nabla^2 \mathbf{u}_f\right)}{\sqrt{\pi\nu_f\,(t-\Gamma)}} d\Gamma \tag{1.8}$$

$$\mathbf{F}_m = -\frac{1}{2} m_f \frac{d}{dt}\left(\mathbf{u}_p - \mathbf{u}_f - \frac{1}{40} d_p^2 \nabla^2 \mathbf{u}_f\right) \tag{1.9}$$

where $\mathbf{G}$, d, μ and ν are gravitational acceleration, diameter, dynamic, and kinematic viscosities, respectively. While Γ is the time instant between 0 and t. There are two types of derivatives used in these equations, where d/dt is the substantial derivative following the particle motion. The $\mathbf{F}_D$ is the drag force due to fluid viscosity and relative fluid-particle velocity, and it can be defined with different expressions based on the type of flow (compressible or incompressible). The $\mathbf{F}_B$ is essentially the viscous drag force due to fluid

viscosity and fluid-particle relative acceleration [40]. The $\mathbf{F}_B$ is typically neglected when inter-particle collisions are trivial, such as in dilute suspensions, and the particle-to-fluid density ratio is very high [41, 42]. As the particle movement displaces the fluid, $\mathbf{F}_m$ is the force necessary to accelerate this displaced fluid. While $\mathbf{F}_a$ is the force exerted on the particle by the pressure gradient across the particle, which can be rewritten in terms of fluid acceleration. These $\mathbf{F}_B$, $\mathbf{F}_m$, and $\mathbf{F}_a$ forces become relevant if the carrier phase density is equal to or greater than the particulate phase density ($\rho_f \geq \rho_p$) [42]. This is not the case in gaseous turbulent flows laden with solid, inertial particles. In most numerical analyses, the gravitational force is neglected for simplicity. Moreover, it is commonly assumed that if $\rho_p/\rho_f \gg 1$, which is true for inertial particles, the only force acting on the particles is the drag force [39]. Apart from these forces, there is also a particle lift force driven by particle rotation [43]. This lift force is generally much less than the drag force, and therefore, it can be disregarded in most applications. This helps in simplifying Equation (1.4), which is expressed as:

$$\frac{d\mathbf{u}_p}{dt} = -\frac{3\pi\mu_f d_p}{m_p}\left(\mathbf{u}_p - \mathbf{u}_f\right) C_D \tag{1.10}$$

For spherical particles, substituting $m_p = 1/6\pi d_p^3 \rho_p$ in Equation (1.10) gives:

$$\frac{d\mathbf{u}_p}{dt} = -C_D \frac{(\mathbf{u}_p - \mathbf{u}_f(x_p))}{\tau_p}, \qquad \text{where } \tau_p = \frac{\rho_p d_p^2}{18\mu_f} \tag{1.11}$$

here τ_p is the particle momentum timescale and represents the time an inertial particle takes to adapt to the local changes in the flow. In other words, it is the time a particle released in a fluid stream from rest takes to achieve 63% of the fluid velocity, which originates from the equation of particle motion:

$$\frac{d\mathbf{u}_p}{dt} = C_D \frac{\mathbf{u}_f - \mathbf{u}_p}{\tau_p} \Rightarrow \mathbf{u}_p = \mathbf{u}_f + (\mathbf{u}_{p,0} - \mathbf{u}_f) e^{(-t\, C_D/\tau_p)} \tag{1.12}$$

Starting from rest, the initial velocity of particle is $\mathbf{u}_{p,0} = 0$, if $t = \tau_p/C_D$ then Equation (1.12) can be written as $1 - e^{-1} = 63\%$.

In momentum TWC, the use of Equation (1.11) adds another challenge as, in this case, $u_f(x_p)$ is expected to be the undisturbed fluid velocity at the particle's location.

This velocity is not assessable in TWC as by definition, this coupling scheme establishes an effect of particles on the local fluid. As a result, most numerical studies utilize the disturbed local fluid velocity with the justification that if particles are much smaller than the Kolmogorov length scale, then the effect of disturbed local fluid velocity on other turbulence statistics is negligible [28].

As mentioned above, the effect of particles is felt by the fluid in the form of an additional dissipation of the TKE. This requires that the reaction drag of the particle is incorporated into the fluid momentum equation, which leads to enhanced dissipation in the transport equation of TKE:

$$\frac{D\ \mathrm{TKE}}{Dt} = \mathcal{PD} + \mathcal{T} + \mathcal{P} + \varepsilon + \mathcal{D} + S_p, \text{ where } \mathrm{TKE} = \frac{1}{2}\overline{u_i' u_i'} \tag{1.13}$$

here $|\cdot|'$ is the fluctuating component computed from Reynolds decomposition and $\overline{|\cdot|}$ is the mean value. In Equation (1.13), $\mathcal{PD}$, $\mathcal{T}$, $\mathcal{P}$, ε and $\mathcal{D}$ are terms for TKE diffusion due to pressure, transport, production, dissipation, and viscous diffusion, respectively. To account for the TKE modulation because of particle reaction drag force, a source term S_p is also incorporated in Equation (1.13). These terms are mathematically expressed as:

$$\mathcal{PD} = -\frac{1}{\rho_f}\frac{\partial \overline{u_i' P_f'}}{\partial x_i} \tag{1.14}$$

$$\mathcal{T} = -\frac{1}{2}\frac{\partial \overline{u_j' u_j' u_i'}}{\partial x_i} \tag{1.15}$$

$$\mathcal{P} = -\overline{u_i' u_j'}\frac{\partial \overline{u_i}}{x_j} \tag{1.16}$$

$$\varepsilon = \nu_f \overline{\left(\frac{\partial u_i'}{\partial x_j}\right)^2} \tag{1.17}$$

$$\mathcal{D} = \nu_f \frac{\partial^2 \mathrm{TKE}}{\partial x_i^2} \tag{1.18}$$

$$S_p = -\frac{1}{\rho_f}\overline{u_i' F_p'} \tag{1.19}$$

The term S_p in Equation (1.13) accounts for the additional dissipation of TKE (but may also be a source of TKE). However, in general, the presence of particles may affect all other terms in this equation [44]. Hence, particles can have a significant effect on the overall turbulence.

Note that in compressible flows, the thermodynamic aspects of the flow are modeled through the equation of energy conservation, which is closed with the state equation. These details will be covered in more detail in the subsequent chapters.

1.2 Particle Clustering

In particle-laden turbulent flows, particle clustering is a particularly perplexing phenomenon that has captivated scientists for decades. This is because particle clustering contradicts the conventional understanding that turbulence enhances mixing. The concept that turbulence enhances mixing originates from the fact that based on the stochastic nature of turbulence, the fluid exerts an arbitrary force (direction and magnitude wise) on each particle, which should disperse particles uniformly. But, particles tend to form densely populated clusters, in turn creating regions with very small particle concentrations in the flow. This particle clustering phenomenon is essentially due to the difference in fluid-particle inertia.

In turbulent flows, particles leave the vortices due to the centrifugal force exerted on the particles by the turbulent eddies and collect in the areas where vorticity is low and strain-rate is high [45]. These areas are also referred to as convergence zones which are located between vortices. This process is commonly referred to as *particle clustering*, and this mechanism of particle clustering is called Preferential Concentration (PC) [46]. Note that there are numerous other clustering mechanisms such as clustering of particles at zero-acceleration points [47], regions with sharp scalar gradient (*scalar front*) [48], due to fluid-particle drift velocity [49], particle history effect [50], and turbophoresis [51, 52]. However, the commonly employed mechanism to describe particle clustering is PC due to its intuitive nature.

All of these mechanisms of particle clustering can be understood with the help of the Stokes number (St), which is mathematically expressed as a ratio of the particle-to-fluid timescales [20] :

$$St = \frac{\tau_p}{\tau_f} = \frac{\rho_p d_p^2}{18\rho_f \nu_f} \frac{1}{\tau_f} \tag{1.20}$$

For τ_f, typically Kolmogorov timescale (τ_η) is employed, such that $St = \tau_p/\tau_\eta \approx 1$ is associated with maximum particle clustering [46], due to PC. In other words, the partial responsiveness of $St \approx 1$ particles to turbulent eddies causes them to fling out of these eddies [53]. Whereas, $St \ll 1$ and $St \gg 1$ particles are considered tracer-like [54] and ballistic [55], respectively. The tracer particles can follow fluid streamlines and therefore they can stay within vortices, and the ballistic particles are non-responsive to smaller eddies and primarily react to larger turbulent eddies. Hence, these two types of particles do not yield notable clustering. On the other hand, turbulent jet flows uniformly distribute $St \ll 1$ particles within the jet. The particles with $St \approx 1$ fling out of the local eddies due to the centrifugal force acting on them. Thus, they can be completely expelled from the jet core [56]. In contrast, due to their ballistic nature, $St \gg 1$ particles primarily travel along the jet centerline with minimal radial dispersion. These three particle dispersion mechanisms are referred to as vortex, centrifugal, and inertial mechanisms [57].

The choice of the turbulent timescale for defining St is also problematic. Although most studies use τ_η as stated earlier, particles of different inertia respond to different length scales in the flow [58]. The choice of turbulent timescale also depends on the type of flow. For instance, in Homogeneous Isotropic Turbulence (HIT) generally Kolmogorov [59, 60] and integral (τ_l) [61] timescales are preferred. These turbulence timescales can be represented as:

$$\tau_l = \frac{\mathrm{TKE}^{\frac{3}{2}}}{\varepsilon \; u_{rms}} \tag{1.21}$$

$$\tau_\eta = \left(\frac{\nu_f}{\varepsilon}\right)^{\frac{1}{2}} \tag{1.22}$$

here u_{rms} is the root-mean-squared of the fluid velocity. While in turbulent jet flows, St is delineated with τ_l computed from jet diameter (d_j) and inlet velocity (u_j) [62, 63], or with

jet convective timescale (τ_c) [64, 65] which is essentially the large eddy timescale. Where, τ_c is defined as:

$$\tau_c = \frac{r_{1/2}}{u_c} \tag{1.23}$$

where $r_{1/2}$ and u_c are jet half-width and centerline velocity, respectively. These differences in the definition of St further complicate the modeling of particle-laden turbulence flows, especially in polydispersed flows, where each particle species has a distinct acceleration [66] and tends to segregate in unique regions of the flow [67].

Considering this discussion, an intuitive solution for avoiding particle clustering is to refrain from particles with $St \approx 1$. However, particle St evolves in turbulent flows. Firstly, even under isothermal conditions, τ_l drops and τ_η escalates as the HIT decays. While in jet flows τ_c increases downstream from the jet inlet. Moreover, with particle heating, the local fluid parameters such as $\rho_f(x_p)$ and $\mu_f(x_p)$ also change, which further affects St. It is unclear, from past research, if particle clustering behavior adapts to this evolution of St. For the scenario where particles show maximum clustering at $St \geq 1$, particle clustering is elucidated with *non-local history* mechanism. In this mechanism, particles retain the memory of interacting with turbulent eddies along their path history [50]. Thus, it is evident that past studies rely on St for predicting particle clustering even if higher particle clustering is observed at $St \not\approx 1$.

For quantifying particle clusters, a range of methods has been proposed over the years. One of the earliest methods is called *box-counting* in which the domain is divided into boxes of a certain size and the number of particles in each box is counted [68]. By comparing the Probability Density Function (PDF) of these particles with a random process expressed with a Poisson distribution, the extent of particle clustering is estimated. Another well-established method determines particle dispersion via *Lyapunov exponents* [69]. The Lyapunov exponents estimate the rate of divergence and convergence of particle trajectories to compute particle clustering [70]. One of the most commonly used methods is Radial Distribution Function (RDF), which performs a scale-based cluster quantification [71, 72]. The RDF computes the probability of finding particles within a certain radial

distance from a reference particle. Thus, a higher number of particles within this radial distance indicates particle clustering, and a lower number of particles suggests voids. Another well-known method is *Voronoï analysis* in which the domain is divided into cells such that each cell contains only one particle [73]. In this case, the PDF of cell size (volume or area) compared with a Poisson distribution of a random process depicts the intensity of particle clustering. A higher probability of smaller cells suggests that particles are clustered.

1.3 Research Motivation

Particle clustering has been an active area of research due to its involvement in some crucial engineering applications, as stated earlier. In the aerospace sector, particularly, metallic particles are being extensively studied as a viable propellant, as space exploration is shifting to small (10-500 kg) and cost-effective satellites. This requires a replacement for the conventional cryogenic fuels, which are arduous to handle and store [74], and are often toxic [75]. Additionally, a joint venture of the Canadian Space Agency (CSA) and National Aeronautics and Space Administration (NASA), Lunar Gateway, and the construction of a space station on Mars requires frequent transportation of energy resources and other payloads [76, 77, 78, 79]. Conventional fuels are generally transported in a compressed (liquid) state, which makes their transportation impractical as this requires large storage tanks [80], while these particles can be stored in compact containers. Efforts are also underway to develop methods for preparing propellants from the raw materials available on the Moon and Mars [81, 82]. This field is known as In-Situ Resource Utilization (ISRU). As metals such as aluminum and iron are abundant in both of these extraterrestrial bodies, they can be processed to prepare these metallic particles [83, 84]. This will drastically reduce the size of a spacecraft by decreasing the quantity of the propellant it will carry at the launch, as the propellant for the return trip will be provided at the extraterrestrial station [85]. Thus, a substantial decrease in the manufacturing and operational costs of a spacecraft will be observed. Likewise, since the combustion of these particles does not

produce greenhouse gases, their use is environmentally friendly [86, 87].

Another major inspiration is solar particle receivers, where metallic nanoparticles dispersed in a carrier fluid are used as a heating medium [88, 89]. Here, a solar field consisting of heliostats concentrates sun rays onto a particle receiver. Particles absorb the solar rays and transfer this heat to a carrier fluid that is transparent to the sunlight. This heat can be used to produce hydrogen via water-splitting thermo-chemical processes [90], or for generating electricity with Brayton cycle [91]. The use of particles enables these systems to achieve temperatures upwards of 1000 °C [92], which is essential for achieving higher efficiency in these systems [93]. Considering its significant potential for extracting hydrogen, which is a great energy-carrying source and green power generation, research in this field is also gaining momentum.

Moreover, in cold spray advanced additive manufacturing techniques, particles with temperature below their melting point are accelerated to supersonic speed with a carrier gas, and their kinetic energy is used to form a bond with the substrate material upon impact [11]. Because cold spray techniques use low temperature, they offer numerous benefits [94]. Firstly, since the feedstock does not melt, particles retain their material and microstructure properties and do not undergo oxidation, which helps in avoiding material defects. This also results in superior coating strength, as it creates a more resilient and denser coating [95]. The low-temperature nature of this manufacturing technique also aids its use on substrates that are sensitive to temperature [96]. Thus, this technique is used in the aeronautical and automotive industries for coating materials to avoid chemical and mechanical wear [97, 98].

In the discussion above, three critical applications of particle-laden flows are highlighted as they are the primary motivation behind this research. Like most thermal applications, in particle combustion in a satellite engine and solar particle receiver, a uniform distribution of particles is essential for their efficient operation. On the other hand, in cold spray techniques, the effort is to keep the particles within the jet; albeit based on inertia, particles can disperse out of the jet [99]. Therefore, to ensure that particles are contained within

the jet and have high kinetic energy, the standoff distance between the nozzle and the target surface is kept small. However, past literature does not agree on the exact standoff distance [100]. In this case, a shorter standoff distance results in high residual stress in the coating, while a longer standoff distance will cause particle kinetic energy to drop and enhance particle travel in the radial direction. Both of these phenomenon drops the coating efficiency. Thus, in these applications, it is critical to predict the dispersion/clustering behavior of particles for optimum operation.

1.4 Problem Statement

As stated earlier, the St-based prediction of particle clustering is credible in isothermal conditions as St primarily models particle clustering as a particle and fluid dynamics effect (recall Equation (1.20)). But, since St is defined with the bulk or instantaneous values of the fluid parameters, it does not model the changes in the fluid variables in thermal applications. For example, in gas, the rise in temperature drops the local gas density and enhances viscosity. The decline in density at the location of particle clusters essentially creates a divergent flow field that pushes particles away [21], and can disintegrate clusters. Hence, this effect can lead to more uniform particle dispersion.

Conversely, the effect of change in fluid viscosity has been neglected in past studies. This is because, in most numerical studies where detailed local three-dimensional fluid data are available, fluid viscosity is often modeled as a constant for simplicity. This is particularly problematic because a common assumption in such numerical analysis is that if the particle-to-fluid density ratio is $\rho_p/\rho_f \gg 1$ then the only major force acting on the particles is the viscous drag force [39]. The rise in fluid viscosity with temperature increases the drag force on the particles. Thus, by keeping viscosity constant, this effect is completely overlooked. Furthermore, the change in fluid viscosity upon heating also alters the decay rate of turbulent kinetic energy [101], which changes the turbulent timescales and consequently the St. If particles are heated at different rates, the changes in turbulence characteristics

and St will only be observed if temperature-dependent viscosity is modeled. Note that in the thermal applications that inspired this research, particles rapidly receive and transfer heat to the local gas. This effect is further exaggerated by the small size of these particles, which gives them a higher effective surface area (ratio of particle surface area to volume). Thus, the aggressive heating of the gas at the location of particle clusters can considerably alter the local kinematic and thermodynamic properties of the fluid as compared to the fluid where there are little to no particles. This can lead to local mechanisms that can potentially influence particle clustering. In this case, particle clustering can be severely under- or overpredicted in sensitive applications such as propulsion applications, which can substantially modify the thrust profile.

Considering this unexplored aspect of particle clustering, in the present thesis, the clustering of inertial particles in different turbulent flows is investigated using Direct Numerical Simulations (DNS) to contribute to the understanding of particle behavior in applications where the thermodynamic changes in the local fluid are non-negligible.

1.5 Objectives

The objectives of this research are segregated based on four scientific questions that led to four independent studies, that are:

1. In a particle-laden flow consisting of more than one particle size (bidispersed in the present case), how does the temperature-driven viscosity affect the clustering of individual particle species? To analyze this, different size-based combinations of bidispersed particles were modeled in decaying HIT, in fluids with gas-like (viscosity increases with temperature) and liquid-like (viscosity decreases with temperature rise) viscosity. For modeling fluid viscosity, a power-law viscosity model was employed. To highlight this viscosity-based clustering, only the effect of fluid on the particles was modeled using OWC in momentum, while fluid-particle energy was modeled with TWC.

2. From the first study, a novel viscosity-driven clustering mechanism called Viscous Capturing (VC), was discovered. As per this mechanism, particles in a cluster get entrapped in a viscous cloud of gas upon heating via enhanced drag force. As a result, the clustering of heated particles increases with the rise in viscosity, and consequently, heated particles experience higher clustering compared to unheated particles under similar turbulent conditions. However, at this stage, the prerequisites for viscosity-based clustering to be dominant were unclear. To delineate this, viscosity-modulated clustering of heated bidispersed particles was investigated with different particle loading densities in decaying HIT. This is also crucial because, in the first study, a simplifying assumption was made that only fluid can influence the particles, while particles cannot exert a reaction drag force on the fluid (OWC). This back-reaction force of the particles can not only attenuate turbulence [26], but it can also potentially cancel out VC. This turbulence modulation is a direct function of particle loading density [27]. For this purpose, fluid-particle momentum and energy were modeled with TWC.

3. The second study brought forward two critical conditions that cause VC to take hold, that are: (1) particles should already be clustered before particle heating is initiated; and (2) these clusters should be large and unevenly distributed in space. Since these conditions are fulfilled at higher particle loading densities, the VC effect increases with particle loading density. Once VC takes effect, it is dominant enough that even the enhanced particle back-reaction force at elevated particle loading density cannot resist it. But, will it hold in a spatially and temporally evolving flow that is closer to practical applications such as cold spray advanced manufacturing? To answer this, particle clustering in a heated subsonic particle-laden jet flow was modeled. In this study, TWC was employed for fluid-particle momentum and energy interactions, and the dispersion of four different particle sizes was analyzed.

4. In the final investigation of this thesis, the radial dispersion of inertial particles in supersonic turbulent jet flow was scrutinized. As in supersonic jet flows, local

viscosity changes are overshadowed by the variation in the density field, therefore particle heating and local viscosity changes were not studied. Instead, the local mechanisms that cause particles of different inertia to disperse radially, density, and dilatation-based clustering of particles were assessed in this study.

It can be observed that the findings and the scientific questions originating from one study led to the subsequent analysis. Therefore, all four studies are tightly coupled. Moreover, these investigations started with a very fundamental approach and slowly transitioned to more applied aspects of the particle-laden flows to cater to the engineering applications that inspired this research.

Chapter 2

Role of Viscosity in the Preferential Concentration of Heated, Bidispersed Particles

Reference: A. Saieed, M. M. Rahman, and J. P. Hickey. Role of viscosity in the preferential concentration of heated, bidispersed particles. *International Journal of Multiphase Flow*, 155:104185, 2022, DOI.

Abstract

We study the effect of temperature-dependent viscosity on the PC of bidispersed, externally-heated solid particles in decaying isotropic turbulence via DNS. More specifically, we investigate the role of liquid- and gas-like viscosity–which respectively decrease and increase with temperature–on the PC of small and large particles due to turbulence. The bidispersed particles enhance the overall distribution compared to monodispersed flows as the voids created by the particles of one size are occupied by the other particles. Particle clusters emerge irrespective of the Stokes number although the clustering characteristics

differ based on the functional form of the temperature-dependent viscosity. When particles are externally heated in a variable viscosity flow, the Kolmogorov-based Stokes number, St_η, is not sufficient to predict PC. Increased clustering is observed, especially for small-sized particles, as the fluid is heated and turbulence decays. This increased clustering is explained through a VC mechanism in which the initial clustering, prior to the onset of heating, is responsible for the creation of local hot spots in the flow as the particles are heated. In a gas, these higher temperature regions have higher viscosity which causes other particles to be *captured* due to the increased drag. The increased drag of the gas results in a lower fluid-particle drift velocity as compared to the liquid, despite the significantly lower turbulent kinetic energy of the flow. The relative distribution of the particles as a function of vorticity and strain rate magnitude reveals a bimodal distribution in which a higher proportion of the particles aggregate in mid- and high-strain/vorticity regions as the turbulence decays.

2.1 Introduction

Particle-laden flows arise in many geophysical phenomena, such as water droplets carried in clouds and dust particles in the air. They are also increasingly prevalent in many modern engineering applications, such as metallic dust flames [102], and particle-laden solar receivers [103]. In these applications, the heat transfer between the solid and continuum phases (either gas or liquid) plays a defining role. Thus, efforts are directed at creating efficient interphase thermal transfer by promoting a homogeneous particle distribution within a turbulent flow.

Phenomenologically, the inhomogeneous particle distribution is predominantly the result of the centrifugal force from the vortices, which expels the particles from high vorticity to high strain rate regions in a turbulent flow [46, 71, 104]–this phenomenon is known as PC. As turbulence is a multi-scale process, the vortical-based justification remains incomplete in explaining clustering in high-Reynolds number flows. To extend this explanation,

it has been argued that particles gather in regions of zero acceleration [105, 106] which are located in the convergence zones between two or more coherent vortical structures in the flow [46]. Chen et al. [47] studied this phenomenon numerically and stated that the inertial particles tend to avoid the streamline curvatures of the flow field and gather at the points of zero-acceleration and advect with them. As the fluid acceleration is null at these points, there is no net force acting on the particles to change their position when the particles are moving at the local fluid velocity. On the other hand, another explanation of particle clustering was contributed by Chun et al. [49], where clustering at scales smaller than Kolmogorov length scales occurs due to the fluid-particle relative drift velocity, which brings them close to each other. Hence, although many proposed mechanisms explain particle clustering, including for compressible flows [53], there is a general consensus on the importance of particle clustering in turbulent flows.

PC creates zones of high-particle concentration and, by extension, zones of low-particle concentration. When the particles are heated, for example, through radiation [107] or induction [108], the heat is readily transferred to the continuum phase in the immediate vicinity of the particles, whereas the gas farther away experiences a delay in the heat transfer [109]. These two zones of high and low particle concentration are separated by a region of significant temperature (or any other scalar field) gradient known as *front* [48, 110]. Thus, particle clustering results in irregular heating, regions of unequal temperature distribution, and consequently uneven expansion of the gas. It was reported that PC can hinder the particle-to-gas heat transfer by up to 25% [19]. Hence, understanding the formation of these clusters and their impact on interphase heat transfer is crucial for state-of-the-art particle-laden flow applications with heat transfer.

The primary variables governing the particle dispersion are particle size and weight, as well as turbulence characteristics (defined mainly by the integral, Taylor and Kolmogorov scales) [111]. These parameters directly influence the particle Stokes number (St), which is considered to be the fundamental quantity regulating the particle distribution in a continuum phase [112, 113]. The Stokes number is a measure of the particle inertia as it relates the particle characteristic timescale (τ_p) with an appropriate turbulent timescale

(τ_f). Mathematically, it is expressed as [20]:

$$St = \frac{\tau_p}{\tau_f} \tag{2.1}$$

here τ_p is the time required for the particle to adjust to the changes in the flow field; a particle with small τ_p rapidly adapts to changes in the flow and vice versa. The mathematical definition of τ_p is [114]:

$$\tau_p = \frac{\rho_p d_p^2}{18\rho_f \nu_f} \tag{2.2}$$

where $\rho_{p/f}$, d_p and ν_f are the particle/fluid density, particle diameter and fluid kinematic viscosity, respectively.

The turbulent timescale, τ_f, can be defined based on a relevant characteristic timescale of the turbulence, such as Kolmogorov (τ_η) or integral (τ_l) timescales. There exists a general agreement that the PC is maximum at intermediate Stokes number; for St based on Kolmogorov scale, this corresponds to unity ($St_\eta \approx 1$) [115]. Particles with $St_\eta \ll 1$ closely espouse the flow streamlines, whereas $St_\eta \gg 1$ possess substantially higher inertia, which causes them to follow their own trajectory with a reduced influence of the small scale turbulence [116, 117]. However, it is also observed that clustering occurs at all Stokes numbers. In the literature, this is explained with two different St_η-based regimes. For particles with St_η less than unity, the primary reason for clustering is the centrifugal force as explained earlier [46]. Whereas, for particles with $St \geq 1$, the centrifugal force may not be the dominant cause of clustering. In this case, clustering is ascribed to a time-based *non-local* mechanism, where particles cluster due to the memory effect of them interacting with the turbulent flow field along their path history [50].

Determining the propensity of particles to cluster is more complex than simply looking at the Stokes number. As seen in the above discussion, τ_η is commonly used for defining particle distribution and St, since clustering is primarily governed at the dissipation scale [117, 118]. Yet, the choice of an appropriate timescale is more nuanced as the particle response to turbulence depends on the particle size [58]. This is particularly important in polydispersed flows, which contain a range of particle sizes. Additional complexities arise

when the particles are externally heated. As can be observed from Equation (2.2), the particle relaxation time can change as the local fluid viscosity and density–both a function of temperature–about the heated particles vary with time and space. The change in the particle timescale is a function of the state of the fluid: in a gas, the viscosity increases with temperature, whereas it decreases in a liquid. In both phases, the fluid density (generally) decreases with the increase in temperature, although the magnitude of the change is much greater in gas, assuming the liquid does not undergo a phase change. Therefore, these critical factors govern the value of the St and, concomitantly, impact the distribution of the particles.

In addition to the temporal change of the particle timescale, the turbulence characteristics are modified in a temporally evolving flow. In this regard, the Kolmogorov (τ_η) and integral (τ_l) timescales are given as:

$$\tau_\eta = \left(\frac{\nu}{\varepsilon}\right)^{\frac{1}{2}} \tag{2.3}$$

$$\tau_l = \frac{(\mathrm{TKE})^{\frac{3}{2}}}{\varepsilon \ u_{rms}} \tag{2.4}$$

In these equations, TKE is the turbulent kinetic energy and ε is the dissipation rate of TKE. Thus, as turbulence decays, τ_η starts to increase as ε decreases. While, TKE, ε and u_{rms} simultaneously drop in such a way that τ_l depicts an overall decreasing trend as per Equation (2.4). Similarly, in accordance with Equation (2.1), as the turbulence decays, St_η decreases, while St_l increases. This contradictory response of large and small timescales towards decaying turbulence can play a significant role in the distribution of particles that are of different sizes. This is especially critical if the particles are heated, as it also varies the local density and viscosity. This is crucial in practical applications where a range of particle sizes exists [119], which correspond to a variety of St at any given instance [67]. Therefore, ensuring the uniform distribution of polydispersed particles is a remarkably convoluted task.

Although most of the previous literature is focused on the numerical [120, 121, 122] and experimental [123, 73] understanding of monodispersed particle-laden flows, a number

of studies have also been conducted on the behavior of polydispersed cases. Saw et al. [67] compared the clustering characteristics of a polydispersed and monodispersed flow. By using DNS, they modeled polydispersed flow comprising 250 discrete St_η between 0.01 and 1.2, and revealed that different species of particles gather in different locations in the flow. Zhou et al. [112] also reported a similar observation in bidispersed flows. Therefore, a better overall particle distribution is obtained in polydispersed particles. Likewise, Ayala et al. [124] studied polydispersed flows and reinforced this observation by reporting that particles of different sizes respond to different scales of turbulence. Additionally, the enhancement in particle distribution in bidispersed flows was also attributed to the difference in acceleration of the two particle sizes (high particle-particle relative velocity), which results in superior diffusion [66]. Saw et al. [125] studied the clustering and coalescence of droplets in a range of St_η. Considering that clustering is most pronounced at the dissipation scale, they used the Kolmogorov scale to characterize the particle distribution. It was observed that in polydispersed flows at $St_\eta \ll 1$, the particle clustering enhances with the increase in St_η, similar to monodispersed flows [49]. Pan et al. [126] further added that for large particles with $St_\eta > 1$, the clustering intensity dwindles with the increase in St_η. The turning point between these two trends is $St_\eta \approx 1$, where maximum PC occurs [127].

The dispersion characteristics of heated polydispersed particles have not gained much attention, as most of the research on heated particle-laden flows has focused on monodispersed particles [22, 128]. In this regard, a pioneering study was reported by Rahmani et al. [129] in which they compared the distribution of radiatively heated mono- and polydispersed Nickel particles in a turbulent channel flow. At low St_η, they did not notice any significant difference in the distribution of mono- and polydispersed particles. However, at intermediate and reasonably high St_η ranging from 0.08 to 0.85 and 0.21 to 2.31, polydispersed particles showed substantially better particle distribution than their monodispersed counterparts. In addition, polydispersed particles resulted in a more uniform temperature of the gaseous phase. They also explained this even particle and temperature distribution by the difference in centrifugal force acting on the inertial particles of dissimilar sizes, which causes them to gather in distinct regions around the same vortex. Thus, this size-wise clus-

tering of polydispersed particle flow results in a better homogeneity in the aggregate.

Based on the discussion above, a fundamental scientific question that deserves closer scrutiny is the effect of fluid viscosity on the grouping of heated particles, as it has not been studied hitherto. The importance of temperature-dependent gas viscosity on the particle distribution was noted by Mouallem and Hickey [101]. By inductively heating particles with different heating response times in gas, they observed, unsurprisingly, an increased TKE decay rate when particles were heated rapidly. However, the influence of the viscosity on clustering was not the main focus of their study. Hence, it is possible that PC is affected by the temperature-dependent viscosity, since the fluid timescales directly govern the evolution of St_l and St_η in decaying turbulence. If this is true, then our existing knowledge of heated particle distribution might not be directly applicable to clustering sensitive applications.

Considering the discussion above, in this contribution, we conduct DNS to understand the distribution of heated bidispersed particles with a liquid- and gas-like temperature-dependent viscosity in decaying isotropic turbulence. Hence, Section 2.2 expands on the methodology employed in this research. The obtained results are discussed in Section 2.3, and Section 2.4 outlines the summary the present work.

2.2 Methodology

In this study, DNS were carried out using a highly parallelized (the code runs on multiple processors in parallel using Message Passing Interface (MPI) scheme) finite difference, open-source code, namely the Pencil-Code [130]. This code was extended to include temperature-dependent viscosity–following a power-law–of a representative liquid- and gas-like phase. Three cases, with different bidispersed particle sizes, are simulated with liquid- and gas-like temperature-dependent viscosity; comparative constant viscosity simulations are also investigated. The fluid and particles were respectively modeled using Eulerian and Lagrangian point particle tracking schemes. A tri-linear interpolation of the continuum phase was used to advance the particle position. For the fluid-particle momen-

tum integration, a collisionless, OWC scheme was employed in order to isolate the effect of temperature-dependent fluid viscosity on particle dispersion. A similar approach was adopted by Carbone et al. [110] for investigating the interaction of fluid-particle temperature fields. On the other hand, for the energy equation, a TWC was selected. A sixth-order finite difference method is employed for spatial derivatives, and a third-order Runge-Kutta scheme is used for time marching.

Particle-laden decaying HIT was simulated in a cubic box of characteristic length 2π using 384^3 grid cells, and periodic boundary conditions were imposed in all three spatial directions. A total of $500,000$ spherical particles, of two different sizes, were randomly dispersed in the domain. To investigate various effects of particle St, three initializing simulations with different bidispersed particle sizes were first simulated, without heating, and with a solenoidal forcing term in order to sustain the HIT [131] prior to the turbulence decay. These initializing simulations will be referred to as *base cases* in the text. The initializing simulations were run for about 4-5 eddy turnover times, which allowed for the stabilization of the turbulence characteristics such as the root-mean-square velocity (u_{rms}).

Before discussing the parameters of this article, note that all simulation parameters are presented in consistent but arbitrary units. Although the variable density Navier-Stokes equations were solved, both gas- and liquid-like cases were run at a nearly incompressible limit. The Mach number of the simulations at the start of the turbulent decay was 0.086 based on the maximum local velocity. For the flow field initialization (prior to the particle heating and turbulence decay), the particle temperature was stabilized to 300; thus, for the initialization, we assume a constant viscosity. To sustain the turbulence, a forcing was applied at a low wavenumber to provide energy to the larger eddies; the forcing wavenumber was $k = 1.5$, which is almost equal to the minimum wavenumber of the simulation ($k = 1.29$). The Taylor-based Reynolds number ($Re_\lambda = u_{rms}\lambda/\nu_f$, where λ is the Taylor length scale) of 98 is achieved once the flow is fully developed. Similarly, $k_{max}\eta \approx 10$ was obtained in the present study, which ensures the complete resolution of the small scales [3]. Where k_{max} is the maximum wavenumber. The turbulence characteristics, at the end of the initialization, are listed in Table 2.1. These parameters are identical in the three base

Table 2.1: The characteristics of the fully developed HIT.

Variable	Symbol	Liquid Cases	Gas Cases
Taylor Reynolds number	Re_λ	94	98
Turbulent Reynolds number	Re_T	489	510
Average root-mean-square velocity	u_{rms}	0.40	0.52
Turbulent kinetic energy	TKE	0.10	0.13
Rate of dissipation	ϵ	0.0048	0.0050
Turbulence forcing length scale	L_{force}	4.19	4.19
Kolmogorov timescale	τ_η	0.84	0.84
Kolmogorov length scale	η	0.053	0.053
Integral timescale	τ_l	14.58	19.59
Integral length scale	l	6.59	9.37

cases due to OWC in the momentum equation, as the only difference between the base cases is the particle size. As seen in Table 2.1, two slightly different time instances were selected as initial conditions for the gas- and liquid-like simulations. Since the decaying viscosity of the liquid imposed a more stringent resolution requirement, a time instant with a slightly lower turbulence intensity was selected. The gas simulations were initialized at a later time instant, which had a higher instantaneous turbulent kinetic energy. Despite the instantaneous difference in the turbulent kinetic energy between the gas and liquid cases, the overall turbulence statistics remain similar.

After initialization–and once the statistically steady state was achieved–the forcing was turned off and particle heating was initiated. For each of the three statistically-steady base cases, two different temperature-dependent viscosity models were used to account for the viscous effects during the turbulence decay: (1) an increasing viscosity with increasing temperature model, which corresponds to the typical viscosity behavior of a gas, and (2) a decreasing viscosity with increasing temperature model, which corresponds to a liquid. The functional form of these viscosity models is presented in the next subsection. For

Table 2.2: Combinations of small and large particle radii and the corresponding St_l and St_η at $t = 0$ of the gas and liquid simulations with heating.

Base Case	1		2		3	
Particle Species	Large	Small	Large	Small	Large	Small
Particle Radius	0.0047	0.0012	0.0106	0.0028	0.0183	0.0028
Stokes Number	St_l	St_η	St_l	St_η	St_l	St_η
Gas	0.10	0.19	0.46	0.94	1.40	0.95
Liquid	0.21	0.22	1.10	1.11	3.30	1.11

simplicity, we neglect the phase change that could arise in the liquid-like case.

The particle radii along with corresponding integral-scale Stokes number St_l (large particle) and Kolmogorov Stokes number St_η (small particle) values at $t = 0$ of the three gas and liquid simulations are listed in Table 2.2. As shown in this table, in the present study, we refer to the small particles only by St_η and the large particles by St_l, recognizing that these Stokes number definitions can be used to define both particle sizes. We selected this notation to simplify the discussion as we know that the motion of small and large particles is primarily governed by Kolmogorov and integral timescales, respectively. Considering Table 2.2, from here onward each of the six simulations (three base cases each with gas and liquid) will be referred by the phase of the carrier fluid (either liquid or gas) and its corresponding base case number (either 1, 2 or 3 with differing particle sizes). For instance, Gas 1 stands for gas phase and base case number 1, while Liquid 1 represents liquid carrier phase and base case 1 of small and large particle radii. The particle heating, as discussed later, is the same in all cases.

2.2.1 Carrier Phase

The governing equations of the fluid mass, momentum and energy conservation are as follows [132]:

$$\frac{\partial \rho_f}{\partial t} + \frac{\partial \rho_f u_{f,i}}{\partial x_i} = 0 \tag{2.5}$$

$$\frac{\partial \rho_f u_{f,i}}{\partial t} + \frac{\partial \rho_f u_{f,i} u_{f,j}}{\partial x_j} = -\frac{\partial P_f}{\partial x_i} + \frac{\partial \mu_f}{\partial x_j}\left(\frac{\partial u_{f,i}}{\partial x_j} + \frac{\partial u_{f,j}}{\partial x_i} - \frac{2}{3}\frac{\partial u_{f,k}}{\partial x_k}\delta_{ij}\right) + F_i \tag{2.6}$$

$$\frac{\partial \left(\rho_f c_{f,v} T_f\right)}{\partial t} + \frac{\partial \left(\rho_f c_{f,p} T_f u_{f,j}\right)}{\partial x_j} = \frac{\partial}{\partial x_j}\left(\kappa_f \frac{\partial T_f}{\partial x_j}\right) + Q_{pf} \tag{2.7}$$

where P and T are the thermodynamic pressure and temperature, while u_i is the fluid velocity in i^{th} direction. Similarly, κ_f, $c_{f,p}$, and $c_{f,v}$ are the fluid thermal conductivity, specific heat at constant pressure and volume, respectively. We note that the thermal conductivity is computed based on a constant Prandtl number assumption, whereas the viscosity was computed using a power-law, as described below. F_i is the forcing term, which was prescribed to develop HIT during the initialization; this term is $F_i = 0$ once the particles are heated and the turbulence decays. Given the low Mach number, the conservation of energy only accounts for the internal energy, which is a function of temperature. Note that the gravitational force was neglected in our study.

As per the above-stated objectives, two temperature-dependent viscosity models were implemented. The other thermophysical properties of the fluid, such as specific heat, were not modified. This is obviously a simplification as the viscosity can be defined from a molecular dynamic perspective and it is dependent on the thermodynamic properties of the fluid. Also, from a molecular dynamics perspective, it is expected that changes in the viscosity will be mirrored by changes in thermal conductivity, which are also not modified between our gas- and liquid-like simulations. Finally, we do not account for phase change in the liquid-like simulation. These simplifications, albeit slightly reductive of the actual physics, were consciously made to clearly isolate the temperature-dependent viscous effects from the other thermophysical aspects of the flow. Based on this, the power-law form of

the gas viscosity is:

$$\mu_f = \nu_{f,0}\rho_f \left(T/T_0\right)^{\frac{2}{3}} \tag{2.8}$$

here μ_f is the dynamic viscosity, while subscript 0 represent a reference value. To model the liquid-like viscosity, the mathematical expression is:

$$\mu_f = \nu_{f,0}\rho_f \left(T_0/T\right)^{\frac{2}{3}} \tag{2.9}$$

Comparing Equations (2.8) and (2.9), it is clear that the gas and liquid viscosities are identical except for the inverted temperature ratio. The initial kinematic viscosity in the base simulations was 0.0034. For brevity, we will denote the simulations as a *gas* when Equation (2.8) is used, and as a *liquid* when the viscosity is defined with Equation (2.9). As we are using the ideal gas law to relate the thermodynamics in both cases (albeit at a very low Mach number), we are formally not simulating a true liquid but, instead, isolating the effects of change in fluid viscosity with temperature on particle distribution, as discussed above. It should be noted that T_0 in these expressions is 273, which was taken as the initial temperature of the base simulations. Therefore, once the heated simulations of the gas and liquid carrier phases were started, their corresponding viscosities underwent a slight readjustment, which was small enough that it did not affect the consistency of the results. Also note that in Section 2.3 normalized dynamic viscosity ($\mu* = \mu_f/\mu_{f,0}$, where $\mu_{f,0}$ is the reference dynamic viscosity just before heating) will be employed for analysis.

In this analysis, the $c_{f,p} = 1$ and adiabatic index $\gamma = 1.4$. Thus, $c_{f,v} = 0.714$, which is similar to an ideal gas. To ensure a higher thermal relaxation time τ_t (as discussed in Section 2.2.3), $\kappa_f = 0.2$ is used. Considering that the motivation of this research is the combustion of metallic particles in an inert gas for propulsion application, this value is close to the κ_f of Helium.

2.2.2 Particulate Phase

The Lagrangian equations of motion for the particles are:

$$\frac{dx_{p,i}}{dt} = u_{p,i} \tag{2.10}$$

$$\frac{du_{p,i}}{dt} = \frac{C_D}{\tau_p}\left(u_{f,i}\left(x_{p,i}\right) - u_{p,i}\right) \tag{2.11}$$

where $u_{p,i}$ and $u_{f,i}(x_{p,i})$ are the particle velocity at i^{th} position and local fluid velocity at the particle position $x_{p,i}$. The term C_D is the drag coefficient experienced by each particle dispersed in the carrier phase. It is a function of the local flow Reynolds number (Re) and is defined based on the Schiller-Naumann correlation [133]:

$$C_D = 1 + 0.15Re_p^{0.687} \tag{2.12}$$

here Re_p is the particle Reynolds number:

$$Re_p = \frac{d_p|u_i - u_{p,i}|}{\nu_f} \tag{2.13}$$

where $|u_i - u_{p,i}|$ represents the local velocity difference between the fluid and particle.

2.2.3 Heating Module

Particles were externally heated using the model proposed by Mouallem and Hickey [101]. The particle heating term Q_p is mathematically given as:

$$Q_p = m_p c_p \frac{(T_{max} - T_p)}{\tau_{heat}} \tag{2.14}$$

here T_{max} represents the maximum temperature the particles can reach from the external heat source, and τ_{heat} is the timescale of the particle heating which was unity in our simulations. As per Equation (2.14), heat flux is a function of $T_{max} - T_p$, which is realistic since in most thermal applications, the heat flux drops as the maximum temperature is approached. Readers are referred to Mouallem and Hickey [101] for more details.

Additionally, particle-fluid heat transfer Q_{pf} can be defined as:

$$Q_{pf} = \frac{m_p c_p \ Nu_p}{2\tau_t}\left(T_p - T_f(x_p)\right) \tag{2.15}$$

In Equation (2.15), m_p, Nu_p, T_p and c_p are the mass, Nusselt number, temperature, and heat capacity of the particles, respectively. The term $T_f(x_p)$ it the temperature of the

local fluid at the particle location. Similarly, τ_t is the thermal relaxation time which was prescribed as 10 in our study. Based on this, the thermal Stokes number ($St_{th} = \tau_t/\tau_\eta$) of the particle heating is 11.9. Note that a smaller value of τ_t correlates to a faster transfer of heat from the particles to the carrier fluid. While, Nu_p was computed using Ranz-Marshall equation [134]:

$$Nu_p = \frac{h_p d_p}{\kappa_f} = 2 + 0.6 Re_p^{0.5} Pr^{0.3} \tag{2.16}$$

here Pr is the Prandtl number ($Pr = \mu_f c_p/\kappa_f$), and h_p is the convective heat transfer coefficient.

2.2.4 Radial Distribution Function

Since the primary focus of this study is to analyze clustering in bidispersed flows, the distribution of the particles was studied by evaluating the RDF. It is a statistical method that computes the probability of finding particles at a certain distance from a reference particle. The RDF is mathematically defined as:

$$\text{RDF} = \frac{dN_p(\text{r})}{4\pi r^2 n_0 \text{dr}} \tag{2.17}$$

As per the above equation, the RDF of unity represents the uniform distribution, while higher values indicate clustering [135]. In Equation (2.17), $dN_p(r)$ is the number of particles that lie within the distance r and $r + dr$ from the reference particle and n_0 stands for the particle concentration per volume. For this analysis, separate RDF curves were evaluated for large and small particles for a better understanding of their clustering behavior. These plots will be discussed in Section 2.3. There are other methods of determining particle clustering, such as Voronoï analysis [136] and box counting [68], yet for this study RDF was preferred as it is the most widely accepted method for characterizing PC [137].

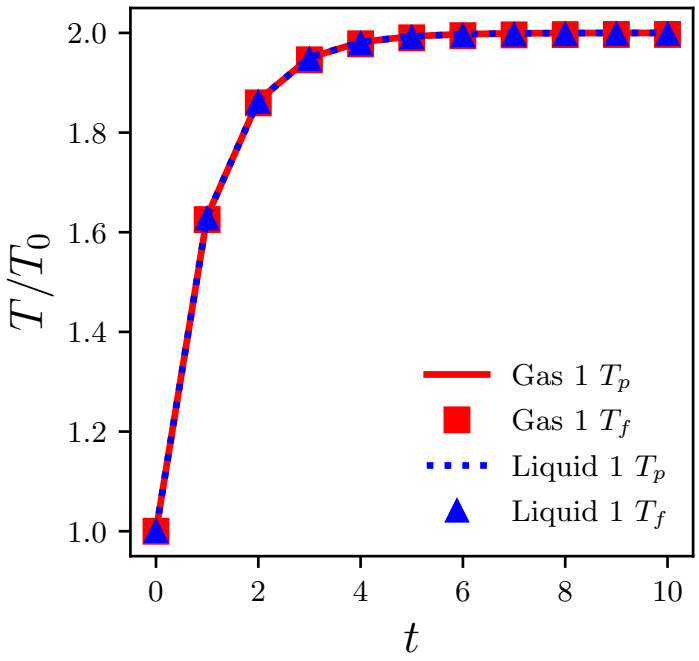


Figure 2.1: Comparison between the evolution of the particle and fluid temperatures normalized with temperature at $t = 0$ of heating.

2.3 Results

To assess the heat transfer characteristic between the dispersed and continuum phases, the evolution of the particle and fluid temperatures in the decaying HIT for Gas 1 and Liquid 1 are analyzed. Here, the average particle and fluid temperatures normalized with the initial temperature at $t = 0$ was computed during the turbulence decay, as shown in Figure 2.1. As expected, the particle and fluid temperature curves for both test cases perfectly overlap. This is due to the fast thermal timescale of the heat transfer ($\tau_t = 10$), which depicts a rapid adaptation of the fluid temperature to the temperature of the particles. The obtained curves can be divided into two heating regimes following the study by Pouransari and Mani [19]. Here, the initial rapidly rising temperature, until about $t = 4$, is called the

fast initial particle heating, while the flat section of the curve is called *slow mixture heating*. Similar particle heating plots were reported by Bae et al. [138], Mouallem and Hickey [101], Rahmani et al. [129] and Dai et al. [139]. Hence, a good particle-fluid coupling is obtained for both liquid and gas simulations.

2.3.1 Evolution of Timescales

As stated earlier, in decaying HIT the evolution of St_l (the larger of the bidispersed particles) and St_η (the smaller of the bidispersed particles) is primarily governed by the respective characteristic timescales of the turbulence. In this regard, Figure 2.2 shows the evolution of the turbulence timescales, namely τ_l (integral) and τ_η (Kolmogorov), normalized with their respective values at $t = 0$–at the start of the turbulence decay. Since all the base cases of gas and liquid perfectly overlapped due to momentum OWC, only Gas 1 and Liquid 1 are shown in this figure. Note that upon heating, the gas and liquid viscosities varied from 1.0 to 1.7 and 1.0 to 0.6, respectively. A heated, Constant Viscosity (CV) case was also simulated–with a bidispersed particle size identical to Gas 2 and fixed viscosity ($\mu*$), the value of which is shown in the brackets. This comparative case is plotted as a reference. Gas 2 is selected as a reference case for this and the following plots as it showed maximum clustering among all the cases considered, see Section 2.3.3.

In Figure 2.2, the timescales of the liquid and gas cases follow the expected trends: τ_l monotonically decreases, while τ_η increases as the TKE decays in the continuum phase. We note that the slopes of these timescales are substantially different between the gas and liquid cases. Notably, the τ_l curve is steeper in the gas phase in comparison to the liquid. This can be attributed to the rise in gas viscosity with temperature which results in greater viscous dissipation giving τ_l, and consequently the TKE, a rapid decay rate (see Figure 2.3).

In terms of τ_η, it can be noticed that in liquid, τ_η initially increased and then decreased until $t = 4$ before rising again. By expanding the definition of τ_η in Equation (2.3), we see that the Kolmogorov timescale is inversely proportional to the average spatial gradients

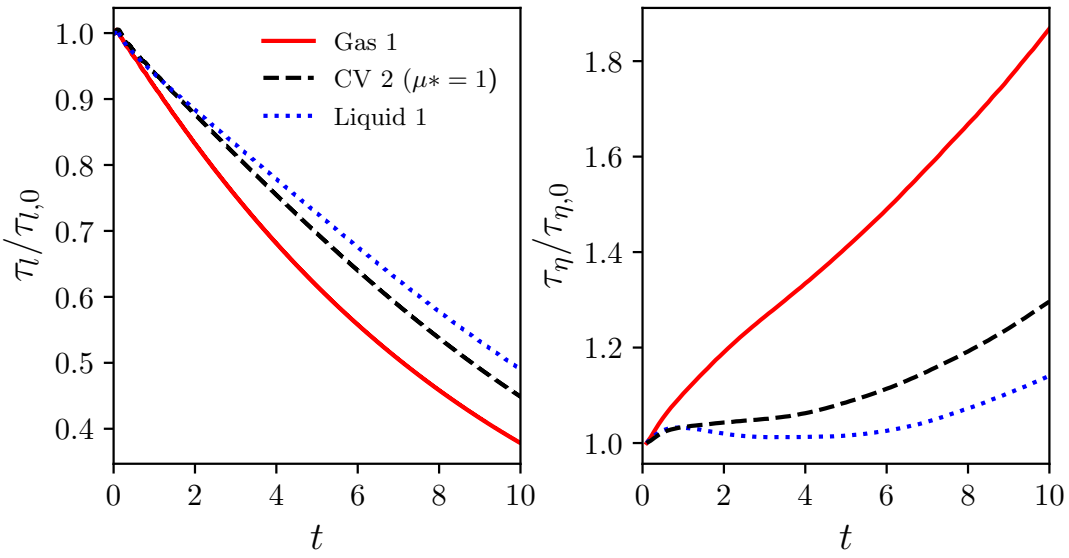


Figure 2.2: Evolution of normalized τ_l (left) and τ_η (right) with the flow time.

of the velocity fluctuation (the viscosity cancels out). As the liquid initially heats up–and the viscosity drops–the rapid readjustment causes the average velocity gradients to fall (resulting in an increase in τ_η). After the initial transience, the lower viscosity of the flow increases the effective Reynolds number (temporarily reducing τ_η) until around $t = 4$, when the bulk viscosity/temperature of the fluid starts to plateau (recall Figure 2.1) and viscous decay takes hold (increasing τ_η).

Comparing Gas 1 and Liquid 1 plots with CV 2 ($\mu* = 1$) also immediately highlights the significance of temperature-dependent viscosity and its potential impact on particle distribution. To further test this effect, Gas 2 was also simulated with no heating (not shown here) and it was found that, except for the initial TKE surge due to aggressive heating, the heated and non-heated Gas 2 cases nearly overlapped. This clearly suggests that heating alone (at constant viscosity or for a similar change in viscosity) does not significantly affect the TKE decay rate. It is the change in viscosity of different cases that alters the rate of TKE decay. This further supports the motivation of this study.

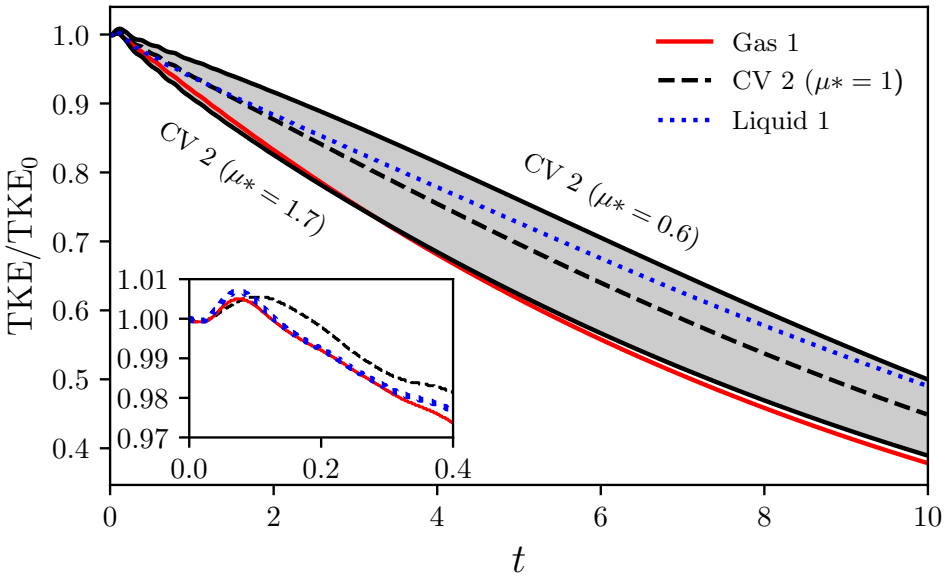


Figure 2.3: Variation in normalized TKE with respect to the flow time. The shaded area represents the boundaries of TKE (solid black lines) as the viscosity increases from 0.6 to 1.7. Here only Gas 1 and Liquid 1 cases are shown as all gas and liquid cases overlapped due to OWC.

2.3.2 Evolution of Stokes Number

Figure 2.4 (left) shows the change in St_l (large particles) over time. In this plot, there are two critical concepts. Firstly, even though all cases display an increase in St_l with time, the rise in the liquid cases was much greater than their gas counterparts. This can be attributed to the simultaneous rise in τ_p and decrease in τ_l (both contributing to a rise in St_l) as the fluid heats up and viscosity drops. Secondly, at the beginning of each simulation, the St_l of the gas curves shows a small dip before monotonically rising from about $t = 1$. However, the liquid cases show a sharp increase at the early times. This behavior is also true for Gas 1 and Liquid 1, although it is not evident from the plot due to the scale of the other curves. This initial transience is the result of a sudden rise in TKE (see Figure 2.3)

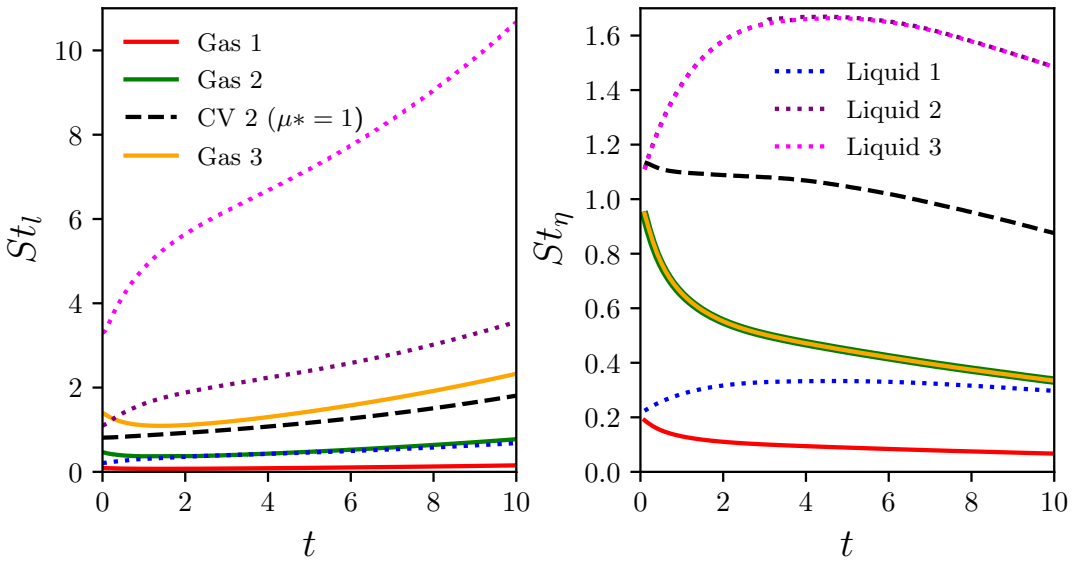


Figure 2.4: Evolution of St_l (left), large particles, and St_η (right), small particles, with time.

and rapid adaptation of the flow to the sudden heating. As discussed earlier, the higher viscosity of gas was able to quickly dissipate this energy spike, resulting in a rapid drop of St_l at the early times. The difference in gas and liquid St_η plots is also attributed to the aforementioned reasons. We note a consistent change in the slope of St_η in the liquid cases at about $t = 4$. This corresponds to the time at which particle temperature stops increasing (recall Figure 2.1); thus viscosity stops decreasing and remains constant. At this point, the liquid cases demonstrate a monotonically decreasing St_η. Additionally, notably different curves of Gas 2 and CV 2 ($\mu* = 1$) again highlight that the Stokes number behavior–especially St_η–is a strong function of temperature-dependent viscosity.

2.3.3 Quantification of Particle Clustering

For analyzing the preferential clustering, the RDF was computed at three characteristic time instances: at $t = 1$, 10, and the timestep at which TKE has decreased by half between

$t = 0$ and 10. These timesteps were selected as they represent the characteristic snapshots of the flow evolution, where $t = 1$ depicts the state of particles shortly after the heating was initiated. The time $t = 10$ was chosen to delineate the state of the flow after a significant drop in TKE. The point of half TKE decay represents the mid-point between these two limit states. Considering the faster TKE decay rate in gas as depicted in Figure 2.3, the TKE of gas halved at about $t = 4$, whereas for the liquid this was observed around $t = 5$.

RDF at $t = 1$

It can be seen in Figure 2.5 (A) that except for Gas 1 and Liquid 1 (characterized, at the start of the turbulence decay, by $St_\eta = 0.19$ and 0.22, respectively), the smaller particles had a greater propensity towards clustering than the larger particles. This can be attributed to the fact that the small particles, in cases 2 and 3, have St_η close to unity. It can also be observed that both liquid and gas cases (for the same base case number) show nearly identical RDF curves. This is also because at $t = 1$, the corresponding base cases of gas and liquid have St_η equally distant from unity (Figures 2.4), and the viscosity change remains modest after this short time evolution. The reduced clustering of the smaller particles in Gas 1 and Liquid 1 (compared to the base cases 2 and 3) is due to their much smaller St_η values. At $t = 1$, St_η of Gas 1 was 0.13 and for Liquid 1 it was 0.29. Since these values are significantly smaller than unity, these smaller diameter particles depicted substantially less clustering. This behavior of small particles of Gas 1 and Liquid 1 was observed throughout this study.

In terms of large particles (Figure 2.5 (B)), at $t = 1$ Gas 1 and Liquid 1 depicted the maximum clustering. This is because the large particles in this base case have the smallest diameter compared to the other base cases. Thus, they are most easily affected by the integral scale eddies. Conversely, the large particles of the other gas and liquid cases are not as readily influenced by the turbulence, hence they showed less clustering. The large particles in this study also retained this characteristic clustering pattern at the other two timesteps.

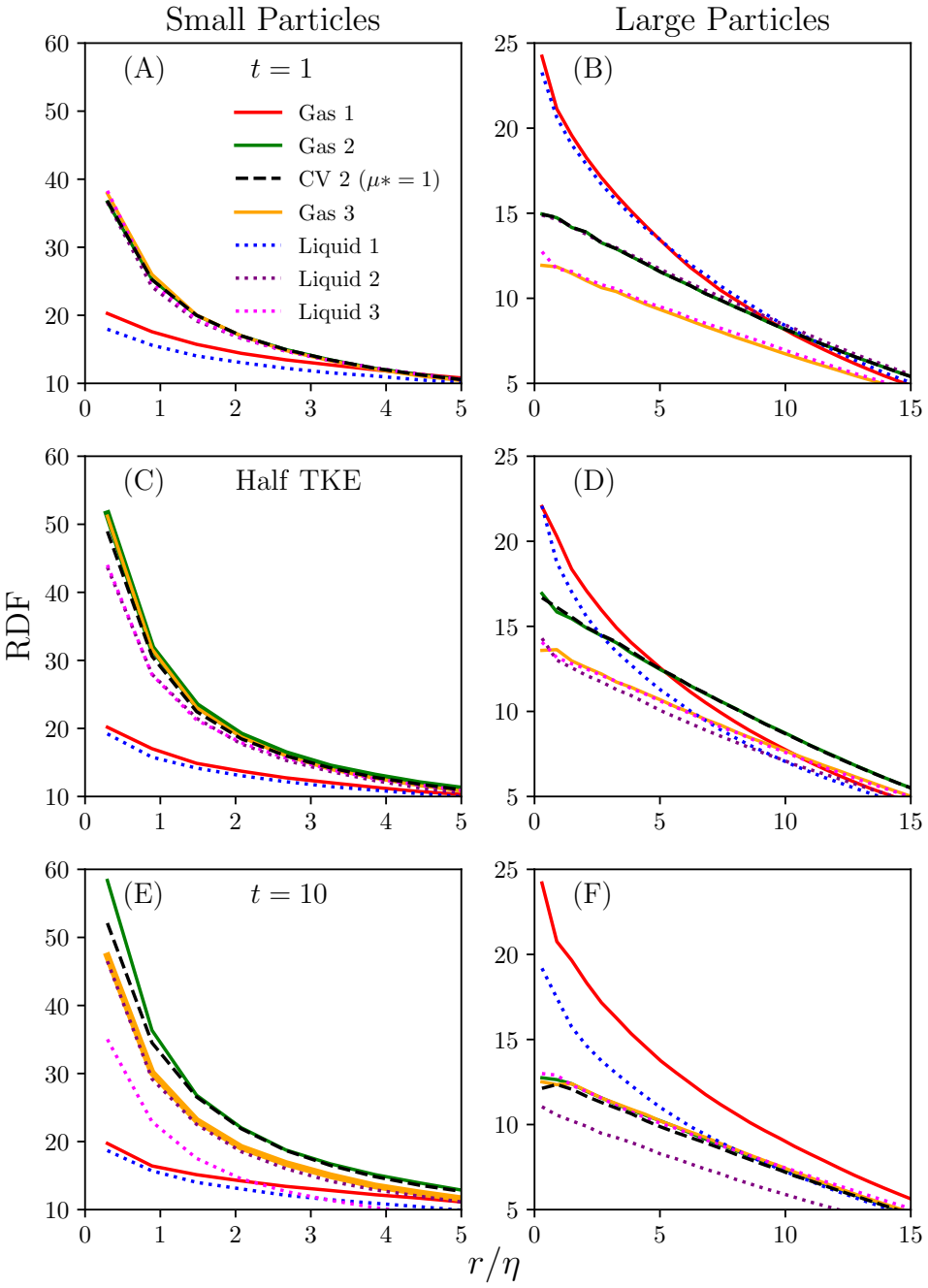


Figure 2.5: RDF of the small (left column) and large (right column) particles at $t = 1$, half TKE and $t = 10$.

RDF at Half TKE

Figure 2.5 (C) shows the RDF plots of small particles at about the midpoint during the TKE decay. As the TKE has decayed considerably, the gas and liquid RDF curves of the smaller particles start to show larger discrepancies. This is because particle clustering lags behind the thermodynamic and kinematic changes in the flow–particle clustering is a reaction to these changes. Additionally, at this time instant, both gas and liquid cases have reached their final viscosity (recall temperature evolution in Figure 2.1). Here, Gas 2 and 3 both have $St_\eta = 0.47$, thus their RDF curves are not only alike but they also display the highest clustering at this stage. Similarly, the small particles in Liquid 2 and 3 have RDF curves that collapse and show significant clustering as their $St_\eta = 1.67$. Note that despite having $St_\eta < 1$, Gas 2 and 3 showed higher clustering than Liquid 2 and 3. This could be because of the higher viscous push on the particles in gas which causes them to gather in the convergence zones. Another possible reason is the VC of the particles in different high-viscosity regions in gas which is described in Section 2.3.4. Moreover, as per Figure 2.5 (C), the small particles of Gas 1 and Liquid 1 show almost equal level of clustering at half TKE, despite having significantly different viscosities and St_η values. Here, in Gas 1 the $St_\eta = 0.09$ is much less than in Liquid 1 ($St_\eta = 0.33$), yet the lower viscosity/drag force in the liquid enhanced particle dispersion.

RDF at $t = 10$

Figures 2.5 (E) and (F) show the RDF plots of small and large particles at $t = 10$. Here, because of the significant decay in the TKE, the difference between small and large particles is the most prominent. In Figure 2.5 (E), Gas 2 (small) showed the highest level of clustering with $St_\eta = 0.33$. While, despite having similar St_η, Gas 3 (small) adopted the second highest peak. A similar trend can be seen in Liquid 2 (small) and Liquid 3 (small) as both cases had $St_\eta = 1.48$. This pattern is particularly interesting as each carrier fluid phase has identical viscosity in base cases 2 and 3. However, even though the smaller particles of base cases 2 and 3 are equal in size, the larger particles of base

case 2 are smaller than those of base case 3. Therefore, the larger particles of base case 3 generate more heat and, as a result, more aggressively transfer this heat to the surrounding fluid. This altered the local turbulence field by decreasing the local density and caused the particles of base case 3 to be pushed away, yielding less clustering in Gas 3 and Liquid 3.

Comparing Figures 2.5 (A), (C) and (E) highlights a critical effect. As the TKE decayed, the St_η dropped in Gas 2 and 3 from $St_\eta = 0.65$ at $t = 1$ to $St_\eta = 0.33$ at $t = 10$, yet these base cases still showed the highest clustering at all three timesteps. This contradicts the trend in literature that $St_\eta \approx 1.0$ corresponds to the maximum clustering. Moreover, higher clustering in Gas 2 and 3 cannot be attributed to the non-local mechanism (recall Section 2.1), as in the present simulations Gas 2 and 3 did not experience $St_\eta \geq 1$ at the previous timesteps. On the other hand, Liquid 2 and 3 did not deviate from the classical particle distribution behavior at any timestep. Hence, it can be stated that with increasing viscosity, the clustering behavior is decoupled from St_η. In other words, as the flow is temporally evolving, maximum clustering will not necessarily be observed at $St_\eta \approx 1.0$ as seen in classical particle-laden flows. Instead, the VC effect, discussed below, which is tied to the history of the particle evolution in the flow is more important. This highlights that St_η alone cannot be used for predicting clustering in externally heated particles. This explanation is further tested by comparing Gas 2 and CV 2 ($\mu* = 1$) plots in Figure 2.5. As per Figure 2.4, the St_η of CV 2 ($\mu* = 1$) in general monotonically dropped from 1.1 at $t = 1$ to 0.87 at $t = 10$. Hence, at all three timesteps the St_η of CV 2 ($\mu* = 1$) was close to unity. In this regard, if fluid temperature-dependent viscosity (VC) was not dominantly controlling particle clustering, then the smaller particles of CV 2 ($\mu* = 1$) should have depicted the highest clustering. Yet, it is evaluated to be below Gas 2, even though Gas 2 St_η is less than half of CV 2 ($\mu* = 1$), especially at $t = 10$.

Heating and Decaying TKE Effects

Thus far, we have discussed the aggregate effects of particle heating within decaying turbulence. Since both the heating and decaying turbulence can individually influence particle

clustering, in this subsection, we seek to delineate the influence of each of these effects. This is also important because we want to check if higher clustering, for instance at $t = 10$, is just the result of clusters taking time to develop, or if their formation is the direct result of thermodynamic and kinematic changes in the flow. Considering this, we have conducted additional simulations with sustained turbulence (forced TKE), namely with (both a gas- and liquid-like viscosity) and without particle heating. To understand the effect of TKE decay on clustering, we first consider the *No Heating* cases in Figure 2.6 (A) and (D). It can be seen in Figure 2.6 (A) that the time-based distribution of smaller particles in gas is similar in both forced and decaying TKE cases without particle heating. In terms of larger particles (Figure 2.6 (D), the difference between the two cases becomes apparent at higher time instances ($t \geq 6$). However, since smaller particles are mostly responsible for clustering, this disagreement between the two test cases is not critical in this analysis. Hence, it is safe to say that the effect of decaying or sustained turbulence alone does not play a defining role in the clustering of smaller particles.

In terms of the heating cases, Figures 2.6 (B), (C), (E) and (F) suggest that forced and decaying turbulence simulations show more significant differences in the particle distribution. This can be attributed to the local density fluctuations at the particle position due to heating. Additionally, temperature-dependent viscosity also played a significant role in particle clustering, as liquid cases showed greater disagreement between the forced and decaying TKE plots. This supports the claim that particle heating and concomitantly the change in the temperature-dependent viscosity dominate the clustering characteristics of particles.

2.3.4 Viscous Capturing

In the current simulations, the primary force acting on the particles is due to drag. The drag force is directly tied to the drift velocity, which is a local measure of the relative fluid-particle velocity, as shown in Equation (2.11). Additionally, drag force is correlated with the local viscosity of the flow through the coefficient: $\frac{C_D}{\tau_p} = \frac{C_D 18 \rho_f \nu_f}{\rho_p d_p^2}$. Note that the

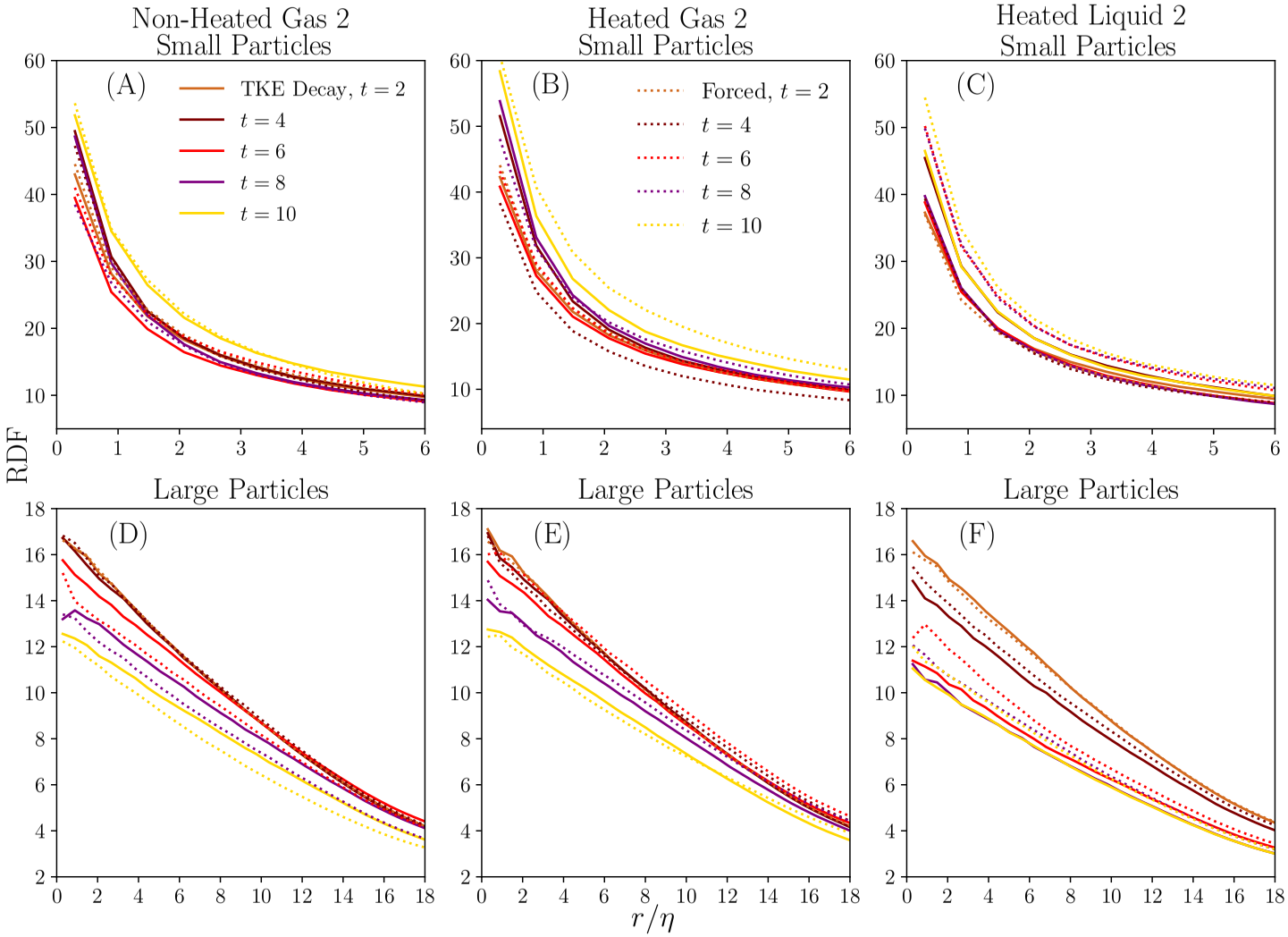


Figure 2.6: RDF of the small and large particles of base case 2 at even timesteps under different conditions.

coefficient of drag, C_D, is only weakly dependent on viscosity. For the same drift velocity, a higher viscosity will result in a higher drag force on the particle, which acts to reduce the drift velocity. Thus, an increase in the gas viscosity with temperature will result in a greater number of particles that move with the fluid velocity as compared to liquid. This feature is sketched in Figure 2.7 for gas, while Figure 2.8 shows the PDF of the normalized drift velocity. In this figure, fluid-particle drift velocity was computed at the locations where the local temperature was one standard deviation higher than the global mean temperature at each timestep. Hence, only the drift velocity in the high-temperature zones (with higher viscosity in gas and lower viscosity in liquid) was considered. For clarity the peak values of the PDF in Figure 2.8 at $|u_i - u_{p,i}|/u_\eta \approx 0$ are summarized in Figure 2.9. It can be seen that the gas cases typically depicted higher peak values at $|u_i - u_{p,i}|/u_\eta \approx 0$, which suggests that in gas, more particles are moving at a velocity closer to that of the fluid as compared to liquid.

Based on the discussion above, to explain the increased clustering of the small particles in gas, we propose a VC mechanism. VC arises when the clustering of heated particles creates a region of higher fluid viscosity (in a gas) which surrounds the zones of higher particle clustering. The higher viscosity, which means larger drag, causes the particles to move with the heated fluid (Figure 2.8). As other particles interact with the regions of higher viscosity, the increased drag effectively *captures* them. Thus, VC enhances particle clustering when the viscosity increases with temperature, irrespective of the instantaneous Stokes number of the flow. Additionally, once captured, these particles are less likely to leave these viscous regions due to higher viscous dissipation which weakens the vortex and, especially along the stagnation plane, the particle-and-fluid velocity is very similar in hot regions as shown in Figures 2.8 and 2.9, thus this limits the drag force. This behavior is termed *viscous restraining*. In the liquid cases, we also observe an increased clustering with time as the turbulence decays, although it is not as prominent as in the gas. In this case, the reduction of viscosity results in a reduced particle drag, hence particles are less readily transported by the continuum phase, meaning that the particles will have a tendency to remain in the cluster, despite showing a slower decay of the TKE (compared to the gas

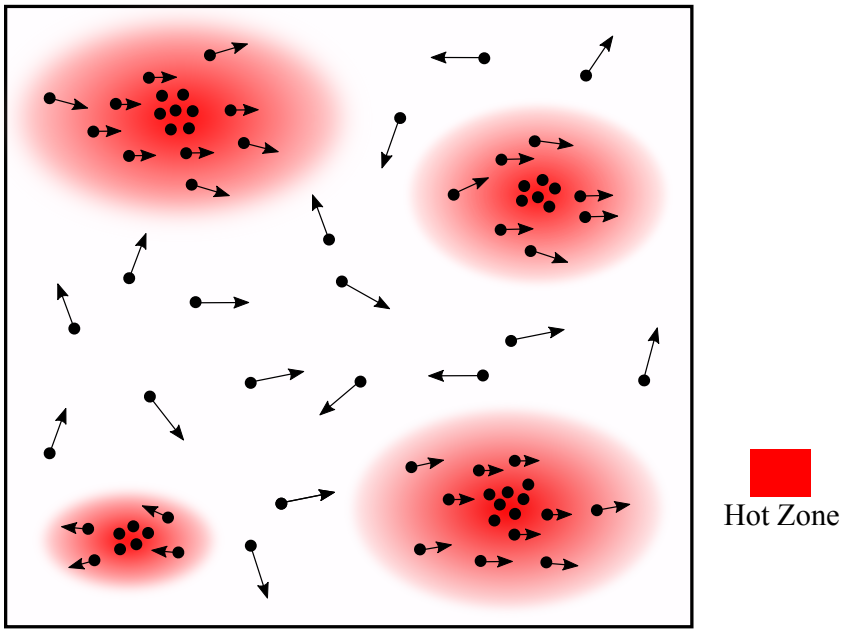


Figure 2.7: Effect of heating on discrete particle drag force in a gas. Arrows present fluid-particle drift velocity: the longer the arrow, the higher the drift velocity.

cases).

2.3.5 Particle Distribution and Heating

Figures 2.10 and 2.11 show the temperature and particle distribution (in a 2D slice) at the selected timesteps. It can be observed that particle clustering occurs in all the test cases irrespective of the St, as shown earlier, and these clusters result in hot and cold temperature zones in the fluid. Similar to the RDF plots, base case 1 resulted in the lowest particle clustering in both phases, while base case 2 showed the highest overall clustering at all timesteps. Another important observation is that base case 2 depicts thread-like particle clusters (a characteristic clustering shape due to vortical forces [53]), which share the same high-strain location as the hot fluid. This can be attributed to the gathering of

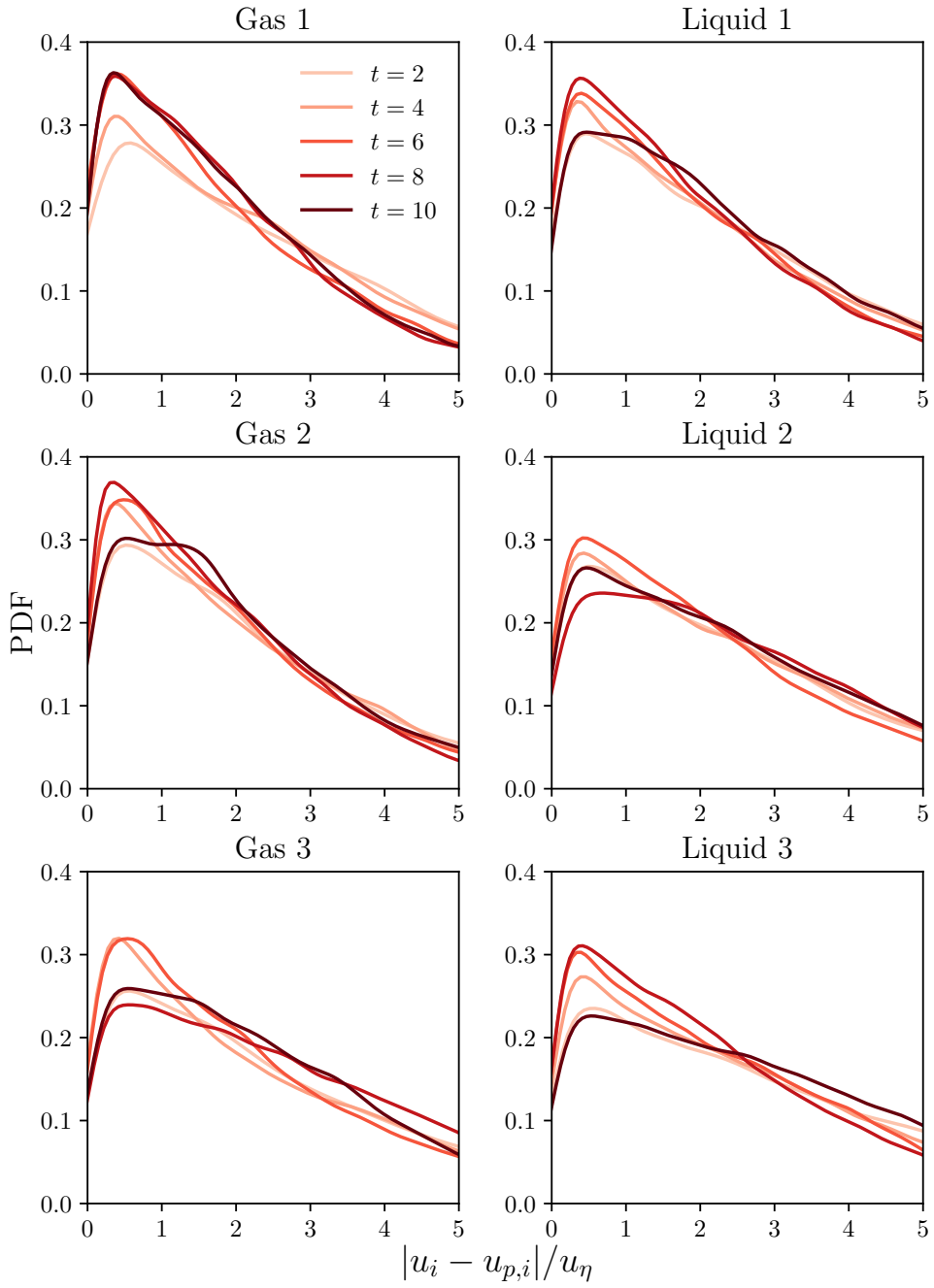


Figure 2.8: PDF of fluid-particle drift velocity normalized with Kolmogorov velocity ($u_\eta = \eta/\tau_\eta$) in heated gas and liquid at even timesteps.

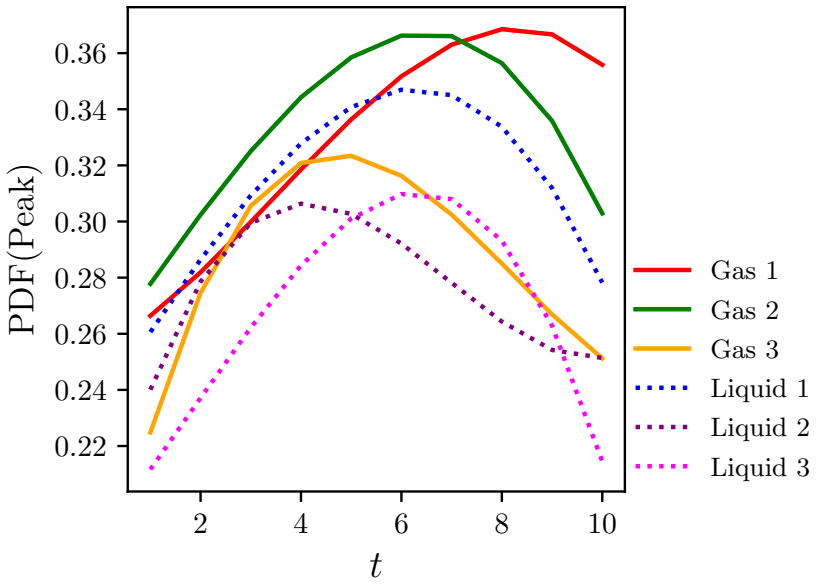


Figure 2.9: Trend-lines of the peak values of normalized fluid-particle drift velocity PDF at each timestep.

particles at the thermal fronts (similar to the scalar fronts observed in Bec et al. [48] and Carbone et al. [110]). These thread-shaped clusters also exist in base case 3, however, their location at these timesteps is slightly different from the hot fluid. This is because of the greater inertia of base case 3 particles, which results in a larger fluid-particle drift velocity and enables the particles to pass through these fluid temperature fronts with ease.

Moreover, by comparing Gas 2 ($t = 10$) contours with Figure 8 (a) of a similar monodispersed analysis of Mouallem and Hickey [101], it can be seen that bidispersed particles show considerably less clustering than the equivalent monodispersed flow. This is primarily due to the filling of voids created by the particles of one size by the other as small and large particles gather in different strain rate and vorticity regions (Section 2.3.6). Yet, although bidispersed particles delivered reasonably enhanced heat and particle distribution, clustering still existed.

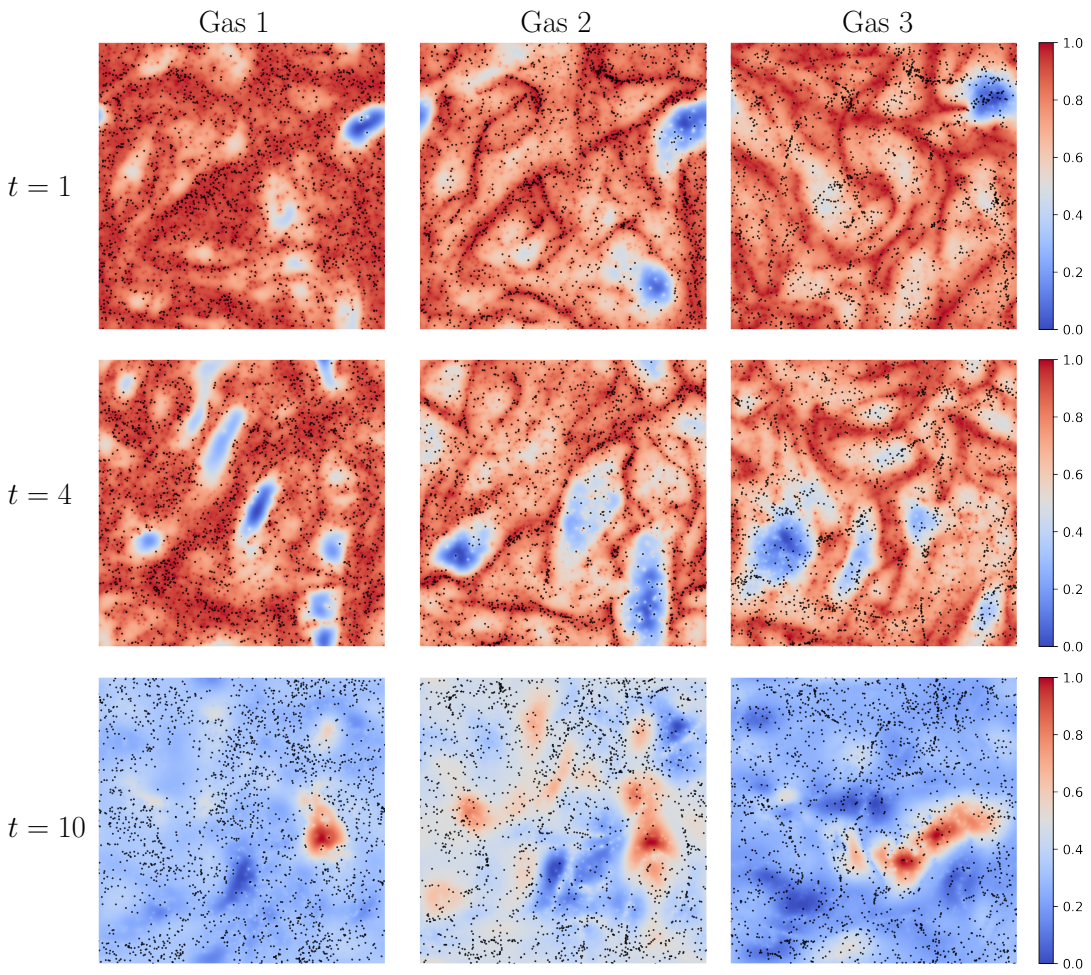


Figure 2.10: Temperature contours of gas with particle distribution, in a $2\pi \times 2\pi$ slide, at three different time snaps. The temperature is normalized by its maximum value at each timestep.

2.3.6 Strain Rate and Vorticity

The distribution of the particles as a function of the local magnitude of the strain rate and vorticity of the continuum phase is analysed in Figures 2.12 and 2.13. In order to assess the relative distribution of the particles, the PDF of particles is normalized by the probability of occurrence of these kinematic variables in the flow (at the respective timestep). This is done to examine if certain strain rates and vorticity regions would affect the grouping of

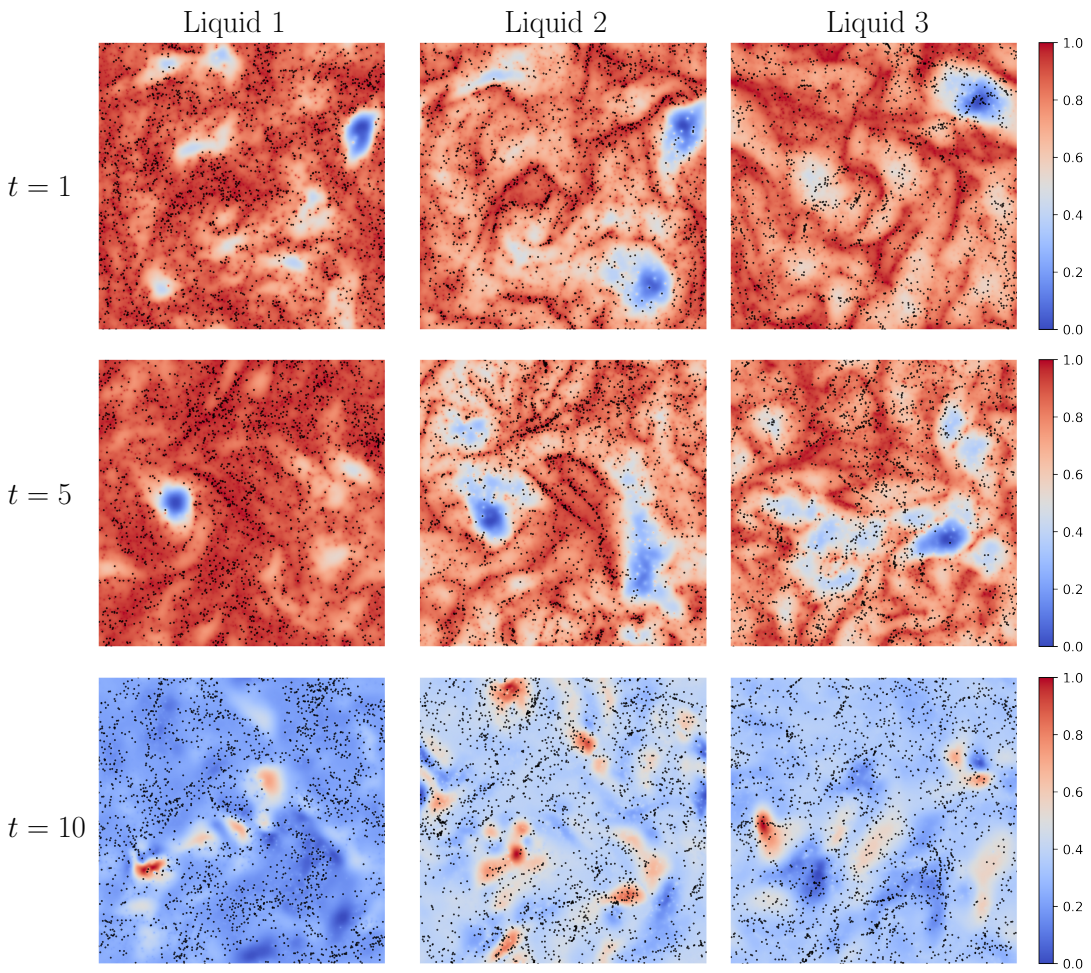


Figure 2.11: Temperature contours of liquid with particle distribution, in a $2\pi \times 2\pi$ slide, at three different time snaps. The temperature is normalized by its maximum value at each timestep.

the particles.

Before analyzing these plots, it is important to shed some light on the relationship between strain rate, vorticity, ε and ν. As per definition, strain rate (S) is the rate of deformation of the flow field which is mathematically expressed as the symmetric part of the fluid velocity gradient ($\nabla \mathbf{u}$). While, vorticity (Ω) is the measure of local rotation of the velocity field, numerically computed as the curl of flow velocity ($\nabla \times \mathbf{u}$). Hence, as the isotropic turbulence decays, the maximum velocity gradient and curl are expected to

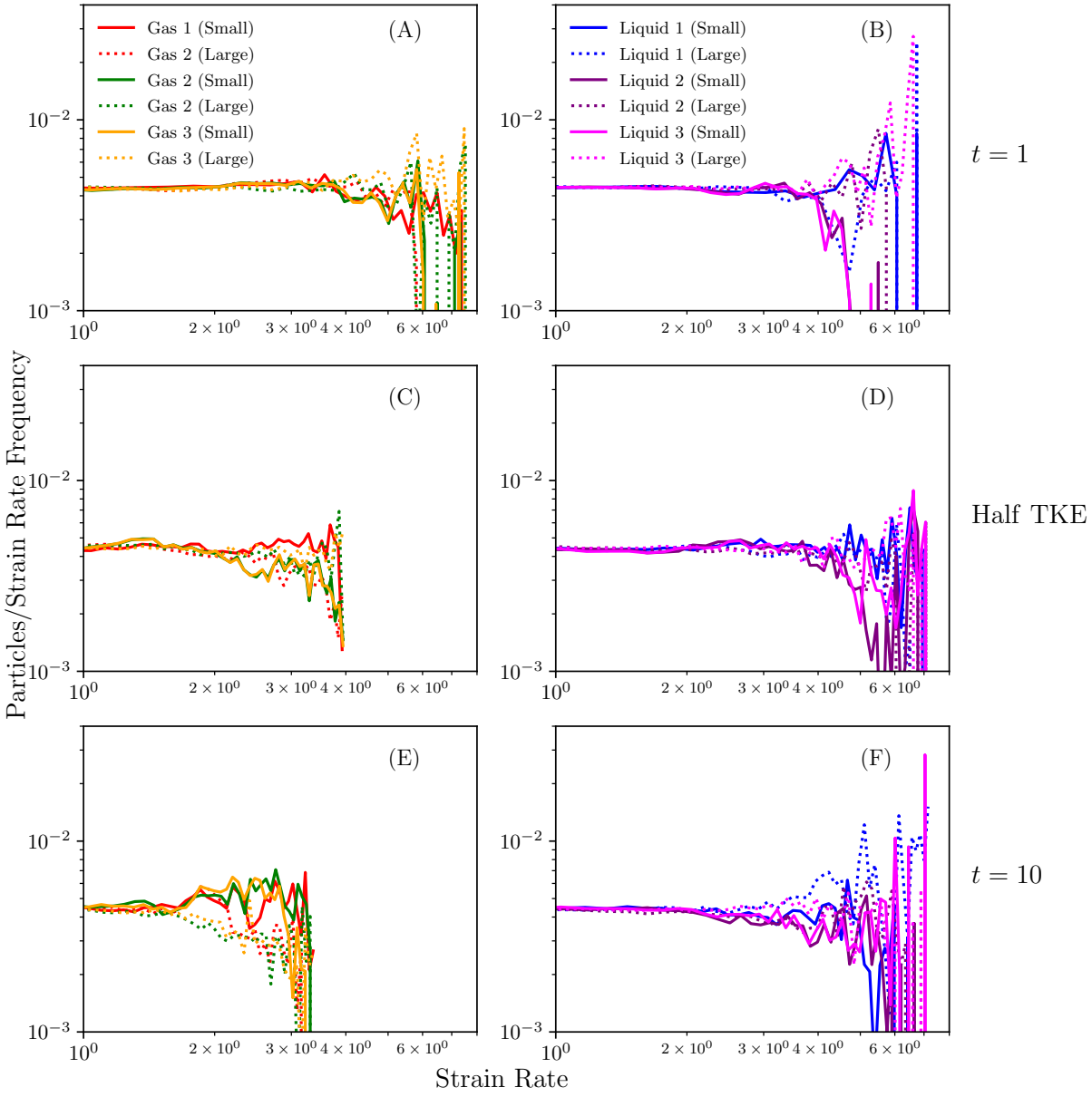


Figure 2.12: Distribution of particles in gas and liquid with strain rate at $t = 1$, half TKE and $t = 10$.

decay, albeit more rapidly for the increased viscosity of the gas than for the liquid.

Strain Rate

Figure 2.12 shows the size-wise particle-to-strain rate frequency curves of the gas and liquid cases. As we normalize the particle distribution by the occurrence frequency of the strain rate, we are able to assess the relative clustering of the particles in the strain rate domain. For both the gas and liquid cases, the initial section of the curves overlap. This suggests a good correlation between the number of particles and the occurrence frequency of the strain rate; a similar behavior is also observed for vorticity plots (Figure 2.13). Note that in this analysis we are only interested in the peak values, especially at high strain rates.

In Figure 2.12, it can be seen that particles tend to settle in medium to high-strain rate regions. Likewise, starting from $t = 1$ when TKE is high, larger particles depicted greater settling in high strain rate regions. This trend decreased with time and at $t = 10$, smaller particles took over this trend. This can be explained with filtering effect in which as the St increases (St_l here, see Figure 2.4), particles stop responding to timescales smaller than the particles response time [140, 141]. This renders larger particles less responsive to the fluid, thus decreasing their concentration in the high-strain rate regions. This behavior suggests a size-based particle distribution as stated earlier, especially in the context of particle heating. Additionally, it can also be observed in Figure 2.12 that although liquid cases show similar trends at $t = 1$ and half TKE, the trends of large and small particles are relatively similar at $t = 10$. Considering Equation (2.4), as TKE decays more slowly in liquid, τ_l in liquid is higher than gas at later timesteps (Figure 2.2). Thus, as per filtering effect larger particles in liquid respond to more timescales at $t = 10$ as compared to gas. Additionally, the particle concentration peaks are much higher in the liquid. This is due to higher fluid-particle velocity fluctuations in liquid based on lower viscous dissipation.

Vorticity

Figure 2.13 presents the distribution of particles in different vorticity regions. Unexpectedly, the particle distribution with vorticity is similar to the strain rate plots. Yet, as

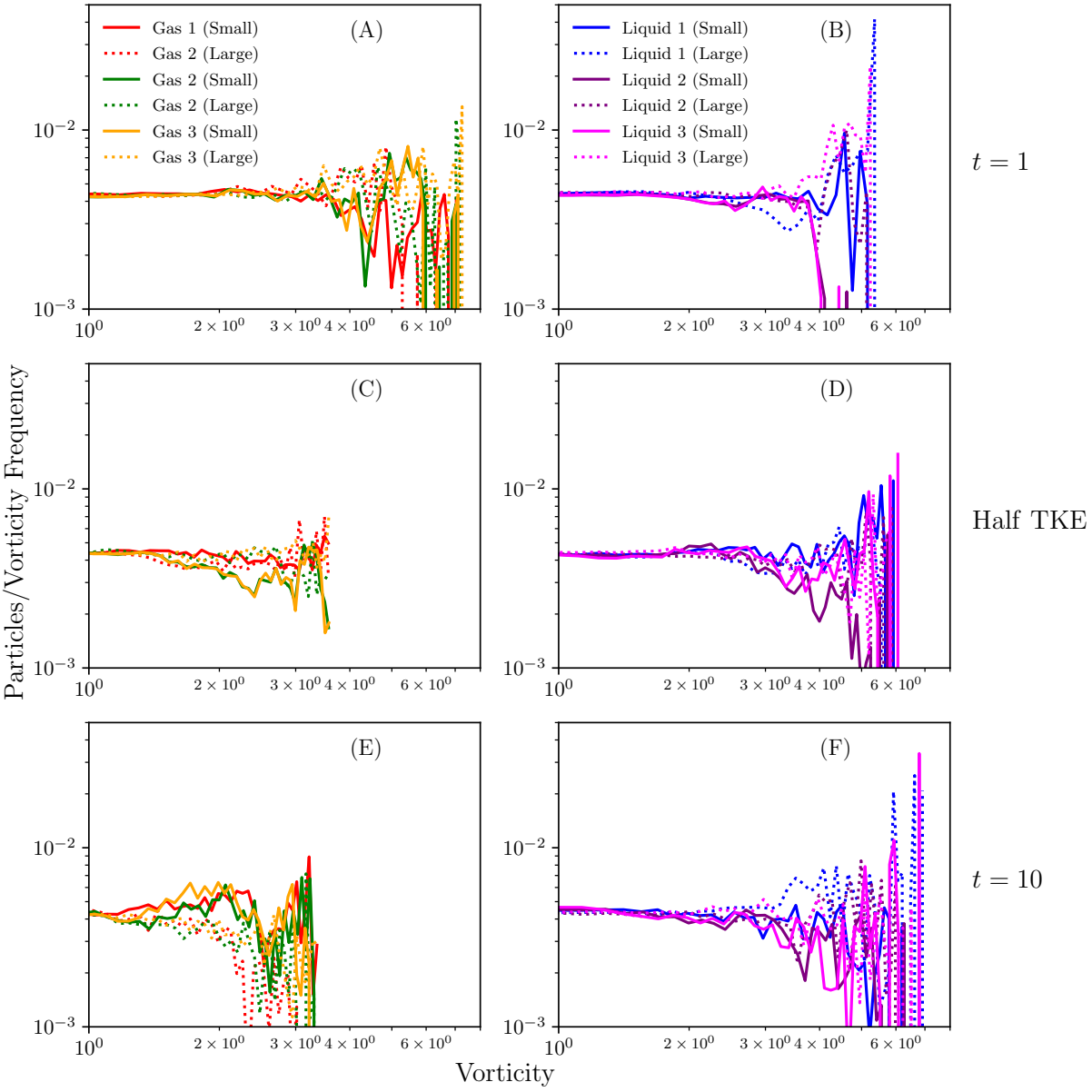


Figure 2.13: Distribution of particles in gas and liquid with vorticity at $t = 1$, half TKE and $t = 10$.

previously noted in the literature, particles cluster in low vorticity regions, which is especially evident with smaller particles in the gas. In the gas-like viscosity cases, this trend

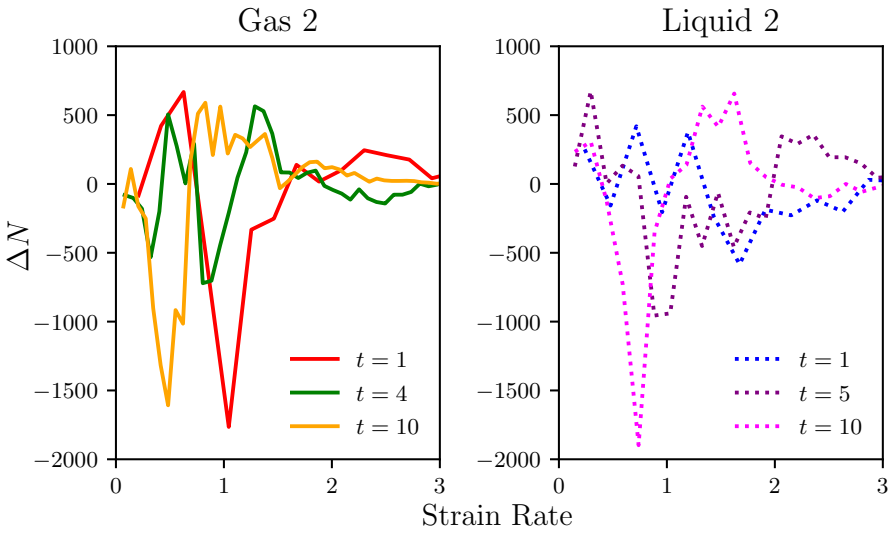


Figure 2.14: The difference between the number of small and large particles (ΔN) in different strain rate regions.

can be explained by VC which holds particles in different vorticity regions. In the case of liquid, however, the higher concentration of particles in such regions is due to the low drag force and consequently high drift velocity (Figure 2.8) of the particles.

Figures 2.12 and 2.13 provide proof of the concept that particles of different sizes globally settle in different strain rate and vorticity regions. However, for a better understanding of this phenomenon, a study of polydispersed flow with momentum TWC is required. This will be analyzed in a future study.

In Figures 2.12 and 2.13, the normalized particle concentration highlights the importance of strain rate and vorticity occurrence frequency, as the higher existence of a certain strain rate or vorticity region enables more particles to either settle or avoid that region. However, this normalization causes the details of particle distribution in low strain rate and vorticity regions to be lost. Thus, the non-normalized number difference of smaller and larger particles (ΔN) with respect to strain rate and vorticity in Gas 2 is shown in Figures 2.14 and 2.15. These figures highlight that low strain rate regions are populated

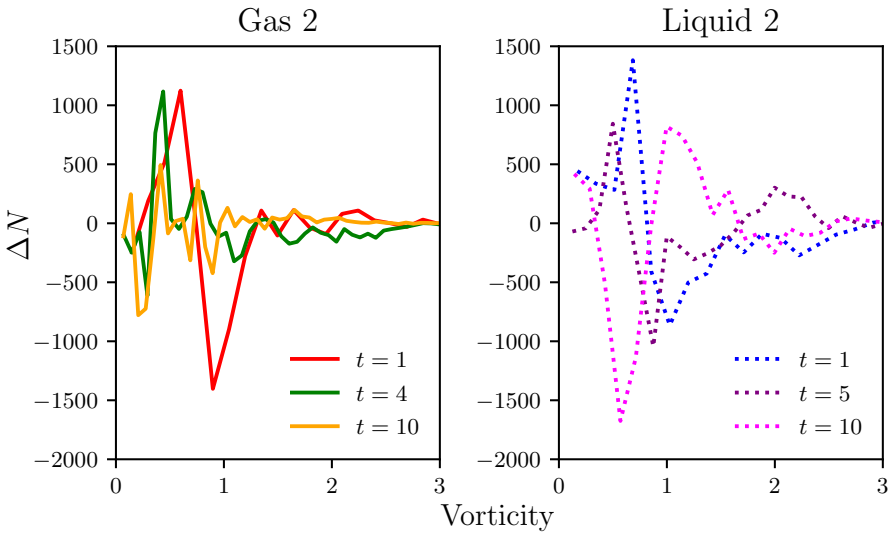


Figure 2.15: The difference between the number of smaller and larger particles (ΔN) in different vorticity regions.

by larger particles, while smaller particles dominate in low vorticity locations. This further proves that the voids of one particle size are filled by the other size. To further elaborate this trend Figure 2.16 presents the 3D distribution of particles and vortices in Gas 2. It can be seen in Figure 2.16 (A) that smaller particles tend to cluster around the vortical structures, whereas larger particles are not significantly influenced by them (Figure 2.16 (B)). Lastly, Figure 2.3 (C) shows that the voids created by smaller particles are filled by larger particles. Although not presented here, similar results are observed in Liquid 2.

2.4 Summary

A DNS investigation was conducted to study the clustering of heated bidispersed particles in variable viscosity carrier fluids. The focus of this work was on understanding the effect of gas- and liquid-like temperature-dependent viscosity on the PC. Three base cases, each containing particle species of two different diameters, were simulated in decaying isotropic

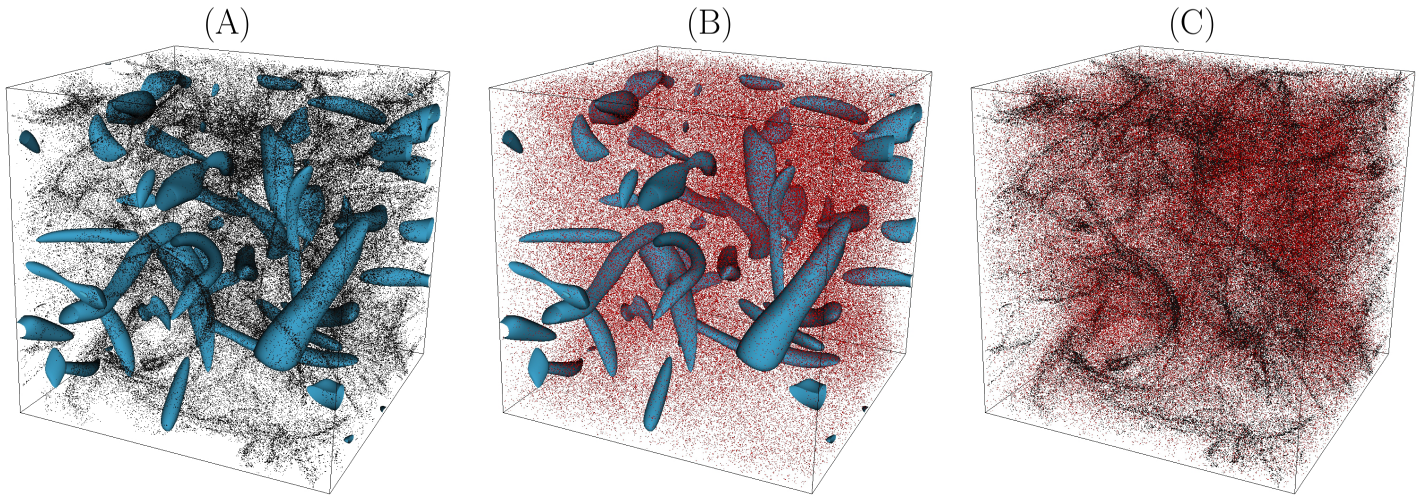


Figure 2.16: Distribution of (A) small particles and vortical structures, (B) large particles and vortical structures, and (C) small and large particles in the 3D domain of Gas 2 at $t = 10$. Here, small and large particles are represented by black and red colors, respectively, while vortices are shown with teal blue structures.

turbulence. For the two carrier fluids, all operating parameters were kept alike except the viscosity–the gas viscosity increased with temperature following a power-law, while the viscosity decreased with temperature in the liquid. Based on this, following are the primary findings of this research:

- In classical decaying isotropic turbulence, St_l is expected to increase and St_η decreases as the flow evolves. Yet, in our study, the external particle heating combined with the temperature-dependent viscosity caused the St_l and St_η evolution to deviate from the standard trend in decaying isotropic turbulence.

- Overall, the smaller particles showed a much higher PC than the larger particles in both gas and liquid. Similarly, particles in the liquid phase depicted better dispersion as compared to gas, due to the lower drag force when heated.

- VC is a proposed mechanism by which the increased fluid viscosity acts to enhance the particle clustering as the turbulence decays, irrespective of the Stokes number of the flow.

- At high viscosity and low TKE, PC in gas is decoupled from its characteristic St_η values. Hence, $St_\eta \approx 1$ based prediction of particle clustering is not accurate in applications involving particle heating or increasing fluid viscosity.

- It was also discovered that instead of particles settling in high strain rate and low vorticity regions, bidispersed particles tend to prefer moderate to high strain rate and medium-low to high vorticity regions. In terms of lower values of these parameters, smaller particles settle in low vorticity and larger particles show an inclination towards low strain rate regions. Thus, further probing is required to characterize the global distribution of bi- and polydispersed particles based on vorticity and strain rate. Correspondingly, it is also important to take into account the occurrence frequency of different strain rate and vorticity regions as particle clustering is highly dependent on these parameters.

- The gathering of particles in a range of vorticity and strain rate regions, dissimilar dispersion behavior of heated large and small particles, as well as the influence of one heated particle size on the distribution of the other indicates that at any given instance, particles of different sizes cluster at distinct turbulent scales and locations. Hence, polydispersed particles are a superior choice for clustering-sensitive applications.

From this study, it was found that fluid viscosity plays a critical role in the distribution of heated particles. Therefore, it should be considered as one of the key parameters when designing a heated multiphase system.

Chapter 3

Viscosity-Modulated Clustering of Heated Bidispersed Particles in a Turbulent Gas

Reference: A. Saieed, and J. P. Hickey. Viscosity-modulated clustering of heated bidispersed particles in a turbulent gas. *Journal of Fluid Mechanics*, 979:A46, 2024, DOI.

Abstract

The clustering of externally and evenly heated particles is enhanced by the increased viscosity of heated fluid in the vicinity of these clusters–a phenomenon known as VC. Herein we study, via DNS of decaying turbulence, the effect of temperature-driven viscosity on clustering with different particle loading densities. We employ momentum and energy TWC, and gas viscosity is modeled by a power-law to understand the role of the increased drag and particle back-reaction force on the clustering intensity. For the continuum and dispersed phases Eulerian and Lagrangian-point-particle schemes have been used, neglecting inter-particle collisions. We found that the enhanced viscosity-driven clustering is a

strong function of particle loading density, as the increase in particle number density enables the formation of large uneven clusters before heating, which is the main condition for VC to take effect. Higher number density should result in greater turbulent modulation and negate local temperature-based viscous effects leading to VC. However, due to higher local particle number density in the clusters and interphase heat transfer, increased drag force prevails in such cases and delivers excessive clustering. By conditionally sampling the particle velocity and temperature inside the clusters, it is found that the thermodynamic and kinematic properties of the particles in the clusters are highly correlated, and this correlation increases with the particle loading density. Therefore, based on the particle number density, temperature-based viscosity can considerably enhance the clustering of heated particles and alter the effect of particles on the underlying turbulence.

3.1 Introduction

The homogeneous distribution of heated particles in a fluid is one of the most fundamental operating conditions of numerous advanced engineering applications, such as particle solar receivers [103] and the combustion of metallic dust for propulsion [142]. The uneven distribution not only generates temperature gradients in the continuum phase, but also results in non-uniform expansion of the gas [21]. This happens because a higher concentration of particles in one region creates a dearth of particles in other regions. These areas of significant concentration can have a local particle number density up to sixty times higher than the global average [143]. This is undesirable for thermal systems, as it can reduce the efficiency of particle-fluid heat transfer by up to 25% [19], and creates strong temperature fluctuations [144, 89]. These fluctuations grow further with the intensity of clustering [145]. For particle combustion applications, the grouping of particles can partially or even completely impede particle combustion in the center of a cluster [18]. Such phenomena are evidently unacceptable for any thermal system, and therefore, efforts are made to have a homogeneous distribution of the particulate phase at all times.

Inertial particles are known to form clusters in a turbulent flow. This phenomenon is driven by particle (weight and size), fluid (density and viscosity), and turbulent characteristics [111]. The competing effects of these parameters are accounted for in the particle Stokes number, St, which is often considered as the primary non-dimensional number governing particle clustering [112]. Essentially, St is the ratio of particle and fluid timescales and is used to define particle behavior in a turbulent flow ranging from tracer (very *small* particles, closely following the streamlines of the flow) [54] to ballistic particles (very *heavy* particles, easily passing through turbulent eddies) [55, 146]. Mathematically, St is defined as [20]:

$$St = \frac{\tau_p}{\tau_f} \tag{3.1}$$

where τ_p is the particle momentum response timescale and is given as [114]:

$$\tau_p = \frac{\rho_p d_p^2}{18 \rho_f \nu_f} \tag{3.2}$$

here subscripts p and f denote the particle and fluid phases, while d, ρ, and ν are diameter, density, and kinematic viscosity, respectively. Moreover, in Equation (3.1), τ_f represents an *appropriate* timescale of the turbulent flow. This is because particles predominantly respond to different turbulent timescales based on their size/inertia, and therefore particle clustering is scale dependent [58]. Additionally, in polydispersed flows, particles of different sizes collect in distinct regions of the flow [67], and under similar conditions, different particle species have different acceleration [66]. This suggests that particle clustering can be driven by any scale of the turbulent flow. However, integral, τ_l [147], and Kolmogorov, τ_η [68], timescales are most commonly used to characterise particle-laden flows [61]. The expressions for τ_l and τ_η are:

$$\tau_l = \frac{(\text{TKE})^{\frac{3}{2}}}{\varepsilon \; u_{rms}} \tag{3.3}$$

$$\tau_\eta = \left(\frac{\nu_f}{\varepsilon}\right)^{\frac{1}{2}} \tag{3.4}$$

where u_{rms} is the root-mean-square of the fluid velocity, TKE is the turbulent kinetic energy and ε is the turbulent kinetic energy dissipation rate.

The past literature agrees on the fact that particles with $St \ll 1$ (tracer particles) and $St \gg 1$ (ballistic particles) do not show much clustering [116, 117]. Particles with $St \approx 1$, however, depict the maximum clustering [58]. Albeit, there are various explanations for this phenomenon, the most common among these is the PC or *centrifugal effect*, where inertial particles centrifuge out of vortices, local high vorticity regions, and gather in local high strain rate regions, between vortices [45, 46]. On the other hand, enhanced particle clustering has been observed at St much different from unity [118], an observation that is difficult to reconcile with conventional clustering mechanisms. Yoshimoto and Goto [148] argued that since turbulence is a multiscale phenomenon, clustering is inevitable provided that $\tau_\eta \leq \tau_p \leq \tau_l$, and in this case particles can exhibit considerable clustering at $St_\eta \neq 1$. They observed particle clustering at $St_\eta \gg 1$ where particles gathered at larger scales. A more accurate explanation is that the particles depict higher clustering at any scale with timescale τ^*, provided that their $St = \tau_p/\tau^* \approx 1$. Consequently, two St-based regimes were defined, where at $St < 1$ clustering is attributed to the centrifugal force [46], while at $St \geq 1$ clustering is due to a *non-local temporal* (*history*) effect [50]. In the latter mechanism, particles carry the memory of having $St \approx 1$ in the past and then cluster at a later time when their St is greater than unity.

The above-stated mechanisms hold well for unheated particle-laden flows. However, when particles are heated, a feedback loop is created between particle clustering, local temperature variations, and hydrodynamic forces [145]. Even in this case, ignoring temperature-driven fluid viscosity maintains the validity of conventional clustering mechanisms. For example, Pouransari et al. [21] analyzed turbulence modulation due to heated particles in decaying HIT with constant viscosity. By focusing on the density-based variations, they observed maximum particle clustering at $St \approx 1$, and consequently a higher uneven expansion of gas, which enhanced turbulence at the cluster (small) length scales. The gas expansion (decrease in local density) creates a divergent flow field that pushes the particles away from each other. This dilatation effect increases with particle loading, resulting in a lower propensity for clustering. Pouransari and Mani [22] investigated the influence of clustering on interphase heat transfer using DNS. They reported that the

mean particle-to-fluid heat transfer is a function of St, where $St \approx 1$ delivered the most inhomogeneous heat transfer. Rahmani et al. [129] studied the influence of polydispersed particle-size distribution on preferential clustering and particle-fluid heat transfer characteristics in a channel flow with fluid-particle TWC. They attributed maximum clustering and inhomogeneous heat transfer to $St \approx 1$, even in polydispersed flow, which otherwise delivers superior dispersion and heat transfer compared to monodispersed particles. Pouransar and Mani [19] also investigated the effect of particle clustering on heat transfer statistics in a channel flow. They reported that at maximum clustering ($St \approx 1$) the temperature fluctuation is up to 35% of the average temperature rise. In all of these studies, higher clustering and its corresponding impact on turbulence and temperature statistics were attributed to $St \approx 1$. In fact even in momentum TWC where particles can considerably modulate turbulence, the above St based clustering characterization holds (see Frankel et al. [149] for example), if the temperature-driven change in viscosity is neglected.

Note that under the constant viscosity assumption, the drop in density reduces the drag force on the particles. In practice, however, particle heating drops the density and increases the dynamic viscosity (μ_f) of the local gas, where viscous effects are expected to be much stronger than density effects. In our study, compared to the initial values, ρ_f dropped only by 3.6%, while μ_f increased by roughly 60% with the increase in temperature. The overall domain volume and density are constant, and this 3.6% drop in ρ_f refers to the local maximum change in ρ_f. This small decrease in local ρ_f is due, in part, to the increase in domain pressure because of the triply-periodic boundary condition. If the average domain pressure were constant, the density would decrease proportional to the increase in temperature, while the viscosity would alter with a power-law of temperature. Hence, the effect of temperature-driven viscosity will remain a considerable factor. Additionally, the temperature-driven variation in viscosity is critical as it greatly alters the turbulent flow field and dynamics of the vortical structures [150]. As per Equation (3.2), the rise in ν_f considerably alters τ_p which consequently changes the particles' St number. In decaying turbulence–which is representative of turbulence in many engineering flows–τ_l decreases, while τ_η increases with time, which also affects the values of St. The compounding effects

of these variations have a unique influence on particle clustering. Therefore, our primary focus is on the clustering originating from the increase in viscosity and the resulting rise in particle drag force.

In a recent analysis, we observed higher clustering in a heated bidispered particle-laden flow when variable viscosity was used in comparison to a constant viscosity case [151]. It was found that as the gas temperature-driven viscosity increased, the clustering of smaller particles increased even when their St based on the Kolmogorov scale ($St_\eta = \tau_p/\tau_\eta$) decreased from 0.65 to 0.33–a trend opposite to the conventional assumption. This was surprising because an identical constant viscosity case with the evolution of St_η from 1.1 to 0.9 showed lower clustering than in the aforementioned simulation. This counterintuitive behavior cannot be elucidated even with the history effect, as particle clustering continuously increased, while St_η kept declining below unity. We argued that this high clustering is the result of VC, where a particle cluster prior to heating creates a viscous cloud around itself upon heating, which retains the already clustered particles and captures more particles as a result of the higher drag force on them.

Albeit VC is a compelling argument that adequately explained the deviation of particle clustering from the clustering predicted by St (where maximum clustering is observed at $St \approx 1$), we made some simplifying assumptions to isolate the effect of temperature-dependent viscosity on particle dispersion. The most important among these is the OWC of fluid-particle momentum, where only the fluid exerted a drag force on the particles, and consequently, the particles could not resist the VC. Although this assumption has been used earlier [110], it is crucial to test VC in the regime where particle drag on the carrier fluid is non-negligible (momentum TWC).

Analyzing the turbulent energy spectrum in TWC suggested that particles attenuate energy at low wavenumber (k) and augment it at high wavenumbers [26], and this effect enhances with the rise in particle number density [27]. The increase in small-scale energy escalates ε, which in return increases the rate of energy transfer from the large to small scales, consequently enhancing l and dropping η [152]. Boivin et al. [28] found that the

TKE dissipation increases with the increase in particle loading. By examining the exchange rate of fluid-particle energy, they reported that larger turbulent eddies drag the inertial particles, whereas particles drag the smaller eddies with them. Hence, particles act as *sink* at larger scales and *source* at smaller scales, and this effect augments with the rise in particle loading. In a comprehensive review on particle-laden flows, Balachandar and Eaton [23] concluded that even in dilute particle-laden flows, turbulence modulation is prevalent as particles impart their kinetic energy on the fluid. Additionally, turbulence modification is also known to be maximum at $St \approx 1$ [153]. In terms of particle size, Gore and Crowe [154] observed that smaller particles decrease TKE as they are moved by the local fluid, whereas larger particles increase TKE as they drag the fluid with them. The strength of this phenomenon also depends on the number of particles in the system.

Considering the discussion above, we are interested in characterizing the effect of temperature-dependent gas viscosity on clustering at different particle loading densities, as the particles are rapidly heated to reach a temperature double their initial temperature. This analysis will bring out the prepotent impact of increasing drag force on the particle during heating, which has been greatly overlooked due to the constant viscosity assumption. Here, particle-particle collisions were neglected, and only the drag force was taken into account. In this case, it is expected that the rise in drag force will correlate the kinematic and thermodynamic parameters of the particles and fluid inside a cluster.

By decreasing the global number of particles, we decrease the number of particles in each cluster/viscous cloud, and also reduce the particle clustering capacity [155, 156]. This will help to understand whether viscous clouds still form and capture particles when the local particle loading in each cloud drops and the particle-fluid heat transfer is reduced. We hypothesize that the rise in localized heating with particle loading density will enhance VC, despite the increase in particles' ability to resist local viscous effects due to their reaction drag on the fluid. Furthermore, particle-back reaction force can also potentially aid viscosity-driven clustering, as it reduces the local fluid velocity fluctuations, which in return drops the transfer of heat via turbulent fluid diffusion [157]. Note that the parameters in this study are presented in arbitrary but consistent units. Thus, present

results can be interpreted in any consistent units system. This article is structured such that Section 3.2 states the computational setup of this study, while simulation results are discussed in Section 3.3. A summary of the present analysis is provided in Section 3.4.

3.2 Methodology

In this study, DNS were conducted using a slightly modified version of the open-source, high-order finite difference code known as Pencil-Code [130]. Three particle number densities were tested with two particle sizes (bidispersed particles); the number of large and small particles had a 50 : 50 ratio in each particle loading scenario. The radii of the two particle species were 0.0028 and 0.0106, which are identical to the test case *Gas 2* of Saieed et al. [151]. Hereon, the two particle sizes will be referred to as *small* and *large* particles in the text. We employed bidispersed flow because we wanted to study the clustering characteristics of particles responding to different turbulence scales, without further complicating our simulations which already involved particle heating, turbulence decay and heat diffusion. The global number of particles tested is 5×10^5 (similar to our previous study), 2.5×10^5 and 1.6×10^5. For conciseness, we will refer to these simulations as L_5, $\mathrm{L}_{2.5}$ and $\mathrm{L}_{1.6}$, respectively. Here, L represents the loading and the subscripts 5, 2.5 and 1.6 are the multiples of 10^5 in their respective loading numbers. We also simulated particle number densities 1.2×10^5 ($\mathrm{L}_{1.2}$), 0.5×10^5 ($\mathrm{L}_{0.5}$), 0.1×10^5 ($\mathrm{L}_{0.1}$) and 0.05×10^5 ($\mathrm{L}_{0.05}$). However, these simulations were not included in the main analysis (except for comparison in a few places) as it was found that below $\mathrm{L}_{1.6}$, particle clustering depends on Taylor-based Reynolds number ($Re_\lambda = u_{rms}\rho_f\lambda/\mu_f$, here λ is Taylor length scale) of the flow (see Section 3.3.1). Note that the volume fraction (Φ_v) of L_5, $\mathrm{L}_{2.5}$, and $\mathrm{L}_{1.6}$ simulations is in the $O(10^{-3})$ which is just at the point where particle-particle collisions ($\Phi_v > 10^{-3}$) becomes relevant [4]. For simplification, we employed momentum TWC. The volume fraction of $\mathrm{L}_{0.5}$ is in the $O(10^{-4})$ which is almost in the OWC regime, but we also modeled it with momentum TWC for consistency. We used *Triangular Shaped Cloud* scheme, which employs

2^{nd} order spline interpolation from 27 grid points for modeling fluid-particle interaction.

First of all, three base simulations were run with the same initial parameters but different particle number densities (L_5, $L_{2.5}$ and $L_{1.6}$). For the development of HIT, these simulations were carried out in a $2\pi^3$ periodic box, resolved into a 384^3 grid with a solenoidal forcing, F_i [131]. We used 384^3 grid to accurately interpolate particle motion from the fluid and keep the temperature gradient across each cell small and accurate. Likewise, the present forcing scheme is temporally delta-correlated in k space, meaning that all the random forcing points are correlated at a particular time instance but vary between timesteps.

These initializing simulations without particle heating were conducted for approximately five large eddy turnover times of L_5 case. Here, L_5 took the longest time to develop equilibrium between the large scale energy addition and small scale energy dissipation. The L_5 simulation was also extended to ten eddy turnover times to ensure that the mean turbulent characteristics remain stable after five turnover times (not shown here). The instantaneous TKE showed non-negligible oscillations about an average value even after five turnover times, which is a known problem in forced HIT both in spectral [158] and linear forcing [159, 160]. These temporal fluctuations, along with the fact that particle heating also adds energy to the flow which could destabilize the simulations, were the reasons why we did not use forced turbulence when running the particle heating simulations. Note that the forcing adds energy at the large scale, while particle heating adds energy at the particle/cluster scale. Here, $k_{max}\eta > 12$ (k_{max} is the maximum wavenumber) was obtained, suggesting that the small scales are fully resolved [3].

These simulations solved the compressible Navier-Stokes equation, but we neglected the kinetic energy in the energy equation in order to decouple fluid velocity and temperature– only fluid internal energy is considered in the energy equation. This assumption is only valid in the low Mach number cases. This was verified in our $L_{1.6}$ case, in which the maximum local Mach number never exceeded 0.08. Given the conservation of mass and the fixed volume of the triply-periodic DNS domain, the mean gas density remained constant

at $\rho_f = 1.08$ (prescribed value), but particle heating altered the local gas density in the vicinity of particles. After fully developed HIT was achieved, the artificial forcing was removed, allowing turbulence to decay, and particle heating was initiated. Of interest is the period of turbulence decay and particle heating over the first ten time units. Table 3.1 lists the turbulent characteristics at the beginning of the particle heating simulations. In Table 3.1, the turbulent Reynolds number is defined as $Re = u_{rms}\rho_f l/\mu_f$. The simulation setup of all three base cases was identical, including the forcing function, but the difference in the number of particles (due to momentum TWC) resulted in the base simulations having slightly different turbulent characteristics.

The most critical turbulence characteristic in Table 3.1 is the Taylor-based Reynolds number, Re_λ, as it determines the resolution of small scales and if clustering is governed by a single or multiple turbulent scales [105]. Ireland et al. [161] stated that particle clustering is independent of Re_λ for $St < 1$, which is the case in the present heating simulations, as discussed in Section 3.3.4. However, for further assurance, we decreased F_i in $L_{2.5}$, $L_{1.6}$, $L_{1.2}$ and $L_{0.5}$ to match the Re_λ of L_5 and compared clustering in the original and reduced Re_λ cases. Since Re_λ does not scale linearly with the forcing function, there was about $5-10\%$ difference in the Re_λ of the original and Re_λ matched cases compared to Re_{λ,L_5}. But, we will see in Section 3.3.1 that only those particle loading densities were selected in which clustering is insensitive to Re_λ. Therefore, this difference of $5-10\%$ is considered trivial in these cases. Note that we opted to use identical forcing and overall simulation setup in our test cases, based on Re_λ independence analysis. Particle clustering was quantified with the RDF, which counts the number of particles within a certain radial distance from a reference particle (see Saieed et al. [151] for details). This analysis is explained in Section 3.3.1. Note that the l/η ratio of our lowest (L_5) and highest ($L_{1.6}$) Re_λ cases is 41.8 and 52.3, respectively. Comparing these ratios with $Re_\lambda = 88$ of [161] that is $l/\eta = 55.8$ suggests that despite the low Re_λ, our scale separation is adequate. Our mean energy spectrum, $\overline{E(k)}$ in Figure 3.5 also shows good resolution of the small scales and we also obtained $-5/3$ slope in the $\overline{E(k)}$, albeit with the shorter inertial range due to the momentum TWC.

Parameter	Symbol	L_5	$L_{2.5}$	$L_{1.6}$
Particle loading	N_p	5×10^5	2.5×10^5	1.6×10^5
Average root-mean-square velocity	$\overline{u_{rms}}$	0.19	0.28	0.32
Turbulent kinetic energy	TKE	0.018	0.035	0.052
Dissipation rate	ε	0.0006	0.001	0.0015
Taylor Reynolds Number	Re_λ	53	68	78
Turbulent Reynolds Number	Re	200	286	343
Integral timescale	τ_l	22.33	15.65	13.04
Integral length scale	l	4.18	4.18	4.18
Kolmogorov timescale	τ_η	2.65	1.96	1.64
Kolmogorov length scale	η	0.10	0.088	0.080

Table 3.1: Characteristics of the fully developed HIT.

We employed point-particle approach for both particle species in this analysis. For small particles, this is a straightforward choice, as for all the considered cases $d_p/\eta = O(10^{-2})$; the point-particle method typically assumes $d_p/\eta \ll 1$. As per Table 3.1, the ratio d_p/η for L_5 to $L_{1.6}$ larger particles is in the $O(10^{-1})$. According to Balachandar and Eaton [23], for particles with $\rho_p > \rho_f$ and $d_p \approx O(\eta)$, point-particle assumption can be used. Our $\rho_p/\rho_f \approx 1400$ and particle Reynolds number is $Re_p \leq 1$. Hence, the use of point-particle approach is justified.

Table 3.2 summarizes the initial St values (prior to heating) of the present simulations. For this work, the smaller particles are defined by the Kolmogorov scale, as they are about 18 times smaller than the Kolmogorov scale. Due to filtering effect [141, 140], larger particles will correspond to the integral scale, as they are about 5 orders of magnitude smaller than η. In momentum TWC, the energy transfer from large to small scale has two routes: the classical energy cascade and particles taking energy from the large scales and feeding it to the small scales. This affects the inertial scale (see Figure 3.5) and therefore it is plausible to assume that larger particles correspond primarily to the integral scale.

Case	L_5		$L_{2.5}$		$L_{1.6}$	
Particle radius	0.0106	0.0028	0.0106	0.0028	0.0106	0.0028
Stokes number	St_l	St_η	St_l	St_η	St_l	St_η
	0.37	0.51	0.33	0.63	0.33	0.68

Table 3.2: Particle St_l and St_η values at the start of heating simulations.

Consequently, St based on the Kolmogorov scale ($St_\eta = \tau_p/\tau_\eta$) is used to characterize the smaller particles and St calculated from the integral scale ($St_l = \tau_p/\tau_l$) is used for larger particles, as shown in Table 3.2. In the present case, the initial values of St_η are different, since TKE and ε decrease with increasing particle loading [28]. As clustering is maximum at the scale where St (based on that scale) is unity, an increase in clustering can be observed at the integral scale. Thus, we use St_l for comparing simulations as L_5, $L_{2.5}$ and $L_{1.6}$ start with similar St_l.

3.2.1 Continuum Phase

The conservation equations of the carrier phase mass, momentum, and energy are:

$$\frac{\partial \rho_f}{\partial t} + \frac{\partial \rho_f u_{f,i}}{\partial x_i} = 0 \tag{3.5}$$

$$\frac{\partial \rho_f u_{f,i}}{\partial t} + \frac{\partial \rho_f u_{f,i} u_{f,j}}{\partial x_j} = -\frac{\partial P_f}{\partial x_i} + \frac{\partial \mu_f}{\partial x_j}\left(\frac{\partial u_{f,i}}{\partial x_j} + \frac{\partial u_{f,j}}{\partial x_i} - \frac{2}{3}\frac{\partial u_{f,k}}{\partial x_k}\delta_{ij}\right) + F_i + F_p \tag{3.6}$$

$$\frac{\partial \left(\rho_f c_{f,v} T_f\right)}{\partial t} + \frac{\partial \left(\rho_f c_{f,p} T_f u_{f,j}\right)}{\partial x_j} = \frac{\partial}{\partial x_j}\left(\kappa_f \frac{\partial T_f}{\partial x_j}\right) + Q_{pf} \tag{3.7}$$

here T, p and $u_{f,i}$ are the temperature, pressure and gas velocity in the i^{th} direction. While the specific heat of the fluid at constant volume/pressure and thermal conductivity are expressed as $c_{f,v}/c_{f,p}$ and κ_f, respectively. In Equation (3.6), F_p represents the local reaction force that the particles exert on the fluid, and thus accounts for the fluid-particle

momentum TWC. This force is opposite to the fluid drag on the particle and is given as:

$$F_p = m_p \frac{u_{p,i} - u_{f,i}(x_p)}{\tau_p} \tag{3.8}$$

where m_p and $u_{p,i}$ are particle mass and velocity, while $u_{f,i}(x_p)$ is the (disturbed) fluid velocity at the particle location, x_p. As per the TWC scheme, $u_{f,i}(x_p)$ should be the undisturbed fluid velocity at the particle location. This can affect the drag force prediction [162], and may require correction to the disturbed velocity for estimating the drag force. Horwitz and Mani [163] proposed a regime diagram that can be used to determine if a model requires velocity correction. According to their $d_p/\eta = O(10^{-2})$ and $St_\eta = O(10^{-1})$, our smaller particles lie in the regime where a correction is not needed. While large particles may require correction considering their $d_p/\eta = O(10^{-1})$ and equivalent $St_\eta = O(10^{0})$ lies on the bordering line between TWC correction and "other multiphase flow" regimes. However, since the St_η of our larger particles is small and decreases further with time (due to the increase in τ_η as the turbulence decays), velocity correction can be neglected without a considerable effect on the results.

Similarly, the expression for the temperature-dependent gas dynamic viscosity (μ_f) is as follows:

$$\mu_f = \mu_{f,0} \left(\frac{T}{T_0} \right)^{\frac{2}{3}} \tag{3.9}$$

here subscript 0 stands for the initial/reference value. The initial kinematic viscosity was $\nu_{f,0} = 0.0034$ and the temperature of the base simulations was $T_0 = 273$.

3.2.2 Particulate Phase

The Lagrangian equation set for the particles is given as:

$$\frac{dx_{p,i}}{dt} = u_{p,i} \tag{3.10}$$

$$\frac{du_{p,i}}{dt} = \frac{C_D}{\tau_p} \left(u_{f,i}\left(x_p\right) - u_{p,i} \right) \tag{3.11}$$

where C_D is the particle drag coefficient, defined by the Schiller-Naumann equation [133]:

$$C_D = 1 + 0.15Re_p^{0.687}, \quad Re_p = \frac{d_p|u_{p,i} - u_{f,i}(x_p)|}{\nu_f} \tag{3.12}$$

here Re_p is the Reynolds number of the particles and $|u_p - u_f(x_p)|$ is the local fluid-particle drift velocity.

3.2.3 Particle Heating Model

We adopted Mouallem and Hickey [101] particle heating model, which externally and uniformly heats the particles. The gaseous carrier phase is transparent to this heating and absorbs heat from the particles via conduction (in the immediate vicinity of particles) and convection (gas far from particles). In this model, particle heating, Q_p, and particle-to-fluid heat transfer, $Q_{p,f}$, terms are defined as:

$$Q_p = m_p c_p \frac{(T_{max} - T_p)}{\tau_{heat}} \tag{3.13}$$

$$Q_{pf} = \frac{m_p c_p \ Nu_p}{2\tau_t} (T_p - T_f(x_p)) \tag{3.14}$$

In Equations (3.13) and (3.14), m_p, c_p and T_p are particle mass, heat capacity, and temperature, respectively. Whereas, $T_f(x_p)$ is the local gas temperature at the particle position. Similarly, T_{max} is the maximum particle temperature (prescribed as 600) that can be attained via external heating. The particle heating timescale τ_{heat} was set to 1.0 for rapid heating and the particle-to-fluid heat transfer timescale τ_t was 10 for fast heat transfer. It is worth mentioning that the heating is governed by the particle-fluid temperature difference, and the heat flux drops as the temperature of the fluid increases.

In Equation (3.14), the particle-fluid Nusselt number is computed with the Ranz-Marshall correlation [134]:

$$Nu_p = 2 + 0.6 \ Re_p^{\frac{1}{2}} \ Pr^{\frac{1}{3}} \tag{3.15}$$

here Pr is the Prandtl number. To characterize the increase in particle clustering due to the rise in local temperature-dependent viscosity at each particle loading density, simulations

are carried out with Heated (H) and Non-Heated (NH) particles. Although the primary focus of this analysis is on the effect of particle loading density on VC, however results of H and NH cases are compared in a few places to highlight some critical aspects of particle clustering.

3.3 Results

3.3.1 Re_λ Independence

To verify if particle clustering–characterized by RDF–is independent of Re_λ for our simulation setup, we compare the cases with actual and Re_λ matched to L_5 (Re_{λ,L_5}), as shown in Figure 3.1. This comparison implies that clustering in $L_{2.5}$ and $L_{1.6}$ is independent of Re_λ, but we see a non-negligible difference in RDF plots of $L_{1.2}$ and $L_{0.5}$ smaller particles. This is plausible since higher Re_λ generates more smaller scales in the flow, while the largest scale in the domain is restricted by the domain size. There is a slight difference between the original Re_λ (solid lines) and $Re_\lambda = Re_{\lambda,L_5}$ curves of larger particles. However, since this difference is significantly less than the difference we observe for the smaller particles of $L_{1.2}$ and $L_{0.5}$, we consider it negligible. This analysis is critical as it narrowed our comparison to L_5, $L_{2.5}$ and $L_{1.6}$ where particle clustering is independent of Re_λ, and therefore prevented the erroneous comparisons of particle clustering with lower loading density cases.

3.3.2 Particle Heating

Considering the point-particle assumption, each particle has a uniform temperature (Biot number, $Bi \ll 1$). Using Equation (3.15), Nu_p was found to be less than 2.6, which, according to the Ranz-Marshall expression, implies that conduction is the primary mode of heat transfer in the test cases. As heat conduction is a local phenomenon, it can enable/enhance other local phenomena such as thermal viscosity-driven clustering.

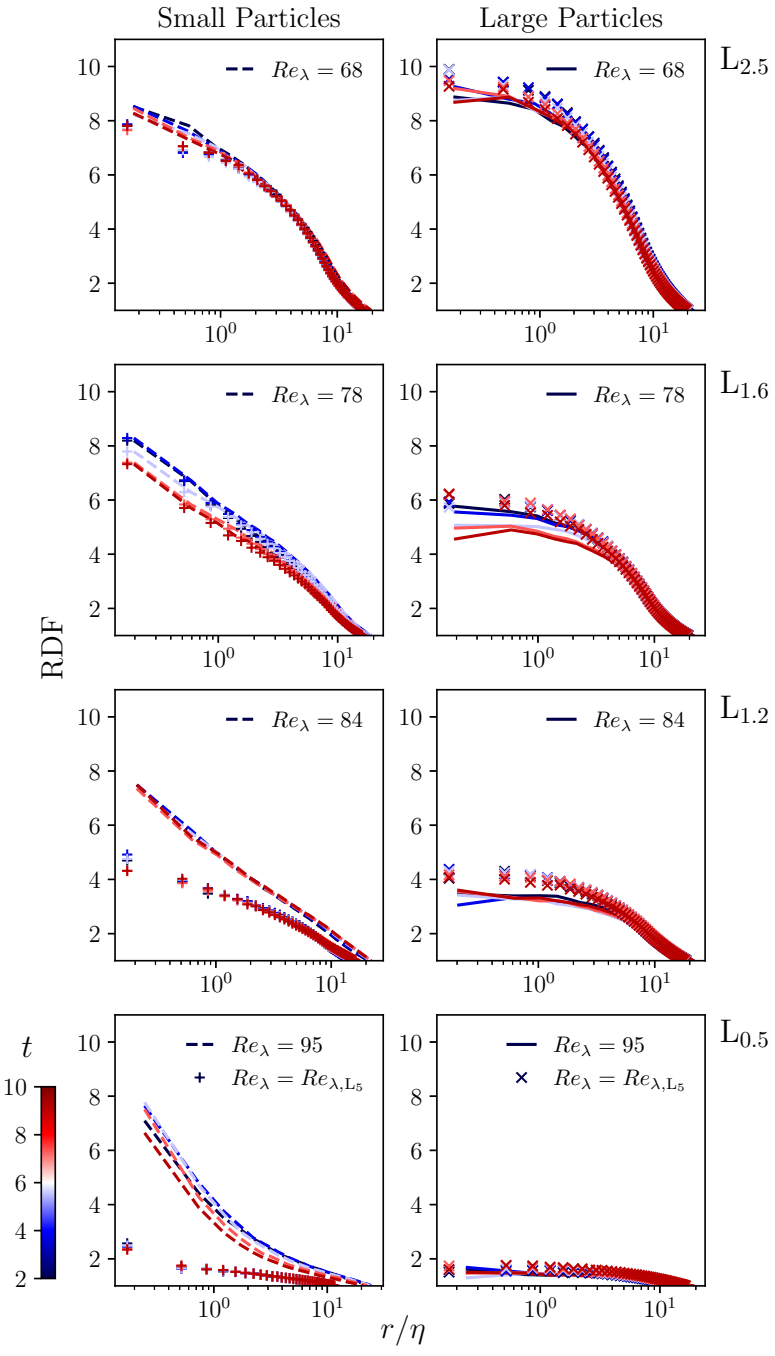


Figure 3.1: The dependence of particle clustering (RDF) on Re_λ.

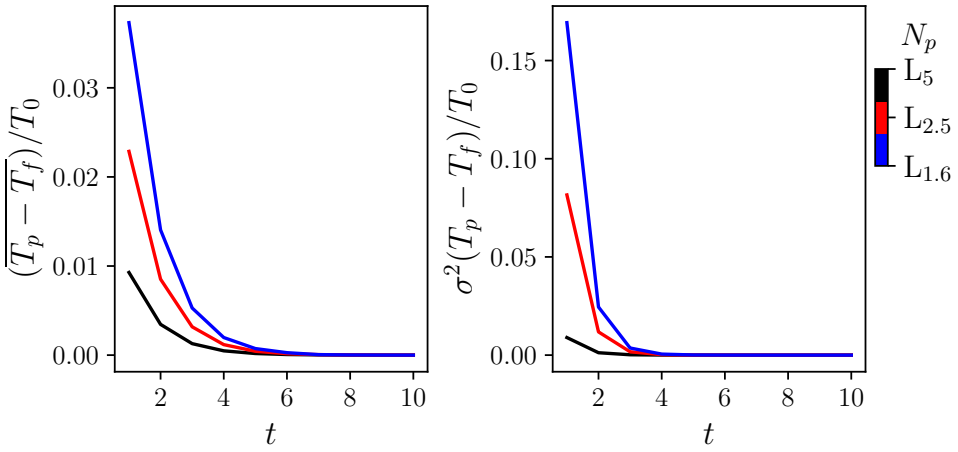


Figure 3.2: The average difference between particle (T_p) and fluid (T_f) temperatures (left), and the variance (σ^2) of this temperature difference (right), normalized with the temperature at $t = 0$ of heating (T_0).

As a consequence of the rapid particle heating, it is expected that the particle and fluid will reach their maximum prescribed temperature quickly and the particle-fluid temperature difference will be small. This can be observed in Figure 3.2 (left), as the particle-fluid temperature difference drops to zero around $t = 5$, which also implies that the increase in μ_f stops roughly at this time. Consequently as per Figure 3.2, at $t = 1$ the particle-fluid temperature difference in L_5 is about 1%, which increased to 30% in $L_{0.05}$ (not shown here). This suggests that the rate of increase in gas viscosity drops with the decrease in particle loading, which will hinder the development of the fluid viscosity-based clustering, as discussed later. The increase in particle-fluid temperature difference with the drop in loading density is due to the reduction in heat transfer to the carrier fluid at lower loading densities. We also included the normalized variance (σ^2) of particle-fluid temperature difference in Figure 3.2 (right), which portrays a trend similar to the mean temperature difference. This suggests the absence of any significant local viscosity fluctuations, and hence the fluid viscosity varies with the rise in fluid temperature.

3.3.3 Turbulence Modulation

To quantify the effect of particle reaction drag force, the heating of different particle loadings, and the resulting change in viscosity on the underlying turbulence, we plot the evolution of the Taylor length scale in Figure 3.3. Because the Taylor microscale bridges the energy transfer between the integral and Kolmogorov scales, it indicates the impact of different test conditions on turbulence. It is apparent that the decay rate of λ is similar in all the test cases; however, particle heating significantly raises λ between $t = 0$ and 2. This can be justified with rapid particle heating, which increases TKE of the flow via pressure-dilatation at scales comparable to the size of particle clusters [21]. Therefore, the Taylor length scale augments as $\lambda = \sqrt{10\nu_f \mathrm{TKE}/\varepsilon}$. The rise in TKE can also be witnessed in Figure 3.4 in the form of a TKE jump right after the onset of heating. Although this slight transience is short-lived, it produces strong and long-lasting effects on other parameters such as λ, as the added energy is then passed down to the smaller scales, imparting a prolonged influence on the corresponding turbulent parameters. The drop in particle loading reduces fluid-particle energy exchange [152, 28]–the overall TKE increases with the decrease in particle loading [164, 165]–, and also delays the increase in fluid temperature and viscosity, which then slows the rate of TKE decay, as shown in Figure 3.4. A critical takeaway here is that in comparison to NH cases, the difference in λ between heating and $Re_\lambda = Re_{\lambda,\mathrm{L}_5}$ cases is minimal. This is another proof that the present comparison of L_5, $\mathrm{L}_{2.5}$ and $\mathrm{L}_{1.6}$ clustering behavior is valid.

Another important parameter depicting turbulence modulation by particles is the energy spectrum, as it determines the energy distribution among different turbulent scales. As discussed in Section 3.1, in momentum TWC, particles add energy to the small scales of turbulence at the expense of energy at the large scales [26], and this effect increases with increasing particle loading [27]. Similar trends are observed in the mean energy spectrum, $\overline{E(k)}$, plots in Figure 3.5. This figure presents the energy spectrum prior to particle heating ($t = 0$), such that only particle loading influences the energy distribution among the turbulent scales. Moving from L_5 to $\mathrm{L}_{0.05}$ shows the transition from the region where

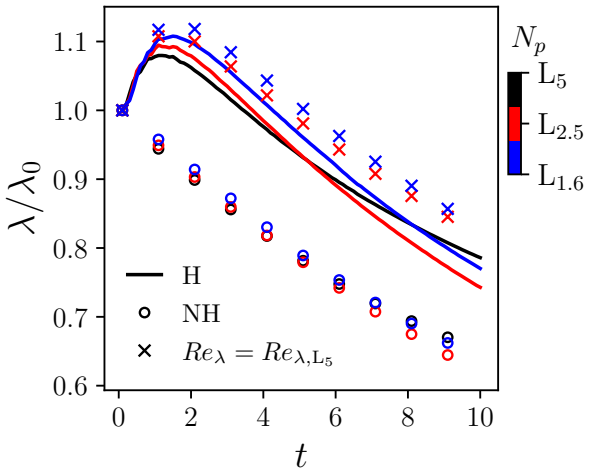


Figure 3.3: The evolution of normalized Taylor micro-length scale (λ). Here, H and NH in the legend represent simulations with heated and non-heated particles.

particle back-reaction is significant to where the particles stop enhancing the energy of the smaller scales. Note that the inertial range in Figure 3.5 is small (L_5 to $L_{0.5}$), which is due to the momentum TWC where fluid energy is also transferred from large to small scales via particles. Additionally, our low Re_λ also caused the inertial range to be small.

3.3.4 Timescales and Stokes Number

In decaying HIT, the integral timescale monotonically decreases, while the Kolmogorov timescale increases. Particle heating can potentially alter this standard behavior, however, present results are consistent with the classical trends despite the slight logarithmic curves of timescales, as depicted in Figure 3.6. This is because for τ_η, as per Equation (3.4), the increase in ν_f is divided by the rise in TKE dissipation rate ($\varepsilon = 2\nu_f S_{ij} S_{ij}$, where $S_{i,j} = 1/2\left(u'_{i,j} + u'_{i,j}\right)$ is the strain-rate and u' is the fluctuating velocity component). While, for τ_l the increase in ν_f decreases the velocity fluctuations (TKE), which according to Equation (3.3) is divided by the increase in ε. On the other hand, in an incompressible

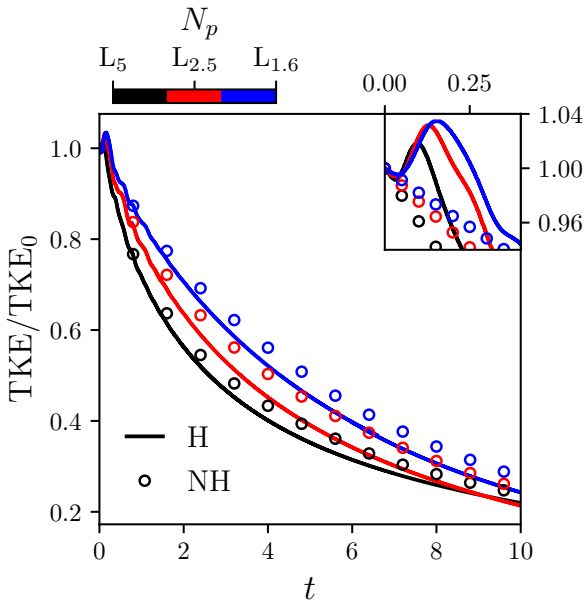


Figure 3.4: The temporal evolution of normalized TKE in H and NH cases.

flow without heating–constant ν_f and τ_p–, St_l and St_η monotonically increase and decrease, respectively, as depicted by the NH curves in Figure 3.7. But, since ν_f in Equation (3.2) is not normalized, our heating St_l and St_η curves depart from the conventional trends–variable τ_p. Here, St_η shows the greatest deviation due to a smaller d_p^2, which is overpowered by the increase in ν_f in the denominator of Equation (3.2). Hence, in the initial heating transient when the viscosity rapidly changes with temperature, St_η drops abruptly. It is overall clear that particle heating considerably alters the turbulent characteristics of the flow, which should affect particle clustering characteristics.

3.3.5 Clustering Quantification

Looking at the St_l and St_η, the main question is, does particle clustering adapt to the changes in St and still portray maximum clustering at $St \approx 1$? As per Figure 3.7, it

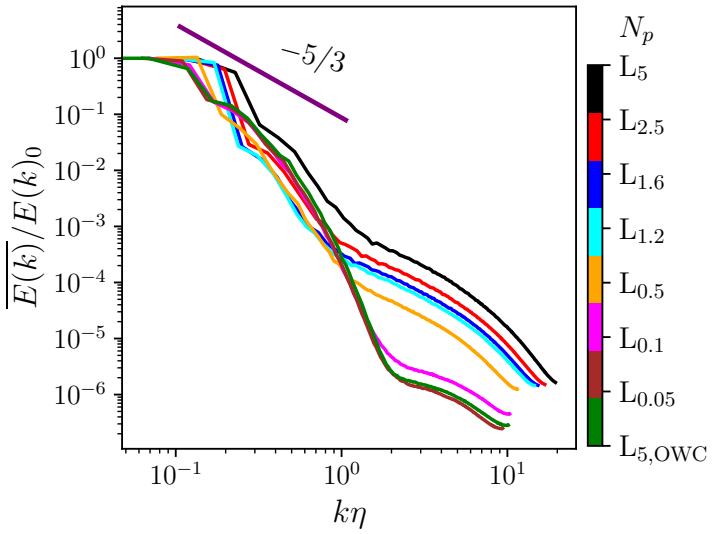


Figure 3.5: The mean energy spectrum ($\overline{E(k)}$) of the test cases at $t = 0$ of H simulations, normalized with its initial value. The $L_{5,OWC}$ is identical to present L_5, except with momentum OWC.

is expected that the larger particles will show higher clustering, especially towards the end of the simulation, where the St_l approaches unity. An opposite trend is expected for smaller particles considering the evolution of their St_η. To test this, we computed RDF of the three test cases as shown in Figure 3.8. We also repeated these cases without heating, which shows particle clustering in the absence of thermodynamic changes in the fluid. Here, the clustering in NH cases can be explained by the history effect for larger particles and enhanced clustering at dissipative scales for smaller particles. In the absence of temperature-based viscous effects, the H and NH RDF curves should overlap. We observe a dissimilar trend in Figure 3.8 for L_5 and $L_{2.5}$. But, before elucidating this, it is worth highlighting that the clustering pattern of small and large particles inverts from L_5 to $L_{1.6}$; larger particles show more clustering in L_5, and small particles show greater clustering in $L_{1.6}$. A similar trend was also witnessed in Saieed et al. [151] where in *Gas 1* and *Liquid 1* larger particles depicted higher RDF than smaller particles, while an opposite pattern

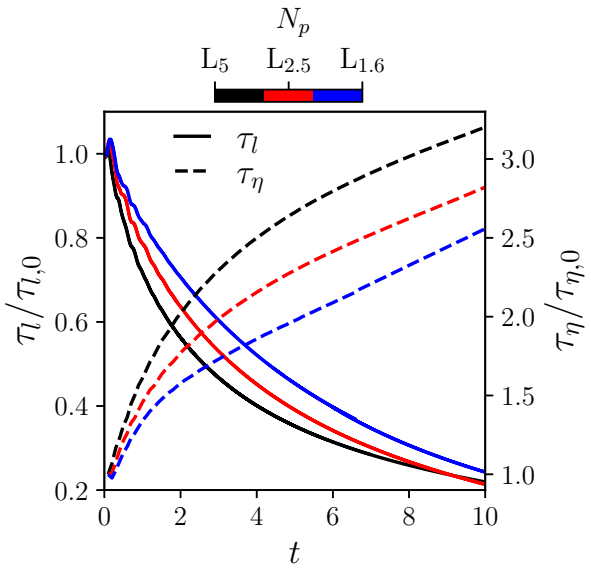


Figure 3.6: The evolution of integral (τ_l) and Kolmogorov (τ_η) timescales normalized with their initial values.

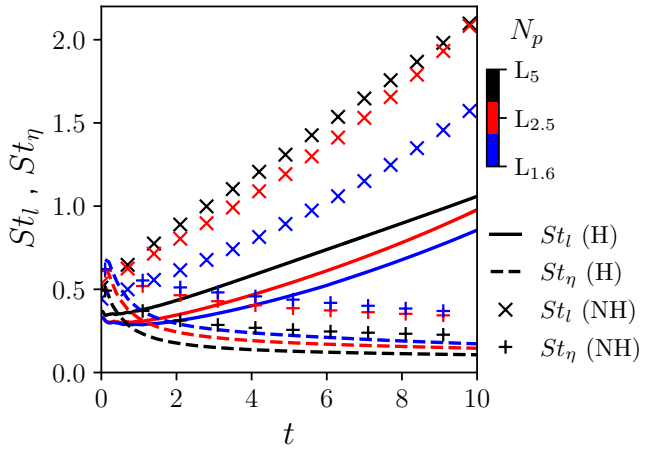


Figure 3.7: The temporal evolution St_l and St_η in the heating regime.

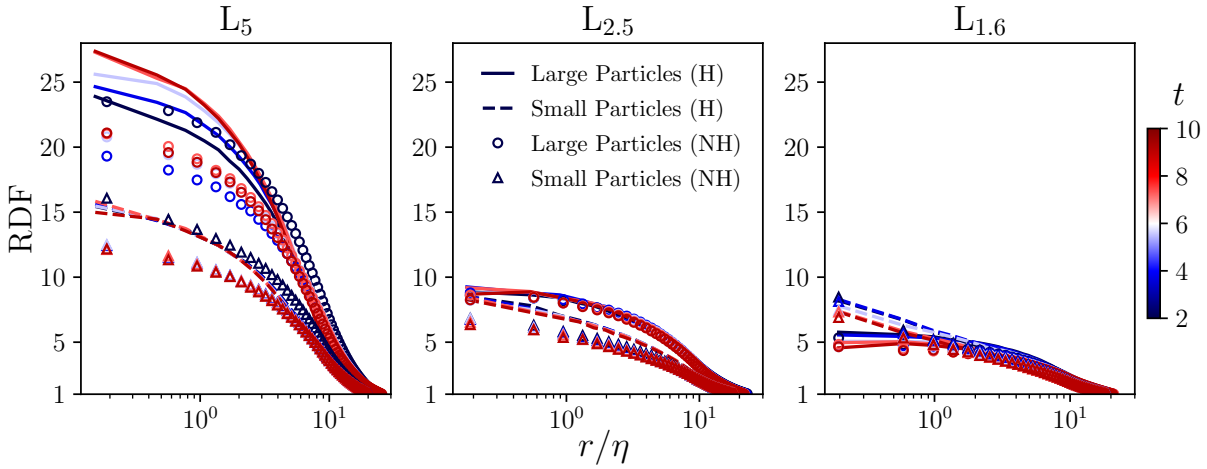


Figure 3.8: The RDF of small and large particles at even timesteps.

was observed in the other cases. This is a turbulence-driven effect (as discussed later), and thus we are not concerned with whether smaller or larger particles show greater clustering. Our focus is on the increase in clustering–of either particle species–due to the increase in viscosity upon heating.

Before analyzing the heating results, we need to grasp the clustering pattern of each particle species prior to heating. We see that St_l and St_η values at the start of the heating simulations are comparable as per Figure 3.7. Thus, both particle species should have similar clustering at the onset of heating. We observed this trend in $L_{2.5}$ and weakly in $L_{1.6}$, but not in L_5. This is potentially due to the forcing scheme used, which adds energy to the flow at random locations, increasing the local velocity fluctuations and gradient. Towards the end of base simulations when St_l and St_η have approached their values at $t = 0$ in Figure 3.7, the addition of energy would disperse the particles, potentially breaking clusters. The particles in test cases $L_{2.5}$ and $L_{1.6}$ have enough empty spaces to stay dispersed once a cluster breaks, before particles form new clusters. Hence, they also show very low clustering at the start of heat (Figure 3.8). The lack of large empty spaces in L_5 results in the formation of a new cluster as one cluster breaks, resulting in higher clustering. However,

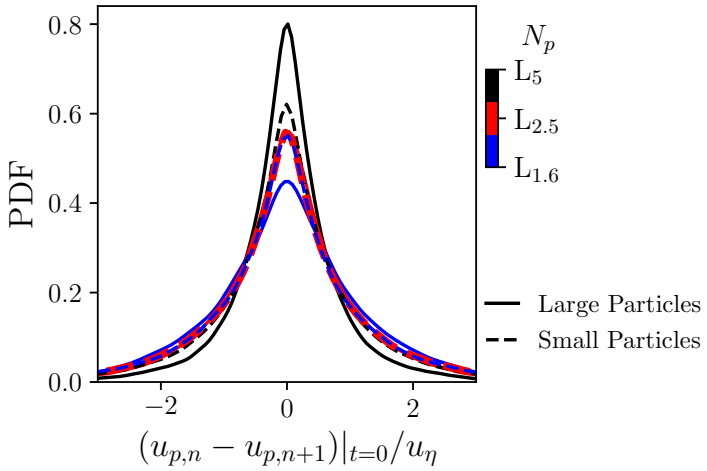


Figure 3.9: PDF of normalized particle-particle relative velocity at $t = 0$ of heating. Here, n present the n^{th} particle.

even in this scenario, both particle species of L_5 should depict similar initial RDF curves. This difference in initial clustering is due to the difference in drag force experienced by the two particle sizes. The drag force experienced by larger particles is on average about $O(10^1)$ higher than that of smaller particles. The random addition of TKE pushes larger particles more, forcing them to disperse and then form clusters. Hence, we cannot use St_l and St_η to delineate particle clustering at the onset of heating.

To this end, we evaluated the PDF of particle-particle relative velocity just prior to heating ($t = 0$), as illustrated in Figure 3.9, to elucidate clustering at $t = 0$ as particle clustering is a function of this relative velocity [49, 50]. This PDF indicates the number of particles of each species possessing similar velocity. Therefore, a tighter PDF shows a greater clustering capability of a particle species. We see a good agreement between the PDF peaks and the initial RDF curves. For example, the PDF of L_5 larger particles is higher than its smaller particles, while both species of $L_{1.6}$ show similar PDF curves. On the other hand, relative velocity curves of small and large particles of $L_{2.5}$ perfectly overlap.

Now that the initial clustering pattern of each particle species is understood, we can

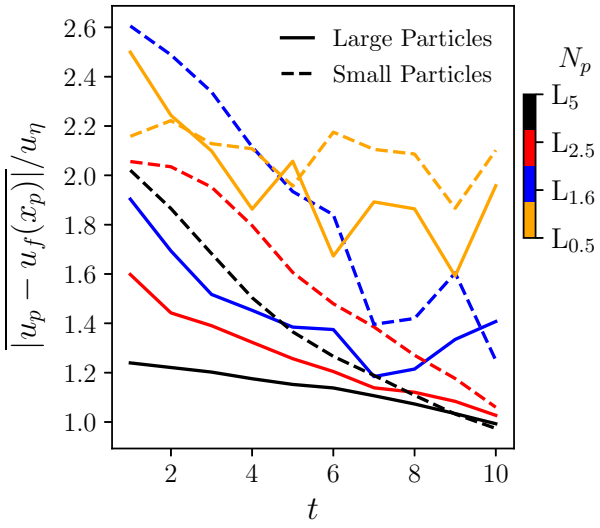


Figure 3.10: The temporal evolution of fluid-particle mean drift velocity ($\overline{|u_p - u_f(x_p)|}$) in the hot regions, normalized with the Kolmogorov velocity ($u_\eta = \eta/\tau_\eta$).

explain the VC by collating H and NH particles' RDF plots in Figure 3.8. Comparing these curves of L_5 shows opposite trends in the two simulation sets, while the difference between these two simulations (H and NH) decreases with particle loading. This highlights a crucial phenomenon that, only well-formed clusters before heating establish VC upon heating, and the probability of cluster formation before heating dwindles with the reduction in particle loading. In the case of finite heating, the fluid reaches its maximum temperature and viscosity before the VC takes any dominant effect. Hence, the difference between heating and non-heating simulations decreases with particle loading.

3.3.6 Viscous Capturing

To further elucidate the RDF trends with the VC mechanism, we evaluated the mean particle-fluid drift velocity in regions with temperature one standard deviation higher than the average fluid temperature (hot regions or HR)–$T_{HR} > \overline{T_f} + \sigma(T_f)$, where σ is the

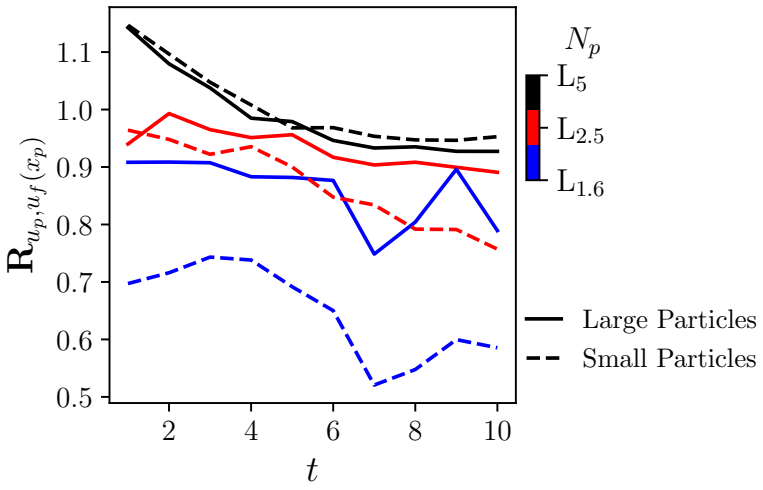


Figure 3.11: The temporal evolution of fluid-particle velocity distance correlation coefficient ($\mathbf{R}_{u_p,u_f(x_p)}$) in the hot zones.

standard deviation–in the heating simulations, as shown in Figure 3.10. The strength of VC can be determined by the low local particle-fluid drift velocity in T_{HR} regions as higher viscous drag on particles correlates the fluid and particle velocities. In Figure 3.10, we see that larger particles of L_5 not only show the lowest drift velocity, but the drift velocity increases with the decrease in particle loading. Plausibly, lower particle loading results in more unoccupied fluid volume, where fluid does not exchange energy with the particles and consequently possesses higher TKE, see Figure 3.4. This high-energy fluid disperses viscous clouds, and therefore the local fluid velocity fluctuations at the particle location increase with the drop in particle loading, raising the drift velocity. Overall, the high RDF and low drift velocity in heated cases clearly suggest the important role of VC.

A surprising observation in Figure 3.10 is the monotonic decrease in L_5 and $L_{2.5}$ drift velocities. In a turbulent flow–whether particles are clustered or unclustered–, it is expected that particles experience finite spatial translation between consecutive time instances due to local fluid velocity variance, and thus fluctuating drift velocity curves should have been

observed. To highlight this, the drift velocity of $L_{0.5}$ is also plotted in Figure 3.10 which clearly validates this phenomenon. Minor fluctuations in $L_{1.6}$ suggest only marginal VC at this particle loading. Additionally, on average the drift velocity of both particle species of $L_{0.5}$ was roughly 2.5 times higher than that of L_5 particles, which further highlights the aforementioned relationship between VC and particle loading. It is worth mentioning that we do not take inter-particle collisions into account, which is a reasonable and common assumption based on the global particle loading considered. But particle loading in a cluster can be significantly higher than the global average, and as a result, inter-particle collisions can have negligible (reduced effect of particle-particle collisions due to increased viscosity) to detrimental (particles disperse after collisions) impact on VC. However, this requires further scrutiny of VC mechanism with four-way momentum coupling for a definitive conclusion.

Considering the particle-fluid drift velocity in Figure 3.10, it is expected that the intensity of viscous capturing determines the particle-fluid velocity correlation in hot zones. To test this, we evaluated the distance correlation coefficient ($\mathbf{R}_{u_p,u_f(x_p)}$) between particle and fluid velocities in the hot zones, as depicted in Figure 3.11. We observe a good agreement between the drift velocity trends in Figure 3.10 and $\mathbf{R}_{u_p,u_f(x_p)}$ values, where cases with low drift velocity result in higher correlation between particles and fluid velocities. Therefore, VC correlates the fluid-particle velocity in a cluster and the intensity of VC determines the strength of this correlation.

3.3.7 Fluid-Particle Acceleration

The effect of fluid viscosity is directly reflected in the acceleration experienced by each particle species, as the viscous drag is the only force acting on the particles. Conventionally, smaller particles should adapt to the fluid acceleration, whereas larger particles should show a higher tendency to follow their own path due to their higher momentum. These trends can be seen in Figure 3.12, where the negative values depict deceleration, while positive values represent acceleration. In this figure, acceleration was found by computing the

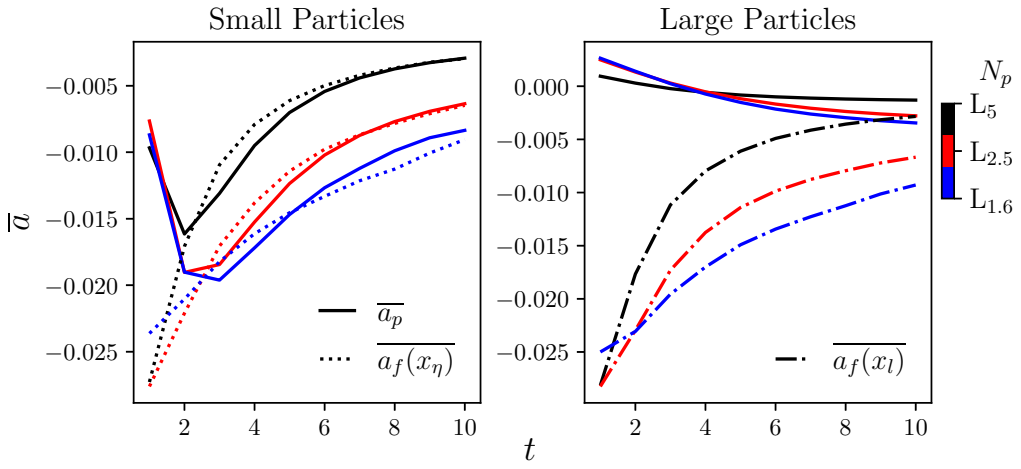


Figure 3.12: The temporal evolution of mean small and large particle acceleration magnitude. The local fluid acceleration at small ($\overline{a_f(x_\eta)}$) and large ($\overline{a_f(x_l)}$) particle location is also provided for comparison. Note that these curves are non-normalized.

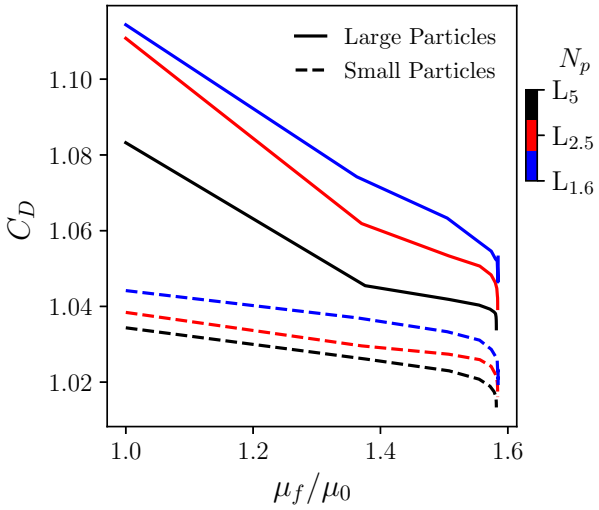


Figure 3.13: The behavior of mean particle drag coefficient (C_D) with respect to the normalized dynamic viscosity.

difference in the mean velocity magnitude of each particle species between two consecutive timesteps. The same procedure was repeated for the magnitude of the fluid acceleration at the particle location. As expected, smaller particles rapidly adapt to the fluid deceleration and re-adjustment to the evolving drag force, which attenuates very slowly, see Figure 3.13. In contrast, larger particles initially accelerate due to their much higher drag coefficient (Figure 3.13), which forces them to adapt to the local fluid with a high-velocity variance. Recall that the fluid is faster than the particles; as in the base simulations, we forced the fluid to energize the particle motion. On the other hand, as the mean particle drag coefficient (C_D) dwindles, particles transition from an accelerating to a decelerating regime after $\mu_f/\mu_0 = 1.4$ (Figure 3.13). The increase in large particle deceleration is in the order $L_5 < L_{2.5} < L_{1.6}$, exactly opposite to the VC effect in the three test cases. This is because the difference in the acceleration of large particles and $\overline{a_f(x_l)}$ of L_5 is much smaller than in other cases; in fact, its acceleration curve is almost a plateau at zero. Hence, the L_5 larger particles are well-correlated with the local fluid acceleration and are spatially traveling with the same fluid at their location.

The continuous adaptation of the acceleration of small particles to the fluid suggests that they are taking energy from the fluid, while the continuous rise in the deceleration of $L_{2.5}$ and $L_{1.6}$ larger particles indicates that they are adding energy to the fluid–as per the classical behavior [154]. To confirm this, the difference in the mean turbulent kinetic energy ($\overline{\mathrm{TKE}(x_\eta) - \mathrm{TKE}(x_l)}$) at the location of small and large particles is computed in Figure 3.14. According to the convention, the turbulent kinetic energy at the location of the larger particles should be greater than their smaller counterparts. Here, only L_5 shows an unconventional trend. This is only possible if the particles do not add energy to the fluid and follow the fluid according to Figure 3.10. In other words, apart from altering particle clustering behavior, VC also impacts the turbulence modulation by particles.

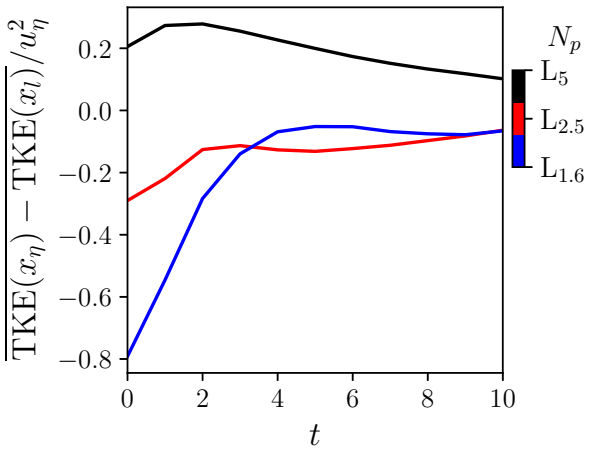


Figure 3.14: The temporal evolution of normalized difference in mean TKE at the position of small (x_η) and large (x_l) particles.

3.3.8 Particle Distribution

Strain Rate and Vorticity

It was found with momentum OWC that particles of different sizes congregate in a range of strain rate (S) and vorticity (Ω) zones, see Figures 14 and 15 of Saieed et al. [151]. In TWC, we expect the local S and Ω fluctuations to be damped by the particles as S and Ω are the symmetric and skew-symmetric parts of $\nabla\mathbf{u}$, respectively. Furthermore, the extent of local increase in viscosity also determines the attenuation in local S and Ω. We see this phenomenon in Figure 3.15, which presents the temporal distribution of particles in different S and Ω regions. Similar to the previous plots, L_5 shows opposite trends compared to $\mathrm{L}_{2.5}$ and $\mathrm{L}_{1.6}$, where its larger particles are sampling low S and Ω regions. Enhanced clustering of L_5 larger particles produce a higher attenuation of S and Ω. The extent of VC also causes the particles to temporally reside in the same local fluid (inside a viscous cloud), resulting in particles' local S and Ω values drop with time. If the particles were not captured and restrained in local high viscosity regions, a particle cluster would disintegrate

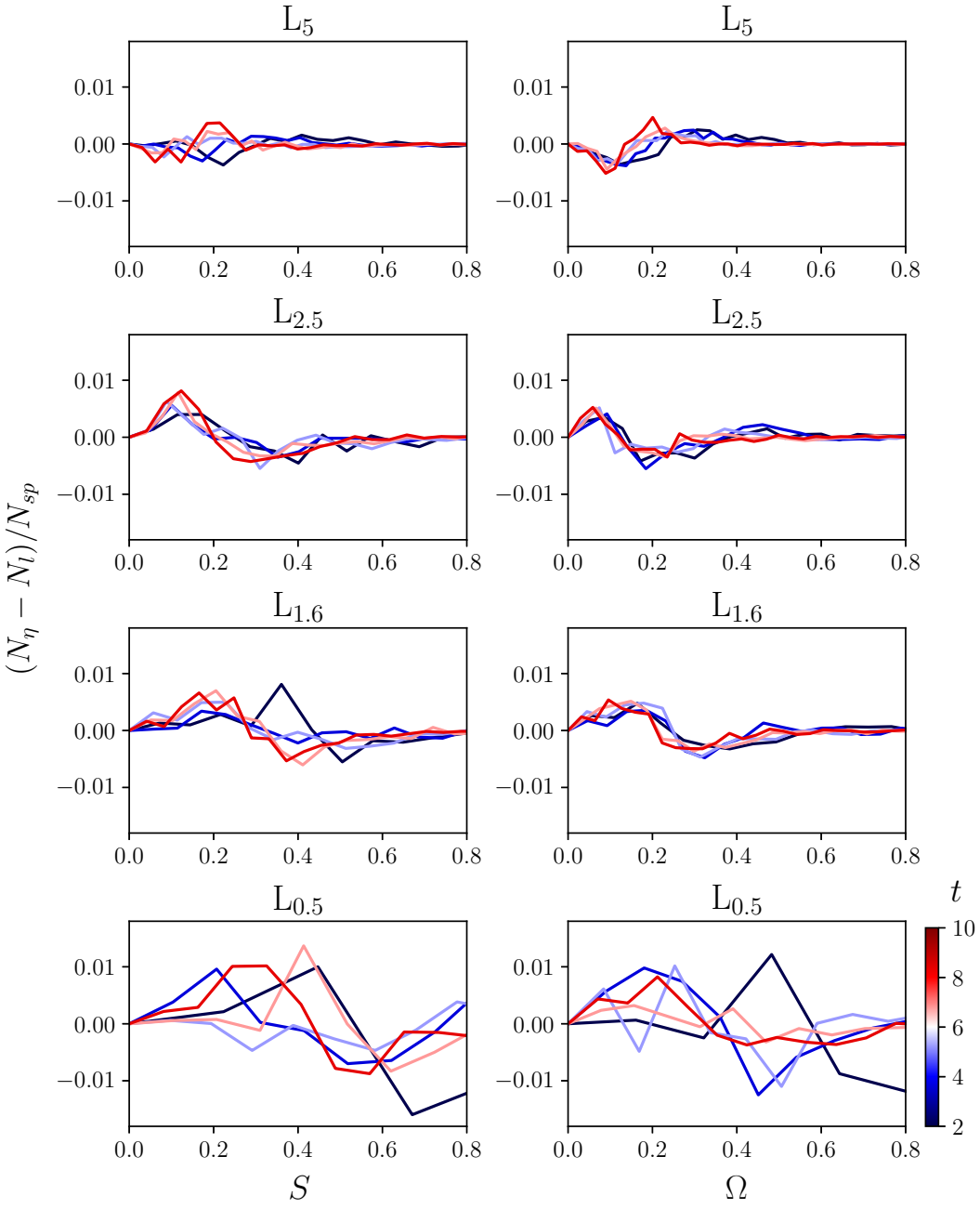


Figure 3.15: The normalized difference in the number of small (N_η) and large (N_l) particles in different strain rate, S, (left column) and vorticity, Ω, (right column) regions at even timesteps.

in $t = O(\tau_\eta)$ [166]. In fact, even if a cluster experiences partial disintegration, the curves in Figure 3.15 would display much more fluctuations; the separating particles would reside in different S and Ω regions at adjacent timesteps. This trend can be seen in the $L_{0.5}$ plots.

Based on the understanding of PC [46], as St_l approaches unity the larger particles should move into high S and low Ω regions. While, as St_η drops further below unity, smaller particles should reside in high Ω regions. We do not see this in Figure 3.15. This is because the above explanation applies to the local maxima and minima of S and Ω, but we present particle number densities in a global (computed over the entire domain) context. The main observation here is that the local viscous effects greatly influence particle behavior in the fluid and cause them to globally sample certain S and Ω regions depending upon the strength of VC. Albeit, the local sampling of inertial particles in high S (low Ω) regions is a plausible explanation of particle clustering in unheated cases, VC can cause particles to remain temporally captured in different S and Ω regions of the domain. Therefore, this global description of particle location can be critical for thermal applications of particle-laden flows, although it requires further testing in continuous flow scenarios such as channel flow.

Cluster Identification

To identify individual particle clusters in the flow, we employ a method known as Density Based Spatial Clustering of Application with Noise (DBSCAN) [167], which is an unsupervised machine-learning algorithm. Similar tools have been successfully applied to a posteriori analysis in a variety of turbulent flows [168, 169, 170]. We chose DBSCAN for this analysis because of its ability to spatially localize particle clusters, where it identifies particles in each cluster and labels them separately. This greatly aids in conducting other statistical analyses on the clustered particles, as shown later in this section. Furthermore, DBSCAN method is theoretically similar to RDF which we used earlier in Sections 3.3.1 and 3.3.5, as it also counts the number of particles from a certain distance from a reference particle, as discussed below.

Case	L_5		$L_{2.5}$		$L_{1.6}$	
Particle radius	0.0106	0.0028	0.0106	0.0028	0.0106	0.0028
D	0.055	0.055	0.065	0.060	0.070	0.060

Table 3.3: Particle species specific values of ϵ for cluster identification in 3D snapshots.

The DBSCAN method identifies regions of high particle density by segregating data into core and noise points based on two parameters; inter-particle distance, D, and minimum number of neighbouring particles, $N_{cl,min}$, required to form a cluster. Here, $N_{cl,min}$ or more particles at a distance D from a core particle belong to a cluster, while the other particles are noise points and are considered unclustered. Note that D and $N_{cl,min}$ are input parameters and require careful estimation, as cluster identification is highly sensitive to these parameters. Determining $N_{cl,min}$ is straightforward, as it is typically taken as twice the number of considered data dimensions [171]. For example, $N_{cl,min} = 6$ for a 3D data set. The estimation of D on the other hand, is slightly complex as it requires a good understanding of the data and some experience with the DBSCAN method. For finding D, a k-distance plot is required, which bins the particles based on their minimum distance from the nearest neighbour. This plot has a characteristic *elbow* shape, and the prevailing idea is to take D equal to the inflection point on the curve.

In light of the above discussion, we take $N_{cl,min} = 6$ for our 3D snapshots. Next, we computed the species-specific k-distance plots for all test cases that resulted in ϵ as shown in Table 3.3. Note that our k-distance plots exhibited two inflection points, which is normal. As per the DBSCAN guideline, we chose the smallest D values.

Returning to Section 3.3.5, there is still an unanswered question; why the clustering of L_5 smaller particles (RDF curves in Figure 3.8) is not temporally evolving, despite sharing the domain with L_5 larger particles showing strong VC? In the other two test cases, this can be attributed to weaker VC. Furthermore, the reasonably high RDF at $t = 2$ also implies that L_5 smaller particles are clustered prior to heating, a prerequisite for VC. To

answer this, we estimate the distribution of clusters using DBSCAN in the 3D domain. We also extracted 2D slices from the 3D clustering snapshots and mapped them on 2D temperature contours at the center of the domain. These are illustrated in Figure 3.16. Visualizing the 3D snapshots shows that, albeit L_5 smaller particles are clustered, such clusters are much smaller and well-distributed in comparison to L_5 larger particles. Such small clusters can be witnessed in all other 3D snapshots. This indicates that in addition to well-formed clusters, VC also requires *large* unevenly distributed clusters in the domain. It can be seen that the clusters are not exactly in the shape of a cloud. In fact, they are elongated in the shape of tubes/threads similar to caustics of suspended particles [69], as they are confined by a virtual boundary of a sharp temperature gradient called *front* [48], as depicted by the 2D contours of Figure 3.16.

In a fluid domain, particles with vastly different history paths can assemble in a region. In the absence of any external factor, such as heat, these particles carry their history even in shared space. This implies that the distribution of particle velocity in a cluster should be similar to particle velocity distribution in the entire domain. We see this trend in smaller particles as per Figure 3.17, yet a much tighter PDF is obtained for $u_{p,c}$ of larger particles. These particles inside a cluster have similar and the highest temperature in the domain, see Figure 3.18, which correlates the particle velocity field via increased drag. In these figures, the peak velocity and temperature PDF of clustered larger particles are approximately 1.4 and 2 times higher than the PDF of the entire domain. Thus, VC greatly overpowers the particle history path, forcing the particles to remain in a hot zone. Figures 3.17 and 3.18 also suggest that the difference between the global and clustered particles' velocity and temperature PDFs drops as the particles loading decreases.

Next, we want to test if VC retains particles over time. The particle history inherently should vastly alter the number of particles per cluster in the absence of VC. To assess this notion, we computed the average number of particles in a cluster per cluster length as demonstrated in Figure 3.19. Similar to Figure 3.10, the temporal fluctuation increases as the VC effect loses its strength from L_5 to $L_{1.6}$. We also note that the number of particles per cluster increases significantly due to VC. Hence, it is clear from the discussion in this

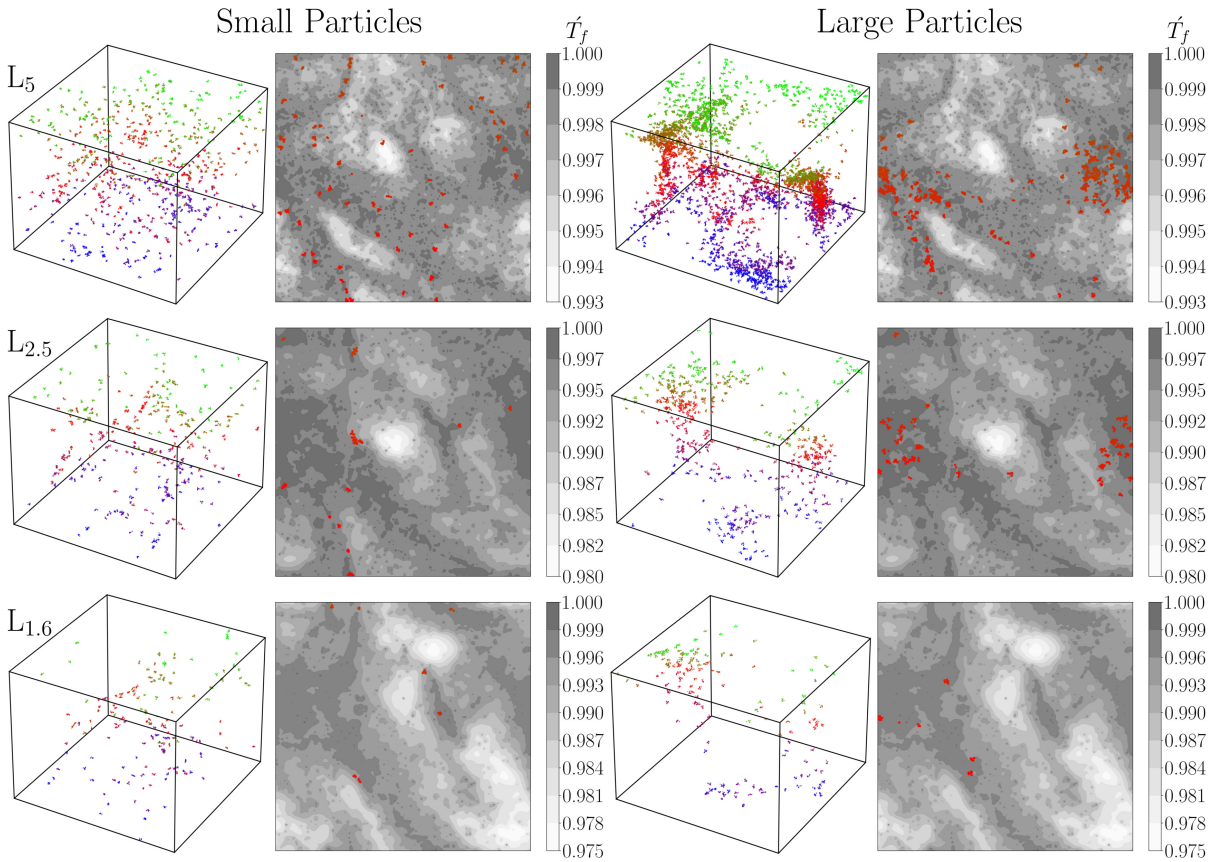


Figure 3.16: Clusters identification using DBSCAN method at $t = 2$ of heating. These 3D snapshots represent the overall distribution of clusters in the domain, whereas the 2D slices show the normalized temperature ($\acute{T}_f = T_f/T_{f,max}|_{t=2}$, where $T_{f,max}|_{t=2}$ is the maximum fluid temperature at $t = 2$) and clusters distribution in 2D slice of depth= 5η computed at the center ($x = 0$) of the box domain. Here, each particle cluster is identified with a different color, and unclustered particles are removed.

section that the control of temperature-driven viscosity on particle clustering is a strong function of particle loading density.

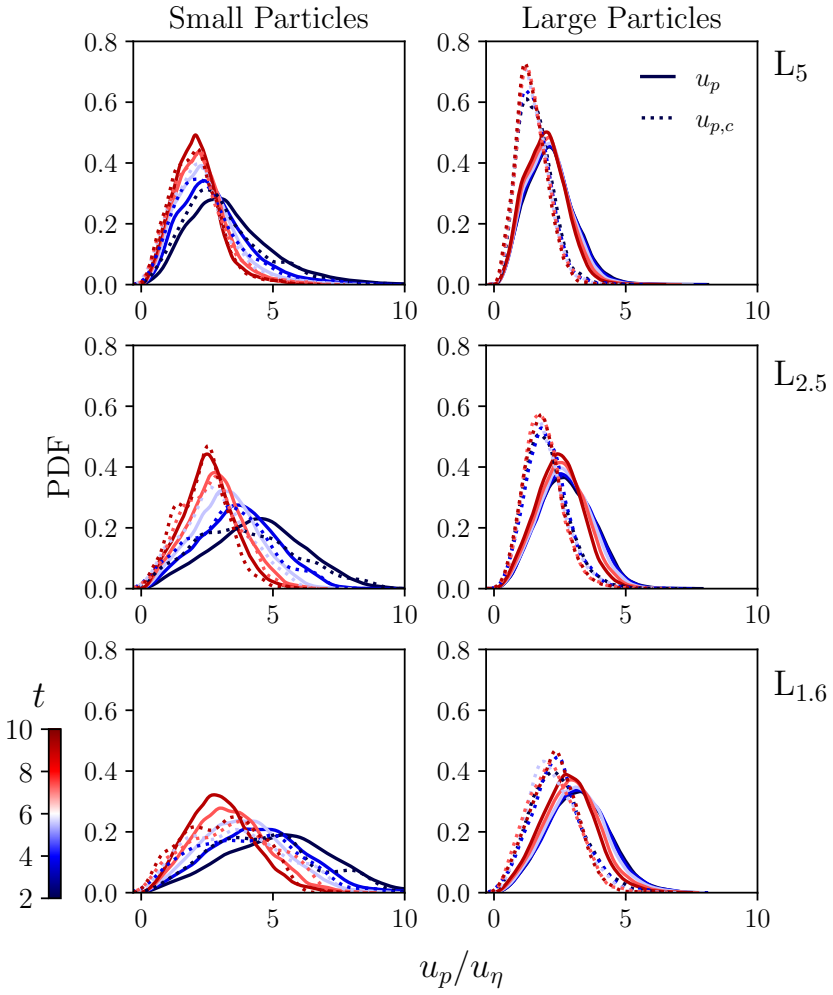


Figure 3.17: PDF of normalized particle velocity (u_p) and clustered particle velocity ($u_{p,c}$).

3.3.9 Mathematical Interpretation of Viscous Capturing

Considering the significance of thermoviscous effects on the turbulence and particle dispersion, another scientific question is why St and particle clustering do not evolve together, since St already accounts for μ_f? This is because τ_p, and consequently St, accounts for the instantaneous μ_f, but it does not consider the spatial and temporal change in μ_f. As

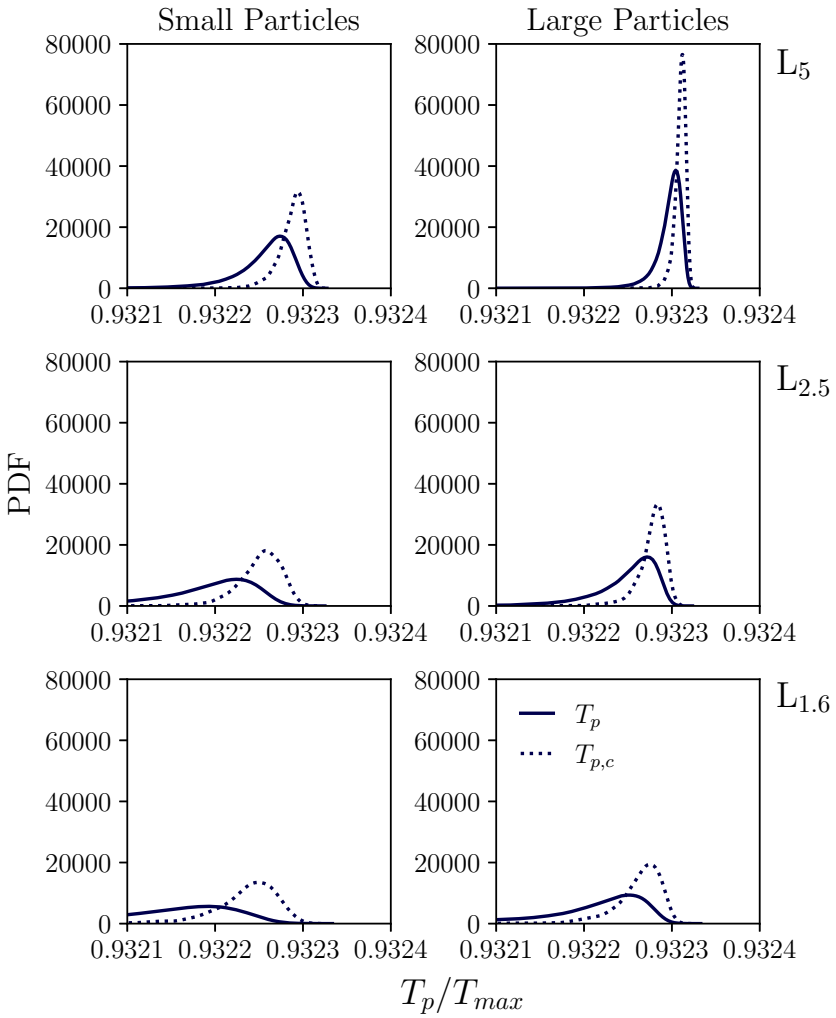


Figure 3.18: The PDF of normalized particle temperature in the entire domain (T_p) and in clusters ($T_{p,c}$) at $t = 2$ of heating. Where, T_{max} is 600. Only one timestep is shown as a similar distribution is obtained at other timesteps.

established in this study, the changes in μ_f and the corresponding effects on the particles and fluid turbulence play a critical role in governing particle clustering. Thus, we propose a mathematical explanation to account for VC in heated systems. Recall that VC is tied to

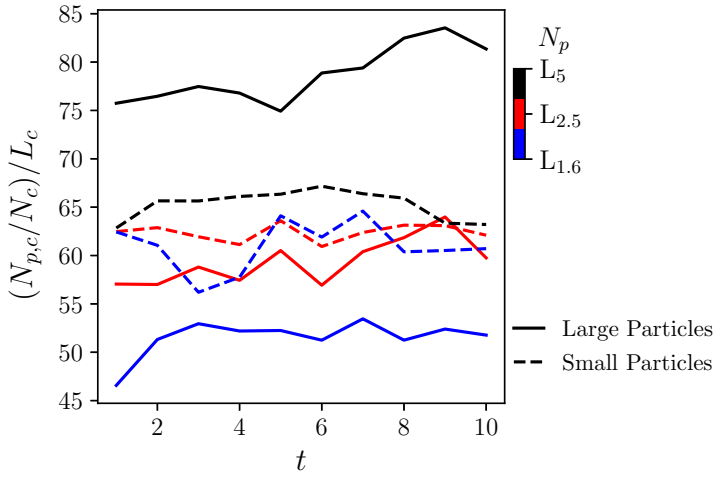


Figure 3.19: The average number of particles in a cluster per cluster characteristic length (L_c). Here, $N_{p,c}$ and N_c are the number of clustered particles and the number of clusters in the domain, respectively.

the ability of higher viscosity gas to capture and retain particles passing through it. This ability is tied to the drag force which is enhanced within the viscous region, and is directly linked to the particle acceleration. Therefore, if we substitute particle relaxation timescale (Equation (3.2)) into the equation of Lagrangian particle motion (Equation (3.11)), we get:

$$\frac{du_{p,i}}{dt} = \frac{C_D 18 \mu_f}{\rho_p d_p^2} \left(u_{f,i}\left(x_p\right) - u_{p,i} \right) \tag{3.16}$$

here C_D has a weak dependence on fluid viscosity (and thus temperature) and can, for mathematical tractability, be assumed constant in the present analysis.

Noting that power-law form of the viscosity (Equation (3.9)), we can write:

$$\frac{du_{p,i}}{dt} = \frac{C_D 18}{\rho_p d_p^2} \Delta u \, \mu_0 \left(\frac{T}{T_0} \right)^{\frac{2}{3}} \tag{3.17}$$

where $\Delta u = u_{f,i}\left(x_p\right) - u_{p,i}$. We can now separate purely hydrodynamic components,

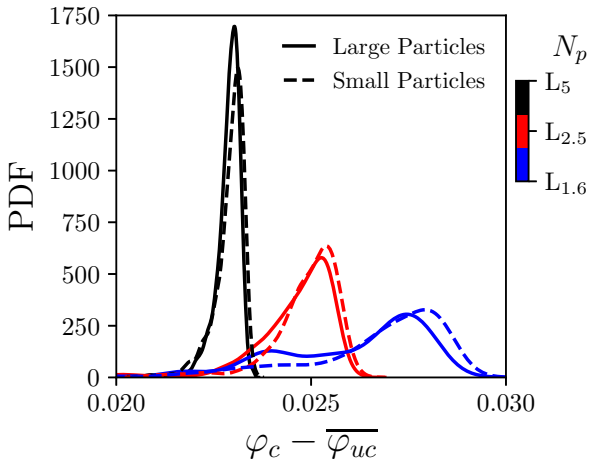


Figure 3.20: PDF of $\varphi_c - \overline{\varphi_{uc}}$ at $t = 2$.

denoted as:

$$F_{hydro} = \frac{C_D 18}{\rho_p d_p^2} \Delta u \mu_0 \tag{3.18}$$

This component is related to the particle drag force without a variable viscosity effect. This term is modified by the coefficient of VC (φ):

$$\varphi = \left(\frac{T}{T_0} \right)^{\frac{2}{3}} \tag{3.19}$$

here T is the fluid temperature in the vicinity of a particle. Therefore, the equation of Lagrangian particle motion can be expressed as:

$$\frac{du_p}{dt} = \varphi F_{hydro} \tag{3.20}$$

As shown earlier, viscosity-driven clustering is tied to a higher φ. To verify this, we compute the coefficient, φ, for the fluid at the location of the clustered (φ_c) and unclustered (φ_{uc}) particles. We plot the PDF of their difference at $t = 2$ in Figure 3.20. Since the number of clustered and unclustered particles can vary at each timestep and we are primarily concerned with φ_c, we subtracted the mean coefficient of unclustered particles

($\overline{\varphi_{uc}}$) from that of clustered particles. The peak and spread of the PDF($\varphi_c - \overline{\varphi_{uc}}$) matches our previous plots, where L_5 larger particles show more VC than their smaller counterparts, and this trend slowly inverts in lower particle loading numbers. Note that this difference in φ_c and φ_{uc} accounts for the spatial change in temperature-based viscous effects, while T in the numerator of Equation (3.19) increases with time due to particle heating.

We acknowledge that this formulation of φ is very simplistic and assumes C_D as constant, which is not true in practice. However, it adequately demonstrates the VC trends in agreement with the RDF of the present particle loading densities. A comprehensive mathematical model of φ warrants a more thorough testing of thermoviscous effects on particle dispersion, especially with higher Reynolds number simulations. We leave this for future analysis.

3.4 Summary

A DNS study of particle-laden decaying HIT modeled with TWC in momentum and energy is conducted to test the effect of particle number density on the temperature-dependent viscosity-based particle clustering. For this, a power-law model was used for specifying temperature-dependent gas viscosity, and two particle species were used for three cases with different particle loading numbers. The particle-fluid momentum and energy interactions were modeled with TWC. It is observed that the particle loading determines the strength of VC. Since higher loading density enhances the change of cluster formation before heating and also the local particle number density inside a cluster, it governs the fluid viscosity-based clustering. Depending on the strength of the VC, a particle species can considerably deviate from its conventional clustering behavior. Similarly, particle loading has a significant influence on the energy distribution between the turbulent scales. Higher particle loading density substantially alters the energy spectrum by transferring energy from the integral scales to the dissipative scales via particles, which shrinks the Taylor microscale. Higher particle loading also decreases local fluid velocity fluctuations, which

aids in the retention of VC.

The global sampling of particles in distinct S and Ω regions is also a strong function of particle loading and consequently the extent of VC. The particles viscously captured reside in the same local fluid within a viscous cloud over time, and therefore, the S and Ω at particle location dwindle temporally. Hence, the increasing fluid viscosity can considerably stabilize the global distribution of particles in distinct S and Ω regions, and in this case, the particles appeared to be temporally stuck in these regions. This global S and Ω-based distribution of particles is critical as it outlines the high and low particle concentration regions during turbulence decay. Lastly, we visualized individual particle clusters in the 3D domain with the DBSCAN method, which further expanded the requirement of preformed clusters prior to heating for VC to be noticeable. We found that the preformed clusters must be large in size and unevenly distributed. Small clusters might themselves be somewhat evenly distributed in the domain, albeit particles are inhomogeneously distributed. Thus, they do not produce the same high local viscosity effect and cannot be captured or retained as particles in large unevenly distributed clusters. We also applied temperature and velocity-based conditional sampling on the clusters and found that the thermodynamic and kinematic parameters of the particles are greatly correlated inside clusters. This phenomenon also increased with the rise in particle loading density.

Phenomenologically, VC will only take effect if particles receive an even amount of heat regardless of their location (inside or outside the cluster), which is the case here. But, if particles experience a shadowing effect, which is a considerable factor in radiative heating [172, 173], the temperature inside a particle cluster would be lower than the temperature at the periphery of the cluster. In such a case, a particle cluster will not be able to create a strong viscous cloud. Hence, VC is not expected to be a dominant factor–even if observed at all–in controlling particle distribution in radiative heating. Also, note that there was no heat conduction between particles due to uniform particle heating and fast particle heating timescale (based on the heating model of Mouallem and Hickey [101]), and the inter-particle collisions were neglected. The presence of these effects might considerably affect VC.

In systems where the aforementioned conditions of higher particle number density and uniform particle heating are met, particles will show notably higher clustering and unconventionally modulate turbulence. This can be substantially detrimental for applications such as particle solar receivers, combustion of nanothermites in satellite engines and thermal spray coatings, etc. Furthermore, since viscous clouds can restrain particles, in extreme cases, particles might be spatially restricted in certain flow regions. However, this hypothesis requires further scrutiny in a continuous flow scenario.

Chapter 4

Viscosity-Driven Clustering of Heated Polydispersed Particles in Subsonic Jet Flows

Reference: A. Saieed, and J. P. Hickey. Viscosity-driven clustering of heated polydispersed particles in subsonic jet flows. *International Journal of Heat and Fluid Flow*, 112:109754, 2025, DOI.

Abstract

The clustering of heated particles is known to increase with the rise in local gas viscosity, even at particle Stokes number $St < 1$. Despite being a dominant effect that holds in TWC, this rise in clustering has been only probed in a triply periodic box via DNS, in which the flow evolves temporally and the total volume (and mean fluid density) is fixed. We conduct DNS to study the dispersion of heated polydispersed particles in a spatially developing subsonic confined jet flow, where energy and momentum are modeled with TWC. Although there is only a 16% increase in gas viscosity in the heated particle-laden

simulation, it is sufficient to limit the particles within the central hot region of the jet. The particles traveling laterally start clustering at a thermal front created at the outer periphery of the jet. Thus, their lateral dispersion is also limited. Despite starting with the same St values as their unheated counterparts, the concentration of heated particles sharply declines in the lateral direction, yielding more concentrated clusters. This is a compounding effect, where the presence of particles within the jet can produce more significant thermal changes inside the jet, which can further restrict the lateral movement of the particles. Experiencing identical eddies inside the jet causes particles of all sizes in the heating case to cluster at similar locations in the domain. These findings can considerably aid applications such as targeted drug delivery and cold spray coating techniques.

4.1 Introduction

Heated particle-laden jets are frequently observed in nature as volcanic plumes that contain hot ash and molten rock [174] as well as geothermal geysers consisting of steam, water droplets, and rocks [175]. Similarly, these jet flows are also common in advanced engineering applications such as thermal spray coating techniques [176], powder metallurgy [177], and metallic particle combustion in satellite engines for thrust generation [10]. In particle-laden thermal systems, the operational efficiency inherently relies on the uniform distribution of particles. This is particularly important as it leads to a uniform heat distribution, which is crucial for these applications. However, particles intrinsically tend to cluster due to their inertia [45].

Over the years numerous explanations have been put forward to elucidate particles' affinity towards clustering and the most widely regarded among these is the PC. In PC, turbulent eddies exert centrifugal force on the particles, thus pushing them out of higher vorticity regions into high-strain regions, which are between these eddies [46]. It is reported that PC can generate particle clusters with a particle number density up to sixty times greater compared to the domain average [143]. This consequently also produces voids in

the flow field with little to no particles. This uneven distribution of particles causes the particle-to-fluid heat transfer to drop by up to 25% [19] and, in combustion applications, it can entirely impede combustion within a cluster [18]. Therefore, inertia-based clustering of particles is particularly problematic, and consequently, a fundamental focus in thermal applications is to avoid clustering.

Particle clustering is primarily governed by the response of inertial particles to the local turbulence in the flow field. This is characterized by a dimensionless parameter called the *Stokes number* (St), which is the ratio of the particle momentum (τ_p) to the turbulence timescale (τ) [20]. Particle dispersion is a multi-scale phenomenon where particles react to turbulent eddies of different sizes based on their inertia [58, 122]. However, in a round jet, the particle dynamics is typically governed by the large-scale coherent turbulent structures [56]. This inspired the use of the jet convective timescale (τ_c) in the definition of the St [178], which is similar to the large eddy timescale of the jet. The convective timescale is the ratio of jet half-width ($r_{1/2}$) and centerline velocity (u_c). Thus, St is given as:

$$St = \frac{\tau_p}{\tau_c} = \frac{\rho_p d_p^2 u_c}{18 \rho_f \nu_f r_{1/2}} \tag{4.1}$$

In Equation (4.1), the subscripts f, p and j are used to define the fluid, particle and jet parameters, respectively. Additionally, d, ν and ρ are for diameter, fluid kinematic viscosity and density. Past research suggests that typically in unheated particle-laden jet flows, particles with $St \leq 1$ spread and cluster within the jet [179]. At the lower end of this range with $St \ll 1$, particles are tracer-like and their dispersion is similar to the jet flow [180]. However, particles with $St \to 1$ but $St < 1$ show inertial characteristics and start collecting at the outer periphery of the jet [64]. These particles do not cross the outer shear layer of the jet because their inertia is not large enough to pass through this layer. The $St \gg 1$ particles travel and cluster at the centerline of the jet core since they are primarily ballistic and therefore they are not affected by the local eddies [179]. Generally, $St < 1$ and $St \gg 1$ particles deliver acceptable dispersion as they mainly stay within the jet. On the other hand, the $St \approx 1$ particles, which are known for depicting maximum

clustering in isotropic turbulence [58], can be completely pushed out of the jet by the large eddies due to their higher dispersion rate than the local fluid [56]. Understandably, this class of St particles is deemed the most troublesome for thermal as well as jet flow applications.

The above St-based description of particle dispersion is reliable if we only consider the dynamic changes in the fluid flow under isothermal conditions [181]. However, the involvement of particle heating causes the fluid thermodynamic parameters to alter along with the dynamic variables of the flow. This is concerning as the two fundamental effects, namely the decrease in local gas density and increase in viscosity due to particle heating, can substantially modulate turbulence [182]. Moreover, variation in the density and viscosity directly influences particle clustering. The decrease in density in the vicinity of a cluster pushes particles away (enhancing dispersion by creating a local diverging flow field) [21]. The rise in gas viscosity raises clustering according to a phenomenon called VC [151]. As per the VC effect, a large cluster rapidly increases the local gas temperature and viscosity. This high viscosity gas, termed as a *viscous cloud*, then offers higher drag to the particles it envelops, compared to the relatively cold surrounding fluid, promoting these particles to remain clustered. Such viscous clouds also capture more particles in the domain. Hence, the overall particle clustering increases. In the flows where VC is present, maximum particle clustering can be observed at $St < 1$ instead of $St \approx 1$.

The temperature-driven rise in fluid viscosity attenuates turbulence due to enhanced dissipation in gas. The presence of particles reduces turbulence via momentum and energy exchange between the two phases [183], since particle motion is typically governed by the local flow. This effect is enhanced with the rise in particle loading density and St [184]. Turbulence attenuation also increases with particle clustering, as it creates regions of high particle concentration [185]. Generally in jet flows, as particle axial momentum is higher, particles make a jet narrower while increasing its centerline velocity [183] and reduce turbulence fluctuation by as much as 50% [186]. To incorporate the effect of particles on the local flow field in numerical studies, TWC is employed, which we also used in this study. In TWC, turbulence kinetic energy (TKE) is attenuated by the particles [4]. This

can cause the St to drop considerably such that according to the conventional predictions particles start depicting tracer-like behavior with respect to the large-scale eddies. Thus, theoretically, turbulence attenuation in this case should diminish VC and result in higher particle dispersion.

In HIT with momentum and energy TWC, VC was found to be stronger at higher particle loading density [187]. This is because, at higher particle loading density, the two primary conditions required for the VC to take effect are fulfilled. Firstly, the rise in particle loading density increases the ability of particles to form clusters before heating [155]. Secondly, it also raises the concentration of particles in these clusters. Thus, in our previous studies of particle clustering in a HIT box, particles appear restricted within clusters based on the intensity of the VC. Although we do not vary particle loading density in the present study, this effect is important because in a jet, aside from clustering, particles are mainly concentrated along the centerline [99]. Thus, it is possible that in a spatially and temporally evolving flow, particles can be spatially restricted in the domain in such a manner that even particle reaction drag force cannot diminish VC. This is particularly important to test in spatially evolving flows because in a triply periodic box, even when the local fluid and particles appear to be going away, their separation distance can still decrease as they are reinjected into the domain from the opposite boundary due to periodicity. Additionally, because the domain volume was fixed in the HIT box, the drop in density upon heating was attenuated by the increase in domain pressure. This kept the overall density constant, producing a more significant rise of 60% in the gas viscosity. Hence, it is possible that this higher rise in local viscosity favored VC.

To probe the preceding hypothesis and the overall validity of VC in a spatially evolving flow, we investigate the effect of temperature-dependent viscosity on heated particle clustering dynamics in a subsonic turbulent jet flow. Our choice of a heated particle-laden jet was inspired by its importance in engineering applications. We restrict this study to particle-laden circular jets with two-way fluid-particle momentum and energy coupling; for simplicity, the gravitational force and inter-particle collisions are neglected. Note that the rise in gas viscosity is expected to be considerably smaller in the subsonic jet flow

compared to the HIT case, as particles only occupy a small portion of the domain. Also, cold fluid continuously enters the domain at the inlet and heated fluid leaves the domain at the outlet, further limiting the rise in fluid viscosity. To this end, we scrutinized the dispersion characteristics of heated polydispersed particles consisting of four different sizes, using DNS. The particle diameters are kept small enough ($d_p \ll \eta$, where η is the Kolmogorov length scale) to be modeled as point-particles [23], while simultaneously providing a sizeable range of St.

This article is organized as follows: the methodology is provided in Section 4.2, results are discussed in Section 4.3 and a research summary is presented in Section 4.4.

4.2 Methodology

In this analysis, we conducted DNS using an in-house version of an open-source finite difference code called Pencil-Code [130]. Here, the point-particles and fluid are modeled with the Lagrangian and Eulerian schemes, respectively. For computing spatial derivatives a sixth-order compact finite-difference method is employed, whereas for time integration third-order Runge-Kutta method is used. In the present Lagrangian point-particle scheme, the particle trajectories are resolved with a tri-linear interpolation scheme. These particle-laden jet flow simulations are composed of three sub-simulations (see Figure 4.1), as explained below:

4.2.1 Simulation Methodology

Forced Homogeneous Isotropic Turbulence

As a first step, a DNS of a triply periodic box with characteristics length of $9d_j$ (where $d_j = 1$ is the jet diameter) is carried out to generate HIT (without particles) with the help of a solenoidal forcing function [131], as shown in Figure 4.1. This DNS box is

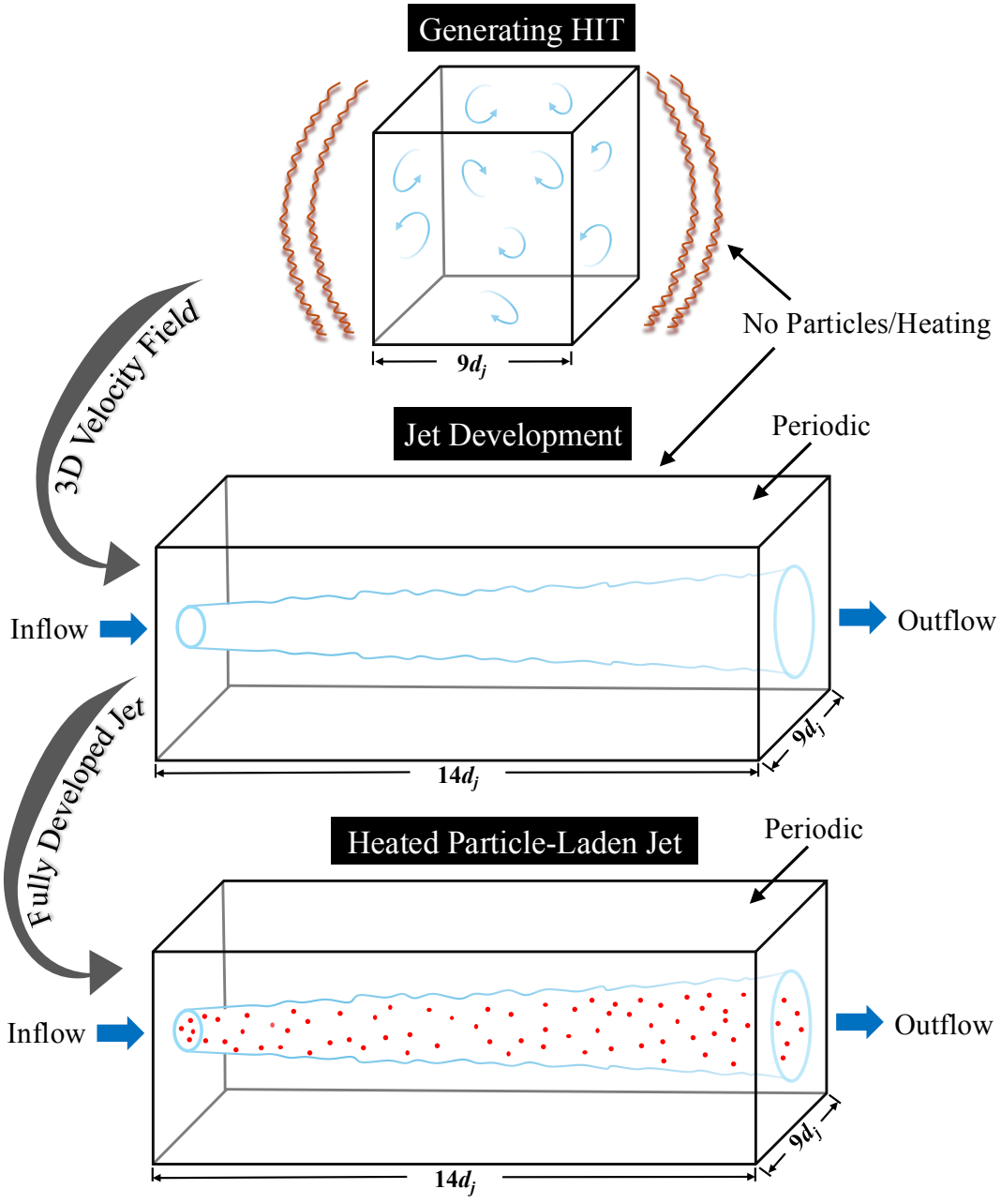


Figure 4.1: Schematic of the present simulation setup.

resolved into a mesh of 256^3 cells. The employed forcing function is a delta-correlation in wavenumber space, such that the random forcing points are correlated at a given time, but differ between two time instances. We sustained this forcing until the mean turbulence statistics stabilized, indicating the statistical equilibrium state between the injection of energy at the large scales and dissipation at the small scales. The development of this state can be determined with the fluid velocity root-mean-square (u_{rms}) which starts fluctuating about a constant average. This simulation is carried out for $200\tau_l$, where the large eddy timescale, τ_l, is computed at the inlet of the jet simulation. The Taylor Reynolds number of the simulation is $Re_\lambda = u_{rms}\lambda/\nu_f = 77$. Here, the jet inlet large eddy timescale $\tau_l = r_j/u_j = 0.5$, r_j is the jet radius and u_j is the mean jet inlet velocity, and λ is Taylor length scale.

Developing Subsonic Jet

After establishing stable HIT, snapshots of the 3D instantaneous velocity fields are periodically projected onto the inlet of a rectangular domain (see Figure 4.1) with a dimension of $14d_j \times 9d_j \times 9d_j$ in the streamwise (x) and two lateral (y and z) directions. All the dimensions (x, y and z) in this article are presented in terms of d_j. For conciseness, we will not mention d_j with dimensions from here onward, unless a different variable is used for the normalization. This domain is prescribed with periodic boundary conditions in y and z directions, while inflow and outflow boundary conditions are set at its inlet and outlet, as shown in Figure 4.1. Spurious boundary reflections at the inlet [188] and outlet [189] are minimized via Navier-Stokes Characteristics Boundary Condition (NSCBC). At the inlet, fluid is allowed to enter the domain only through a circular jet inlet of d_j with $u_j = 1$ (inlet Mach number is $Ma = 0.24$ computed from the jet centerline velocity), and the rest of the inlet plane is a wall. Since our Mach number is small, we are essentially in an incompressible regime, albeit we still solve compressible Navier-Stokes equations as discussed in Section 4.2.2. The y and z boundaries should also have outflow boundary conditions, however, we used periodic boundary conditions at these boundaries due to a limitation of

our code where a discontinuity arises at the corners where boundaries meet. Moreover, by prescribing periodic boundary conditions in the lateral directions, we eliminate wall effects which are not the focus of this study.

We discretize this rectangular domain into a grid of $384 \times 256 \times 256$ cells in the x, y and z directions. This simulation is carried out without particles to develop a stable jet. This jet is allowed to evolve for about 3 Flows Through Time (FTT), such that the normalized axial velocity (u_x) and axial turbulent intensity ($U' = (\overline{u'^2})^{1/2}$, where u' is the fluctuating component of velocity) profiles become self-similar as shown in Figure 4.2. In this figure, the normalized u_x overlaps with the Gaussian curve, while U' reasonably collapses onto the experimental data of Hussein et al. [1]. Hence, the present simulation model is suitable for further analysis. Note that despite modeling a domain length of $x = 14$, we restrict our analysis to $x = 10$ in this study to eliminate any imperfection arising from the boundary reflections at the outlet, in the form of pressure and velocity fluctuation, which can distort the eddy structures. We do see a minor effect of periodic boundary condition at $x = 10$ where, for example, the u_x/u_c curve of $x = 10$ lifts up beyond $y/r_{1/2} \approx 1.25$ instead of collapsing on the other curves. However, this effect is negligibly small.

Heated Particle-Laden Jet

Once the jet is statistically fully developed, $150,000$ particles are introduced at a constant injection rate (1000 particles/τ_l) into the jet over the entire duration of the simulation (5 FTT), as depicted in Figure 4.1. These $150,000$ particles are evenly divided between the four particle species. This simulation is run for 2 FTT to stabilize the transience created by the introduction of particles. After the initial transience is dampened, simulations with H particles and NH particles are carried out for another 3 FTT each. Data are recorded in this phase, which is discussed in the rest of this article. Note that separate H and NH simulations are conducted to highlight the rise in particle clustering based on the temperature-driven gas viscosity. After particle entrainment into the jet stream, particle heating is initiated after $x = 1$ for numerical stability. This is because, to rapidly heat

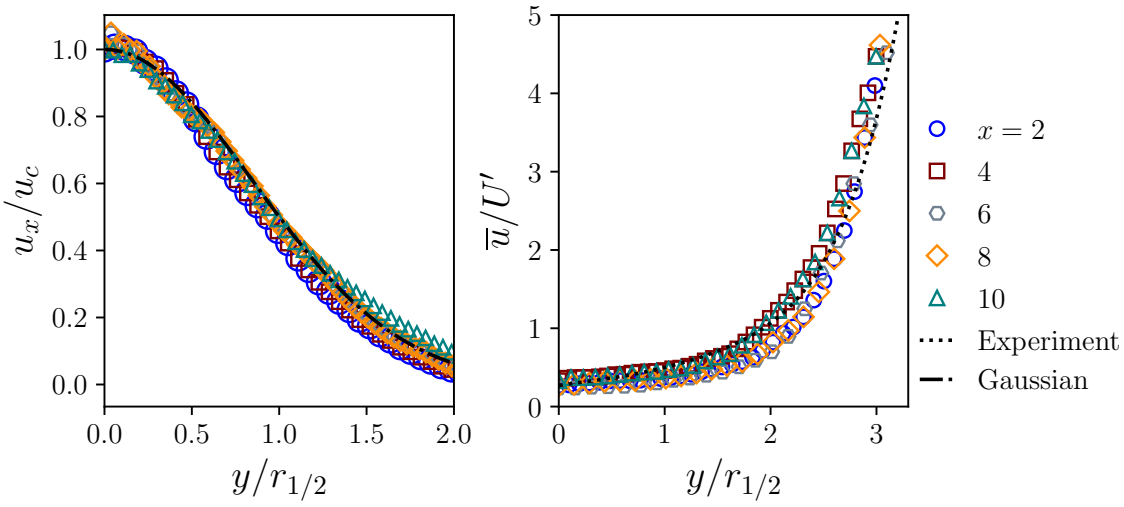


Figure 4.2: Jet axial velocity, u_x (left) and axial turbulent intensity, $U' = (\overline{u'^2})^{1/2}$ (right), at five downstream locations, shown as a multiple of d_j. Here u_x and U' are normalized with the centerline velocity (u_c) and jet mean velocity ($\overline{u}$), respectively. The present radial profiles of U' are compared with the experimental data of Hussein et al. [1], shown as a dotted line.

the particles and transfer this heat to the local gas (required for the local viscous effects to be noticeable), we prescribed fast particle heating ($\tau_{heat} = 1$) and particle-to-fluid heat transfer ($\tau_t = 4$) timescales, as discussed later in this section. Thus, the local changes caused by the sharp rise in particles and gas temperatures close to the inlet destabilized the simulations.

The considered particle loading density leads to a volume fraction of $O(10^{-6})$, which divides the one- and two-way momentum coupling regimes [4]. However, these particles are introduced within the jet diameter of $d_j = 1$, and a majority of these particles are concentrated along the axis of the jet. Consequently, the local volume fraction at the center of the jet is found to be as high as $O(10^{-4})$, which falls in the TWC regime. Therefore, TWC is employed in this study. The entrained particles consist of four particle diameters that are $d_p = 0.001$, 0.003, 0.004 and 0.006 at the jet inlet. For brevity, we will denote

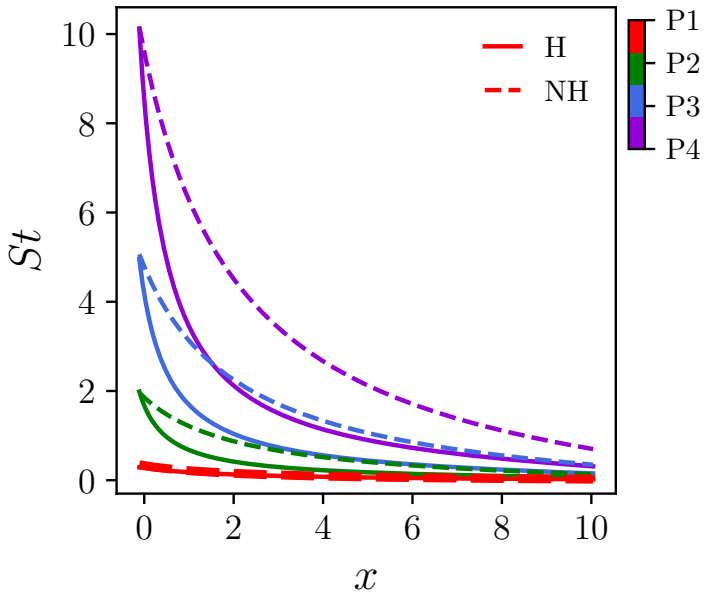


Figure 4.3: Temporally averaged evolution of the H and NH particles' St along the jet centerline.

these particle sizes with P1, P2, P3 and P4. The particles are introduced into the flow with a random x-velocity at the inlet. The resulting particle Stokes numbers at the inlet, St_0 (subscript 0 represents initial/reference value), are stated in Table 4.1. The St_0 is computed from Equation (4.1) such that at the jet inlet $r_{1/2} = r_j$ and $u_c = u_j$. Note that both H and NH particle-laden simulations start with identical St_0.

We purposely opted for the $St \leq 10$ regime for the largest particle species, as studies on this regime are scarce [190]. Moreover, $St \approx 1$ is often encountered in industrial

Particle species	P1	P2	P3	P4
Particle diameter, d_j	0.001	0.003	0.004	0.006
Initial Stokes number, St_0	0.6	2	5.1	10.4

Table 4.1: Particle diameter and initial Stokes number (St_0) in the present simulations.

Particle species	P1	P2	P3	P4
$St_{x=10}$ of H	0.02	0.15	0.31	0.60
$St_{x=10}$ of NH	0.02	0.13	0.34	0.64

Table 4.2: Stokes number ($St_{x=10}$) of H and NH particles at $x = 10$

applications, such as in pulverized coal burners [191]. In isothermal conditions, the particle clustering pattern also changes around $St \approx 1$, where particles start showing maximum clustering in HIT as established in Section 4.1. With the spatial evolution of a decaying jet, the τ_c dwindles (u_c drops and $r_{1/2}$ increases). This causes the St of all the particles of both H and NH cases to drop to $\lessapprox 0.6$ as shown in Figure 4.3, where St is computed from Equation (4.1). Table 4.2 is depicting the particle Stokes number at $x = 10$ denoted by $St_{x=10}$. Hence, all particle sizes are expected to approach tracer-like behavior by $x = 10$, especially the P1 to P3 particles. The sharp decline in the H curves in Figure 4.3 is due to the rise in temperature-dependent dynamic viscosity (μ_f), expressed as:

$$\mu_f = \mu_{f,0} T_f^{\frac{2}{3}} \tag{4.2}$$

here $\mu_{f,0} = \rho_{f,0}\nu_{f,0}$ is the initial value of dynamic viscosity that is $\mu_{f,0} = 0.001$. On the other hand, the initial fluid density is $\rho_{f,0} = 1$, and since $\rho_p/\rho_{f,0} = 1500/1 \gg 1$, the only force experienced by the particles is the viscous drag force [39]. Based on this, the flow Reynolds number is $Re = u_j r_j/\nu_{f,0} = 500$. Additionally, we assume that all the particles are spherical and since these particles are modeled as point-particles, each particle has a uniform density and temperature.

4.2.2 Governing Equations

Particulate Phase

The dimensionless Lagrangian equations for the point-particles are given as:

$$\frac{dx_{p,i}}{dt} = u_{p,i} \tag{4.3}$$

$$\frac{du_{p,i}}{dt} = \frac{C_D}{\tau_p}\left(u_{f,i}(x_p) - u_{p,i}\right) \tag{4.4}$$

here $u_{p,i}$ is the instantaneous particle velocity and $u_{f,i}(x_p)$ is the velocity of the gas at the particle position. The subscript i represents the i$^{\text{th}}$ component. While, C_D stands for the particle drag coefficient [192], which is defined as:

$$C_D = \frac{24}{Re_p}\left[\frac{C_{Di}\left(1 + e^{\left(0.427/Ma_p^{4.63}\right) - \left(3/Re_p^{0.88}\right)}\right)}{1 + (\xi)\left(3.82 + 1.28e^{(-1.25/\xi)}\right)}\right] \tag{4.5}$$

where ξ is the ratio of particle Mach number ($Ma_p = |u_{p,i} - u_{f,i}(x_p)|/c$, c is the local speed of sound) and Reynolds number ($Re_p = d_p|u_{p,i} - u_{f,i}(x_p)|/\nu_f$). The term $C_{Di} = 1 + 0.15Re_p^{0.687}$ is the drag coefficient defined with Schillar-Naumann equation [133]. Although Equation (4.5) is better suited for high M flows, however, its simple implementation and excellent validation even at low M flows [193] inspired its use in the present study.

Particle Heating Model

We employed the particle heating model of Mouallem and Hickey [101], to escalate particle temperature from an initial value of $T_{p,0} = 1$ to the final maximum temperature of $T_{p,max} = 2$. As per this model, the equation set for particle heating (Q_p) and particle-fluid heat transfer (Q_{pf}) is:

$$Q_p = \frac{m_p c_p \left(T_{p,max} - T_p\right)}{\tau_{heat}} \tag{4.6}$$

$$Q_{pf} = \frac{m_p c_p N u_p \left(T_p - T_f(x_p)\right)}{\tau_t} \tag{4.7}$$

In the above equations, c_p is particle heat capacity, m_p is particle mass, T_p is instantaneous particle temperature, $T_p(x_p)$ is the gas temperature at the location of a particle, and Nu_p is the particle Nusselt number. As depicted by Equation (4.6), the present heat flux is a function of the temperature difference and decreases as T_p approaches $T_{p,max}$. Once $T_{p,max}$ is reached, particle heating ceases and particles maintain their final temperature. The heat transfer term Q_{pf} between the particles and fluid is modeled with a *Triangular Shaped*

Cloud scheme which computes second-order spline interpolation on the surrounding 27 mesh points.

Gaseous Phase

The non-dimensional equations of mass, momentum and energy for the continuum phase are:

$$\frac{\partial \rho_f}{\partial t} + \frac{\partial \rho_f u_{f,i}}{\partial x_i} = 0 \tag{4.8}$$

$$\frac{\partial \rho_f u_{f,i}}{\partial t} + \frac{\partial \rho_f u_{f,i} u_{f,j}}{\partial x_j} = -\frac{\partial P_f}{\partial x_i} + \frac{\mu_f \partial}{\partial x_j}\left(\frac{\partial u_{f,i}}{\partial x_j} + \frac{\partial u_{f,j}}{\partial x_i} - \frac{2\partial u_{f,k}}{3\partial x_k}\delta_{ij}\right) + F_p \tag{4.9}$$

$$\rho_f T_f \frac{Ds}{Dt} = \frac{\partial}{\partial x_i}\left(\kappa_f \frac{\partial T_f}{\partial x_i}\right) + 2\rho_f \nu_f \mathbf{S} : \mathbf{S} + \zeta \rho_f \left(\frac{\partial u_{f,i}}{\partial x_i}\right)^2 + \rho_f Q_{pf} \tag{4.10}$$

here s, ζ, κ_f, P_f, T_f, δ_{ij} and $\mathbf{S}$ are entropy, fluid bulk viscosity, thermal conductivity, pressure, temperature, Kronecker delta and shear-rate tensor, respectively. The term F_p in the momentum Equation (4.9) is the particle reaction drag force on the fluid and is defined as:

$$F_p = m_p C_D \frac{(u_{p,i} - u_{f,i}(x_p))}{\tau_p} \tag{4.11}$$

4.3 Results

According to Figure 4.3, because the St of the corresponding particles in H and NH cases start decaying from the same values, a similar clustering pattern should be obtained even at later time instances, as per the *history* effect [50]. Note that St evolution is similar between some of the H and NH cases; for example the evolution of P1 is nearly identical for both cases, similarly the NH P2 and P3 follow closely the H P3 and P4, respectively, after $x = 2$. If the history effect is suppressed by the local instantaneous kinematic variations in the flow, at least the particles with overlapping curves should demonstrate comparable clustering. This is expected because the thermodynamic difference in H and NH case is

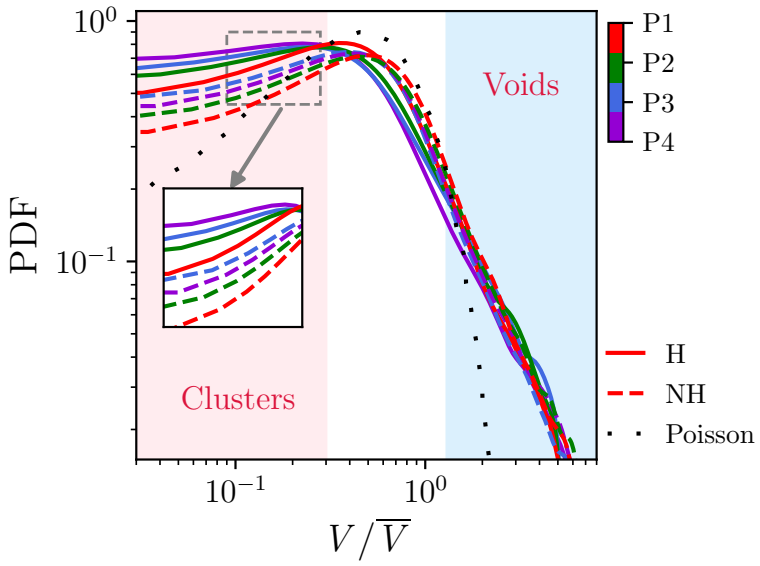


Figure 4.4: PDF of normalized Voronoï cell volume (V) compared with the random Poisson distribution (dotted line). Here $\overline{V}$ is the mean volume of all the cells, while V is computed by temporally averaging Voronoï cell volume over 3 FTT.

fairly modest. For example, the maximum rise in viscosity in H simulation is about 16%, while it was 60% in the HIT case [187] as stated earlier. Thus, even marginally higher clustering in the H case will suggest a strong influence of the local rise in gas viscosity on particle clustering.

We first check if we get higher clustering in the H case compared to the NH simulation. For this purpose, we divided the domain into Voronoï cells and computed the PDF of the Voronoï cell volume (V), as shown in Figure 4.4. In this figure, the present curves intersect the random Poisson distribution at two points, which mark the boundaries of the regions depicting particle clustering (low V) and voids (high V). It is apparent that in the jet flow case, the probability of smaller V is higher in H particles than the random Poisson curve and the NH particles. Hence, they are depicting higher clustering, similar to the HIT studies. Note that our plot is different from the regular PDFs of Voronoï cell

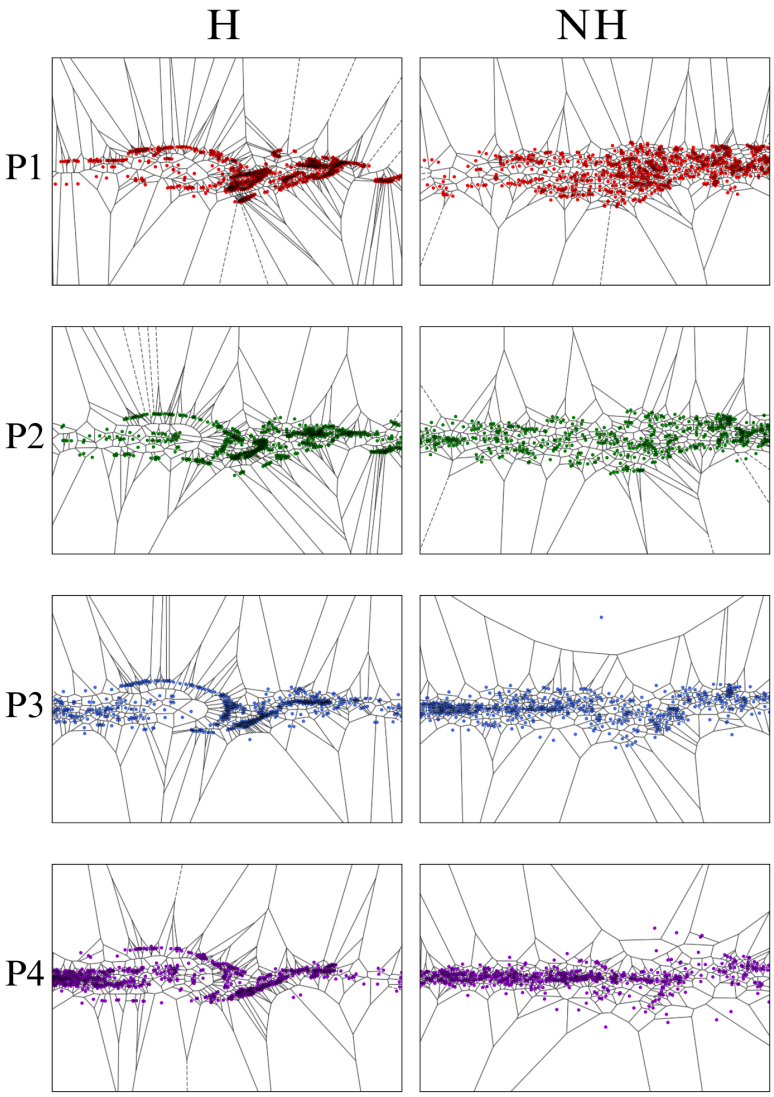


Figure 4.5: 2D Voronoï tessellation diagram of the H and NH particles at the center of the domain. The thickness of each slice is $5\delta n_z$, where δn_z is the cell size in the z-direction. The length (x) and height (y) of these plots are $10d_j$ and $9d_j$ respectively.

volume [137]. This is because, in the jet flow case, there is a significant variation between the cell sizes since only the center region of the domain has particles, as shown in the 2D Voronoï tessellation diagram in Figure 4.5. This figure presents particle clustering in a slice of thickness $5\delta n_z$ at the center of the domain, where δn_z is the cell size in the z-direction. Here we see that the NH particles depict the conventional trends in which smaller particles disperse more and larger particles travel along the centerline. In contrast, the H particles are considerably more clustered. The observed rise in the clustering of H particles and their overall clustering pattern is surprising considering that the rise in fluid temperature, with a decrease in density, causes the jet to spread more than an unheated jet; TWC enables particles to resist viscous effects via turbulence attenuation; and the local thermal effects are minimal, as stated earlier. All of these aspects should nullify the effect of local viscosity-driven clustering.

As shown in the 2D Voronoï diagram (Figure 4.5), the H particles are not spreading laterally according to the conventional trends. If this is true for the entire domain, then the H particles should show steeper decay in particle concentration (θ) in the lateral direction. This can be seen in Figure 4.6. Notably, the larger particles of the H case show less dispersion than their NH counterparts, even though they are anticipated to disperse only slightly. The lower radial dispersion of the H particles further restricts the thermal changes within the center of the domain, which can cause more particles to remain within this region.

A compelling observation in Figure 4.5 is that the NH particles depict the classical trends (larger particles are clustering in the jet core [179], and smaller particles are clustering/spreading in the lateral direction [180]). In contrast, all four particle species of H case are clustered in a thread-like pattern at identical radial locations irrespective of size. This is against the St-based conventional dispersion behavior of the particles. The two larger particle species of the H case (P3 and P4) initially depict reasonably higher concentrations at the jet center, but this trend rapidly changes downstream. A plausible explanation is that the rise in vorticity (due to entrainment) as the jet travels downstream, which reorganizes the particles.

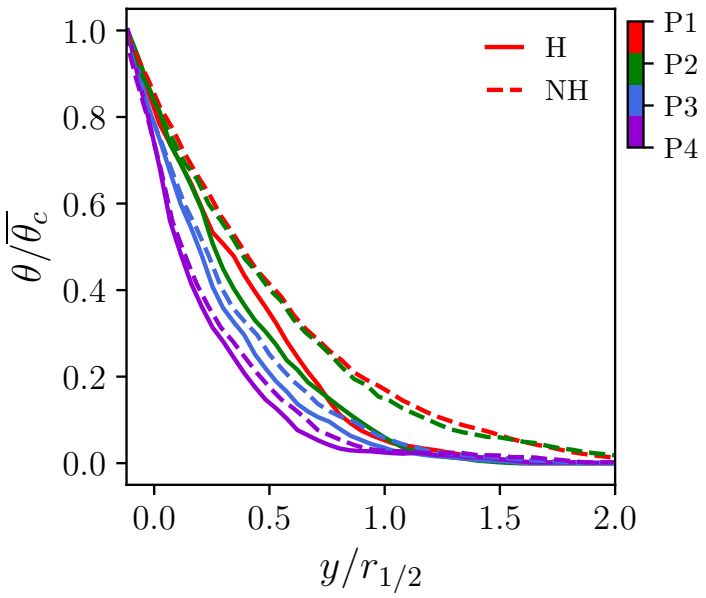


Figure 4.6: Temporally and azimuthally averaged radial concentration of H and NH particles (θ) normalized with the mean centerline particle concentration ($\overline{\theta_c}$).

The lower radial dispersion of the H particles can be further analyzed with vorticity magnitude $||\Omega||$ as depicted in Figure 4.7, where $||\cdot||$ represents magnitude. The $||\Omega||$ is higher in the NH case (justifying the large radial dispersion of NH particles) because of the dissipation caused by the rise in viscosity in the H case. But this low $||\Omega||$ is accompanied by higher drag force which pulls the particles out of the jet centerline. Downstream, the $||\Omega||$ at the centerline decreases which reduces the radial push on the particles, enhancing the probability of particles resisting radial dispersion. Thus, the initial $||\Omega||$ pushes the P3 and P4 away from the centerline. However, if this is true then why are H particles not spreading out of the jet similar to the NH particles?

To address this question, we probe the radial fluid-particle slip velocity, that is:

$$u_{pf} = |u_p - u_f(x_p)| \tag{4.12}$$

Note that the intrinsic expansion of the jet exerts a radial drag force on the particles.

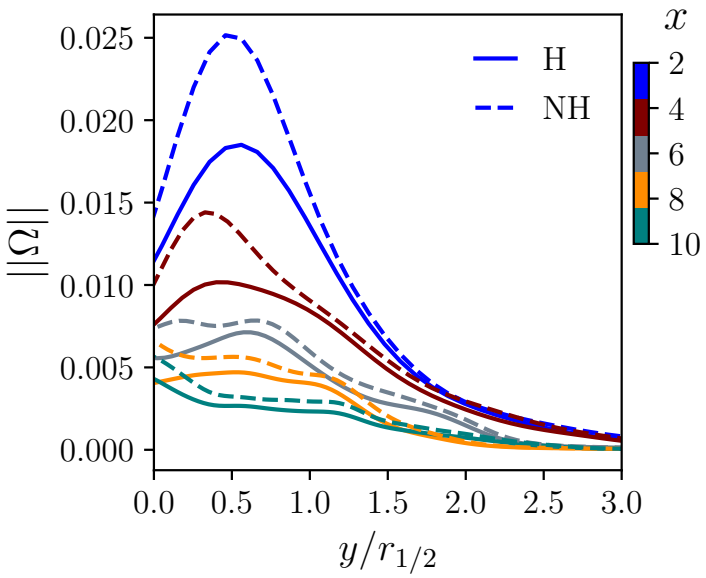


Figure 4.7: Temporally and azimuthally averaged radial evaluation of the magnitude of vorticity ($||\Omega||$) at five downstream locations.

Hence, if particles are following the fluid in the radial direction, u_{pf} will fall and vice versa. In Figure 4.8, as expected the temporally and azimuthally averaged radial fluid-particle slip velocity, $\overline{u_{pf}}$, of the H particles is higher than its NH counterparts, and the slip velocity in the NH case decays after reaching its peak around $x = 4$. Whereas in the H case it remains consistently higher than the NH case. This indicates that in the NH case, particles start moving in the direction of the radial drag force, but the H particles resist this radial push. This peak around $x = 4$ is the result of particles being introduced at the inlet with random x-velocity and zero radial velocity components. Thus, particles take some time to adapt to the drag in the radial direction from the fluid. The increase in u_{pf} based on particle size is due to the rise in particle inertia, which enables larger particles to be unresponsive to a higher radial drag force. These observations imply that the drag in the radial direction is trying to push the particles laterally in the H case. However, these particles are able to retain their axial momentum and instead collect in certain regions of the flow. Therefore,

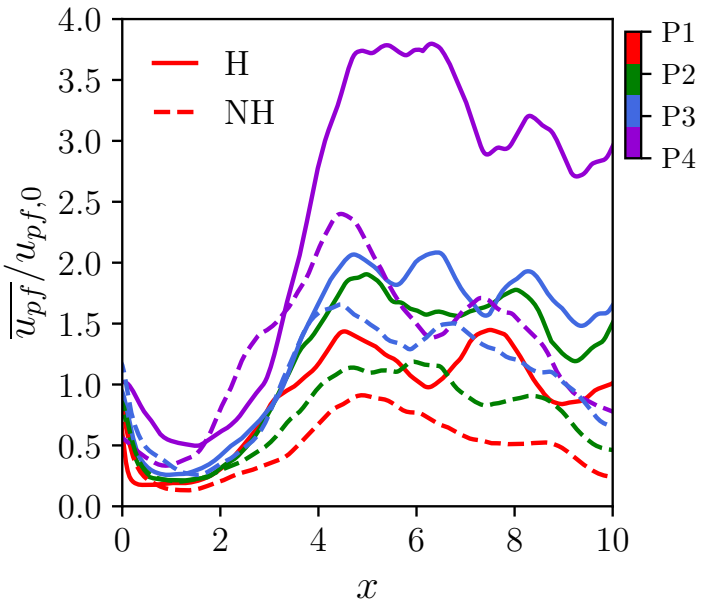


Figure 4.8: Average radial particle-fluid slip velocity ($\overline{u_{pf}}$) in the streamwise direction, normalized with its initial value ($u_{pf,0}$).

particle clustering is certainly not being controlled by the local kinematic changes, at least not entirely.

Reverting to Figure 4.3, in the NH case, the higher clustering of P3 and P4 can be attributed to their St approaching unity downstream, while their St declines slowly. But, we cannot blame $St \approx 1$ for higher clustering in H as its St rapidly drops below unity, while all four particle species show higher clustering. Since the only difference between these two simulations is the local thermodynamic changes, this disagreement between their particle clustering should be linked to the local gas viscosity, similar to our HIT study. If this is correct, then how is the rise in local viscosity augmenting particle clustering in a spatially evolving flow? To answer this, we present the contours of the high viscosity regions of H simulation, overlaid with the scatter plot of particle position, in Figure 4.9. Here, all four particle sizes are present within the jet central region. The main reason behind this is since

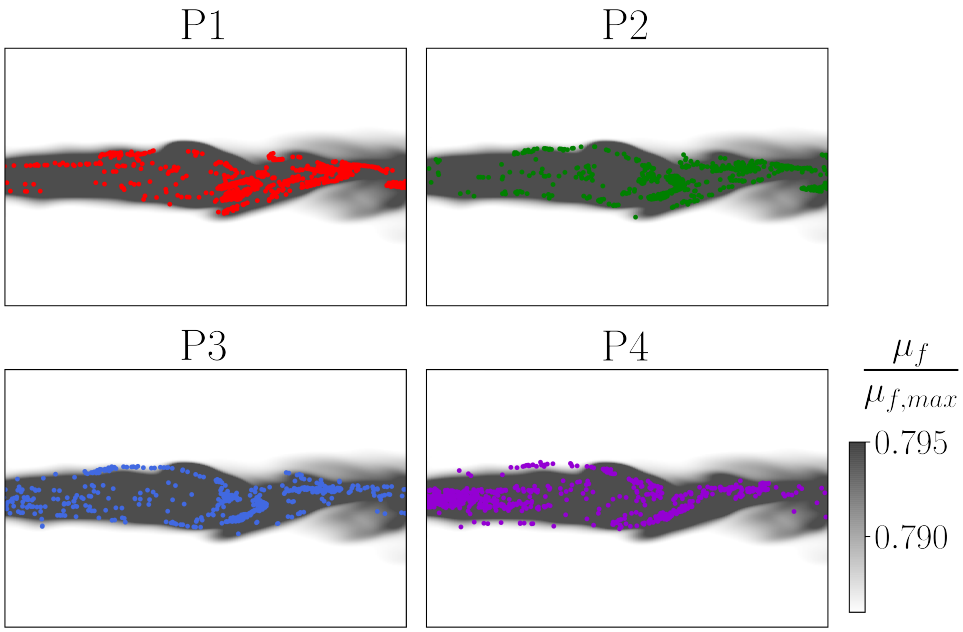


Figure 4.9: Contours of the high viscosity region of the jet overlaid with particles, in a thin slice of thickness $5\delta n_z$ at the center of the domain of the H case. The fluid viscosity is normalized with the maximum dynamic viscosity of the fluid, $\mu_{f,max}$. The length (x) and height (y) of these plots are $10d_j$ and $9d_j$ respectively.

particles are introduced within the jet diameter at the inlet, upon heating they cause the temperature/viscosity of the entire central region of the jet to increase. This restricts the radial movement of the particles via increased drag force.

The above explanation is plausible, but, surprisingly, none of the H particles are spreading out of this high-viscosity region, as stated earlier. In fact, particles seem to be clustering at the outer edge of the high viscosity region in Figure 4.9. This can be explained by the ability of particles to cluster at a *thermal front* [48, 110], which is a location where a sharp temperature (and viscosity in the present case) gradient exists. This is shown in Figure 4.10 which bins the number of particles based on the magnitude of the radial component of the temperature gradient ($||\nabla_r T||$) at the location of the particles. In this figure,

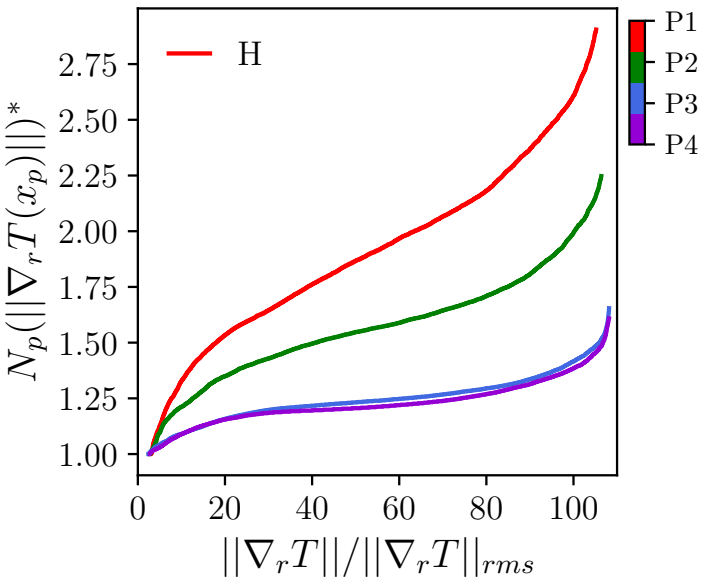


Figure 4.10: Normalized number of particles ($N_p(||\nabla_r T(x_p)||)^*$) binned based on the magnitude of the radial component of the temperature gradient ($||\nabla_r T||$) at the location of the particles.

$N_p(||\nabla_r T(x_p)||)^*$ is the normalized number of particles in these locations, and is defined as:

$$N_p(||\nabla_r T(x_p)||)^* = \frac{N_p(||\nabla_r T(x_p)||)}{N_{p,0}(||\nabla_r T(x_p)||)} \tag{4.13}$$

here $N_{p,0}(||\nabla_r T(x_p)||)$ is the number of particles in the first bin. As per Figure 4.10, the number of particles peaks in the regions with high $||\nabla_r T||$, suggesting that particles are collecting in the regions where $||\nabla_r T||$ is high (at the outer edge of the jet). Although in the current simulations, the temperature field is not strictly a passive scalar as per the description of Bec et al. [48]. However, our results align with the observation of Bec et al. [48] in that the particles tend to collect near the thermal front of the jet. Hence, the particles experiencing higher lateral dispersion, encounter this thermal front as they travel laterally and start clustering there. Since these particles cluster at the thermal front, they do not travel outside the jet, as shown in Figure 4.9. Based on this, unlike the HIT case

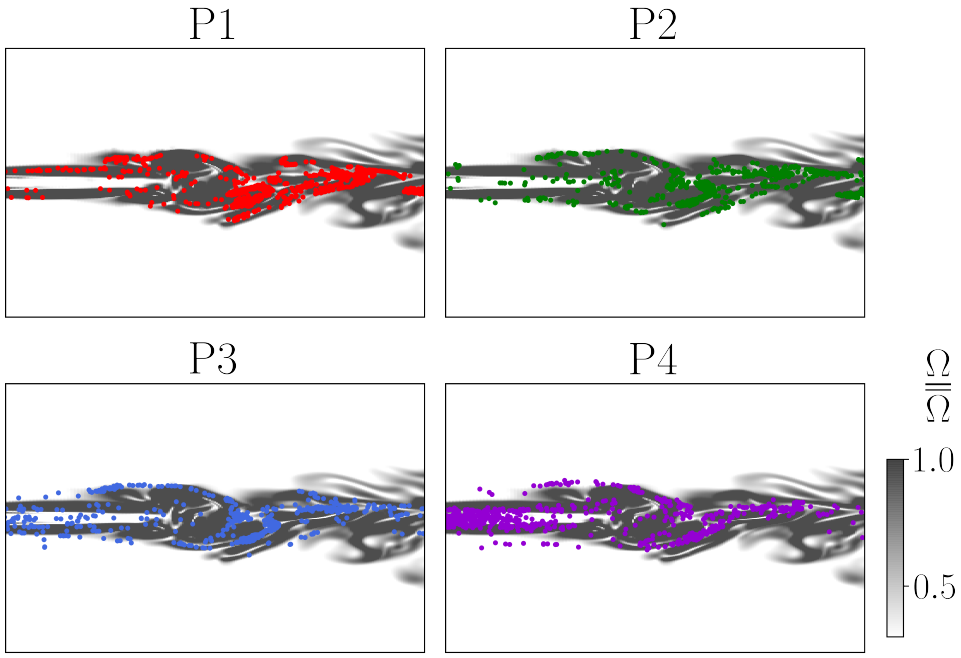


Figure 4.11: Contours of the normalized vorticity overlaid with particles, in a thin slice of thickness $5\delta n_z$ at the center of the domain of the H case. Here, $\overline{\Omega}$ is the spatially averaged vorticity. The length (x) and height (y) of these plots are $10d_j$ and $9d_j$ respectively.

where particles developed individual viscous clouds, in a heated particle-laden jet flow, the entire central region of the jet acts as one large viscous cloud, restraining all of the particles.

Hitherto, we have established that enhanced gas viscosity confines particles within the hot region of the jet. Now an even more intricate issue is why H particles are clustering at similar locations regardless of their size? This clustering pattern is surprising as particles with different inertia naturally cluster at unique length scales/locations [67]. We take a phenomenological approach to elucidate this trend. As particles are confined within the narrow hot region of the jet, they are subjected to identical large-scale eddies. Unable to centrifuge these particles out of the jet, these eddies correlate these particles spatially and cause them to cluster at similar locations within the jet. This can be observed in

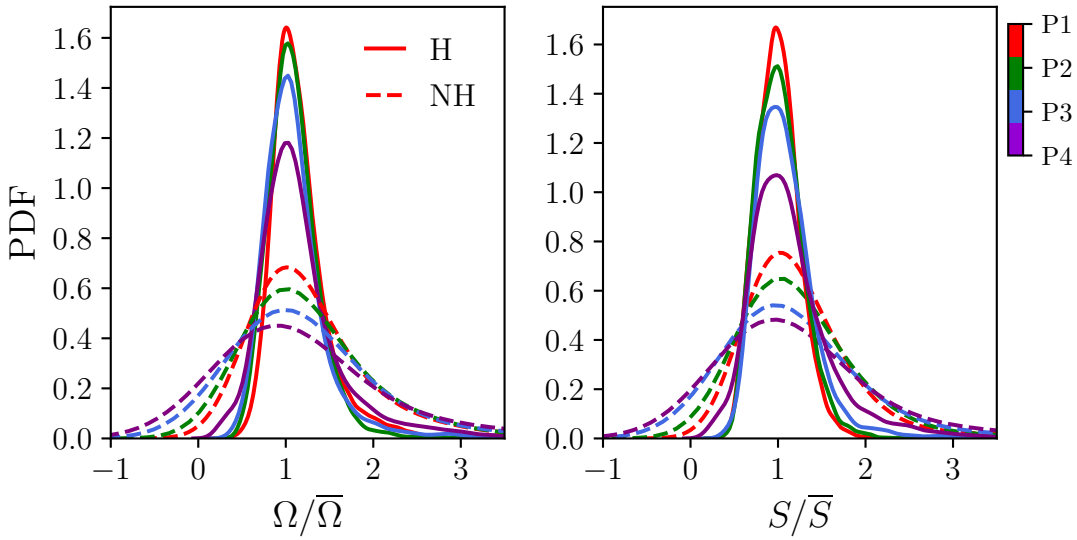


Figure 4.12: The PDF of vorticity (Ω) and strain-rate (S) at the particle location, normalized with their mean values, respectively.

Figure 4.11, where particles are mapped on a $5\delta n_z$ thin slice of vorticity contour at the center of the domain. Here, particles are clustered between the high-vorticity zones, based on the centrifugal force on the particles exerted by these large-scale eddies.

This trend is quantified in Figure 4.12, where the PDFs of vorticity (Ω) and strain-rate (S) of the H particles depict sharp peaks at similar Ω and S values. This suggests a high probability of finding all four particle species of H case at similar locations. The PDFs of NH particles are more spread out with shorter peaks, implying that these particles are present in more diverse Ω and S regions.

We can further statistically assess this trend of particle clustering at similar locations with the second-order structure function of the local fluid velocity at the particle position ($S^2_{u_f(x_p)}$), which is defined as:

$$S^2_{u_f(x_p)} = \overline{|u_f(x_p + D) - u_f(x_p)|^2} \tag{4.14}$$

here D is the inter-particle distance. The clustering of heated articles at similar locations

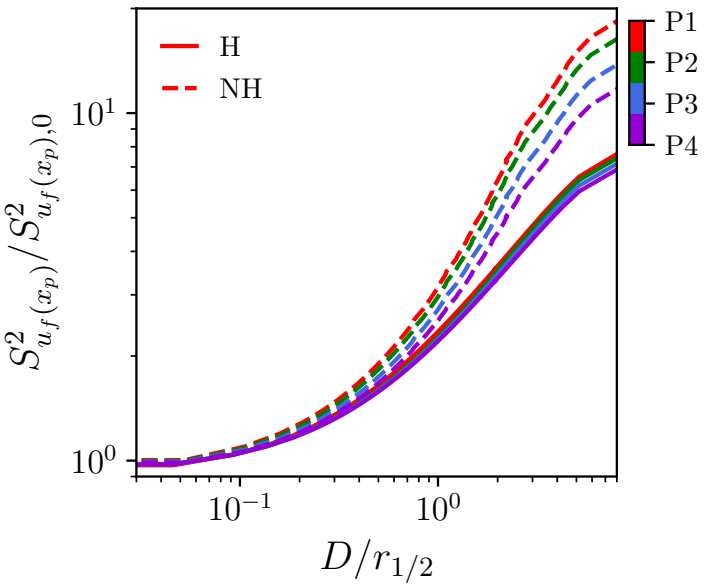


Figure 4.13: Normalized second order structure function ($S^2_{u_f(x_p)}$) of fluid velocity at the location of H and NH particles. Here, $S^2_{u_f(x_p),0}$ is the value of the first bin of $S^2_{u_f(x_p)}$.

implies that particles of all species should face identical local fluid velocity. Thus, the $S^2_{u_f(x_p)}$ of all four heated particle species should overlap. We see this trend in Figure 4.13. Moreover, it can also be observed in this figure that $S^2_{u_f(x_p)}$ of H particles is lower than their NH counterparts. This infers that the local fluid velocity at the location of H particles is well-correlated. This reinforces our hypothesis that as particles are restrained within the jet, they face the same eddies and therefore cluster at similar locations.

Considering the explanation above, although the local fluid velocity at the particle position is well-correlated, particles concentrated between vortices by large-scale eddies come from different flow regions and should carry a non-trivial particle-particle relative velocity (u_{pp}). This phenomenon is known as *caustics* [161]. The u_{pp} is expressed as:

$$u_{pp} = u_{p,n} - u_{p,n+1} \tag{4.15}$$

where n is representing the n^{th} particle. These particles can only stay clustered if the

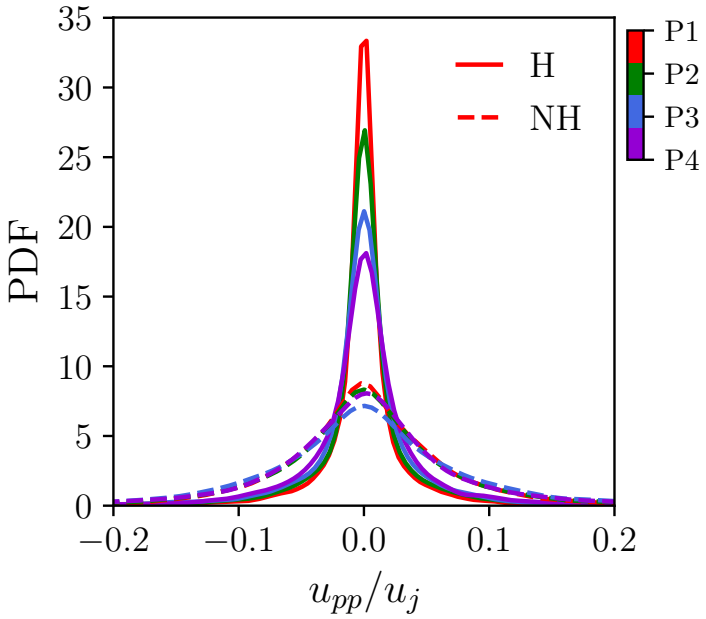


Figure 4.14: The PDF of temporally averaged inter-particle slip velocity (u_{pp}) of the considered four particle species, normalized with the jet inlet velocity (u_j).

velocity difference between them is small. In other words, for particles to be spatially restricted and clustered at similar locations in the domain, their inter-particle velocity should be correlated. In the present study, this effect can only transpire if the local rise in drag via enhanced viscosity dominates particle dynamics. We see this trend in Figure 4.14, where the H particles show a tighter PDF at a $u_{pp} = 0$. Note that particles traveling with similar velocity have a higher probability of forming and staying clustered as clustering is a function of the particle-particle slip velocity [49, 50]. The NH case once again demonstrates a wider distribution of u_{pp}, indicating higher particle dispersion.

As discussed earlier, there are two conditions for VC to be dominant [187]. The first condition is automatically satisfied by introducing particles within the jet d_j, which results in higher particle loading density within the jet (recall Section 4.2.1). Hence, at $x = 1$ when particle heating is initiated, particles are close to each other which leads to the heating of

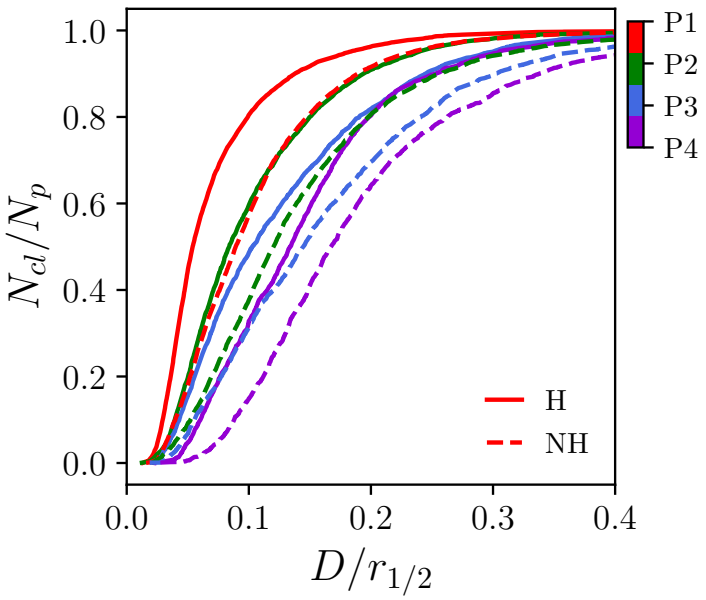


Figure 4.15: Number of clustered particles (N_{cl}) versus the inter-particle distance (D), normalized with the total number of particles of each species (N_p).

the entire central region of the jet and particles getting locked in this hot region. The second condition for VC to take effect is that we need clusters with high particle concentrations. This is because, upon particle heating these clusters will create a more significant rise in the local gas viscosity. Up till now, the fulfillment of this condition is unclear in the present scenario. To assess this, we employ the DBSCAN [167], which segregates the clustered and noise particles based on two parameters; inter-particle distance (D) and the minimum number of particles required to form a cluster ($N_{cl,min}$). Here, $N_{cl,min}$ is taken as twice the number of dimensions of the data [171]. In our case, particle location data are three dimensional, therefore $N_{cl,min} = 6$. With the increase in D, the N_{cl} should increase, and considering that the H particles are restricted inside the jet, the number of H particles should increase much more rapidly than the NH particles, as demonstrated in Figure 4.15. According to this figure, H particles are more densely packed in the clusters. This suggests that the observations in this study are the result of VC effect, which elevates the clustering

of heated particles even if the rise in viscosity is modest. Hence, our hypothesis that VC can spatially restrain particles in a spatially evolving flow holds.

It is evident in the present analysis that the rise in local gas viscosity can enhance particle clustering even when $St < 1$. Similar observations were reported by Saieed et l. [151] and Saieed and Hickey [187] in decaying HIT. Thus, a new metric is required to predict particle clustering in heated particle-laden flows. We leave this for future investigation.

4.4 Summary

We investigate the viscosity-driven enhanced clustering of heated inertial particles in a subsonic, turbulent jet flow using DNS in a rectangular domain. Four different particle sizes are modeled with the Lagrangian point-particle-tracking method, while the carrier gas is modeled with the Eulerian approach. The inter-phase momentum and energy exchange are simulated with gas-particle TWC. To emphasize the viscosity-based rise in particle clustering, particle-laden jet flow simulations with and without particle heating are carried out, such that each simulation is composed of three sub-simulations: development of HIT, stabilization of a subsonic jet flow, and particle-laden jet flow. With this setup, it is determined that if the two prerequisites of the VC effect are met, VC will take effect even in a spatially evolving flow with only a 16% rise in gas viscosity. In this case, the presence of particles inside the jet at the inlet causes the viscosity of the entire jet center to increase as one large viscous cloud. Within this viscous cloud, particles experience a higher drag force, which correlates the inter-particle velocity. At the outer edge of this viscous cloud, thermal fronts are created. Having an affinity towards clustering at these fronts, particles do not cross these thermal fronts. As particles are locked within this hot region, they face the same large eddies that organize these particles via centrifugal force at similar locations between eddies. Hence, VC will take effect and particles are spatially correlated irrespective of particle inertia/size. Therefore, in a thermal application, VC effect should be accounted for, even if the local rise in viscosity is anticipated to be minor.

In particular, this effect can be beneficial for applications where the lateral dispersion of particles requires articulation, such as cold spray advanced manufacturing techniques and targeted drug delivery.

Note that there are a few constraints in the present study. Firstly, because of heating, the TKE of the H and NH simulations decays at a different rate. The flow Re and M are also low. These parameters do affect the turbulence statistics, but they do not influence the VC effect as it is driven by viscosity rise, which is a thermodynamic property. Moreover, particles are introduced at the jet inlet with random velocity in the x-direction, which results in an adaptation time between the particles and the fluid.

Likewise, the lateral boundaries of the domain are prescribed with periodic boundary conditions instead of outflow, which has a minor effect on our jet. However, since we only consider the near-field region ($x = 10$), our results are not affected by the fluctuations originating from the opposite boundaries. Despite using NSCBC, we observed some spurious boundary reflections at the outlet. However, analyzing results up to $x = 10$ also aided in avoiding spurious fluctuation from the outlet boundary.

Chapter 5

Particle Dispersion in Supersonic Particle-Laden Jets

Reference: A. Saieed, and J. P. Hickey. Particle Dispersion in Supersonic Particle-Laden Jets. *Journal of Fluid Mechanics*. [Under Revision]

Abstract

Particle-laden supersonic jets are often encountered in advanced engineering applications where a comprehensive control of particle dispersion is crucial. Although particle dispersion has been extensively studied in the past, the local mechanisms that cause the radial transport of particles, such that particles leave the jet core, remain unclear in supersonic jet flows. To this end, we conduct a DNS of a confined low Reynolds number perfectly expanded supersonic jet carrying four different-sized particles. Here, particles and gas are simulated with Lagrangian and Eulerian approaches, and the fluid-particle energy and momentum exchange is modeled with TWC. The initial Stokes number of these particles ranges between 1.5 and 6.0. We found that each particle size has a specific axial location, x_r, where they start traveling radially. This location is defined by a local Stokes number

of about $St^* \approx 0.6$; the delay in particles' response to the local eddies in a supersonic flow causes their St^* to drop below unity. The local turbulent structures formed by the jet promote a radial transport of the particles that have similar characteristic time scales. Despite momentum TWC, particles and gas influence each other via different mechanisms. For the considered range of St, particles dominantly influence the fluctuating velocity component of the gas, while gas mainly affects the mean velocity component of the particles. Moreover, particles' reaction to the compressibility effects is a direct function of particle inertia, where the probability of finding larger particles in a high-density gradient and dilatation region is higher.

5.1 Introduction

Particle-laden jets often arise in nature in the form of volcanic plumes [194, 195] and hydrothermal eruptions [196]. Likewise, particle-laden jet flows can be found in numerous advanced engineering applications such as cold spray manufacturing [11, 176]; metallurgy [15]; nanothermite combustion for propulsion applications [9]; targeted drug delivery [13, 197]; transmission of diseases through sneezing and coughing [198, 199]; and particle entrainment in jets used in the final approach of the lander modules to the surface of extraterrestrial bodies [200, 201]. Regardless of the nature of these jets, particle distribution in such flows has been a source of long-standing questions that have motivated numerous research campaigns in this field. To fully grasp particle dispersion in a jet, three main aspects of particle-fluid interaction require understanding. These are discussed in the following subsections.

5.1.1 Particle Clustering

Generally, in turbulent flows, particles are known to eject from vortices based on their inertia and cluster where vorticity is low [46], or in locations where their net acceleration is

zero [106]. The mechanism of particle clustering in low vorticity (high strain-rate) regions due to the centrifugal force exerted on the particles by coherent turbulent structures is called PC, and it is the most widely accepted explanation for turbulence-induced particle clustering. Furthermore, it has been reported that in jet flows, particles preferentially gather in the regions with a local streamwise velocity higher than the mean velocity [202]. Moreover, in general, compressibility and shear play a significant role in particle dynamics, where apart from PC (which is still blamed for clustering [203]), particle clustering intensifies with the increase in compressibility [204]. This is particularly important for high-speed jet flows, which involve significant compressibility and shear.

Regardless of the particle clustering mechanism, clustering is driven by turbulent eddies and particles' response to these eddies based on their inertia. In HIT, tracer particles with virtually no inertia can closely follow the coherent turbulent structures [54]. Therefore, tracer-like particles are often used in experimental techniques such as particle image velocimetry for measuring flow parameters [205]. On the contrary, heavy particles tend to be ballistic, and thus their motion is weakly influenced by the local eddies [23]. A dimensionless parameter called *Stokes number* (St) is typically used to characterize the inertia-based correlation between the particles and turbulence, as discussed later in this section.

5.1.2 Particle Transport

In the context of jets, apart from clustering, particle inertia also determines particle trajectories as the jet develops [63]; whether particles travel within the jet or are dispersed away from the jet centerline. Predicting particle trajectories is critical for numerous applications. For example, in cold spray advanced manufacturing techniques, the goal is to keep the particle inside the high-speed jet, as particle dispersion drops coating efficiency [206]. Favorably, the presence of particles narrows the spreading of the jet and enhances the centerline velocity as particle motion is governed by the kinetic energy of the gas [183]. This effect is desirable for cold sprays. On the other hand, in combustion applications, efficient combustion relies on higher radial dispersion of the fuel droplets [207], considering

that these droplets can coalesce, which can greatly limit their dispersion by increasing the droplet size [208]. Hence, to manage the radial dispersion of particles based on the application, there is a pressing need to delineate the mechanisms that lead to this dispersion.

For estimating the dispersion of particles inside a jet, the Stokes number (St) [20] has been extensively used, which is the ratio of particle momentum response time (τ_p) to a characteristic turbulent timescale (τ). In jet flows, it is reported that the integral/convective timescale (τ_c) of the jet governs particle dispersion [64, 65]. Hence, St can be written as:

$$St = \frac{\tau_p}{\tau_c} = \frac{\frac{\rho_p d_p^2}{18\rho_g \nu_g}}{\frac{r_{1/2}}{u_c}} \tag{5.1}$$

In Equation (5.1), ρ, ν, u, d, and $r_{1/2}$ represent density, kinematic viscosity, flow velocity, diameter and jet half-width, respectively. The subscripts c, g and p denote jet convective/centerline, gas, and particle parameters. The τ_c increases with the axial distance from the jet inlet due to the concurrent effect of increasing $r_{1/2}$ and decreasing u_c. Hence, the local particle St decreases quadratically along the jet centerline [178]. Note that τ_c is analogous to integral timescale (τ_l) and at the inlet it is given as $\tau_l = r_j/u_j$, where r_j and u_j are the jet radius and inlet velocity, respectively. Thus, the initial integral length scale is $L = r_j$.

The dispersion rate of particles with $St \ll 1$ is similar to the turbulence dispersion, which causes particles to spread evenly within the jet; particles with $St \gg 1$ travel along the jet centerline with minimum radial dispersion; particles with $St \approx 1$ depict higher dispersion than the turbulent eddies due to the local vortex based centrifugal force exerted on them, and they can be completely ejected out of the jet [56]. These three dispersion mechanisms are termed vortex, inertial and centrifugal mechanisms [57]. Furthermore, since St decreases axially, a higher local concentration is observed in the jet where local $St \approx 1$ [178]. But eventually in the far-field, particles start behaving as tracers with respect to the large-scale structures, whereas they are ballistic for small-scale velocity fluctuations [63]. Hence, as stated earlier, overall in freeshear flows the dispersion of

particles is driven by large-scale vortex structures generated in these flows [209]. Even in compressible particle-laden flows, which typically involve a larger number of turbulent scales than incompressible flows [210], particle clustering is characterized by the large scales and the corresponding St.

5.1.3 Particle-Turbulence Interaction

Although particle transport is governed by the local mean and fluctuating fluid velocity, the presence of particles modulates the local turbulent flow field. The overarching mechanism is that particles act as a medium of augmenting the transport of energy [211] and momentum [212] between different regions of the flow. Consequently, as compared to a single-phase jet, particles reduce turbulent intensity by up to 50% [186]. This jet modulation is a function of particle loading density [213, 214], St [184], particle-to-fluid density ratio, particle diameter to turbulent eddy diameter ratio, and Reynolds number of the particles (Re_p) [215]. Such interaction between the two phases creates a feedback loop, making this a compounding problem. Thus, to complete the scope of this issue, it is essential to comprehend the particle-based modulation of a jet flow.

In the case of supersonic jet flows, smaller particles have been reported to produce a more pronounced modulation of the jet structure similar to the subsonic case [216]. This is due to the higher specific surface area (ratio of particle surface area to volume) of the smaller particles, which results in stronger fluid-particle momentum exchange at constant particle loading density [177]. Moreover, even at minimal particle loading, particles have been found to move the Mach disk upstream in supersonic jet flows [217]. This effect further enhances with the increase in particle loading [218, 219]. Additionally, phenomena such as attenuation of dilatation, turbulent Mach number, turbulent kinetic energy and dissipation increase with the density of the particles [220], further making the fluid-particle interaction in compressible flows perplexing. As mentioned earlier, the transfer of gas kinetic energy to particles restricts the gas expansion, which decreases the gas density and dynamic pressure in the direction of the flow [221]. In supersonic jets, particles also

weaken the pressure functions radiated by a supersonic jet, by substantially altering the development of turbulent structures [222]. Consequently, the root-mean-square of jet axial (radial) velocity drops by 10% (30%), as compared to an unladen jet [223]. This effect is also a function of particle mass loading, such that these pressure fluctuations decrease with the increase in mass loading [224].

As stated in the discussion above, particle dispersion is primarily credited to the centrifugal force acting on the particles based on particle inertia, even in supersonic flows [99]. Here, PC in the axial direction is attributed to the particle-gas momentum transfer, while radial dispersion is credited to the radial inter-phase velocity difference. Note that in a supersonic jet flow in which the particle velocity is less than the fluid velocity at the inlet, particles keep accelerating after leaving the nozzle, consuming the kinetic energy of the supersonic gas. Since the major component of particle inertia is in the streamwise direction, a question arises: why do particles start traveling in the radial direction in the first place? It is understood that a jet inherently spreads, creating a radial velocity difference between the inertial particle and the local gas. But the particle-gas axial velocity difference is higher in the streamwise direction (up to four times in the present study), and hence particles should keep traveling within the jet center. We hypothesize that there must be an organized turbulent motion that pushes particles out of the central region of the jet. It has been reported that local kinematic and thermodynamic aspects, especially fluid viscosity, can considerably alter particle distribution in HIT [187, 225, 151, 181]. In supersonic jet flows, although the local thermodynamic properties of the fluid will change as the jet evolves, these local thermodynamic properties particularly the fluid viscosity are assumed to have a minor effect on particle dispersion. In a supersonic jet flow, the variation in density and fluid compressibility governs the fluid-particle interaction as discussed earlier in this section. Thus, in this contribution, we probe the dispersion of four particle sizes in a supersonic jet flow using DNS. We aim to investigate the local turbulent eddy-based effects that govern the transition of particles' motion from axial to radial downstream from the inlet. In the rest of this article, we discuss the methodology of our numerical experiments along with the model validation in Section 5.2, the obtained results in Section 5.3, and the

drawn conclusions are reported in Section 5.5.

5.2 Methodology

We carried out DNS to simulate a spatially developing, polydispersed particle-laden perfectly expanded supersonic jet flow using an in-house version of an effectively parallelized, open-source, high-order finite difference code, known as Pencil-Code [130]. A sixth-order scheme is used for spatial derivatives and a third-order Runge-Kutta scheme is employed for time integration. To stabilize our sixth-order spatial scheme, which is inherently unstable with finite difference, a hyperdiffusion term was used. The domain pressure was matched with the inlet pressure of the jet to avoid the formation of large-scale shocks. In other words, the ratio of jet exit to domain pressure is maintained at unity (nozzle pressure ratio, NPR = 1). These simulations are carried out in a rectangular domain with periodic boundary condition in the lateral direction to eliminate wall effects, which are not of interest in the present study. Four particle sizes are considered with TWC using the Lagrangian point-particle tracking scheme, where a tri-linear interpolation method is used for resolving particle trajectories. In this case, the undisturbed local fluid velocity is required to compute the drag force on the particles. However, it is intrinsically unavailable in momentum TWC as particles influence the local flow field [162, 163]. As a result, the Stokes drag on the particles can be underestimated. Thus, the use of the tri-linear interpolation method can be problematic, especially in supersonic flows and may require a correction to capture the particle trajectories accurately. A metric for estimating the error due to this scheme is the ratio of particle diameter to grid cell length d_p/l_{cell}. Since our cell length along x is less than y and z directions ($\Delta x < \Delta y = \Delta z$), we define $l_{cell} = V_{cell}^{1/3}$, where $V_{cell} = \Delta x \times \Delta y \times \Delta z$ is the cell volume. Yang et al. [226] found the tri-linear interpolation method to be invalid if d_p/l_{cell} is large ($O(10^0)$). Moreover, Patel et al. [217] suggested the use of an optimized momentum TWC approach for larger d_p/l_{cell} and shock-particle interaction. However, in our case the highest $d_p/l_{cell} = 0.18$, which is fairly small, and our

Particle	P1	P2	P3	P4
d_p	0.003	0.004	0.005	0.006
St	1.5	2.7	4.2	6.0

Table 5.1: Diameters (d_p) and Stokes number (St) at the jet inlet, of the four particle species (denoted P1 to P4).

jet is shock-free. Hence, we expect the impact of local disturbed fluid velocity on Stokes drag to be minimal.

On the other hand, the diameters and initial St of these particles are presented in Table 5.1. As seen in Table 5.1, we will refer to these particles with increasing diameter as P1, P2, P3 and P4, for brevity. The constant density of these particles is $\rho_p = 1500$. In light of our hypothesis, the use of different particle sizes will enable us to probe the local mechanisms that cause particles to start traveling laterally at different downstream locations. For the continuum phase, the gas with a density of $\rho_g = 1$ is simulated with an Eulerian specification. Our DNS consists of three sub-simulations, as discussed in the following subsections.

5.2.1 Simulation Setup

Development of HIT

The simulation setup is depicted in Figure 5.1. Firstly, HIT is generated in a triply periodic box of $9d_j$ characteristics length discretized into a 256^3 mesh, where d_j is the jet diameter. This simulation is conducted without particles and resulted in a Taylor Reynolds number of $Re_\Lambda = \rho_g u_{rms} \Lambda / \mu_g = 77$, where Λ, u_{rms} and μ_g are the Taylor microscale, fluid root-mean-square velocity and dynamic viscosity, respectively. For HIT development, a solenoidal forcing function is used [131]. This forcing scheme is such that, at any given instance, the random points of energy addition are correlated, but these points vary in time. This

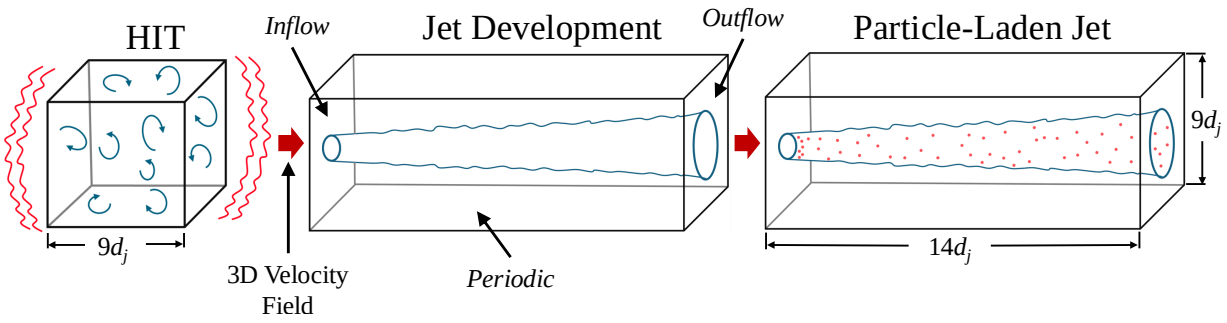


Figure 5.1: Simulation setup depicting three sub-simulations.

simulation is carried out until an equilibrium is established between energy addition and energy dissipation at high wavenumbers (k). This is determined by the fact that the temporal evolution of turbulence statistics such as turbulent kinetic energy (TKE) starts fluctuating about a steady mean value. Note that regardless of the forcing scheme used (linear [159, 160] or spectral [158]) turbulence statistics, especially TKE, depict noticeable fluctuations about a mean value even after the aforementioned equilibrium is established. Since these fluctuations eventually oscillate about a constant mean value, we consider the HIT to be fully developed. This simulation is conducted for about 200 integral timescales ($\tau_l = r_j/u_j$) computed at the inlet of the jet.

Jet Development

Once the HIT is fully developed, 3D snapshots of the mean velocity field from the HIT simulation are cyclically introduced at the inlet of a rectangular domain with dimensions $14d_j \times 9d_j \times 9d_j$. This domain is meshed into $512 \times 256 \times 256$ cells in the x, y and z directions. This resulted in grid cells that are longer in the lateral direction, however, all cells in the domain have the same dimensions. The streamwise mesh has more grid points compared to the lateral directions, as our domain is longer in the axial direction. At the inlet of the jet, a top-hat mean flow profile is assumed. This mean flow is superimposed by the turbulence fluctuations generated by the HIT simulation. The 3D HIT snapshots of the

turbulence fluctuations are convected into the domain, which assures realistic turbulence characteristics within the compressible jet. The pressure at the inlet is set equal to the domain pressure to get a perfectly expanded jet, thus minimizing any shocks or large expansion waves. This was done to avoid shock formation, as the interaction of particles with a shock wave will further complicate our model, and it is not in the scope of this analysis.

At the inlet and outlet of this domain, *inflow* and *outflow* boundary conditions are imposed, respectively. The fluid is allowed to enter the domain only through the jet inlet with diameter $d_j = 1$, and the rest of the inlet is modeled as a wall. The inlet and outlet boundaries suffered from spurious reflections, however these reflections at the inlet [188] and outlet [189] are attenuated with NSCBC.

A periodic boundary condition is prescribed in the two lateral directions (y and z). This is done to deal with a limitation of Pencil-Code, where if outflow boundary condition is imposed on y and z boundaries, the reflections from the edges between these boundaries result in discontinuities. This simulation is run for roughly 7 FTT, such that the initial transience caused by the jet development diminishes and a stable jet flow is established. For assessing this state of the jet, self-similarly of the classical flow statistics is analyzed in Section 5.2.4.

Particle-Laden Jet

From the last state of the jet development simulation, a third simulation is initiated, which is run for an additional 5 FTT. In total, $200,000$ adiabatic particles equally divided into four particle species are released within the jet diameter at the inlet with a steady rate of approximately 1300 particles/τ_l. These particles are introduced with a random velocity in the x-direction such that at the inlet, the particle velocity (u_p) is less than the local gas velocity ($u_g(x_p)$). To avoid shock formation at the particle surface, the particle velocity at the inlet is never below half of the local fluid velocity. Consequently, particles are accelerated by the gas via drag force, as viscous drag is the only force acting on the

particles considering $\rho_p/\rho_g \gg 1$ [39]. Moreover, the gravitational force is also neglected for simplicity.

In this simulation, the first 3 FTT are to stabilize the particle-laden jet flow, as the introduction of particles modulates the jet flow due to momentum TWC. The following 2 FTT are used for collecting the results presented in this paper. Note that all the statistics discussed in this paper are temporally averaged unless stated otherwise. Considering the particle loading density, the maximum instantaneous volume fraction in the overall domain is $\Phi_v \approx O(10^{-6})$, which is within the OWC regime [4]. But, because particles are released within the narrow region of $d_j = 1$ and of the supersonic flow, particles travel within the central region of the jet for a considerable distance. This causes the local Φ_v within the core of the jet to be as high as $O(10^{-4})$, which is within the TWC regime. Moreover, PC in the jet can also result in higher local Φ_v, even though the global Φ_v is in the dilute regime [99]. Hence, momentum TWC is employed in the present study.

5.2.2 Continuum Phase

The non-dimensional equation set for the gaseous phase is given as:

$$\frac{\partial \rho_g}{\partial t} + \frac{\partial \rho_g u_{g,i}}{\partial x_i} = 0 \tag{5.2}$$

$$\frac{\partial \rho_g u_{g,i}}{\partial t} + \frac{\partial \rho_g u_{g,i} u_{g,j}}{\partial x_j} = -\frac{\partial P_g}{\partial x_i} + \mu_g \frac{\partial}{\partial x_j}\left(\frac{\partial u_{g,i}}{\partial x_j} + \frac{\partial u_{g,j}}{\partial x_i} - \frac{2\partial u_{g,k}}{3\partial x_k}\delta_{ij}\right) + F_p \tag{5.3}$$

$$\rho_g T_g \frac{Ds_g}{Dt} = \frac{\partial}{\partial x_i}\left(\kappa_g \frac{\partial T_g}{\partial x_i}\right) + 2\rho_g \nu_g \mathbf{S} : \mathbf{S} + \zeta \rho_g \left(\frac{\partial u_{g,i}}{\partial x_i}\right)^2 \tag{5.4}$$

here the variables T, P, κ, s, $\mathbf{S}$ and ζ depict temperature, pressure, thermal conductivity, entropy, shear-rate tensor and bulk viscosity ($\zeta = 0.0006$), respectively. Here, κ was kept constant. In Equation (5.4), typically a particle-based work term ($F_p \cdot u_p$) is included on the right-hand side. In our study, this term is ignored as it is found to be much smaller (not shown here) than the dissipation term in Equation (5.4). Furthermore, this term becomes significant at high particle loading density, which is not the case in the present simulation.

Therefore, neglecting its contribution to the entropy equation has a negligible effect on the results.

The gas viscosity is modeled with a power law:

$$\mu_g = \mu_{g,0}\, T_g^{2/3} \tag{5.5}$$

where subscript 0 represents the initial/reference state and $\mu_{g,0} = 0.001$ is the initial/reference gas dynamic viscosity. The initial temperature of both particles and gas is $T_0 = 1$.

5.2.3 Particulate Phase

The non-dimensional Lagrangian equations for particle transport are:

$$\frac{dx_{p,i}}{dt} = u_{p,i} \tag{5.6}$$

$$\frac{du_{p,i}}{dt} = \frac{C_D}{\tau_p}\left(u_{g,i}\left(x_p\right) - u_{p,i}\right) \tag{5.7}$$

In Equation (5.7), the particle drag coefficient C_D is adopted from Carlson and Hoglund [192]:

$$C_D = \frac{24}{Re_p}\left[\frac{\left(1 + 0.15Re_p^{0.687}\right)\left(1 + \exp\left(0.427/Ma_p^{4.63}\right) - \left(3/Re_p^{0.88}\right)\right)}{1 + (1/\alpha)\left(3.82 + 1.28\exp\left(-1.25\alpha\right)\right)}\right] \tag{5.8}$$

where α is the ratio of Reynolds and Mach numbers ($\alpha = Re_p/Ma_P$) of the particles. The Ma_p and Re_p are expressed as:

$$Ma_p = \frac{|\mathbf{u}_p - \mathbf{u}_g(x_p)|}{c}, \quad Re_p = \frac{\rho_g\,|\mathbf{u}_p - \mathbf{u}_g(x_p)|\,d_p}{\mu_g} \tag{5.9}$$

here c is the speed of sound. We chose this expression for C_D as it incorporates inertial, compressibility and rarefaction effects. Also, it is valid for particle Mach number of $Ma_p < 2$ and particle Reynolds number $O(10^{-1}) \leq Re_p \leq O(10^2)$. In our case, the average Ma_p in the first $0.5d_j$ of the domain is $Ma_p \approx 0.45$, and the corresponding particle Reynolds number is $Re_p \approx 0.64$. Note that particles are introduced with random velocity in the

Variable	Symbol	Value
Mach number	$Ma = u_j/c$	1.5
Turbulent Mach number of HIT	$Ma_T = u'/u_j$	0.04
Turbulent Mach number of jet	$Ma_T = u'/u_j$	0.13
Inlet Reynolds number	$Re = \rho_g u_j r_j/\mu_g$	500
Turbulent Reynolds number	$Re_T = \rho_g u_{rms} r_j/\mu_g$	125
Integral length scale	$L = r_j$	0.5
Kolmogorov length scale	$\eta = L/Re_T^{3/4}$	0.013

Table 5.2: Turbulence characteristics of the supersonic jet flow.

x-direction, and the gas velocity is the highest close to the inlet. Thus, our Ma_p and Re_p are maximum at the start of the domain. Beyond this, gas decelerates and the particles' velocity approaches the gas velocity, causing the Ma_p and Re_p to drop.

Considering the discussion above, the turbulence parameters of the particle-laden jet flow simulation are given in Table 5.2. For all four particle species $\rho_p/\rho_g \gg 1$, $Re_p \leq 1$ and $d_j < \eta$, here η represent the Kolmogorov length scale. Based on this criteria, the use of the point-particle scheme is justified [23].

The drag force on the particles (F_D) is given as:

$$F_D = 3\pi\mu_f d_p \left(u_{p,i} - u_{g,i}(x_p)\right) \tag{5.10}$$

here u_p is the particle velocity and $u_g(x_p)$ is the gas velocity at the particle's position. Similarly, in Equation (5.3) the term F_p accounts for the back-reaction force on the local gas by the particles due to momentum TWC. This force is defined as:

$$F_p = \sum_i^{N_p} W_p \left(x - x_{p,i}\right) F_D \tag{5.11}$$

where N_p is the total number of particles in a given cell. The term $W_p\left(x - x_{p,i}\right)$ is the weighing function for the TSC approach, which is employed for modeling the two-way

fluid-particle interaction [37]. In TSC, a second-order spline interpolation is carried out on 27 neighboring points on the Cartesian grid. In this approach, a weight function is used to project particle properties onto a grid point, such that this weight function depends on the proximity of a grid point from the particle. The grid point closer to a particle gets a higher weight and vice versa. Thus, in a 3D grid, fluid-particle interaction is projected on $3 \times 3 \times 3$ grid points. In this case, even if two particles are present within the same cell, their proximity to the nearest 27 points will be different. This results in a smooth interaction between the two phases.

5.2.4 Validation

To validate the present simulation setup, we run the jet simulation at the same conditions but without particles, for about 7 FTT. First, we assess whether our $512 \times 256 \times 256$ mesh is grid converged. For this purpose, we run another simulation with $768 \times 384 \times 384$ mesh without particles for 3 FTT. The resulting radial profiles of the axial component of the jet centerline velocity (u_{c_x}) and azimuthally average TKE at the downstream location of $x = 8$ of these two cases are presented in Figure 5.2. Note that in Figure 5.2 and in the rest of the article, all the dimensions such as x and y are normalized with d_j, unless stated otherwise. Reynolds averaged results are presented, instead of Favre averaging, as the density fluctuations are modest in the flow. It can be seen in Figure 5.2 that both curves of the centerline velocity and TKE overlap reasonably well, justifying our mesh selection. The $768 \times 384 \times 384$ results are not as smooth because they were averaged over fewer time frames as compared to the baseline mesh. It should be noted that despite modeling a domain length of $14d_j$, we only showed results up to $x = 10$ as the latter portion of the domain is influenced, to some extent, by the outflow boundary condition. Since the simulations are conducted in Cartesian coordinates, the results are averaged in the azimuthal direction and in time.

To assess that the present TWC scheme is grid-converged, we rerun the particle-laden jet flow simulation with $768 \times 384 \times 384$ mesh. This simulation is carried out for about

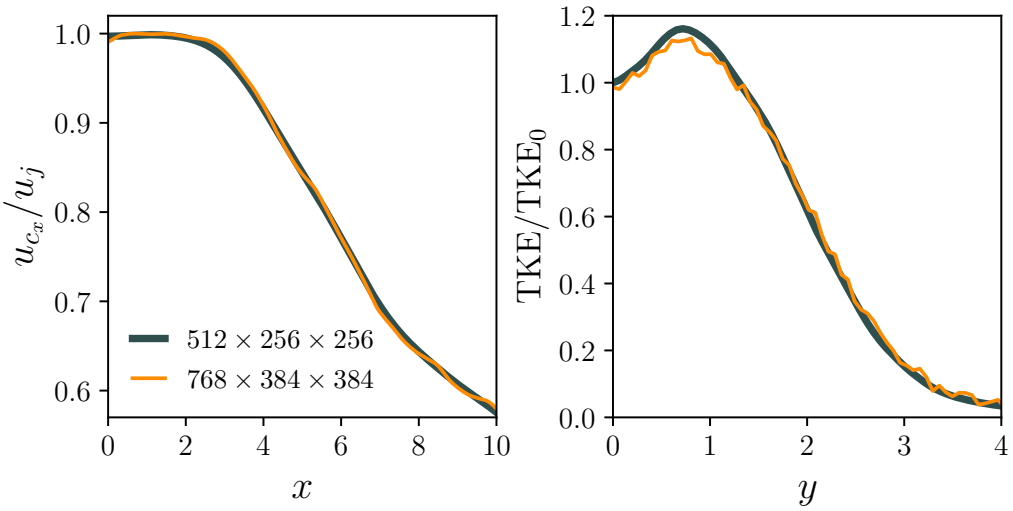


Figure 5.2: Normalized axial component of the jet centerline velocity (u_{c_x}), and azimuthally average TKE at $x = 8$ of the $512 \times 256 \times 256$ and $768 \times 384 \times 384$ meshes.

4 FTT, where the first 3 FTT are used to stabilize the transience due to the introduction of particles within the jet, and 1 FTT is used to compute the present results. Here, we calculate the axial fluid-particle slip velocity (u_{pg}) with Equation (5.24), from the $512 \times 256 \times 256$ and $768 \times 384 \times 384$ mesh simulations, as shown in Figure 5.3. It can be seen in this figure that the u_{pg} curves of the two grids reasonably overlap, which suggests that our TWC at $512 \times 256 \times 256$ mesh is not sensitive to grid refinement.

Since the simulations are conducted in Cartesian coordinates, the results are averaged in the azimuthal direction. For the validation of our simulation, we first compare our axial velocity profile in the radial direction with that of Troutt and McLaughlin [2] (TM), which is defined as:

$$u_x = \exp\left(-2.773\left(\xi + 0.5\right)^2\right); \text{ for } \xi > -0.5 \tag{5.12}$$

In Equation (5.12), ξ is given as:

$$\xi = \frac{y - r_{1/2}}{2r_{1/2}} \tag{5.13}$$

here y is the value along the y-axis. Based on this normalization, the mean axial velocity in

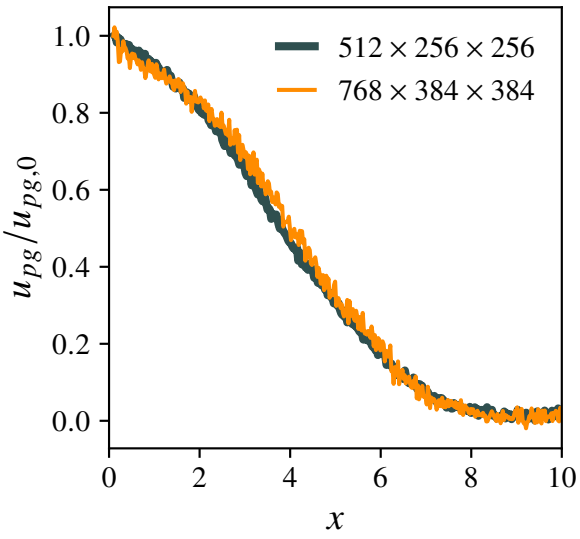


Figure 5.3: Axial fluid-particle slip velocity (u_{pg}) of the $512 \times 256 \times 256$ and $768 \times 384 \times 384$ grids, normalized with the initial value at $x = 0$ ($u_{pg,0}$).

the radial direction collapses reasonably well on the curve obtained from Equation (5.12) from $x = 6$ onward, see Figure 5.4. This suggests that our first-order statistics become approximately self-similar around $x = 6$ which is relatively short. This axial distance is a function of flow Re, and for lower Re, self-similarity is achieved at a shorter axial distance [227]; a short time evolution to reach first-order self-similarity was also shown in other free shear flows [228]. Note that Bogey and Bailly [227] analyzed transitional jets; the present jet flow lies between transitional and fully developed jets as we impose a turbulent plug flow at the inlet (from a separate HIT simulation). However, the similar effect of Re on self-similarity evolution is expected to hold in the present case. According to Figure 5.4, the outer edge of the jet slightly departs from the self-similar curves defined in Equation (5.12). This is due to the periodic boundary condition on the lateral boundaries and the spatially evolving jet which results in non-zero freestream velocity; as this velocity remains small, it does not affect the analysis.

It should be noted that higher-order statistics take longer to achieve self-similarity [228,

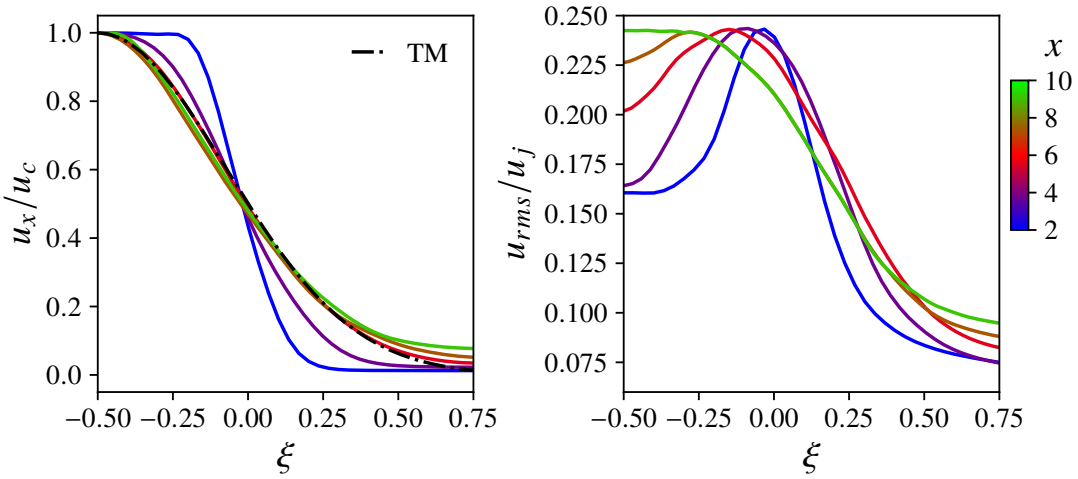


Figure 5.4: Radial evolution of temporal and azimuthal mean axial velocity, u_x (left), and root-mean-square gas velocity, u_{rms} (right), of the single-phase jet flow at five axial locations. In the left plot, TM represent Troutt and McLaughlin [2], particularly the solution of Equation (5.12).

229]. This is because high-order self-similarity requires an equilibrium state to be reached within the turbulence. We can see this in the lateral evolution of the normalized root-mean-square velocity (u_{rms}) of the jet, as shown in Figure 5.4. To determine u_{rms}, we first temporally averaged the 3D fluid velocity field. Then we estimated the fluid velocity fluctuations at each time instance by carrying out a Reynolds decomposition using the instantaneous and temporally averaged velocity fields. By averaging and computing the square root of this 3D array of velocity fluctuations, u_{rms} was determined. Figure 5.4 presents the characteristic u_{rms} curves, with lower u_{rms} at the jet center and higher values near the jet edge. To be precise, the curves of $x = 8$ and 10 do not overlap close to the center of the jet, which is not truly self-similar. A similar lack of self-similarity of higher-order statistics was also observed in the high-speed wake, despite a much longer flow evolution [230], which is tied to the strong memory effects in the freeshear flow evolution. Since our first-order statistics are self-similar and the second-order statistics show the expected

behavior for the considered domain length, our simulation model is acceptable for analyzing the dispersion of inertial particles in a supersonic jet.

5.3 Results

In a supersonic jet, the highest velocity component is located along the jet centerline (recall Figure 5.4), as observed in Figure 5.5 in which vortices are depicted with $\mathcal{Q}$-criterion [231] and particles are colored with the local gas velocity (u_g). The $\mathcal{Q}$-criterion is mathematically defined as:

$$\mathcal{Q} = \frac{1}{2}\left(||\mathbf{\Omega}||^2 - ||\mathbf{S}||^2\right) \tag{5.14}$$

where $\mathbf{\Omega}$ and $\mathbf{S}$ are the rotational and strain-rate tensors, respectively. In Equation (5.14), $||\cdot||$ is representing magnitude. Mathematically, $\mathbf{\Omega}$ and $\mathbf{S}$ are the anti-symmetric and symmetric components of the instantaneous velocity gradient tensor, such that:

$$\mathbf{\Omega} = \frac{1}{2}\left((\nabla \mathbf{u_g}) - (\nabla \mathbf{u_g})^{\mathrm{T}}\right) \tag{5.15}$$

$$\mathbf{S} = \frac{1}{2}\left((\nabla \mathbf{u_g}) + (\nabla \mathbf{u_g})^{\mathrm{T}}\right) \tag{5.16}$$

In Equations (5.15) and (5.16), the superscript T represents the matrix transpose.

As u_g is the highest along the jet centerline (see Figure 5.5), it follows that particles should travel along this center axis due to the higher particle-fluid slip velocity, which governs the direction of the drag force experienced by the particles. However, Figure 5.5 reveals that particles are dispersed away from the jet centerline at different streamwise locations based on their size. In this case, smaller particles are ejected radially from the central region of the jet at a shorter downstream distance as compared to their larger counterparts. As the characteristic size of the largest eddies grows with the streamwise evolution of the jet, it is plausible that the particles of different sizes are preferentially dispersed at distinct axial locations as the turbulent structures grow.

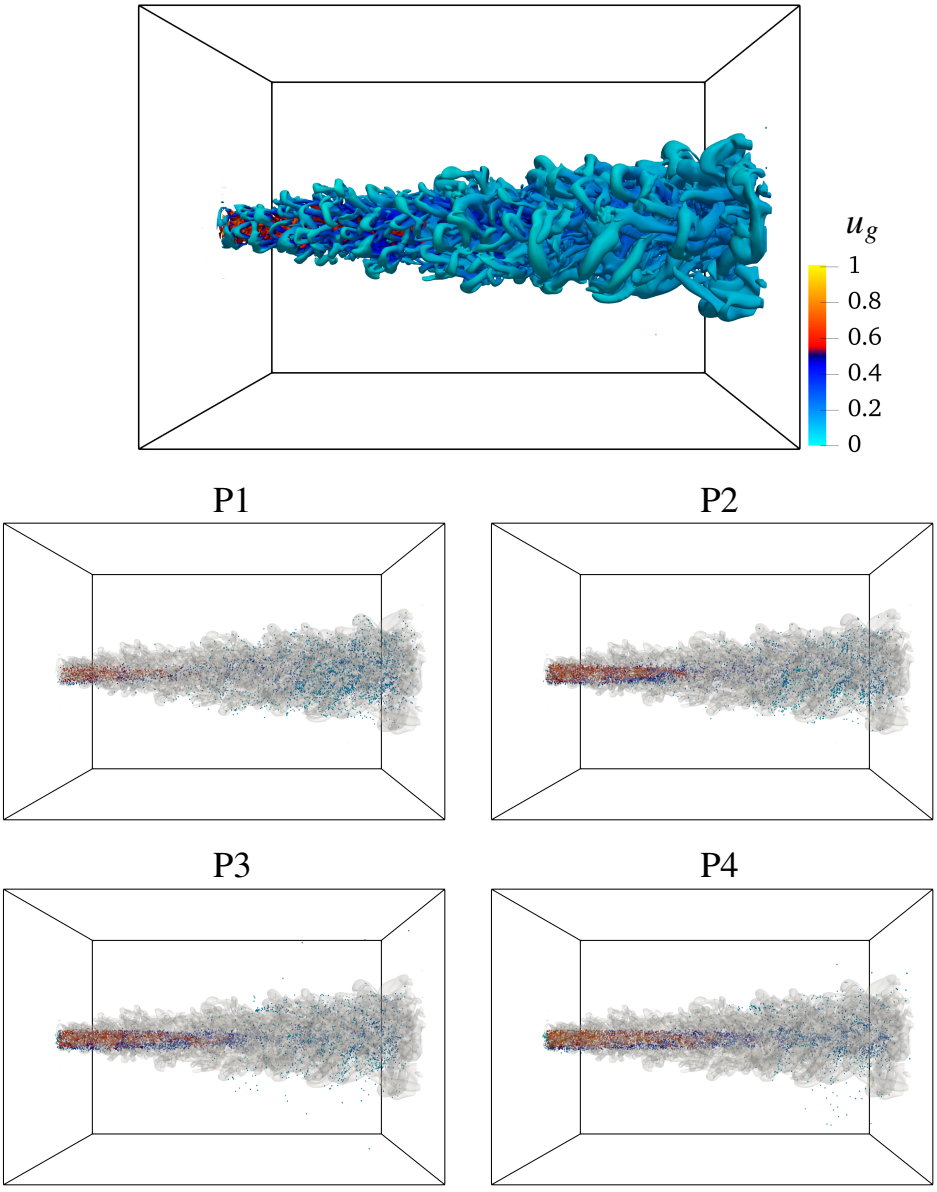


Figure 5.5: Fluid vortices shown with $\mathcal{Q}$-criterion (top), overlaid with particles (bottom) of the considered four species as titled. The vortices in the top image and particles in the bottom four images are colored with the local gas velocity (u_g). Recall that the particle size increases from P1 to P4.

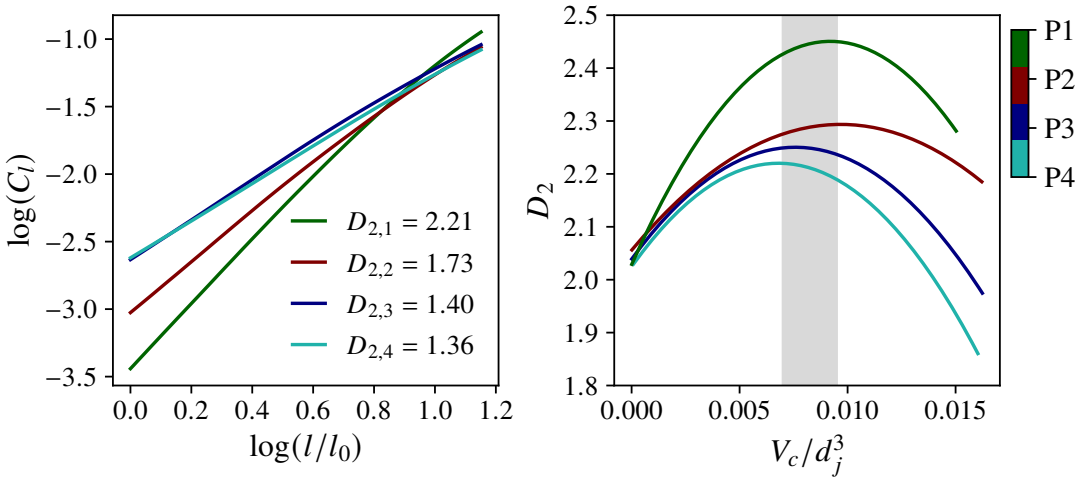


Figure 5.6: Logarithmic correlation integral, $\log(C_l)$ (left), with respect to the inter-particle distance, l, normalized with the initial inter-particle distance, l_0. The correlation dimension (D_2) of each curve is shown in the legend. The variation in D_2 with normalized cluster volume (V_c) is shown in the plot on the right. The gray-shaded area highlights the region containing inflection points.

5.3.1 Fractal Dimension Analysis

To scrutinize the aforementioned hypothesis, we adopt the fractal dimension analysis, as particle dispersion is multi-fractal in nature [122]. Here, particle clustering shows distinct fractal features at different turbulent scales, or, in other words, particles with different inertia primarily respond to eddies of different sizes [58]. Thus, we perform the fractal dimension analysis on the global particle dispersion, as well as on the individual particle clusters. First, we compute the correlation dimension (D_2) of each particle species, which characterizes the dispersion pattern (chaotic or organized) of the particles [232]. The D_2 is expressed as:

$$D_2 = \lim_{l \to 0} \frac{1}{\log(l)} \log(C_l) \tag{5.17}$$

here $C_l = \sum p_i^2$ is the correlation integral and p_i is the probability of finding a particle pair at an inter-particle distance less than l. By plotting the logarithmic correlation integral ($\log(C_l)$) against the log of the normalized separation distance, D_2 can be approximated as the slope of the obtained curve. This is shown in Figure 5.6 (left) and the corresponding D_2 value of each particle species is shown in the legend, marked with the particle species number as a subscript. The fundamental benefit of using D_2 to characterize the dispersion is that it is not dependent on the choice of the length scale. On the other hand, methods such as *box-counting* depend on the box size [233] and *pair-correlation function* is influenced by the radius [137] in which the number of particle pairs is counted.

For D_2, a lower value depicts a more organized (clustered) dispersion of the particles; a higher value shows chaotic dispersion. Furthermore, D_2 indicates the dispersion dimensionality, where values of $D_2 \approx 3$, 2 or 1 imply globular, planar or tubular clustering of particles, respectively [118]. As D_2 decreases with the increase in particle size in Figure 5.6, it validates the qualitative observations of Figure 5.5, where smaller particles are more dispersed as they start spreading laterally after a short axial distance from the inlet, while larger particles primarily travel along the jet axis. This gives P1 and P4 dominantly planar and tubular clusters, respectively. Since P4 particles travel in a narrow region within the jet, they show organized (clustered) dispersion.

By analyzing D_2 of the individual particle cluster, we can probe if the fractal dimension changes based on the cluster size. If it does, it would indicate that the cluster size varies based on the turbulent scale (since particle clustering is governed by particles' dominant correspondence to a turbulent scale), which would hint at the mechanism that causes particles to spread laterally at different downstream distances. Note that D_2 indicates the scale of clustering, where a lower D_2 depicts clustering due to the larger scales, while a higher D_2 relates clustering to the small scale features [209]. Considering the visual observation in Figure 5.5, the scale at which clustering occurs should increase with the increase in particle size. We witness this trend in Figure 5.6 (right), where D_2 is plotted against the cluster volume (V_c). The dispersion dimensionality of these curves also verifies the qualitative observation of Figure 5.5. Here, V_c is determined by using DBSCAN method [167], which

segregates clustered particles from noise/unclustered particles. By computing the convex hull using the x, y and z separation between particles in each cluster, V_c is evaluated. The details of the DBSCAN method in the present context can be found in Saieed and Hickey [187].

The downward curves in Figure 5.6 (right) portray a critical observation: the D_2 rises quasi-linearly until it reaches an inflection point. This inflection point marks the boundary between chaotic (rising D_2 with respect to V_c) and organized (declining D_2 with respect to V_c) dispersion regimes; these inflection points are approximately highlighted with a gray color region. This trend, however, seems counterintuitive because the eddy size increases with the axial distance. But the rise in D_2 with V_c on the left side of the gray region containing inflection points means that particle clustering is governed by turbulence at smaller scales. This can be understood with the fact that in the present $10d_j$ domain length which is essentially the near-field region of the jet, the turbulent fluctuations and thus averaged turbulent kinetic energy (TKE) augments as the local eddy length scale (L_{eddy}) increases downstream, see Figure 5.7. The rise in downstream turbulent fluctuations at the jet centerline can be witnessed in Figure 5.4 (right). Additionally, the TKE in Figure 5.7 is the bulk TKE of the flow, which is computed by averaging TKE in the radial direction for each grid point along the x-axis. Therefore, because we are in the near-field region where shear is high at the inlet (shear layer is significant) and the jet is spreading, the bulk TKE increases as the velocity fluctuations are high in this region ($x = 10$).

In Figure 5.7, the L_{eddy} is computed by identifying vortices with the $\mathcal{Q}$-criterion and labeling dominant vortices on the y-z plane at each x position by applying an approximate threshold ($\mathcal{Q} > \overline{\mathcal{Q}}$). Each detected vortex has a peak value of $\mathcal{Q}$. By identifying the location of this peak $\mathcal{Q}$, and determining the average Euclidean distance between the locations of these peak $\mathcal{Q}$ values of vortex pairs on each y-z plane, the local separation of vortices is estimated. This local separation is temporally averaged for each particle pair at a given x-position, which resulted in L_{eddy}. This provides a more accurate estimate of the local eddy length scale as compared to the $r_{1/2}$, which is often used. However, note that although our later results converge based on this definition of L_{eddy}, the values of L_{eddy} are sensitive to

the applied threshold and the assessment of this sensitivity is left for future consideration. Also, note that L_{eddy} is qualitatively similar to $r_{1/2}$ of the jet, the change in threshold is expected to yield similar trends. This is because selecting a different threshold will alter the magnitude of L_{eddy}, but L_{eddy} will still increase axially, akin to the trend in Figure 5.7.

The discussion above infers that because particles are accelerated in the axial direction by the supersonic gas in the jet core, the natural reaction of the particles is to stay within the central region of the jet, as drag (governed by fluid-particle slip velocity) is higher within this region. This limits V_c at any axial location. Since the jet spreads downstream, particles get more space to form clusters, which raises V_c. However, the rise in V_c is limited by the jet boundary/shear layer. Further rise in V_c can only occur if particles experience a significant radial dispersion and leave the central region of the jet. At the inflection point (inside the gray region in Figure 5.6), the particles' direction of travel develops a radial component. Beyond this, V_c increases, but particles are now facing larger eddies with lower turbulent fluctuations (see Figure 5.4). Additionally, now that the particles are out of the higher velocity central region of the jet that houses smaller eddies (recall Figure 5.5), they lose their axial momentum, which causes particles to react and cluster at larger eddies. This is reflected by the drop in D_2. Evidently, from P1 to P4 the D_2 of the inflection point drops and therefore the scales at which their corresponding clusters form increase. This shows that each particle species leaves the dominantly longitudinal travel in the jet until it meets an eddy corresponding to its inertia (depicted by the inflection point), which pushes it out in the lateral direction. Therefore, this inflection point is a clear indication that particles start spreading radially based on the eddy they dominantly respond to as they travel downstream.

5.3.2 Finite-Time Lyapunov Exponent

To quantify the local eddies that trigger the lateral particle dispersion, an approximation of the axial location (x_r) where particles first leave the jet core is required. For this purpose, the rate of convergence and divergence of particle trajectories along the jet centerline is

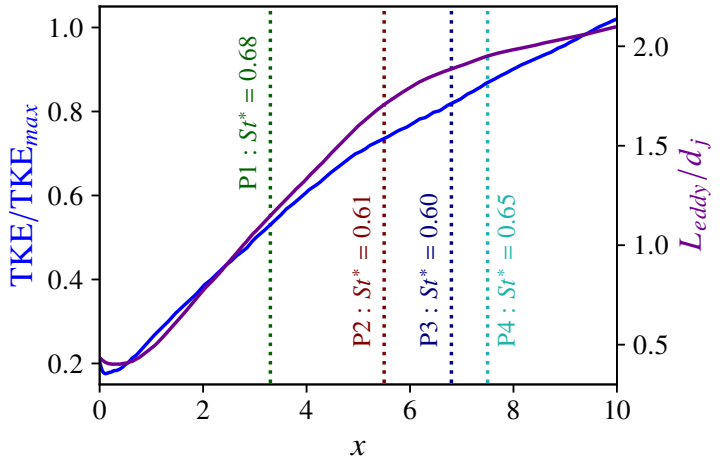


Figure 5.7: Evolution of temporally and spatially averaged turbulent kinetic energy (TKE) and eddy-length scale (L_{eddy}). Here L_{eddy} is normalized with jet diameter d_j. The dotted vertical lines mark the location of respective particle initial radial dispersion, where St^* is the local Stokes number of the particles at that location (discussed in Section 5.3.3).

probed via the Finite-Time Lyapunov Exponent (FTLE) [70]. The FTLE determines the local attractor points by estimating the temporal evolution of the separation between particle pairs. In other words, FTLE characterizes the evolution of particle separation distance over time. If particles only travel within the jet core, their radial velocity component will be substantially smaller than their axial velocity. This will result in small inter-particle separation in the radial direction. By examining the spike in the particle separation distance determined with FTLE, we can estimate the location where particles dominantly start traveling radially. Note that a major rise in FTLE will only occur if particles start dispersing radially because the axial fluid-particle slip velocity is very high; the particles injected in the jet at the inlet reach the outlet at approximately the same time if they stay within the central region of the jet.

We defined FTLE ($\lambda(x)$) with the following mathematical expression:

$$\lambda(x) = \frac{1}{\Delta t} \log \left| \frac{\delta r(x)}{\delta r(x_0)} \right| \tag{5.18}$$

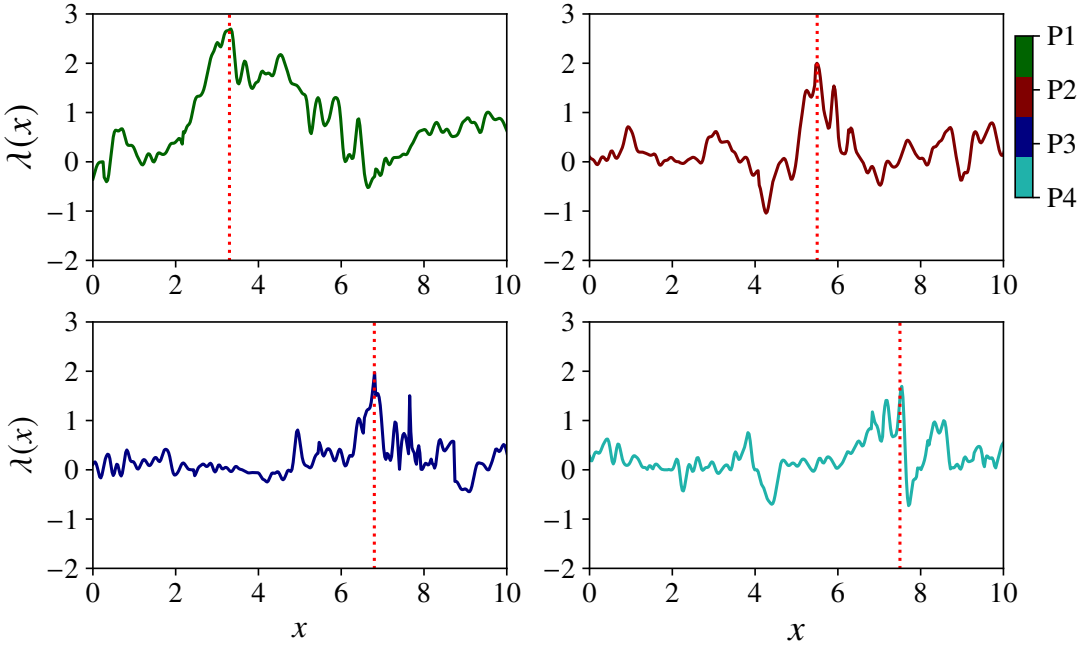


Figure 5.8: FTLE ($\lambda(x)$) computed along the streamwise direction, where $\lambda(x)$ is averaged over all pairs of a particle species on the given y-z plane along x-axis to obtain a single curve. The red dotted line shows the axial location (x_r) of peak particle dispersion.

where $\delta r(x)$ is the separation between the trajectories of a particle pair at a given time, while $\delta r(x_0)$ depicts the initial separation between neighboring particles. The $\delta r(x)$ is computed from the flow map, $\phi(x, u, t)$, which is a function of particle position, velocity and time instance [234]. The $\phi(x, u, t)$ maps a particle's travel from the initial condition to the final destination after integration along the particle trajectory for a given time duration. Thus, to find $\lambda(x)$ in the streamwise direction, we compute $\delta r(x)$ at each x-location using the separation distance between two particle trajectories in the y-z plane at each x-location. To better understand the evolution of the particle pair separation, in this case, $\delta r(x_0)$ is taken as the separation of the particles at the previous y-z plane. Thus, $\lambda(x)$ provides a local estimation of the particle separation at each x-location. For this analysis, we temporally averaged $\lambda(x)$ of all the pairs of each particle species on a given y-z plane.

The values of $\lambda(x) > 0$ and $\lambda(x) < 0$ exhibit divergence and convergence of inertial particle trajectories, respectively. From this, it can be inferred that the axial location of a positive peak corresponds to the maximum divergence of the particle trajectories, and it depicts the position of the first dominant radial dispersion (x_r) of the particles. This trend can be observed in Figure 5.8, where the peak $\lambda(x)$ is farther downstream with increasing particle size, such that the location of the initial radial dispersion for P1, P2, P3 and P4 are $x_r = 3.3$, 5.5, 6.8 and 7.5, respectively. Here, the $\lambda(x)$ drops after x_r. This is because although particles are spreading, there are still particle pairs that are coming close to each other as they spread radially. Therefore, we see significant fluctuations in the present $\lambda(x)$ curves in Figure 5.8.

Also note that similar to D_2 in Section 5.3.1, $\lambda(x)$ values of these peaks drop from P1 to P4, showing an overall drop in the chaotic dispersion (rise in clustering) of the particles. A similar trend can be seen in the 2D contour of $\lambda(x)$ computed within a thin slice at the center of the domain, as depicted in Figure 5.9. We only show the positive values of FTLE in Figure 5.9 to reduce the noise that manifests from the fact that particles are mainly present at the center of the domain, resulting in fewer particle trajectories, while most of the domain is empty. Moreover, we are only concerned with $\lambda(x) > 0$, which quantifies radial dispersion. The depiction of $\lambda(x) > 0$ can also imply that in a particle pair, one particle is dispersing radially, while the other stays close to the jet center. However, in the present discussion, we use $\lambda(x) > 0$ to represent dispersion because even in this case, at least one particle (of the particle pair) is still dispersing. Albeit the contours in Figure 5.9 only show the central region of the domain, the location of the peak FTLE agrees reasonably well with Figure 5.8.

5.3.3 Local Particle Characteristics

Now that the x_r has been determined, we can characterize the turbulent eddies that exist at these locations. But first, we have to characterize particle parameters at x_r that cause particles to react to the local eddies. The most important of these parameters is the particle

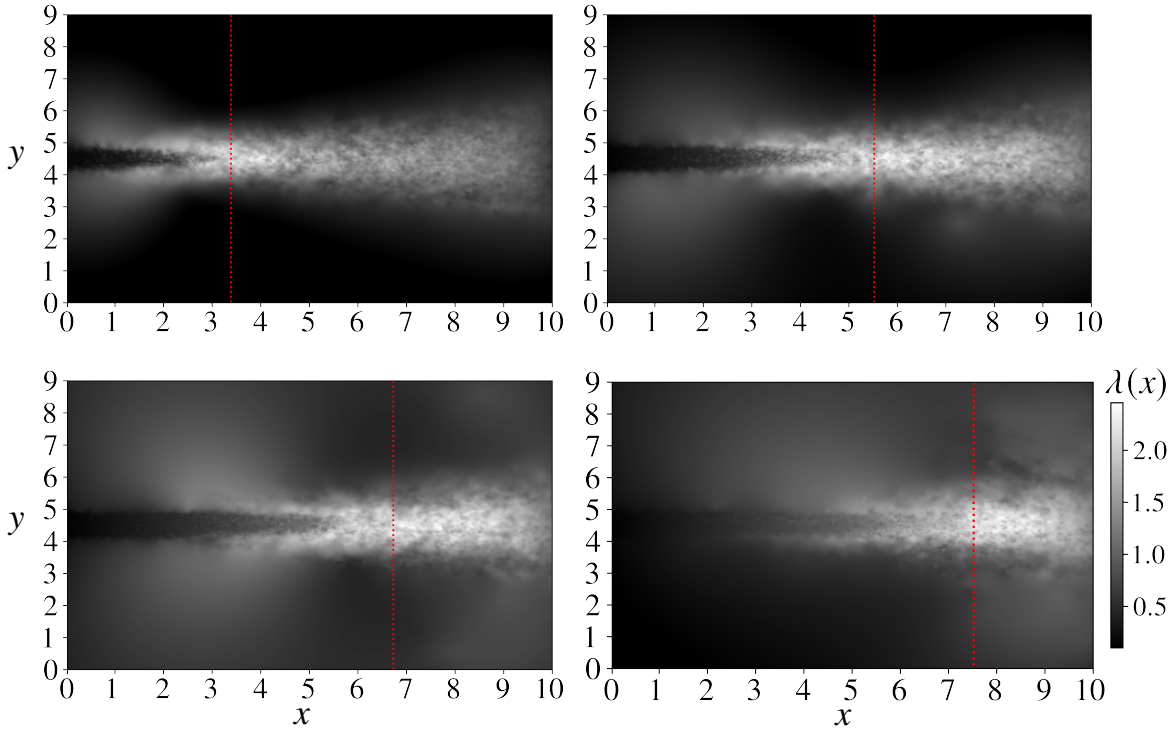


Figure 5.9: Contour of FTLE ($\lambda(x)$) in a thin slice at the center of the domain. Here, only positive (dispersion) values of FTLE are shown. The dotted red color line depicts the x_r of the corresponding particle species.

local Stokes number (St^*). The St^* is computed from the fluid variables at the particle position (x_p) and is defined as:

$$St^* = \frac{\tau_p(x_p)}{\tau_{eddy}} = \frac{\dfrac{\rho_p d_p^2}{18\,\rho_g(x_p)\,\nu_g(x_p)}}{\dfrac{L_{eddy}}{u_{rms}(x_p)}} \tag{5.19}$$

here $\tau_p(x_p)$ is the local inertial timescale of the particles, computed from the local fluid parameters (not the bulk fluid properties), as shown in Equation (5.19). Whereas, τ_{eddy} is the characteristic timescale of the representative eddies at x_p. Note that L_{eddy} is computed

at each grid point along the x-axis using the two-dimensional y-z slice; the details of the computation have been previously discussed in Section 5.3.1. While, $u_{rms}(x_p)$ is the root-mean-square of the local fluid velocity at the particle position (x, y, z). Since St^* is defined with the local fluid parameters, the value of St^* will be different for each particle. To deal with this, we compute the average value of St^* at each y-z plane along the x-direction for each particle species, and then we also temporally averaged St^*.

Starting from the initial local Stokes numbers of 1.5, 2.7, 4.2 and 6.0 for P1 to P4 at the inlet (see Table 5.1), the averaged St^* of each particle species drops to $St^* \approx 0.6$ at x_r, as depicted in Figure 5.7. The decline in St^* is expected as L_{eddy} and the corresponding eddy timescale (τ_{eddy}) increase with the downstream distance. According to Section 5.3.1, L_{eddy} depends on the threshold applied on $\mathcal{Q}$-criterion to determine the dominant vortices. As a result, our St^* is also sensitive to this threshold. This value of $St^* \approx 0.6$ is unexpected because, if $St^* \approx 1.0$ was determined at x_r, particle lateral diffusion could be attributed solely to PC since in this case particle dispersion is characterized by the centrifugal mechanism [57]. This begs the question: is it possible that because particles are in a supersonic flow facing a high drag force in the axial direction, they might experience a delay in responding to the local eddies even when their $St^* \approx 1.0$, and this causes them to disperse at $St^* < 1.0$. This explanation is plausible considering that the particle momentum is mainly in the axial direction as particles are injected at the inlet with random velocity in the x-direction. But then why does their St^* converge to 0.6 at x_r of each particle species, in comparison to any value less than unity?

The above-stated lag in particles' response to the local eddies can be characterized by the evolution of particle axial acceleration ($a_{p,x}$). When particles start traveling radially, their $a_{p,x}$ should drop because their radial velocity starts to grow as the jet spreads, which exerts a radial drag force on the particles. If the downstream location of this peak occurs slightly before x_r then it proves that, based on particle momentum, particles take some time to correlate to the local eddies, and during this time their St^* drops to around 0.6. We can see this in Figure 5.10, where we have marked these downstream peak acceleration values with circular markers. For each particle species, the circular marker is observed

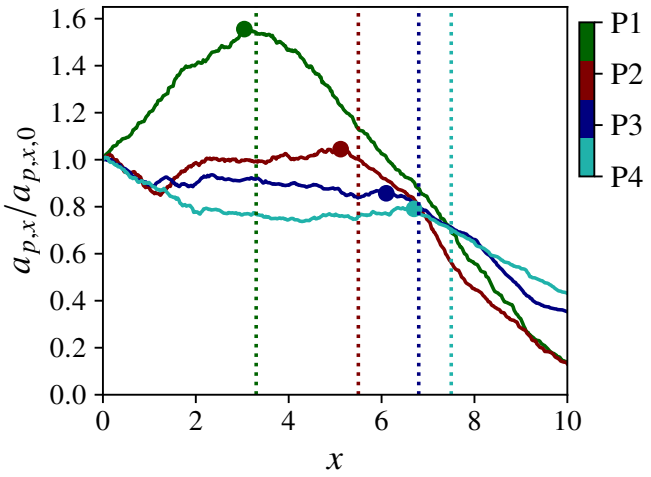


Figure 5.10: Particle axial acceleration ($a_{p,x}$) normalized with the initial value ($a_{p,x,0}$). The dotted lines represent the x_r of the corresponding particle species.

before x_r, and the distance between the downstream $a_{p,x}$ peak and x_r increases with the particle size.

Apart from the above discussion, the acceleration trends in Figure 5.10 also agree with the past literature, where smaller particles initially accelerate rapidly and then experience a sharp drop in acceleration [221]. While larger particles accelerate at a slower rate [216, 235], and their large inertia [236] causes their acceleration to be prolonged. These effects also cause a gradual drop in the acceleration of larger particles as they travel downstream. This is a credible quantitative check, suggesting that our hypothesis regarding the lag experienced by the particles is reasonable.

5.3.4 Local Eddy Characteristics

Due to momentum diffusion, jets spread laterally as they evolve downstream; thus, particles located within the jet will experience a non-zero radial velocity. This results in a radial drag force on the particles, as it impacts the particle-fluid relative velocity ($\boldsymbol{u}_p - \boldsymbol{u}_f(x_p)$).

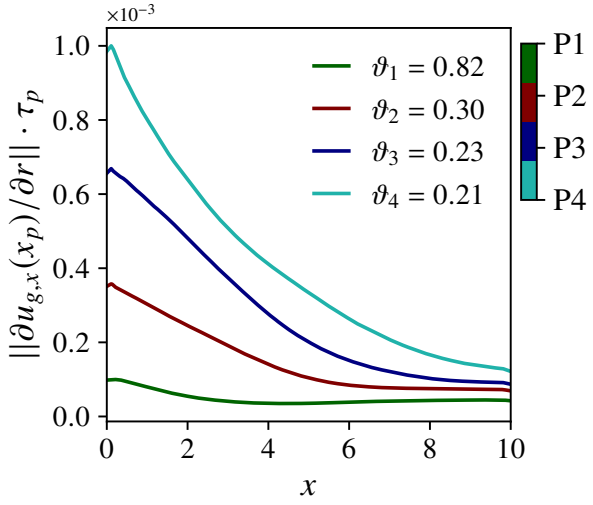


Figure 5.11: Magnitude of the local gas velocity gradient at the particle position in the radial direction, $||\partial u_{g,x}(x_p)/\partial r|| = \sqrt{(\partial u_{g,x}(x_p)/\partial y)^2 + (\partial u_{g,x}(x_p)/\partial z)^2}$, non-dimensionlized with the respective particle aerodynamic timescale (τ_p). Here, $||\cdot||$ represents the magnitude, and ϑ in the legend shows the exponential decay constant of the corresponding particle species.

Additionally, since the maximum jet velocity at any axial location is at the centre of the jet and decreases radially, there exists an axial velocity gradient in the radial direction. In this case, particles tend to migrate towards low shear regions, to sample the zero-acceleration points where the net force on them is zero [47]. By examining the exponential decay constant (ϑ) of this temporally and azimuthally averaged local streamwise gas velocity gradient in the radial direction ($||\partial u_{g,x}(x_p)/\partial r||$), we can estimate how slowly particles respond to this radial push. This is shown in Figure 5.11, where ϑ decreases from P1 to P4. In this case, ϑ is computed by curve fitting the local gas velocity gradient in the radial direction to an exponential decay function. For an arbitrary variable Π, the exponential decay function is $\Pi(x) = \Pi_0\, e^{-\vartheta x}$.

The higher inertia of P4 particles makes them less responsive to this local velocity

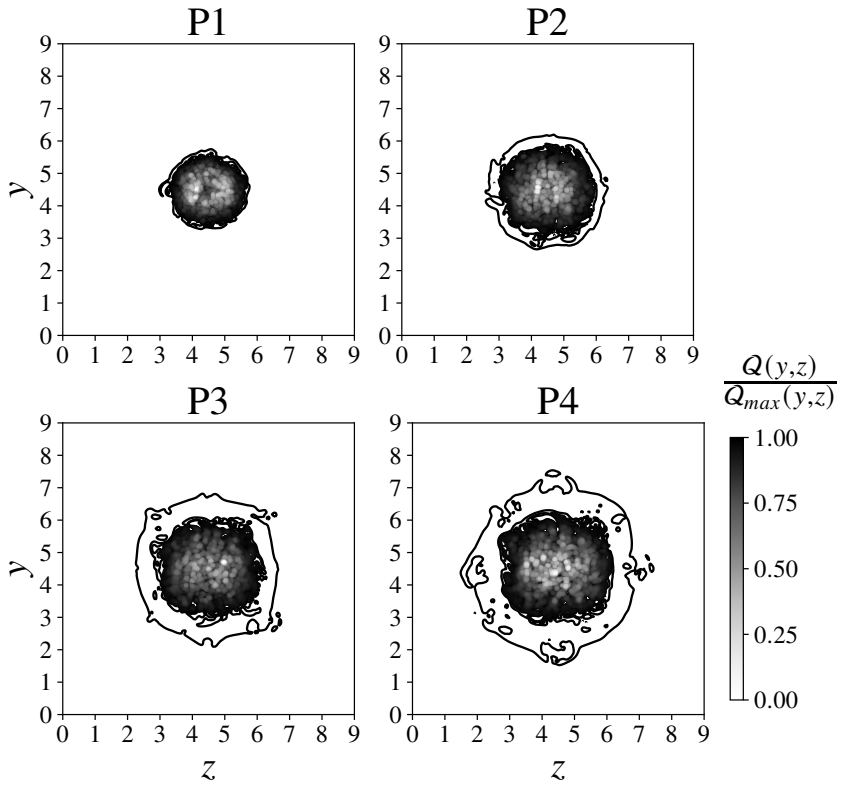


Figure 5.12: Contour of temporally averaged $\mathcal{Q}(y,z)$ on a 2D thin slice in y-z plane at $x_r = 3.3$, 5.5, 6.8 and 7.5 for P1, P2, P3 and P4 particles, respectively. Where, $\mathcal{Q}_{max}(y,z)$ is the maximum value of $\mathcal{Q}(y,z)$ at each x_r plane.

gradient, causing the local velocity gradient to be high and ϑ to be low. Another interesting observation is that each particle curve plateaus roughly around x_r of the corresponding particle. Apart from supporting the x_r determined in Section 5.3.2, ϑ and the location of the plateau of these curves can help predict the transition between the streamwise travel and radial particle dispersion in jet flows. This is because, unlike FTLE, which requires the computation of particle trajectories over time, $||\partial u_g(x_p)/\partial r||$ and ϑ are rather inexpensive and straightforward to compute. Thus, $x_r = x$ such that $d/dx||\partial u_g(x_p)/\partial r||$ approaches zero.

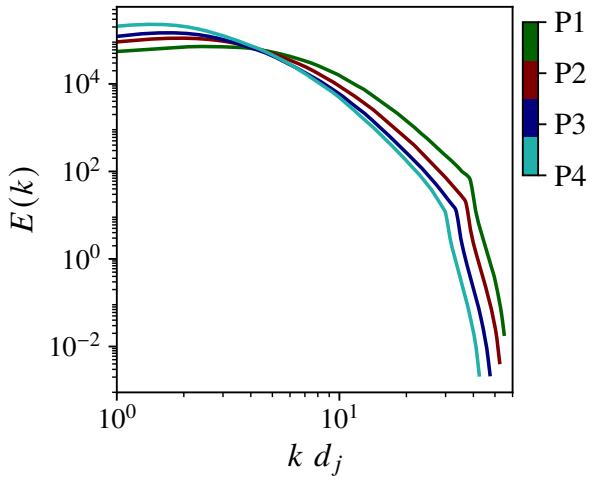


Figure 5.13: Mean 1D energy spectrum computed at the y-z planes at x_r = 3.3, 5.5, 6.8 and 7.5 of the P1, P2, P3 and P4 particles, respectively.

To further understand the local eddy characteristics at x_r of each particle species, we plot the 2D contours of $\mathcal{Q}(y,z)$-criterion at x_r of the considered particle sizes as shown in Figure 5.12. As expected, a noticeable expansion of the jet can be witnessed in this figure from P1 to P4. Due to the shear layer at the outer edge of the jet, the vorticity of the larger eddies away from the jet center is higher, creating a higher radial push on the particles. Hence, it is plausible that the decline in particle St^* and the expansion of $\mathcal{Q}(y,z)$ depicting higher energy eddies at the periphery of the jet creates a correlation between the local eddies and the particles at their corresponding x_r.

We can quantify this rise in the energy of larger eddies with the 1D energy spectrum computed from the two lateral fluctuation velocity components of the fluid at x_r of each particle species on the y-z plane, as depicted in Figure 5.13. It can be observed in this figure that at $x_r = 3.3$ smaller eddies contain higher energy, while at $x_r = 7.5$ larger eddies on the y-z plane possess higher energy. These local eddies at x_r essentially expel particles from the jet via centrifugal force.

Since larger eddies grow downstream, there is a steeper energy change between scales,

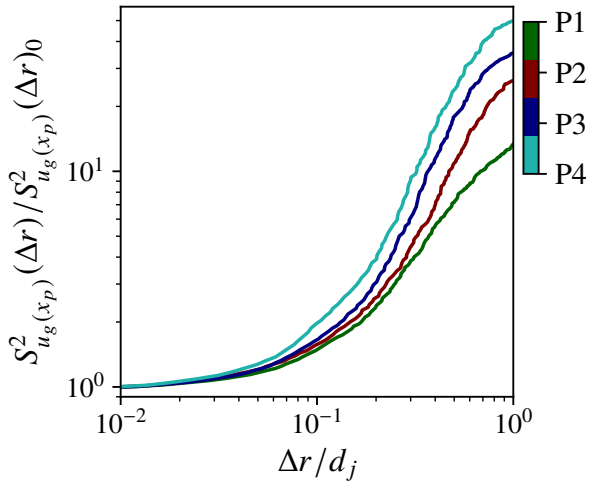


Figure 5.14: Second-order structure function of the local gas velocity ($S^2_{u_g(x_p)}(\Delta r)$) at the particle position, evaluated at the y-z planes at x_r = 3.3, 5.5, 6.8 and 7.5 of the P1, P2, P3 and P4 particles, respectively. The second-order structure function is normalized with its first non-zero value $S^2_{u_g(x_p)}(\Delta r)_0$.

which is crucial for radial particle dispersion. This energy distribution across scales can be assessed with the second-order structure function of local gas velocity ($S^2_{u_g(x_p)}(\Delta r)$), which is the mean square of the velocity difference between two points with a separation distance r. We evaluate $S^2_{u_g(x_p)}(\Delta r)$ at the y-z plane at x_r of each particle species, thus the $S^2_{u_g(x_p)}(\Delta r)$ is mathematically given as:

$$S^2_{u_g(x_p)}(\Delta r) = \overline{(u_g(x_p, r+\Delta r) - u_g(x_p, r))^2}, \quad \text{where} \quad r = \sqrt{y^2+z^2} \tag{5.20}$$

In the above equation, the overline depicts the temporal average. Hence, if $S^2_{u_g(x_p)}(\Delta r)$ is higher, then at the given y-z plane the velocity gradient across particle positions is higher. This will create a higher drag force on the particles in the radial direction. We can witness in Figure 5.14 where the $S^2_{u_g(x_p)}(\Delta r)$ curves increase with particle size, proving that particles are pulled out of the axial motion once they encounter eddies of higher energy. Note that $S^2_{u_g(x_p)}(\Delta r) = 0$ at $r = 0$. Therefore in Figure 5.14, $S^2_{u_g(x_p)}(\Delta r)$ is normalized

with its first non-zero value denoted as $S^2_{u_g(x_p)}(\Delta r)_0$.

5.3.5 Particle-Jet Interaction

Thus far, we have scrutinized the effect of gas on the particles as it directly governs particle dispersion. Now we focus our attention on the modulation of the jet by the inertial particles in the near field. This is crucial as the gas and particles are mutually coupled. Therefore, the local turbulence not only promotes particle dispersion, but the presence of particles also modulates the local eddy structures of the jet.

The local gas velocity experiences the immediate impact of particles, as particles lag behind the gas in the near field due to their inertia. On the one hand, a larger particle momentum means that the particles are less impacted by the smaller-scale turbulence fluctuations. On the other hand, the larger size of the particles promotes the correlation between particle and fluid motion via the increase in drag force on the particles. Note that we increase particle inertia by increasing d_p instead of ρ_p. Of course, the balance of these two effects will govern the particle acceleration as we witnessed in Figure 5.10. In either case, particles will considerably decelerate the local gas. To analyze this, we start by assessing the joint PDF of u_p and $u_g(x_p)$ magnitude over the entire domain, as shown in Figure 5.15. The correlation between u_p and $u_g(x_p)$ is anticipated to drop with the rise in particle size. However, we witness a bimodal distribution in this figure. From P1 to P4, the PDF transition from almost linear growth to where the $u_g(x_p)$ is high while u_p is low. This highlights a significant lag between particle and gas velocities, which is proportional to the drag force on the particle. This enhanced drag force on the larger particles significantly impacts the local gas (recall Equation (5.11)).

To probe the particle-based local modulation of the turbulence, we compute the turbulent kinetic energy (TKE(x_p)) and dissipation rate ($\varepsilon(x_p)$) of the gas at the particle position, defined as:

$$\mathrm{TKE}(x_p) = \frac{1}{2}\overline{u'_{g,i}(x_p) \quad u'_{g,i}(x_p)} \tag{5.21}$$

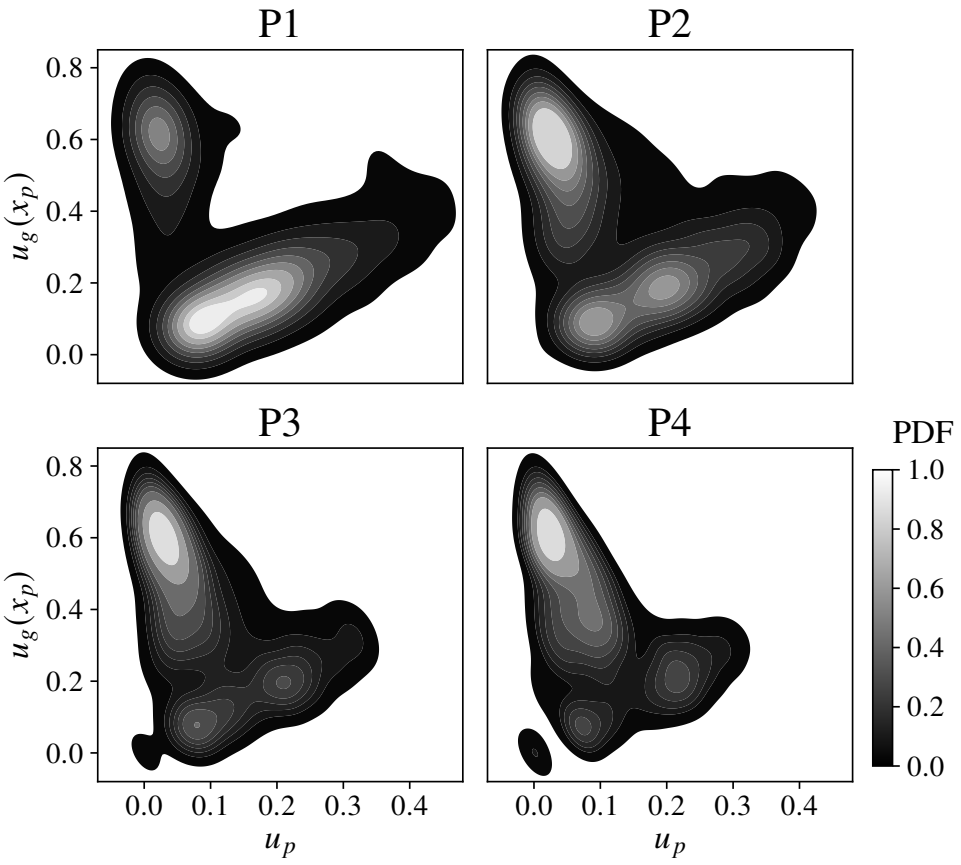


Figure 5.15: Joint PDF of the particle (u_p) and local gas ($u_g(x_p)$) velocities.

$$\varepsilon(x_p) = 2\nu_g(x_p)\overline{\left|\frac{\partial u'_{g,i}(x_p)}{\partial x_k}\ \frac{\partial u'_{g,i}(x_p)}{\partial x_k}\right|} \tag{5.22}$$

where $u'_{g,i} = u_{g,i} - \overline{u_{g,i}}$ in the above equations represent the fluctuating component of the fluid velocity in the i^{th} direction. The averaging, $\overline{u_{g,i}(x,r)}$, is done over time and in the azimuthal direction.

As the joint PDFs indicated (see Figure 5.15), the TKE(x_p) increases with the particle size as shown in Figure 5.16. Note that unlike the overall TKE of the gas in Figure 5.7, TKE(x_p) dwindles downstream. This is reasonable as the slip velocity drops axially, and the back reaction force (producing fluctuations in the local gas velocity) is the only force

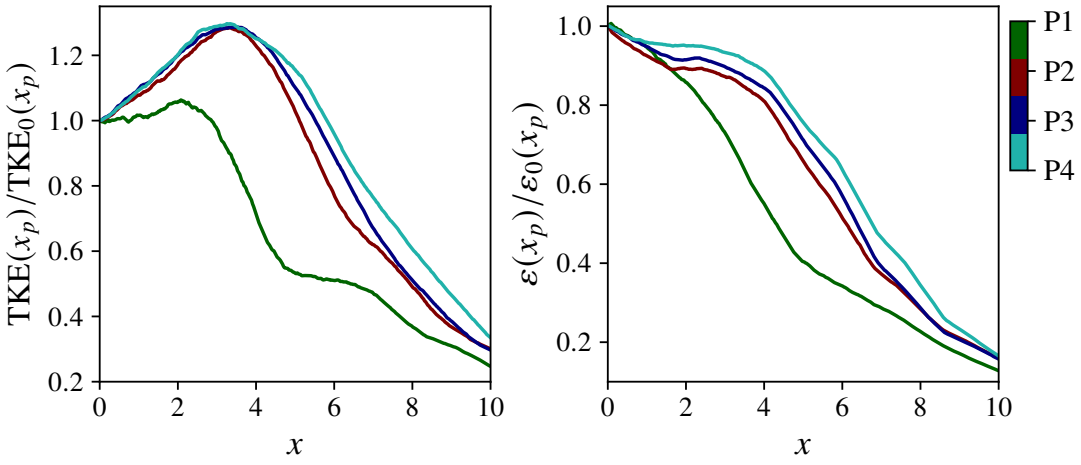


Figure 5.16: Turbulent kinetic energy (TKE(x_p)) and dissipation rate ($\varepsilon(x_p)$) at the location of particles.

particles exert on the local gas, which depends on the particle-gas slip velocity (recall Equation (5.11)). Thus, this drop in fluid-particle slip velocity downstream reduces the fluctuations particles induce in the local fluid velocity field, which results in TKE(x_p) decline in the x-direction. A more plausible explanation for this trend is that as the particles disperse radially downstream, they enter regions with low TKE(x_p). For example, according to Figure 5.4, the flow u_{rms} increases downstream at the centerline, and eventually reaches a maximum value at $x > 6$. On the other hand, the TKE(x_p) reaches its maximum value around $x \approx 4$ and then decreases. Since most particles have started dispersing radially around $x \approx 6$, they are not present in the higher TKE (central) region of the jet. Thus, TKE(x_p) drops downstream. The increase in TKE(x_p) until $x = 4$ can be ascribed to the higher slip velocity and acceleration of particles close to the jet inlet, as they are introduced with a random velocity in the x-direction at the inlet. We see a steeper $\varepsilon(x_p)$ decay after $x = 4$ similar to the TKE(x_p). These trends do not resonate with the classical trends where smaller particles dissipate more energy, while larger particles enhance energy and consequently drop the decay rate of the jet [55]. This is because we are analyzing the local near-field effects on the gas. In the far-field, where gas velocity will experience a

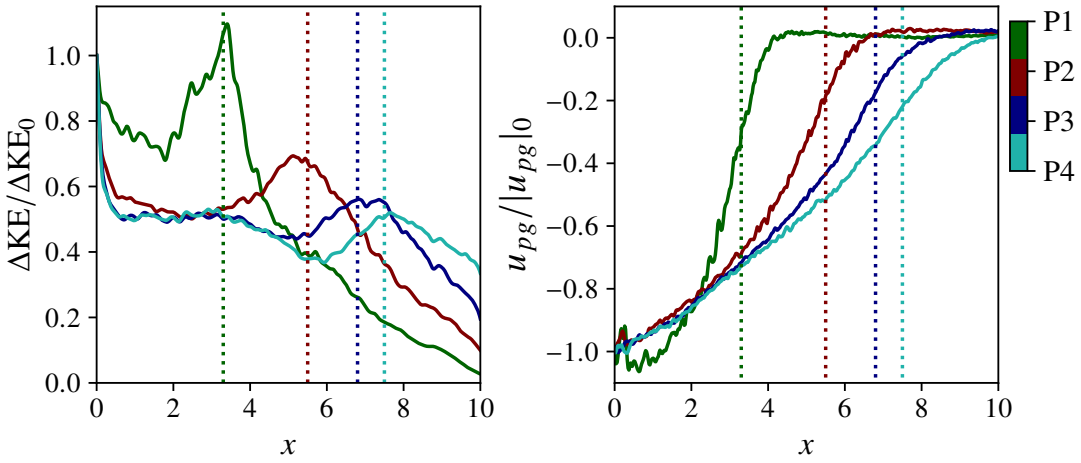


Figure 5.17: Relative kinetic energy of the particles, ΔKE (left), and axial component of particle-gas slip velocity, u_{pg} (right).

significant drop, smaller particles will decelerate with the gas, further taking energy from the flow. But, the larger particles will retain their axial momentum. Therefore, beyond a certain axial position, their velocity will exceed the local gas velocity. In this case, they will start dragging the gas, imparting their kinetic energy onto the gas. Thus, it is clear that close to the inlet, the local turbulence rapidly enhances with particle size in the regime where particles experience higher acceleration via the drag force.

Naturally, we expect that the rise in local turbulent fluctuations in the gas caused by the particles should also influence the particle dynamics. In this case, smaller particles should adapt to these fluctuations more rapidly than their larger counterparts. This can be scrutinized with the particle-gas relative kinetic energy (ΔKE) and slip velocity in the x-direction (u_{pg}), which are defined as:

$$\Delta\mathrm{KE} = \frac{1}{2} m_p \overline{\left(u'_{p,i} - u'_{g,i}(x_p)\right)\left(u'_{p,i} - u'_{g,i}(x_p)\right)} \tag{5.23}$$

$$u_{pg} = \overline{u_{p,x} - u_{g,x}(x_p)} \tag{5.24}$$

These computations are shown in Figure 5.17. The negative sign of u_{pg} suggests that

particles take energy from the local gas in the x-direction and never drag the gas in the considered near-field region, as discussed earlier. We are only showing the axial component of u_{pg} to preserve its sign, while its radial components are negligibly small as compared to the axial component. Note that P1 particles depict the highest slip velocity at $x < 2$. This is because particles are introduced at the jet inlet with a random velocity in the x-direction. This effect rapidly disappears as P1 particles promptly adapt to the local gas velocity, which causes their slip velocity to drop.

Interestingly, the difference in $u'_{p,i}$ and $u'_{g,i}(x_p)$ increases downstream as indicated by ΔKE, while the difference between their mean components drops. Moreover, this increase reaches its peak at x_r. This suggests that, regardless of particle size (in the realm of finite particle inertia), particle velocity fluctuations do not adjust to the local fluctuations and therefore particles are quasi-ballistic to turbulent fluctuations. It is the particle mean velocity component that adapts to the local turbulent fluctuations. Despite the TWC, comparing TKE(x_p) and ΔKE in Figures 5.16 and 5.17, respectively, implies that the effect of the particles on the gas and that of gas on the particles is rather dissimilar. For the present St range, particles mainly alter the fluctuating component of the gas velocity, whereas the gas influences the mean velocity component of the particles. Since the fluid-particle interaction is a function of St [237], this effect should be tested on a broader range of St. It should be noted that we are referring to the dominant effect here. Of course, in a holistic view, both velocity components experience changes. The peak ΔKE at x_r is due to the rise in energy of the local eddies which pushes particles out of the jet's central region. Once outside this region, ΔKE drops because the local velocity fluctuations dwindle rapidly.

The smaller particles are more responsive to the local eddies [46], which promotes the gas-particle momentum exchange. The overall slip velocity in Figure 5.17 demonstrates this trend. Furthermore, since the average particle velocity in the domain is inherently slow in responding to the local changes, we see that the inflection point of u_{pg} occurs after the x_r plane, unlike ΔKE. These two tendencies affirm the validity of our previous observations.

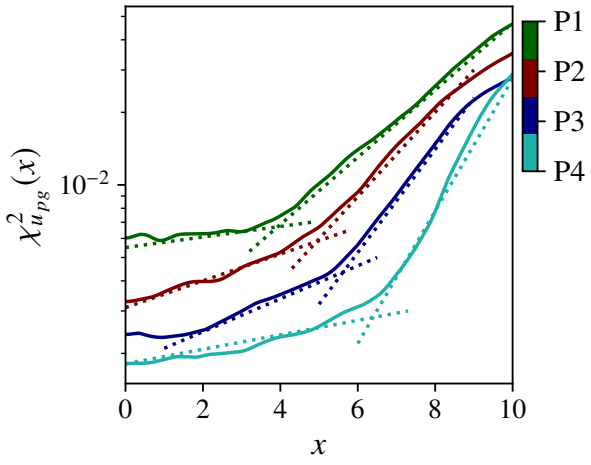


Figure 5.18: Second-order neighboring particle slip velocity function ($\chi^2_{u_{pg}}(x)$). The dotted lines on the plot show the slope.

The fluid-particle slip velocity can further validate the x_r of each particle species. For this purpose, we define a second-order neighboring particle slip velocity function ($\chi^2_{u_{pg}}(x)$), which is given as:

$$\chi^2_{u_{pg}}(x) = \overline{(u_{pg}(x+\varsigma) - u_{pg}(x))^2} \tag{5.25}$$

here ς represents the streamwise separation between two neighboring particles. Note that the streamwise separation distance varies between particle pairs, as inter-particle distance can differ at each instance and based on particle location. By averaging the slip velocity difference between neighboring particles at each streamwise location, the relative change in slip velocity at each streamwise location in the jet is determined. The resulting $\chi^2_{u_{pg}}(x)$ is shown in Figure 5.18, which depicts that the correlation of u_{pg} increases with the particle size. This is expected because larger particles retain their inertia for longer and in the near-field region, gas velocity is still very high. The interesting aspect is that starting from $x = 0$, each curve starts with a shallower slope, and then, at a certain x, its slope becomes steeper. This shallower slope is also longer for larger particles. The change in slope of these curves occurs close to the x_r of the corresponding particles. This analysis reinforces

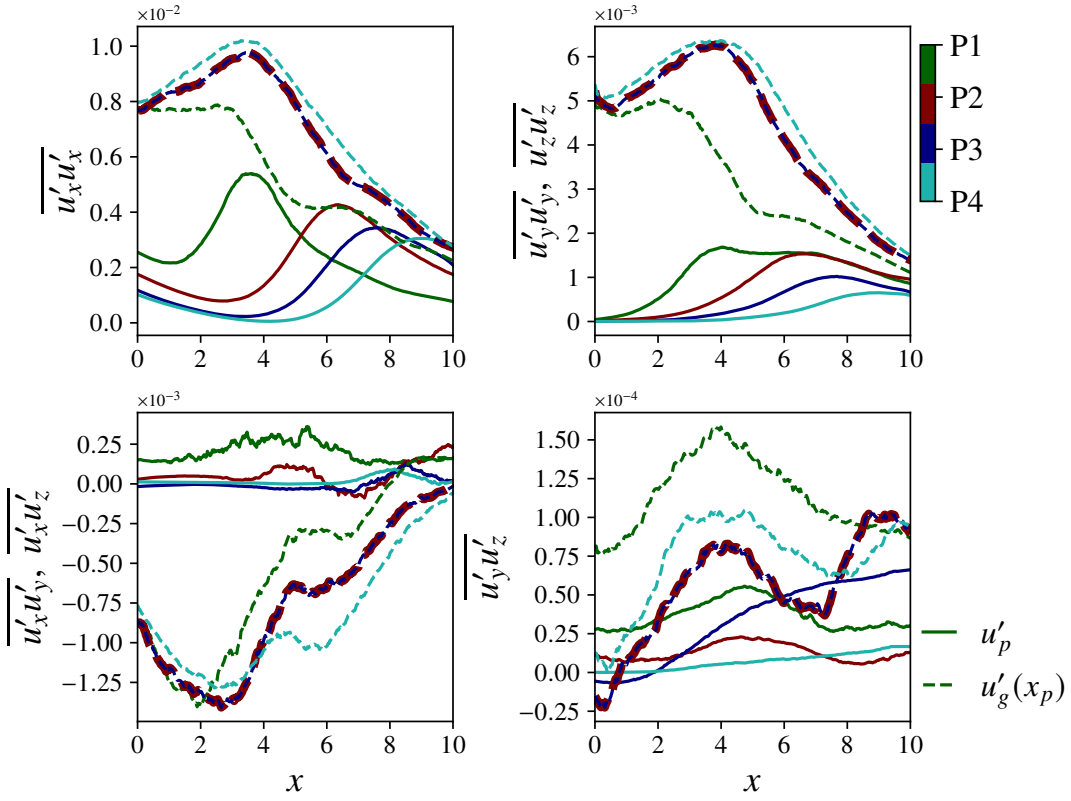


Figure 5.19: Comparison of the averaged product of particle fluctuating velocity components and mean Reynolds stresses ($\overline{u'_i u'_j}$) local gas velocity fluctuations ($u'_p(x_p)$). Note that due to the symmetry of the jet, $\overline{u'_y u'_y} \approx \overline{u'_z u'_z}$ and $\overline{u'_x u'_y} \approx \overline{u'_x u'_z}$. Therefore, we have only shown $\overline{u'_y u'_y}$ (top-right) and $\overline{u'_x u'_y}$ (bottom-left) curves in this plot.

the credibility of x_r.

The pressing question at this point is, how do turbulent fluctuations of the local gas and particle velocity fluctuations in the axial and radial directions correlate? The correlation between particle and gas velocity fluctuations can be probed with the local gas mean Reynolds stress ($\overline{u'_i u'_j}$) and the averaged product of particle velocity fluctuations. We acknowledge that for particles, $\overline{u'_i u'_j}$ represents the correlation between particle fluctuating velocity components and cannot be called Reynolds stress. Here, $\overline{u'_i u'_j}$ explains the momen-

tum transport of the gas and particles due to the local eddies. The normal stresses ($\overline{u_i' u_i'}$) for both gas and particles should be positively correlated as the main thrust of the flow is in the x-direction. Additionally, the jet is spreading laterally downstream, and particles are shadowing the gas with respect to their inertia. The top two plots of Figure 5.19 illustrate this trend in the normal stress components. Here, particle fluctuations do not increase to the same level as the gas fluctuations, similar to the trend observed in Figure 5.17, but they do show a tendency to escalate akin to the gas fluctuations. We also see this trend in $\overline{u_y' u_z'}$ (lateral components), where particle velocity fluctuations try to match the fluctuations in the gas velocity, albeit much more slowly as particle axial inertia does not prefer the radial momentum transfer. It should be noted that the axial location of peak values of particle $\overline{u_y' u_y'}$ and $\overline{u_z' u_z'}$ correlates well with x_r, which implies higher transport of particles in the radial direction around x_r. This validates the robustness of x_r for predicting particle radial dispersion in a jet.

In terms of the momentum transfer between the axial and lateral components ($\overline{u_x' u_y'}$ and $\overline{u_x' u_z'}$), the downstream radial expansion of gas implies negative Reynolds stress, suggesting the growth in lateral fluctuations, as depicted in Figure 5.19. However, particle axial to radial momentum transfer via velocity fluctuations should be minimal compared to the gas because of particle inertia in the axial direction. This momentum transfer should further drop with the increase in particle size, as shown in Figure 5.19. These two phenomena are intuitive, but the compelling observation is that particles are almost entirely ballistic to the axial to lateral velocity fluctuations of the local gas. This disconnect between the gas Reynolds stresses and particle velocity fluctuations signifies that particle radial momentum is exclusively generated by the lateral combination of the gas velocity fluctuations. Thus, a turbulent eddy must align in a specific manner to exert centrifugal force dominantly in the radial direction for particles to be pulled out of the central region of the jet.

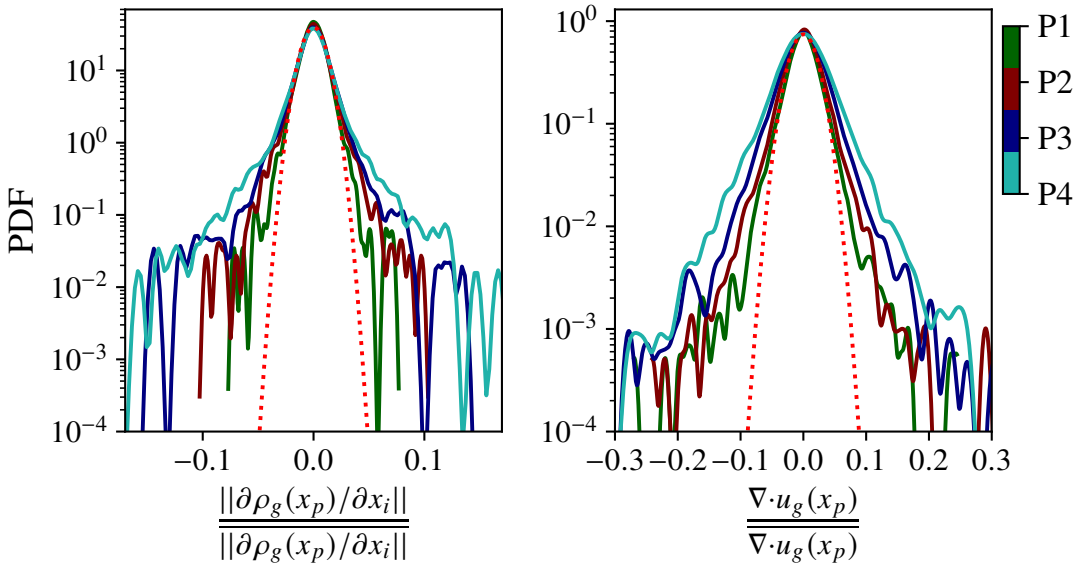


Figure 5.20: PDF of the magnitude of gas density gradient (left) and dilatation (right) computed at the position of particles. We preserved the sign of each component before taking the magnitude and multiplied these signs to the final magnitude value, which gave us a negative sign for the magnitude. The dotted red line presents the Gaussian curve.

5.3.6 Effect of Compressibility on Dispersion

In a supersonic flow, the compressibility effects also govern the dispersion of particles [204]. To assess the effect of compressibility on particle transport, we evaluate the magnitude of local density gradient and divergence of the gas velocity ($u_g(x_p)$) at the location of particles (dilatation of the local fluid). Due to their higher inertia, larger particles are unaffected by small variations in density. We see this trend in Figure 5.20, where smaller particles prefer regions with the probability of minimal density change, while larger particles favor regions with high spatial change in fluid density. Note that we also have negative values for our magnitude. This is because we preserved the sign of each component by multiplying it with the magnitude value. In this figure, the regions with negative density gradients also have significant dilatation. Hence, large particles accumulate in areas with a higher

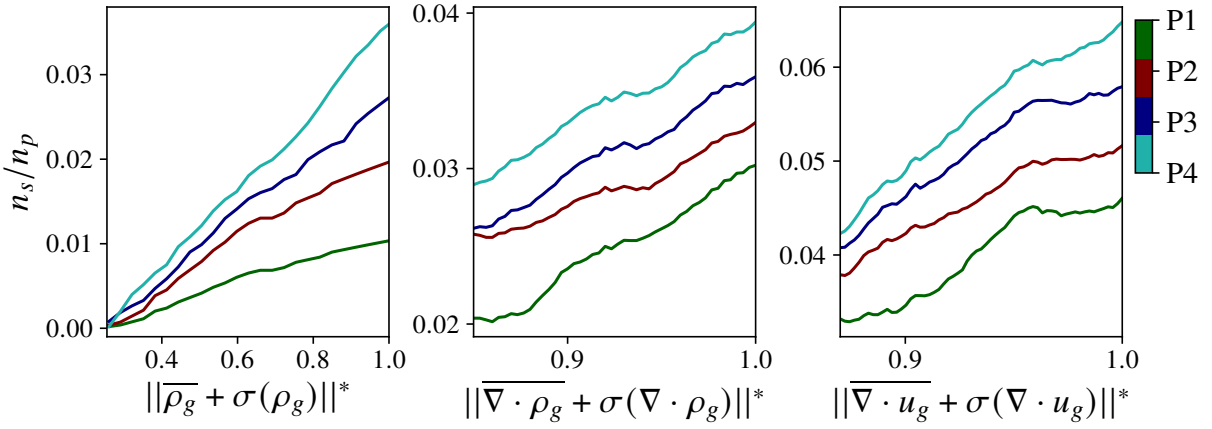


Figure 5.21: Number of particles (n_s) normalized with the total number of particles of a given species (n_p) in the entire domain, sampled in the regions where $\rho_g(x_p) > ||\rho_g + \sigma(\rho_g)||^*$ (left), $\nabla \cdot \rho_g(x_p) > ||\nabla \cdot \rho_g + \sigma(\nabla \cdot \rho_g)||^*$ (middle), $\nabla \cdot u_g(x_p) > ||\nabla \cdot u_g + \sigma(\nabla \cdot u_g)||^*$ (right). Here, σ is the standard deviation and the superscript $*$ represents that the curves are normalized with their maximum value.

probability of dilatation as shown in Figure 5.20. This is potentially because the regions with strong dilatation have low vorticity, where particles tend to cluster due to PC. In other words, strong dilatation corresponds to stagnation points in the flow, where particles form clusters as the net force on them at these locations is zero [47].

Next, we quantify the number of particles of each species (n_s) present in regions with density ($\rho_g(x_p) > ||\overline{\rho_g} + \sigma(\rho_g)||^*$, here the superscript $*$ depicts that the curve is normalised with its maximum value), density gradient ($\nabla \cdot \rho_g(x_p) > ||\overline{\nabla \cdot \rho_g} + \sigma(\nabla \cdot \rho_g)||^*$) and dilatation ($\nabla \cdot u_g(x_p) > ||\overline{\nabla \cdot u_g} + \sigma(\nabla \cdot u_g)||^*$) greater than spatial mean plus one standard deviation (σ). The resulting number of particles in the regions that fulfill these conditions is presented in Figure 5.21. Firstly, following the trends in literature, qualitatively larger particles reside in regions with elevated gas density [203, 238]. The surprising aspect here is that n_s of larger particles rises steeply as $||\overline{\rho_g} + \sigma(\rho_g)||^*$ increases, compared to the smaller particles. This is tied to the affinity of larger particles towards a higher density gradient (see Figure 5.21).

Particles should naturally move to the location of the lower gradient. However, larger particles are slow in responding to the changes in the flow due to their higher inertia. On the other hand, smaller particles rapidly adapt to the variations in the flow and move to the low-density gradient and dilatation areas. Thus, larger particles reside in high-density gradient and dilatation regions. Note that regions with higher dilatation also exhibit low vorticity. Thus, larger particles inherently settle in the regions with high dilatation.

5.4 Discussion

In the present study, we introduced a new parameter x_r which defines the axial position where particles of a certain size/inertia first transition from dominantly axial to radial travel. This is a critical concept for advanced engineering applications. For example, in cold spray advanced manufacturing methods, particles are coated on a surface using their kinetic energy [11]. In this application, typically, an overexpanded jet is employed as it results in higher particle impact velocity as compared to the underexpanded jets [239]. In both over- and underexpanded jets, particles encounter a shock that can considerably slow down particles. In the present case, we simulated a shock-free supersonic jet flow. This will affect particle kinematic properties in the cold spray applications, however, the overall particle dynamics reported in this study are directly applicable to the cold spray techniques. For example, in cold spray manufacturing, larger particles ($d_p > 20\mu m$ according to Li et al. [239]) are guaranteed to impact the substrate due to their ability to travel along the jet centerline. While smaller particles have a higher impact velocity as they can be more readily accelerated by the gas, the trajectories of these particles are prone to deflect from the centerline. Thus, a fine balance is required such that particles carry a higher impact velocity and stay within the jet. Here, x_r can considerably aid in selecting the right particle parameters for the cold spray application.

Moreover, in cold spray methods, it has been reported that the coating efficiency increases as the *stand-off* distance between the nozzle and substrate is raised from the nozzle

exit until an optimal point is reached, after which it starts decreasing [240]. But there is no consensus on what the exact stand-off distance should be, due to the lack of sufficient studies [100]. If the *stand-off* is greater than x_r, particles will start spreading radially. This will drastically drop their axial kinetic energy, and consequently, the overall coating efficiency. With x_r we contribute another critical parameter that can considerably aid in deciding this distance for efficiently coating particles of different materials. By keeping the stand-off distance smaller than x_r, we can ensure that the particles stay within the jet, resulting in a superior particle coating.

Contrarily, there is an effort to use nanothermite particles as propellant [241]. In this case, the exhaust from satellite thrusters can have solid particles, which can be detrimental to the launch facility at the time of lift-off. Since particles retain their inertia, the energetic particles can impinge on the ground structures, which will result in frequent maintenance. This problem can be partially alleviated if we diminish the kinetic energy of the particles. Hence, the distance between the thruster's exhaust and the launch pad can be kept greater than x_r, which will spread out the particles and considerably reduce the impinging velocity of the particles. We have reported an inexpensive method for determining x_r using particle and local fluid parameters, which can profoundly benefit such applications.

5.5 Summary

We conducted DNS to analyze the dispersion characteristics of four particle sizes in a perfectly expanded supersonic jet flow ($Ma = 1.5$). For this purpose, particles were modeled with the Lagrangian point-particle scheme, and gas was modeled with the Eulerian method. The gas-particle interaction was simulated with two-way momentum and energy coupling, with only the drag force acting on the particles (inter-particle collisions and gravitational force were excluded). Our simulation consisted of three sub-simulations: HIT development, jet stabilization, and particle-laden jet simulations. We found that based on particle inertia and the local fluid parameters, there is a clear axial location where particles start

dispersing radially. The St^* defined with the local turbulent length scale for all particle species converged to 0.6 at x_r. This is because, due to axial momentum, particles experience a delay in responding to the local turbulent eddies, exerting a radial push on the particles. Therefore, dropping from a higher St^*, by the time particles start reacting to the local eddies to travel radially, their $St^* \approx 0.6$.

Scrutinizing the eddy structures at x_r, it was found that particle velocity fluctuations do not adapt to the local fluid velocity fluctuations. The fluid velocity fluctuations mainly affect the mean velocity component of the particles. This effect, however, is opposite to the influence of particles on the fluid. Additionally, particles shadow the normal Reynolds stresses of the flow. However, they do not follow the axial to radial stress components of the fluid. This suggests that for particles to be centrifuged out of the jet, turbulent eddies must align in such a way that they primarily exert a force in the radial direction.

Characterizing particles with the local gas density gradient and dilatation implied that in a supersonic jet, smaller particles collect in low-density regions while large particles reside in higher-density zones. The slower response of larger particles to the local changes in the flow causes them to stay in the high-density gradient and dilatation regions. Moreover, since high dilatation regions also possess low vorticity, larger particles naturally tend to collect in these regions.

In this analysis, particle radial dispersion is scrutinized at only one Mach number ($Ma = 1.5$), Reynolds number ($Re = 500$), and a specific range of particle inlet Stokes number ($St = 1.5$ to 6.0). For these parameters, the reported particle dispersion mechanism holds well. However, the present results and the underlying local particle dispersion mechanism should be tested on a broader range of Ma, Re, St, and operating conditions to test its general validity.

Chapter 6

Conclusions

In this research, the dispersion characteristics of inertial particles were studied in HIT, sub- and supersonic jet flows, using DNS. In the HIT and subsonic jet flow, the role of the rise in temperature-driven local gas viscosity on particle clustering was investigated (Chapters 2-4). While in supersonic jet flow, the mechanism of particle radial dispersion based on the local large eddy structures was studied (Chapter 5).

In past literature, particle clustering has been predominantly treated as a particle and fluid dynamics problem, even in thermal applications. Consequently, since the introduction of particle Stokes number (St) in 1985, higher particle clustering is understood to arise at $St \approx 1$. In many engineering applications considering a dispersed phase in a gaseous fluid, it is assumed that if the particle-to-fluid density ratio is much greater than unity, only the drag force acts on the particles. However, temperature-based variation in the local fluid viscosity is often neglected, despite its direct effect on the drag force. Therefore, in the first analysis of this thesis, the local viscosity-driven clustering of heated inertial particles was studied in decaying HIT, using a triply periodic DNS box (Chapter 2). Here, a novel particle clustering mechanism was discovered, called VC. In VC, a preformed particle cluster rapidly heats the gas in its immediate vicinity upon particle heating, thus enveloping itself in a viscous cloud as gas viscosity increases with temperature. By offering

a higher drag force to these clustered particles, this viscous cloud keeps particles clustered and captures more particles in the flow. As a result, heated particles not only depict higher clustering, but this enhanced clustering is observed at $St < 1$.

After proving that particle clustering can be enhanced through temperature-dependent viscous effects, efforts were made to understand the specific conditions that enhance VC. To this end, some simplifying assumptions made in Chapter 2, such as the reaction drag force of particles on the fluid, were removed. This is because the momentum TWC is known to considerably attenuate turbulence, which can concomitantly diminish VC. Thus, in this analysis, three different particle-loading densities were analyzed, which outlined two fundamental prerequisites for VC to take effect:

- Prior to particle heating, particles should already be in a clustered formation.
- These particle clusters should be large in size and unevenly distributed in space.

These two conditions can be fulfilled by having a higher loading density of the inertial particles in the flow. It was determined that regardless of turbulence attenuation by particles and particles' ability to diminish VC via their reaction drag force, if these two conditions are satisfied, VC will take effect and heated particles will depict higher clustering even at $St < 1$. Note that VC is valid if particles are uniformly heated, such that particles at the outer periphery of a cluster and particles within a cluster receive an equal amount of heat.

Until now, VC has been tested in two independent studies using decaying HIT (Chapters 2-3). However, in a triply periodic DNS box, particles and fluid exiting from one boundary are reinjected into the domain from the opposite boundary. Consequently, particles that appear to be going away are essentially coming close to each other after reinjection. Similarly, the triple-periodicity imposes a constant mass in the domain, thus increasing the average pressure with particle heating. This is not a realistic depiction of spatially evolving particle-laden flows. To this end, the clustering of heated particles in a subsonic jet flow was modeled (Chapter 4). Despite only a 16% rise in the local gas viscosity compared to

the 60% rise in decaying HIT simulations, particle heating increased the viscosity of the entire central region of the jet. This caused particles to stay within this region of the jet. The particles that attempted to disperse radially started clustering at the outer edge of the jet, where sharp temperature/viscosity gradients (*thermal front*) exist. Unable to leave the jet, these particles faced identical turbulent eddies, which caused them to cluster at similar locations. Hence, the introduction of particles within the jet core at the inlet satisfied the prerequisites of the VC, and therefore even a moderate rise in gas viscosity spatially restrained particles due to VC. These findings can pave the way for modulating particle dispersion in advanced engineering applications such as target drug delivery, particle-based erosion and deposition in pipes, volcanic eruption and ash dispersion, aggregation of water droplets in clouds leading to precipitation, dispersion of pollutants, transmission of airborne diseases, and advanced ventilation systems, among others.

In supersonic particle-laden flows employed in cold spray advanced manufacturing techniques and metallurgy, it is the local fluid dilatation and compressibility that governs particle dispersion instead of the local fluid viscosity. This is discussed in Chapter 5, where larger particles were found to collect in high-density gradient and dilatation regions. The local mechanisms that cause particles to disperse radially in a Mach $Ma = 1.5$ jet were also investigated. It is determined that the axial location (x_r) where particles first develop a dominant radial velocity component is characterized by a local Stokes number $St^* \approx 0.6$. The slow response of inertial particles to the supersonic flow resulted in their local Stokes number (St^*) dropping below unity before they started dispersing radially. A new metric has been proposed to estimate x_r for particles of different sizes/inertia. Estimating x_r can greatly benefit cold spray technologies, where the effort is to keep the particles within the jet. This can be ensured by keeping the standoff distance between the nozzle exit and substrate less than x_r for a given particle species.

6.1 Future Recommendations

For future research in the domain of heated particle dispersion in turbulent flows, the following research trajectories are proposed:

- In the case of VC, particles were found to depict significant clustering at $St < 1$. This is against the conventional observation where particles depict maximum clustering at $St \approx 1$. Therefore, a robust prediction model is required to estimate particle clustering in turbulence for thermal applications.
- Inter-particle collisions were neglected in this thesis with the assumption that the particle loading density is low enough that particle-particle interactions are trivial. However, VC should be tested with momentum FWC where particles can interact, further aiding its applicability in real scenarios. Moreover, particle clustering brings particles closer and can considerably raise local particle concentration, which enables inter-particle collisions.
- In jet flow simulations, particle dispersion has been tested in the near-field region of the jet. But VC for enhanced clustering and local particle dispersion mechanism should be scrutinized in the far-field of the jet. Likewise, these mechanisms should also be probed in higher Reynolds and Mach number unconfined jets.
- The validity of x_r and St^* should be assessed for a broader range of particle sizes, densities, Reynolds numbers, and St. Moreover, these particle dispersion mechanisms should also be experimentally assessed for practical applications.
- In this study, the local mechanism of particle dispersion was scrutinized in a shock-free jet. Thus, x_r and the particle dispersion mechanisms should be tested in the presence of a shock, in a non-perfectly expanded jet. Additionally, if the fluid-particle slip velocity is high enough, a shock can also form at the particle surface; particle dispersion mechanisms should also be studied in the presence of such shocks, using particle-resolved DNS.

References

[1] H. J. Hussein, S. P. Capp, and W. K. George. Velocity measurements in a high-reynolds-number, momentum-conserving, axisymmetric, turbulent jet. *Journal of Fluid Mechanics*, 258:31–75, 1994.

[2] T. R. Troutt and D. K. McLaughlin. Experiments on the flow and acoustic properties of a moderate-reynolds-number supersonic jet. *Journal of Fluid Mechanics*, 116:123–156, 1982.

[3] S. B. Pope. *Turbulent flows*. Cambridge University Press, 2000.

[4] S. Elghobashi. On predicting particle-laden turbulent flows. *Applied scientific research*, 52:309–329, 1994.

[5] M. Wilkinson, B. Mehlig, and V. Uski. Stokes trapping and planet formation. *The Astrophysical Journal Supplement Series*, 176(2):484, 2008.

[6] A. V. Kolesnichenko. Modeling of the processes of formation of dust fractal clusters in a protoplanetary cloud. *Solar System Research*, 57(7):748–766, 2023.

[7] A. B. Kostinski and R. A. Shaw. Scale-dependent droplet clustering in turbulent clouds. *Journal of Fluid Mechanics*, 434:389–398, 2001.

[8] B. J. Devenish, P. Bartello, J. L. Brenguier, L. R. Collins, W. W. Grabowski, R. H. A. IJzermans, S. P. Malinowski, M. W. Reeks, J. C. Vassilicos, L. P. Wang, et al. Droplet

growth in warm turbulent clouds. *Quarterly Journal of the Royal Meteorological Society*, 138(667):1401–1429, 2012.

[9] S. J. Apperson, A. V. Bezmelnitsyn, R. Thiruvengadathan, K. Gangopadhyay, S. Gangopadhyay, W. A. Balas, P. E. Anderson, and S. M. Nicolich. Characterization of nanothermite material for solid-fuel microthruster applications. *Journal of Propulsion and Power*, 25(5):1086–1091, 2009.

[10] M. Hobosyan, S. E. Lyshevski, and K. S. Martirosyan. Integrated micropropulsion systems with nanoenergetic propellants. In *Nanomaterials in Rocket Propulsion Systems*, pages 403–420. 2019.

[11] A. P. Alkhimov, A. N. Papyrin, V. F. Kosarev, N. I. Nesterovich, and M. M. Shushpanov. Gas-dynamic spraying method for applying a coating, April 12 1994. US Patent 5,302,414.

[12] Z. Zhang and C. Kleinstreuer. Transient airflow structures and particle transport in a sequentially branching lung airway model. *Physics of Fluids*, 14(2):862–880, 2002.

[13] A. Arora, I. Hakim, J. Baxter, R. Rathnasingham, R. Srinivasan, D. A. Fletcher, and S. Mitragotri. Needle-free delivery of macromolecules across the skin by nanoliter-volume pulsed microjets. *Proceedings of the National Academy of Sciences*, 104(11):4255–4260, 2007.

[14] A. Farnoud, H. Tofighian, I. Baumann, G. J. M. Garcia, O. Schmid, E. Gutheil, and M. M. Rashidi. Large eddy simulations of airflow and particle deposition in pulsating bi-directional nasal drug delivery. *Physics of Fluids*, 32(10), 2020.

[15] G. Wei, R. Zhu, S. Yang, S. Hu, L. Yang, and F. Chen. Carbon powder mixed injection with a shrouding supersonic oxygen jet in electric arc furnace steelmaking. *Metallurgical and Materials Transactions B*, 51:2298–2308, 2020.

[16] E. R. F. De Sarabia, J. A. Gallego-Juárez, G. Rodríguez-Corral, L. Elvira-Segura, and I. González-Gómez. Application of high-power ultrasound to enhance fluid/solid particle separation processes. *Ultrasonics*, 38(1-8):642–646, 2000.

[17] E. Riera, J. A. Gallego-Juárez, and T. J. Mason. Airborne ultrasound for the precipitation of smokes and powders and the destruction of foams. *Ultrasonics Sonochemistry*, 13(2):107–116, 2006.

[18] M. M. Rahman, A. Saieed, M. F. Khan, and J.-P. Hickey. Group combustion of dispersed spherical core–shell nanothermite particles. *Thermo*, 2(3):209–231, 2022.

[19] H. Pouransari and A. Mani. Effects of preferential concentration on heat transfer in particle-based solar receivers. *Journal of Solar Energy Engineering*, 139(2), 2017.

[20] C. T. Crowe, R. A. Gore, and T. R. Troutt. Particle dispersion by coherent structures in free shear flows. *Particulate Science and Technology*, 3(3-4):149–158, 1985.

[21] H. Pouransari, H. Kolla, J. H. Chen, and A. Mani. Spectral analysis of energy transfer in turbulent flows laden with heated particles. *Journal of Fluid Mechanics*, 813:1156, 2017.

[22] H. Pouransari and A. Mani. Particle-to-fluid heat transfer in particle-laden turbulence. *Physical Review Fluids*, 3(7):074304, 2018.

[23] S. Balachandar and J. K. Eaton. Turbulent dispersed multiphase flow. *Annual Review of Fluid Mechanics*, 42:111–133, 2010.

[24] L. Brandt and F. Coletti. Particle-laden turbulence: progress and perspectives. *Annual Review of Fluid Mechanics*, 54(1):159–189, 2022.

[25] S Elghobashi. Particle-laden turbulent flows: direct simulation and closure models. *Applied Scientific Research*, 48:301–314, 1991.

[26] R. Letournel, F. Laurent, M. Massot, and A. Vié. Modulation of homogeneous and isotropic turbulence by sub-kolmogorov particles: Impact of particle field heterogeneity. *International Journal of Multiphase Flow*, 125:103233, 2020.

[27] R. Hassaini and F. Coletti. Scale-to-scale turbulence modification by small settling particles. *Journal of Fluid Mechanics*, 949:A30, 2022.

[28] M. Boivin, O. Simonin, and K. D. Squires. Direct numerical simulation of turbulence modulation by particles in isotropic turbulence. *Journal of Fluid Mechanics*, 375:235–263, 1998.

[29] A. D. Paris. *Turbulence attenuation in a particle-laden channel flow*. Stanford University, 2001.

[30] G. Mallouppas, W. K. George, and B. G. M. van Wachem. Dissipation and inter-scale transfer in fully coupled particle and fluid motions in homogeneous isotropic forced turbulence. *International Journal of Heat and Fluid Flow*, 67:74–85, 2017.

[31] F. E. Marble. Dynamics of dusty gases. *Annual Review of Fluid Mechanics*, 2(1):397–446, 1970.

[32] Y. Pan and S. Banerjee. Numerical investigation of the effects of large particles on wall-turbulence. *Physics of Fluids*, 9(12):3786–3807, 1997.

[33] T. M. Burton and J. K. Eaton. Fully resolved simulations of particle-turbulence interaction. *Journal of Fluid Mechanics*, 545:67–111, 2005.

[34] S. E. Elghobashi and T. W. Abou-Arab. A two-equation turbulence model for two-phase flows. *The Physics of Fluids*, 26(4):931–938, 1983.

[35] O. A. Druzhinin and S. Elghobashi. Direct numerical simulations of bubble-laden turbulent flows using the two-fluid formulation. *Physics of Fluids*, 10(3):685–697, 1998.

[36] J. Ferry and S. Balachandar. A fast eulerian method for disperse two-phase flow. *International Journal of Multiphase Flow*, 27(7):1199–1226, 2001.

[37] R. W. Hockney and J. W. Eastwood. *Computer simulation using particles*. crc Press, 2021.

[38] N. Y. Gnedin, S. C. Glover, R. S. Klessen, V. Springel, and V. Springel. High performance computing and numerical modelling. *Star Formation in Galaxy Evolution: Connecting Numerical Models to Reality: Saas-Fee Advanced Course 43. Swiss Society for Astrophysics and Astronomy*, pages 251–358, 2016.

[39] M. R. Maxey and J. J. Riley. Equation of motion for a small rigid sphere in a nonuniform flow. *The Physics of Fluids*, 26(4):883–889, 1983.

[40] C. F. M. Coimbra and R. H. Rangel. General solution of the particle momentum equation in unsteady stokes flows. *Journal of Fluid Mechanics*, 370:53–72, 1998.

[41] J. D. Kulick. *On the interactions between particles and turbulence in a fully-developed channel flow in air*. Stanford University, 1994.

[42] C. B. Rogers. *The interaction between dispersed particles and fluid turbulence in a flat-plate turbulent boundary layer in air*. Stanford University, 1989.

[43] P. G. Saffman. The lift on a small sphere in a slow shear flow. *Journal of Fluid Mechanics*, 22(2):385–400, 1965.

[44] W. Hwang. *Modification of homogeneous and isotropic turbulence by solid particles*. Stanford University, 2005.

[45] M. R. Maxey. The gravitational settling of aerosol particles in homogeneous turbulence and random flow fields. *Journal of Fluid Mechanics*, 174:441–465, 1987.

[46] K. D. Squires and J. K. Eaton. Preferential concentration of particles by turbulence. *Physics of Fluids A: Fluid Dynamics*, 3(5):1169–1178, 1991.

[47] L. Chen, S. Goto, and J. C. Vassilicos. Turbulent clustering of stagnation points and inertial particles. *Journal of Fluid Mechanics*, 553:143–154, 2006.

[48] J. Bec, H. Homann, and G. Krstulovic. Clustering, fronts, and heat transfer in turbulent suspensions of heavy particles. *Physical Review Letters*, 112(23):234503, 2014.

[49] J. Chun, D. L. Koch, S. L. Rani, A. Ahluwalia, and L. R. Collins. Clustering of aerosol particles in isotropic turbulence. *Journal of Fluid Mechanics*, 536:219–251, 2005.

[50] A. D. Bragg and L. R. Collins. New insights from comparing statistical theories for inertial particles in turbulence: I. spatial distribution of particles. *New Journal of Physics*, 16(5):055013, 2014.

[51] M. Caporaloni, F. Tampieri, F. Trombetti, and O. Vittori. Transfer of particles in nonisotropic air turbulence. *Journal of the Atmospheric Sciences*, 32(3):565–568, 1975.

[52] M. W. Reeks. The transport of discrete particles in inhomogeneous turbulence. *Journal of Aerosol Science*, 14(6):729–739, 1983.

[53] N. E. L. Haugen, A. Brandenburg, C. Sandin, and L. Mattsson. Spectral characterisation of inertial particle clustering in turbulence. *Journal of Fluid Mechanics*, 934, 2022.

[54] J. Bec, L. Biferale, M. Cencini, A. S. Lanotte, and F. Toschi. Effects of vortex filaments on the velocity of tracers and heavy particles in turbulence. *Physics of Fluids*, 18(8):081702, 2006.

[55] J. C. W. Njue, F. Salehi, T. C. W. Lau, M. J. Cleary, G. J. Nathan, and L. Chen. Numerical and experimental analysis of poly-dispersion effects on particle-laden jets. *International Journal of Heat and Fluid Flow*, 91:108852, 2021.

[56] J. N. Chung and T. R. Troutt. Simulation of particle dispersion in an axisymmetric jet. *Journal of Fluid Mechanics*, 186:199–222, 1988.

[57] J. Uthuppan, S. K. Aggarwal, F. F. Grinstein, and K. Kailasanath. Particle dispersion in a transitional axisymmetric jet-a numerical simulation. *AIAA journal*, 32(10):2004–2014, 1994.

[58] J. K. Eaton and J. R. Fessler. Preferential concentration of particles by turbulence. *International Journal of Multiphase Flow*, 20:169–209, 1994.

[59] L. I. Zaichik and V. M. Alipchenkov. Statistical models for predicting pair dispersion and particle clustering in isotropic turbulence and their applications. *New Journal of Physics*, 11(10):103018, 2009.

[60] E. Meneguz and M. W. Reeks. Statistical properties of particle segregation in homogeneous isotropic turbulence. *Journal of fluid mechanics*, 686:338–351, 2011.

[61] F. F. Dizaji and J. S. Marshall. On the significance of two-way coupling in simulation of turbulent particle agglomeration. *Powder Technology*, 318:83–94, 2017.

[62] T. C. W. Lau and G. J. Nathan. A method for identifying and characterising particle clusters in a two-phase turbulent jet. *International Journal of Multiphase Flow*, 88:191–204, 2017.

[63] C. M. Casciola, P. Gualtieri, F. Picano, G. Sardina, and G. Troiani. Dynamics of inertial particles in free jets. *Physica Scripta*, 2010(T142):014001, 2010.

[64] Y. Hardalupas, A. M. K. P. Taylor, and J. H. Whitelaw. Velocity and particle-flux characteristics of turbulent particle-laden jets. *Proceedings of the Royal Society of London. A. Mathematical and Physical Sciences*, 426(1870):31–78, 1989.

[65] F. Picano, G. Sardina, P. Gualtieri, and C. M. Casciola. Anomalous memory effects on transport of inertial particles in turbulent jets. *Physics of Fluids*, 22(5), 2010.

[66] R. Dhariwal and A. D. Bragg. Small-scale dynamics of settling, bidisperse particles in turbulence. *Journal of Fluid Mechanics*, 839:594–620, 2018.

[67] E.-W. Saw, J. P. L. C. Salazar, L. R. Collins, and R. A. Shaw. Spatial clustering of polydisperse inertial particles in turbulence: I. comparing simulation with theory. *New Journal of Physics*, 14(10):105030, 2012.

[68] J. R. Fessler, J. D. Kulick, and J. K. Eaton. Preferential concentration of heavy particles in a turbulent channel flow. *Physics of Fluids*, 6(11):3742–3749, 1994.

[69] M. Wilkinson and B. Mehlig. Caustics in turbulent aerosols. *Europhysics Letters*, 71(2):186, 2005.

[70] G. Haller. Distinguished material surfaces and coherent structures in three-dimensional fluid flows. *Physica D: Nonlinear Phenomena*, 149(4):248–277, 2001.

[71] S. Sundaram and L. R. Collins. Collision statistics in an isotropic particle-laden turbulent suspension. part 1. direct numerical simulations. *Journal of Fluid Mechanics*, 335:75–109, 1997.

[72] W. C. Reade and L. R. Collins. Effect of preferential concentration on turbulent collision rates. *Physics of Fluids*, 12(10):2530–2540, 2000.

[73] R. Monchaux, M. Bourgoin, and A. Cartellier. Preferential concentration of heavy particles: a voronoï analysis. *Physics of Fluids*, 22(10):103304, 2010.

[74] J. M. Bergthorson, S. Goroshin, M. J. Soo, P. Julien, J. Palecka, D. L. Frost, and D. J. Jarvis. Direct combustion of recyclable metal fuels for zero-carbon heat and power. *Applied Energy*, 160:368–382, 2015.

[75] P. Surmacz. Green rocket propulsion research and development at the institute of aviation: problems and perspectives. *Journal of KONES*, 23(1):337–344, 2016.

[76] C. Circi. Lunar base for Mars missions. *Journal of Guidance, Control, and Dynamics*, 28(2):372–377, 2005.

[77] M. Anand, I. A. Crawford, M. Balat-Pichelin, S. Abanades, W. Van Westrenen, G. Péraudeau, R. Jaumann, and W. Seboldt. A brief review of chemical and mineralogical resources on the Moon and likely initial in situ resource utilization (ISRU) applications. *Planetary and Space Science*, 74(1):42–48, 2012.

[78] T. Cichan, S. A. Bailey, S. D. Norris, R. P. Chambers, S. D. Jolly, and J. W. Ehrlich. Mars base camp: An architecture for sending humans to Mars by 2028. In *2017 IEEE Aerospace Conference*, pages 1–18. IEEE, 2017.

[79] H. Kalita, M. Donayre, V. Padilla, A. Riley, J. Samitas, B. Burnett, E. Asphaug, M. Robinson, and J. Thangavelautham. GNC challenges and opportunities of CUBESAT science missions deployed from the lunar gateway. *arXiv preprint arXiv:1904.00497*, 2019.

[80] V. Osipov, C. Muratov, H. Hafiychuk, E. Ponizovskaya-Devine, V. Smelyanskiy, D. Mathias, S. Lawrence, and M. Werkheiser. Explosion hazard from a propellant-tank breach in liquid hydrogen-oxygen rockets. *Journal of Spacecraft and Rockets*, 50(4):860–871, 2013.

[81] G. B. Sanders and W. E. Larson. Progress made in lunar in situ resource utilization under NASA's exploration technology and development program. *Journal of Aerospace Engineering*, 26(1):5–17, 2013.

[82] S. O. Starr and A. C. Muscatello. Mars in situ resource utilization: a review. *Planetary and Space Science*, 182:104824, 2020.

[83] G. J. Molina-Cuberos, O. Witasse, J. P. Lebreton, R. Rodrigo, and J. J. López-Moreno. Meteoric ions in the atmosphere of Mars. *Planetary and Space Science*, 51(3):239–249, 2003.

[84] A. Ellery. Sustainable in-situ resource utilization on the Moon. *Planetary and Space Science*, 184:104870, 2020.

[85] K. Sacksteder and G. Sanders. In-situ resource utilization for lunar and Mars exploration. In *45th AIAA Aerospace Sciences Meeting and Exhibit*, page 345, 2007.

[86] Y. Zhou, J. Liu, J. Wang, T. Xv, J. Wang, J. Zhou, and K. Cen. Experimental study on dynamic combustion characteristics of aluminum particles. *Propellants, Explosives, Pyrotechnics*, 42(8):982–992, 2017.

[87] F. Blais, P. Julien, J. Palecka, S. Goroshin, and J. M. Bergthorson. Effect of initial reactant temperature on flame speeds in aluminum dust suspensions. *Combustion Science and Technology*, 194(8):1513–1526, 2022.

[88] T. Tan and Y. Chen. Review of study on solid particle solar receivers. *Renewable and Sustainable Energy Reviews*, 14(1):265–276, 2010.

[89] A. J. Banko, L. Villafañe, J. H. Kim, and J. K. Eaton. Temperature statistics in a radiatively heated particle-laden turbulent square duct flow. *International Journal of Heat and Fluid Flow*, 84:108618, 2020.

[90] A. Steinfeld. Solar hydrogen production via a two-step water-splitting thermochemical cycle based on Zn/ZnO redox reactions. *International Journal of Hydrogen Energy*, 27(6):611–619, 2002.

[91] A. J. Hunt. Small particle heat exchangers. 1978.

[92] C. K. Ho. A review of high-temperature particle receivers for concentrating solar power. *Applied Thermal Engineering*, 109:958–969, 2016.

[93] H. Zhang, H. Benoit, I. Perez-Lopèz, G. Flamant, T. Tan, and J. Baeyens. High-efficiency solar power towers using particle suspensions as heat carrier in the receiver and in the thermal energy storage. *Renewable Energy*, 111:438–446, 2017.

[94] J. Karthikeyan. The advantages and disadvantages of the cold spray coating process. In *The Cold Spray Materials Deposition Process*, pages 62–71. Elsevier, 2007.

[95] M. Ashokkumar, D. Thirumalaikumarasamy, T. Sonar, S. Deepak, P. Vignesh, and M. Anbarasu. An overview of cold spray coating in additive manufacturing, component repairing and other engineering applications. *Journal of the Mechanical Behavior of Materials*, 31(1):514–534, 2022.

[96] J. Villafuerte. *Modern cold spray: materials, process, and applications*. Springer, 2015.

[97] A. Moridi, S. M. Hassani-Gangaraj, M. Guagliano, and M. Dao. Cold spray coating: review of material systems and future perspectives. *Surface Engineering*, 30(6):369–395, 2014.

[98] R. R. Chromik, S. A. Alidokht, M. Shockley, J, and Y. Zhang. Tribological coatings prepared by cold spray. *Cold-Spray Coatings: Recent Trends and Future Perspectives*, pages 321–348, 2018.

[99] M. Li, L. Li, L. Shao, Q. Li, Z. Zou, and B. Li. Numerical analysis of the particle dynamics in a supersonic gas stream with a modified point-particle euler–lagrange approach. *Metallurgical and Materials Transactions B*, 52:1034–1051, 2021.

[100] S. Yin, P. Cavaliere, B. Aldwell, R. Jenkins, H. Liao, W. Li, and R. Lupoi. Cold spray additive manufacturing and repair: fundamentals and applications. *Additive Manufacturing*, 21:628–650, 2018.

[101] J. Mouallem and J. P. Hickey. Induction heating of dispersed metallic particles in a turbulent flow. *International Journal of Multiphase Flow*, 132:103414, 2020.

[102] F. Blais, P. Julien, J. Palecka, S. Goroshin, and J. M. Bergthorson. Effect of initial reactant temperature on flame speeds in aluminum dust suspensions. *Combustion Science and Technology*, pages 1–14, 2020.

[103] W. G. Houf and R. Greif. Radiative transfer in a solar absorbing particle laden flow. *Chemical Engineering Communications*, 51(1-6):153–165, 1987.

[104] JB McLaughlin. Numerical computation of particles-turbulence interaction. *International Journal of Multiphase Flow*, 20:211–232, 1994.

[105] S. W. Coleman and J. C. Vassilicos. A unified sweep-stick mechanism to explain particle clustering in two-and three-dimensional homogeneous, isotropic turbulence. *Physics of Fluids*, 21(11):113301, 2009.

[106] S. Goto and J. C. Vassilicos. Sweep-stick mechanism of heavy particle clustering in fluid turbulence. *Physical Review Letters*, 100(5):054503, 2008.

[107] F. Beyrau, M. A. Hadjipanayis, and R. P. Lindstedt. Ignition of fuel/air mixtures by radiatively heated particles. *Proceedings of the Combustion Institute*, 34(2):2065–2072, 2013.

[108] Y. Zhang and Y. Zhai. Magnetic induction heating of nano-sized ferrite particle. In *Advances in Induction and Microwave Heating of Mineral and Organic Materials*. IntechOpen, 2011.

[109] S. Apperson, R. V. Shende, S. Subramanian, D. Tappmeyer, S. Gangopadhyay, Z. Chen, K. Gangopadhyay, P. Redner, S. Nicholich, and D. Kapoor. Generation of fast propagating combustion and shock waves with copper oxide/aluminum nanothermite composites. *Applied Physics Letters*, 91(24):243109, 2007.

[110] M. Carbone, A. D. Bragg, and M. Iovieno. Multiscale fluid–particle thermal interaction in isotropic turbulence. *Journal of Fluid Mechanics*, 881:679–721, 2019.

[111] S. Sumbekova, A. Cartellier, A. Aliseda, and M. Bourgoin. Preferential concentration of inertial sub-kolmogorov particles: the roles of mass loading of particles, stokes numbers, and reynolds numbers. *Physical Review Fluids*, 2(2):024302, 2017.

[112] Y. Zhou, A. S. Wexler, and L.-P. Wang. Modelling turbulent collision of bidisperse inertial particles. *Journal of Fluid Mechanics*, 433:77–104, 2001.

[113] A. Vié, H. Pouransari, R. Zamansky, and A. Mani. Particle-laden flows forced by the disperse phase: comparison between lagrangian and eulerian simulations. *International Journal of Multiphase Flow*, 79:144–158, 2016.

[114] G. G. Stokes. On the effect of the internal friction of fluids on the motion of pendulums. *Transactions of the Cambridge Philosophical Society*, 9, 1851.

[115] A. D. Bragg, P. J. Ireland, and L. R. Collins. Mechanisms for the clustering of inertial particles in the inertial range of isotropic turbulence. *Physical Review E*, 92(2):023029, 2015.

[116] L. I. Zaichik and V. M. Alipchenkov. Refinement of the probability density function model for preferential concentration of aerosol particles in isotropic turbulence. *Physics of Fluids*, 19(11):113308, 2007.

[117] J. Bec, L. Biferale, M. Cencini, A. Lanotte, S. Musacchio, and F. Toschi. Heavy particle concentration in turbulence at dissipative and inertial scales. *Physical Review Letters*, 98(8):084502, 2007.

[118] L. Baker, A. Frankel, A. Mani, and F. Coletti. Coherent clusters of inertial particles in homogeneous turbulence. *Journal of Fluid Mechanics*, 833:364–398, 2017.

[119] S. Sahu, Y. Hardalupas, and A. M. K. P. Taylor. Droplet–turbulence interaction in a confined polydispersed spray: effect of turbulence on droplet dispersion. *Journal of Fluid Mechanics*, 794:267–309, 2016.

[120] Y. Hardalupas, A. M. K. P. Taylor, and J. H. Whitelaw. Velocity and size characteristics of liquid-fuelled flames stabilized by a swirl burner. *Proceedings of the Royal Society of London. A. Mathematical and Physical Sciences*, 428(1874):129–155, 1990.

[121] L. P. Wang and M. R. Maxey. Settling velocity and concentration distribution of heavy particles in homogeneous isotropic turbulence. *Journal of Fluid Mechanics*, 256:27–68, 1993.

[122] J. Bec. Multifractal concentrations of inertial particles in smooth random flows. *Journal of Fluid Mechanics*, 528:255–277, 2005.

[123] H. Lian. *Droplet preferential concentration in homogeneous and isotropic turbulence*. Imperial College London, 2014.

[124] O. Ayala, B. Rosa, L. P. Wang, and W. W. Grabowski. Effects of turbulence on the geometric collision rate of sedimenting droplets. part 1. results from direct numerical simulation. *New Journal of Physics*, 10(7):075015, 2008.

[125] E. W. Saw, R. A. Shaw, S. Ayyalasomayajula, P. Y. Chuang, and A. Gylfason. Inertial clustering of particles in high-reynolds-number turbulence. *Physical Review Letters*, 100(21):214501, 2008.

[126] L Pan, P. Padoan, J. Scalo, A. G. Kritsuk, and M. L. Norman. Turbulent clustering of protoplanetary dust and planetesimal formation. *The Astrophysical Journal*, 740(1):6, 2011.

[127] R. Letournel, F. Laurent, M. Massot, and A. Vié. Reproducing segregation and particle dynamics in large eddy simulation of particle-laden flows. In *International Conference on Liquid Atomization and Spray Systems (ICLASS)*, volume 1, 2021.

[128] M. Esmaily-Moghadam and A. Mani. Analysis of the clustering of inertial particles in turbulent flows. *Physical Review Fluids*, 1(8):084202, 2016.

[129] M. Rahmani, G. Geraci, G. Iaccarino, and A. Mani. Effects of particle polydispersity on radiative heat transfer in particle-laden turbulent flows. *International Journal of Multiphase Flow*, 104:42–59, 2018.

[130] A. Brandenburg, A. Johansen, P. A. Bourdin, W. Dobler, W. Lyra, M. Rheinhardt, S. Bingert, N. E. L. Haugen, A. Mee, F. Gent, et al. The pencil code, a modular MPI code for partial differential equations and particles: multipurpose and multiuser-maintained. *arXiv preprint arXiv:2009.08231*, 2020.

[131] A. Brandenburg. The inverse cascade and nonlinear alpha-effect in simulations of isotropic helical hydromagnetic turbulence. *The Astrophysical Journal*, 550(2):824, 2001.

[132] The pencil code documentation. *NORDITA*, (pencil-code.nordita.org).

[133] N. Schiller. A drag coefficient correlation. *VDI Zeitung*, 77:318–320, 1935.

[134] W. R. Marshall and W. E. Ranz. Evaporation from drops—part I. *Chemical Engineering Progress*, 48(3):141–146, 1952.

[135] S. Sahu, Y. Hardalupas, and A. M. K. P. Taylor. Interaction of droplet dispersion and evaporation in a polydispersed spray. *Journal of Fluid Mechanics*, 846:37–81, 2018.

[136] M. Momenifar and A. D. Bragg. Local analysis of the clustering, velocities, and accelerations of particles settling in turbulence. *Physical Review Fluids*, 5(3):034306, 2020.

[137] R. Monchaux, M. Bourgoin, and A. Cartellier. Analyzing preferential concentration and clustering of inertial particles in turbulence. *International Journal of Multiphase Flow*, 40:1–18, 2012.

[138] D. Bae, P. Shin, S. Kwak, M. Moon, M. Shon, S. Oh, and G. Kim. Heating behavior of ferromagnetic Fe particle-embedded thermoplastic polyurethane adhesive film by induction heating. *Journal of Industrial and Engineering Chemistry*, 30:92–97, 2015.

[139] Q. Dai, K. Luo, J. Fan, Z. Guo, and Z. Chen. Fluctuations of thermodynamic variables in compressible isotropic turbulence laden with inertial particles. *Physics of Fluids*, 33(9):093312, 2021.

[140] S. Ayyalasomayajula, Z. Warhaft, and L. R. Collins. Modeling inertial particle acceleration statistics in isotropic turbulence. *Physics of Fluids*, 20(9):095104, 2008.

[141] J. Bec, L. Biferale, G. Boffetta, A. Celani, M. Cencini, A. Lanotte, S. Musacchio, and F. Toschi. Acceleration statistics of heavy particles in turbulence. *Journal of Fluid Mechanics*, 550:349–358, 2006.

[142] S. Goroshin, A. Higgins, and M. Kamel. Powdered metals as fuel for hypersonic ramjets. In *37th Joint Propulsion Conference and Exhibit*, page 3919, 2001.

[143] K. D. Squires and H. Yamazaki. Preferential concentration of marine particles in isotropic turbulence. *Deep Sea Research Part I: Oceanographic Research Papers*, 42(11-12):1989–2004, 1995.

[144] R. Zamansky, F. Coletti, M. Massot, and A. Mani. Turbulent thermal convection driven by heated inertial particles. *Journal of Fluid Mechanics*, 809:390–437, 2016.

[145] R. Zamansky, F. Coletti, M. Massot, and A. Mani. Radiation induces turbulence in particle-laden fluids. *Physics of Fluids*, 26(7), 2014.

[146] A. V. S. Nath, A. Roy, R. Govindarajan, and S. Ravichandran. Transport of condensing droplets in taylor-green vortex flow in the presence of thermal noise. *Physical Review E*, 105(3):035101, 2022.

[147] D. A. Khalitov and E. K. Longmire. Effect of particle size on velocity correlations in turbulent channel flow. In *Fluids Engineering Division Summer Meeting*, volume 36967, pages 445–453, 2003.

[148] H. Yoshimoto and S. Goto. Self-similar clustering of inertial particles in homogeneous turbulence. *Journal of Fluid Mechanics*, 577:275–286, 2007.

[149] A. Frankel, H. Pouransari, F. Coletti, and A. Mani. Settling of heated particles in homogeneous turbulence. *Journal of Fluid Mechanics*, 792:869–893, 2016.

[150] F. Zonta, C. Marchioli, and A. Soldati. Modulation of turbulence in forced convection by temperature-dependent viscosity. *Journal of Fluid Mechanics*, 697:150–174, 2012.

[151] A. Saieed, M. M. Rahman, and J.-P. Hickey. Role of viscosity in the preferential concentration of heated, bidispersed particles. *International Journal of Multiphase Flow*, 155:104185, 2022.

[152] S. Elghobashi and G. Truesdell. On the two-way interaction between homogeneous turbulence and dispersed solid particles. I: turbulence modification. *Physics of Fluids A: Fluid Dynamics*, 5(7):1790–1801, 1993.

[153] T. S. Yang and S. S. Shy. Two-way interaction between solid particles and homogeneous air turbulence: particle settling rate and turbulence modification measurements. *Journal of Fluid Mechanics*, 526:171, 2005.

[154] R. A. Gore and C. T. Crowe. Effect of particle size on modulating turbulent intensity. *International Journal of Multiphase Flow*, 15(2):279–285, 1989.

[155] A. Aliseda, A. Cartellier, F. Hainaux, and J. C. Lasheras. Effect of preferential concentration on the settling velocity of heavy particles in homogeneous isotropic turbulence. *Journal of Fluid Mechanics*, 468:77–105, 2002.

[156] L. Guo and J. Capecelatro. The role of clusters on heat transfer in sedimenting gas-solid flows. *International Journal of Heat and Mass Transfer*, 132:1217–1230, 2019.

[157] J. G. M. Kuerten, C. W. M. Van der Geld, and B. J. Geurts. Turbulence modification and heat transfer enhancement by inertial particles in turbulent channel flow. *Physics of Fluids*, 23(12), 2011.

[158] M. R. Overholt and S. B. Pope. A deterministic forcing scheme for direct numerical simulations of turbulence. *Computers & Fluids*, 27(1):11–28, 1998.

[159] C. Rosales and C. Meneveau. Linear forcing in numerical simulations of isotropic turbulence: physical space implementations and convergence properties. *Physics of Fluids*, 17(9):095106, 2005.

[160] M. Bassenne, J. Urzay, G. I. Park, and P. Moin. Constant-energetics physical-space forcing methods for improved convergence to homogeneous-isotropic turbulence with application to particle-laden flows. *Physics of Fluids*, 28(3):035114, 2016.

[161] P. J. Ireland, A. D Bragg, and L. R. Collins. The effect of reynolds number on inertial particle dynamics in isotropic turbulence. part 1. simulations without gravitational effects. *Journal of Fluid Mechanics*, 796:617–658, 2016.

[162] J. A. K. Horwitz and A. Mani. Accurate calculation of stokes drag for point–particle tracking in two-way coupled flows. *Journal of Computational Physics*, 318:85–109, 2016.

[163] J. A. K. Horwitz and A. Mani. Correction scheme for point-particle models applied to a nonlinear drag law in simulations of particle-fluid interaction. *International Journal of Multiphase Flow*, 101:74–84, 2018.

[164] K. D. Squires and J. K. Eaton. Particle response and turbulence modification in isotropic turbulence. *Physics of Fluids A: Fluid Dynamics*, 2(7):1191–1203, 1990.

[165] W. Ling, J. N. Chung, and C. T. Crowe. Direct numerical simulation of the two-way coupled interaction between particles and mixing layer. *Proceedings of the Royal Society of London. Series A: Mathematical, Physical and Engineering Sciences*, 456(2004):2931–2955, 2000.

[166] Y. Liu, L. Shen, R. Zamansky, and F. Coletti. Life and death of inertial particle clusters in turbulence. *Journal of Fluid Mechanics*, 902, 2020.

[167] M. Ester, H.-P. Kriegel, J. Sander, X. Xu, et al. A density-based algorithm for discovering clusters in large spatial databases with noise. In *kdd*, volume 96, pages 226–231, 1996.

[168] D. Fan, J. Xu, M. X. Yao, and J.-P. Hickey. On the detection of internal interfacial layers in turbulent flows. *Journal of Fluid Mechanics*, 872:198–217, 2019.

[169] H. Zhang, D. E. Rival, and X. Wu. Kinematics of the turbulent and nonturbulent interfaces in a subsonic airfoil flow. *AIAA Journal*, 59(6):2155–2168, 2021.

[170] K. Younes, B. Gibeau, S. Ghaemi, and J.-P. Hickey. A fuzzy cluster method for turbulent/non-turbulent interface detection. *Experiments in Fluids*, 62:1–4, 2021.

[171] J. Sander, M. Ester, H.-P. Kriegel, and X. Xu. Density-based clustering in spatial databases: The algorithm gdbscan and its applications. *Data Mining and Knowledge Discovery*, 2:169–194, 1998.

[172] A. Frankel, G. Iaccarino, and A. Mani. Optical depth in particle-laden turbulent flows. *Journal of Quantitative Spectroscopy and Radiative Transfer*, 201:10–16, 2017.

[173] A. J. Banko, L. Villafañe, J. H. Kim, M. Esmaily, and J. K. Eaton. Stochastic modeling of direct radiation transmission in particle-laden turbulent flow. *Journal of Quantitative Spectroscopy and Radiative Transfer*, 226:1–18, 2019.

[174] L. K. Shannon, B Viggiano, R. B. Cal, L. G. Mastin, A. R. Van Eaton, and S. A. Solovitz. Flow development and entrainment in turbulent particle-laden jets. *Journal of Geophysical Research: Atmospheres*, 128(12):e2022JD038108, 2023.

[175] P. Germain, M. Piau, and D. Caillerie. Multiphase flow in explosive volcanic and geothermal eruptions. *Theoretical and Applied Mechanics*, page 145, 2012.

[176] H. Herman and S. Sampath. Thermal spray coatings. In *Metallurgical and Ceramic Protective Coatings*, pages 261–289. Springer, 1996.

[177] M. Li, L. Li, B. Zhang, Q. Li, W. Wu, and Z. Zou. Numerical analysis of the particle-induced effect on gas flow in a supersonic powder-laden oxygen jet. *Metallurgical and Materials Transactions B*, 51:1718–1730, 2020.

[178] F. Picano, G. Sardina, P. Gualtieri, and C. M. Casciola. Particle-laden jets: particle distribution and back-reaction on the flow. In *Journal of Physics: Conference Series*, volume 318, page 052018. IOP Publishing, 2011.

[179] T. C. W. Lau and G. J. Nathan. Influence of stokes number on the velocity and concentration distributions in particle-laden jets. *Journal of Fluid Mechanics*, 757:432–457, 2014.

[180] J. Fan, K. Luo, M. Y. Ha, and K. Cen. Direct numerical simulation of a near-field particle-laden plane turbulent jet. *Physical Review E—Statistical, Nonlinear, and Soft Matter Physics*, 70(2):026303, 2004.

[181] A. Saieed and J. P. Hickey. Viscous capturing of heated particles in one-and two-way coupled turbulence. *Savoirs USherbrooke*, 6:1–6, 2023.

[182] D. Livescu. Turbulence with large thermal and compositional density variations. *Annual Review of Fluid Mechanics*, 52(1):309–341, 2020.

[183] G. Hetsroni and M. Sokolov. Distribution of mass, velocity, and intensity of turbulence in a two-phase turbulent jet. *Journal of Applied Mechanics*, 38(2):315–327, 1971.

[184] Jonathan D Kulick, John R Fessler, and John K Eaton. Particle response and turbulence modification in fully developed channel flow. *Journal of Fluid Mechanics*, 277:109–134, 1994.

[185] K. D. Squires and J. K. Eaton. Effect of selective modification of turbulence on two-equation models for particle-laden turbulent flows. *Journal of Fluids Engineering*, 116(4):778–784, 1994.

[186] S. Yuu, K. Ikeda, and T. Umekage. Flow-field prediction and experimental verification of low reynolds number gas-particle turbulent jets. *Colloids and Surfaces A: Physicochemical and Engineering Aspects*, 109:13–27, 1996.

[187] A. Saieed and J.-P. Hickey. Viscosity-modulated clustering of heated bidispersed particles in a turbulent gas. *Journal of Fluid Mechanics*, 979:A46, 2024.

[188] G. Lodato, P. Domingo, and L. Vervisch. Three-dimensional boundary conditions for direct and large-eddy simulation of compressible viscous flows. *Journal of Computational Physics*, 227(10):5105–5143, 2008.

[189] T. J. A. Poinsot and S. K. Lelef. Boundary conditions for direct simulations of compressible viscous flows. *Journal of Computational Physics*, 101(1):104–129, 1992.

[190] T. C. W. Lau and G. J. Nathan. The effect of stokes number on particle velocity and concentration distributions in a well-characterised, turbulent, co-flowing two-phase jet. *Journal of Fluid Mechanics*, 809:72–110, 2016.

[191] G. J. Nathan, P. A. M. Kalt, Z. T. Alwahabi, B. B. Dally, P. R. Medwell, and Q. N. Chan. Recent advances in the measurement of strongly radiating, turbulent reacting flows. *Progress in Energy and Combustion Science*, 38(1):41–61, 2012.

[192] D. J. Carlson and R. F. Hoglund. Particle drag and heat transfer in rocket nozzles. *AIAA Journal*, 2(11):1980–1984, 1964.

[193] T. Nagata, T. Nonomura, S. Takahashi, Y. Mizuno, and K. Fukuda. Investigation on subsonic to supersonic flow around a sphere at low reynolds number of between 50 and 300 by direct numerical simulation. *Physics of Fluids*, 28(5), 2016.

[194] S. W. Kieffer and B. Sturtevant. Laboratory studies of volcanic jets. *Journal of Geophysical Research: Solid Earth*, 89(B10):8253–8268, 1984.

[195] B. Viggiano, K. Gish, S. Solovitz, and R. B. Cal. Inertial particle clustering due to turbulence in an air jet. *International Journal of Multiphase Flow*, 174:104734, 2024.

[196] R. McKibbin, T. A. Smith, and L. Fullard. Components and phases: modelling progressive hydrothermal eruptions. *The ANZIAM Journal*, 50(3):365–380, 2009.

[197] C. Kleinstreuer, Z. Zhang, and J. F. Donohue. Targeted drug-aerosol delivery in the human respiratory system. *Annual Review of Biomedical Engineering*, 10(1):195–220, 2008.

[198] R. Mittal, R. Ni, and J. H. Seo. The flow physics of covid-19. *Journal of Fluid Mechanics*, 894:F2, 2020.

[199] L. Bourouiba. Fluid dynamics of respiratory infectious diseases. *Annual Review of Biomedical Engineering*, 23(1):547–577, 2021.

[200] L. D. Jaffe. Blowing of lunar soil by apollo 12: Surveyor 3 evidence. *Science*, 171(3973):798–799, 1971.

[201] A. Sengupta, J. Kulleck, S. Sell, J. Van Norman, M. Mehta, and M. Pokora. Mars lander engine plume impingement environment of the Mars science laboratory. In *2009 IEEE Aerospace Conference*, pages 1–10. IEEE, 2009.

[202] D. Li, J. Fan, K. Luo, and K. Cen. Direct numerical simulation of a particle-laden low reynolds number turbulent round jet. *International Journal of Multiphase Flow*, 37(6):539–554, 2011.

[203] Q. Zhang, H. Liu, Z. Ma, and Z. Xiao. Preferential concentration of heavy particles in compressible isotropic turbulence. *Physics of Fluids*, 28(5), 2016.

[204] V. Pérez-Munuzuri. Clustering of inertial particles in compressible chaotic flows. *Physical Review E*, 91(5):052906, 2015.

[205] R. J. Adrian. Scattering particle characteristics and their effect on pulsed laser measurements of fluid flow: speckle velocimetry vs particle image velocimetry. *Applied Optics*, 23(11):1690–1691, 1984.

[206] M. Meyer, S. Yin, and R. Lupoi. Particle in-flight velocity and dispersion measurements at increasing particle feed rates in cold spray. *Journal of Thermal Spray Technology*, 26:60–70, 2017.

[207] S. Basu, A. K. Agarwal, A. Mukhopadhyay, and C. Patel. Introduction to droplets and sprays: Applications for combustion and propulsion. *Droplets and Sprays: Applications for Combustion and Propulsion*, pages 3–6, 2018.

[208] S. R. Gopireddy, R. M. Humza, and E. Gutheil. Modeling and simulation of evaporating spray flows with coalescence in an eulerian framework. *Chemie Ingenieur Technik*, 84(3):349–356, 2012.

[209] L. F. Y. C. T. J. N. T. R. Tang, F. Wen, Y. Yang, C. T. Crowe, J. N. Chung, and T. R. Troutt. Self-organizing particle dispersion mechanism in a plane wake. *Physics of Fluids A: Fluid Dynamics*, 4(10):2244–2251, 1992.

[210] Jesse Capecelatro and Justin L Wagner. Gas–particle dynamics in high-speed flows. *Annual Review of Fluid Mechanics*, 56(1):379–403, 2024.

[211] C. Liu, S. Tang, L. Shen, and Y. Dong. Characteristics of turbulence transport for momentum and heat in particle-laden turbulent vertical channel flows. *Acta Mechanica Sinica*, 33:833–845, 2017.

[212] D. H. Richter and P. P. Sullivan. Momentum transfer in a turbulent, particle-laden couette flow. *Physics of Fluids*, 25(5), 2013.

[213] Y. Levy and F. C. Lockwood. Velocity measurements in a particle laden turbulent free jet. *Combustion and Flame*, 40:333–339, 1981.

[214] Y. Tsuji, Y. Morikawa, T. Tanaka, K. Karimine, and S. Nishida. Measurement of an axisymmetric jet laden with coarse particles. *International Journal of Multiphase Flow*, 14(5):565–574, 1988.

[215] L. P. Yarin and G. Hetsroni. Turbulence intensity in dilute two-phase flows—3 the particles-turbulence interaction in dilute two-phase flow. *International Journal of Multiphase Flow*, 20(1):27–44, 1994.

[216] M. Sommerfeld. The structure of particle-laden, underexpanded free jets. *Shock Waves*, 3:299–311, 1994.

[217] M. Patel, J. S. Rubio, D. Shekhtman, N. Parziale, J. Rabinovitch, R. Ni, and J. Capecelatro. Experimental and numerical investigation of inertial particles in underexpanded jets. *Journal of Fluid Mechanics*, 1000:A60, 2024.

[218] C. H. Lewis Jr and D. J. Carlson. Normal shock location in underexpanded gas and gas-particle jets. *AIAA Journal*, 2(4):776–777, 1964.

[219] P. O. Jarvinen and J. S. Draper. Underexpanded gas-particle jets. *AIAA Journal*, 5(4):824–825, 1967.

[220] Z. Xia, Y. Shi, Q. Zhang, and S. Chen. Modulation to compressible homogenous turbulence by heavy point particles. I. effect of particles' density. *Physics of Fluids*, 28(1), 2016.

[221] H. Yu, S. Yang, J. Hu, and H. Wang. Numerical investigation of wide continuous particle size distribution on the supersonic powder loading oxygen jet. *Powder Technology*, 428:118885, 2023.

[222] B. J. Greska. *Supersonic jet noise and its reduction using microjet injection*. The Florida State University, 2005.

[223] A. Krothapalli, L. Venkatakrishnan, L. Lourenco, B. Greska, and R. Elavarasan. Turbulence and noise suppression of a high-speed jet by water injection. *Journal of Fluid Mechanics*, 491:131–159, 2003.

[224] D. A. Buchta, G. Shallcross, and J. Capecelatro. Sound and turbulence modulation by particles in high-speed shear flows. *Journal of Fluid Mechanics*, 875:254–285, 2019.

[225] A. Saieed and J.-P. Hickey. Clustering characteristics of heated bidispersed particles. *Bulletin of the American Physical Society*, 67, 2022.

[226] X. Yang, F. Li, X. Liu, M. Sun, Y. Yang, Y. Wang, H. Wang, and P. Li. An alternative two-way coupled euler-lagrange scheme to model the performance of finite-size particle in supersonic flow. *International Journal of Multiphase Flow*, 170:104647, 2024.

[227] C. Bogey and C. Bailly. Large eddy simulations of transitional round jets: influence of the reynolds number on flow development and energy dissipation. *Physics of Fluids*, 18(6), 2006.

[228] J. P. Hickey, F. Hussain, and X. Wu. Role of coherent structures in multiple self-similar states of turbulent planar wakes. *Journal of Fluid Mechanics*, 731:312–363, 2013.

[229] D. H. Shin, R. D. Sandberg, and E. S. Richardson. Self-similarity of fluid residence time statistics in a turbulent round jet. *Journal of Fluid Mechanics*, 823:1–25, 2017.

[230] J. P. Hickey, F. Hussain, and X. Wu. Compressibility effects on the structural evolution of transitional high-speed planar wakes. *Journal of Fluid Mechanics*, 796:5–39, 2016.

[231] J. C. R. Hunt, A. A. Wray, and P. Moin. Eddies, streams, and convergence zones in turbulent flows. *Studying Turbulence Using Numerical Simulation Databases, 2. Proceedings of the 1988 Summer Program*, 1988.

[232] P. Grassberger and I. Procaccia. Measuring the strangeness of strange attractors. *Physica D: Nonlinear Phenomena*, 9(1-2):189–208, 1983.

[233] S. Borgani and G. Murante. Box-counting clustering analysis: Corrections for finite sample effects. *Physical Review E*, 49(6):4907, 1994.

[234] T. Günther and H. Theisel. Source inversion by forward integration in inertial flows. In *Computer Graphics Forum*, volume 35, pages 371–380. Wiley Online Library, 2016.

[235] J. Sakakibara, R. B. Wicker, and J. K. Eaton. Measurements of the particle-fluid velocity correlation and the extra dissipation in a round jet. *International Journal of Multiphase Flow*, 22(5):863–881, 1996.

[236] L. Chen, Y. Zhang, P. Li, and G. Pan. Rebound characteristics of wet-shotcrete particle flow jet from wall based on CFD-DEM. *Buildings*, 14(4):977, 2024.

[237] A. Ferrante and S. Elghobashi. On the physical mechanisms of two-way coupling in particle-laden isotropic turbulence. *Physics of Fluids*, 15(2):315–329, 2003.

[238] W. Xiao, T. Jin, K. Luo, Q. Dai, and J. Fan. Eulerian–lagrangian direct numerical simulation of preferential accumulation of inertial particles in a compressible turbulent boundary layer. *Journal of Fluid Mechanics*, 903:A19, 2020.

[239] S. Li, B. Muddle, M. Jahedi, and J. Soria. A numerical investigation of the cold spray process using underexpanded and overexpanded jets. *Journal of Thermal Spray Technology*, 21:108–120, 2012.

[240] J. Pattison, S. Celotto, A. Khan, and W. O'neill. Standoff distance and bow shock phenomena in the cold spray process. *Surface and Coatings Technology*, 202(8):1443–1454, 2008.

[241] F. Halter and C. Chauveau. Recent advances in aluminium particles combustion for propulsion and heat generation. In *16th International Conference on Flow Dynamics (ICFD2019)*, 2019.

[242] N. E. L. Haugen and A. Brandenburg. Hydrodynamic and hydromagnetic energy spectra from large eddy simulations. *Physics of Fluids*, 18(7):075106, 2006.

APPENDICES

Appendix A

Non-Dimensional Governing Equations

A.1 Units

The governing equations in Pencil-Code can be solved with any consistent unit system as they are dimensionally homogeneous. However, for coherence, by default, Pencil-Code uses *Centrimetre-Gram-Second* or *CGS* unit system. As the name suggests, in this system the units of length, mass and time are centimeter (cm), gram (g) and second (s), respectively. While the unit of temperature is Kelvin (K) [132]. Therefore, this unit system can be used for expressing the present simulations and non-dimensionalizing the variables. Thus, to represent each parameter in a non-dimensional form, a dimensional value is divided by a reference value of similar dimensions.

A.2 Non-Dimensionalization

When non-dimensionalizing the governing equations, the characteristic variables used to non-dimensionalize must have consistent units. Furthermore, it is also required that the physical consistency of the resulting non-dimensional equations be conserved. This is ensured by the consistent definition of the dimensionless parameters used in the non-dimensional equations, namely: Reynolds (Re), Prandtl (Pr) and Mach (Ma) in the problem. On the other hand, the thermodynamic consistency of the governing equations is confirmed by the caloric and thermal state equations, which ensure the closure of these equations. In the present case, these two state equations are the ideal-gas law and the thermal energy (E_f) equation:

$$P_f = \rho_f R T_f \tag{A.1}$$

$$E_f = c_{f,v}\, T_f = \frac{1}{\gamma - 1} R T_f, \quad \text{where} \quad \gamma = \frac{c_{f,p}}{c_{f,v}} \tag{A.2}$$

here R ideal gas constant. Note that R, $c_{f,v}$ and $c_{f,p}$ are defined per unit mass. Considering these equations, characteristic reference states are required to non-dimensionalize the governing equations. The dimensions of these state variables are defined with mass ($\mathcal{M}$), length ($\mathcal{L}$), time ($\mathcal{T}$) and temperature (Θ). The typical reference variables that are used to non-dimensionalize are: temperature (T_r), pressure (P_r), length (L_r), time (t_r), density (ρ_r), velocity (u_r), ideal-gas constant (R_r) and dynamic viscosity (μ_r). These reference states can be the initial values of the concerned variables in the simulation, free stream values or values from any other reference process. Here, the subscript r represents the reference state. Note that in this section any parameter expressed with " $\tilde{}$ " is non-dimensional, whereas parameters without this superscript are dimensional except for the universal dimensionless numbers (Re, Pr and Ma). For non-dimensionalizing, we have to select three reference states from which all the other reference states can be computed. However, it is crucial to use reference states that have the required dimensions and do not affect the consistency of Equations (A.1) and (A.2). Therefore, such reference variables are chosen that are prescribed in the simulation and are thermodynamically consistent. Thus,

Reference Variable	Symbol	Description	Units
Density	ρ_r	ρ_r	g cm^{-3}
Temperature	T_r	T_r	K
Velocity	u_r	c	cm s^{-1}
Pressure	P_r	$\rho_r u_r^2$	g cm^{-1} s^{-2}
Length	L_r	u_r/t_r	cm
Time	t_r	L_r/u_r	s
Viscosity	μ_r	$\rho_r u_r L_r/Re$	g cm^{-1} s^{-1}

Table A.1: The selected reference variables.

Equations (A.1) and (A.2) can be non-dimensionalized as:

$$\tilde{P}_f = \frac{P_f}{P_r} = \frac{\rho_f}{\rho_r}\frac{R}{R_r}\frac{T_f}{T_r} \tag{A.3}$$

$$\tilde{E}_f = \frac{E_f}{E_r} = \frac{1}{\gamma - 1}\frac{R}{R_r}\frac{T_f}{T_r} \tag{A.4}$$

Based on unit consistency, Equations (A.3) and (A.4) can be expressed as:

$$[P_r] = [\rho_r][R_r][T_r] \tag{A.5}$$

$$[E_r] = [R_r][T_r] \tag{A.6}$$

here $[\cdot]$ brackets are representing units. Moreover, since the speed of sound ($c^2 = \gamma RT$) is used to non-dimensionalize velocity, P_r can be expressed as [132]:

$$P_r = \frac{\rho_r\ c^2}{\gamma} \quad \Rightarrow \quad [P_r] = [\rho_r][u_r^2] \qquad \text{where} \quad c = u_r \tag{A.7}$$

Considering the discussion above, Table A.1 enlists the 1D equations (as their extension to 3D is trivial) of the reference states selected for this analysis.

A.2.1 Continuity Equation

The equation of continuity in the present analysis is:

$$\frac{\partial \rho_f}{\partial t} + \frac{\partial \rho_f \mathbf{u}_f}{\partial x} = 0 \tag{A.8}$$

Equation (A.8) can be non-dimensionalized by multiplying it with t_r/ρ_r:

$$\frac{t_r}{\rho_r}\frac{\partial \rho_f}{\partial t} + \frac{t_r}{\rho_r}\frac{\partial \rho_f \mathbf{u}_f}{\partial x} = 0 \tag{A.9}$$

where u_f is fluid velocity. As per Table A.1, the second term in Equation (A.9) can be stated as:

$$\frac{t_r}{\rho_r}\frac{\partial \rho_f}{\partial t} + \frac{L_r}{u_r \rho_r}\frac{\partial \rho_f \mathbf{u}_f}{\partial x} = 0 \tag{A.10}$$

Thus, we get:

$$\frac{\partial \tilde{\rho}_f}{\partial \tilde{t}} + \frac{\partial \tilde{\rho}_f \tilde{\mathbf{u}}_f}{\partial \tilde{x}} = 0 \tag{A.11}$$

A.2.2 Momentum Equation

Similarly, the equation of momentum conservation is:

$$\frac{\partial \rho_f \mathbf{u}_f}{\partial t} + \frac{\partial \rho_f \mathbf{u}_f \mathbf{u}_f}{\partial x} = -\frac{\partial P_f}{\partial x} + \frac{\partial \mu_f}{\partial x}\left(\frac{\partial \mathbf{u}_f}{\partial x}\right) \tag{A.12}$$

Equation (A.12) can be non-dimensionalized with $t_r/\rho_r u_r$ and Table A.1. The left-hand side (LHS) of the above equation can be expressed as:

$$\frac{t_r}{\rho_r u_r}\frac{\partial \rho_f \mathbf{u}_f}{\partial t} + \frac{L_r}{\rho_r u_r u_r}\frac{\partial \rho_f \mathbf{u}_f \mathbf{u}_f}{\partial x} \quad \Rightarrow \quad \frac{\partial \tilde{\rho}_f \tilde{\mathbf{u}}_f}{\partial \tilde{t}} + \frac{\partial \tilde{\rho}_f \tilde{\mathbf{u}}_f \tilde{\mathbf{u}}_f}{\partial \tilde{x}} \tag{A.13}$$

Likewise, the right-hand side (RHS) of Equation (A.12) is given as:

$$-\frac{L_r}{\rho_r u_r u_r}\frac{\partial P_f}{\partial x} + \frac{L_r}{\rho_r u_r u_r}\frac{\partial \mu_f}{\partial x}\left(\frac{\partial \mathbf{u}_f}{\partial x}\right) \tag{A.14}$$

Using Table A.1, the above expression can be restated in the following form:

$$-\frac{L_r}{P_r}\frac{\partial P_f}{\partial x} + \frac{L_r}{\rho_r u_r u_r}\frac{\rho_r u_r L_r}{Re}\frac{\partial}{\partial x}\frac{\mu_f}{\mu_r}\left(\frac{\partial \mathbf{u}_f}{\partial x}\right) \Rightarrow -\frac{\partial \tilde{P}_f}{\partial \tilde{x}} + \frac{1}{Re}\frac{\partial \tilde{\mu}_f}{\partial \tilde{x}}\left(\frac{\partial \tilde{\mathbf{u}}_f}{\partial \tilde{x}}\right) \tag{A.15}$$

Hence, the non-dimensional form of Equation (A.12) is given as:

$$\frac{\partial \tilde{\rho}_f \tilde{\mathbf{u}}_f}{\partial \tilde{t}} + \frac{\partial \tilde{\rho}_f \tilde{\mathbf{u}}_f \tilde{\mathbf{u}}_f}{\partial \tilde{x}} = -\frac{\partial \tilde{P}_f}{\partial \tilde{x}} + \frac{1}{Re}\frac{\partial \tilde{\mu}_f}{\partial \tilde{x}}\left(\frac{\partial \tilde{\mathbf{u}}_f}{\partial \tilde{x}}\right) \tag{A.16}$$

In the base simulations, a forcing term (F_i) is added on the RHS of the momentum equation [242]:

$$F_i = \Re\{N f_{\omega(t)} \exp[i\omega(t)x + i\phi(t)]\} \tag{A.17}$$

here $\Re$ represents the real part, $\omega(t)$ is the wave vector, ϕ is the random phase between $-\pi$ and π, and $f_{\omega(t)}$ is the eigenfunction of curl operator. While, $\mathcal{N}$ is the normalizing factor:

$$\mathcal{N} = \acute{f} c \left(\frac{|\omega| c}{\delta t}\right)^{\frac{1}{2}} \tag{A.18}$$

where $\acute{f}$ is the non-dimensional forcing factor and δt is the timestep size. Thus, the dimensions of the forcing function are $\mathcal{L}\ \mathcal{T}^{-2}$. This can be non-dimensionalized with the mean fluid acceleration before incorporating it into the momentum equation.

A.2.3 Energy Equation

The expression for the conservation of energy is:

$$\frac{\partial T_f}{\partial t} + \frac{\partial T_f \mathbf{u}_f}{\partial x} = \frac{1}{\rho_f c_{f,p}} \frac{\partial}{\partial x}\left(\kappa_f \frac{\partial T_f}{\partial x}\right) \tag{A.19}$$

Equation (A.19) can be non-dimensionalized with t_r/T_r. Using Table A.1, the LHS of the above equation is expressed as:

$$\frac{t_r}{T_r}\frac{\partial T_f}{\partial t} + \frac{L_r}{u_r T_r}\frac{\partial T_f \mathbf{u}_f}{\partial x} \quad \Rightarrow \quad \frac{\partial \tilde{T}_f}{\partial \tilde{t}} + \frac{\partial \tilde{T}_f \tilde{\mathbf{u}}_f}{\partial \tilde{x}} \tag{A.20}$$

Likewise, multiplying the RHS of Equation (A.19) with t_r/T_r and μ_r/μ_r:

$$\frac{t_r}{T_r}\ \frac{1}{\rho_f}\frac{\kappa_f}{c_{f,p}\,\mu_r}\ \mu_r\ \frac{\partial}{\partial x}\left(\frac{\partial T_f}{\partial x}\right) \tag{A.21}$$

$$\frac{L_r}{T_r u_r}\frac{1}{\rho_f}\frac{1}{Pr}\frac{\rho_r u_r L_r}{Re}\frac{\partial}{\partial x}\left(\frac{\partial T_f}{\partial x}\right), \quad \text{where} \quad Pr = \frac{c_{f,p}\mu_r}{\kappa_f} \tag{A.22}$$

In this form, the above equation has all the required reference variables, and therefore, the complete energy equation can be expressed as:

$$\frac{\partial \tilde{T}_f}{\partial \tilde{t}} + \frac{\partial \tilde{T}_f \tilde{\mathbf{u}}_f}{\partial \tilde{x}} = \frac{1}{Pr\ Re}\ \tilde{\rho}_f \frac{\partial}{\partial \tilde{x}} \left(\frac{\partial \tilde{T}_f}{\partial \tilde{x}} \right) \tag{A.23}$$

For energy TWC, the particle-to-fluid heat transfer (or energy source) term, Q_{pf}, is added to the RHS of the above equation. This is a dimensional term and can be non-dimensionalized with the particle heating term, Q_p. These two terms are given as:

$$Q_{pf} = \frac{m_p c_{p,p}\, Nu_p}{2\tau_t} \left(T_p - T_f(x_p) \right) \tag{A.24}$$

$$Q_p = m_p c_{p,p} \frac{(T_{max} - T_p)}{\tau_{heat}} \tag{A.25}$$

It should be noted that the term Q_p heats the particles, and then particles transfer this heat in the form of Q_{pf} to the continuum phase.

A.2.4 Entropy Equation

To non-dimensionalize the entropy equation solved in the particle-laden supersonic jet analysis of this thesis, a few thermodynamic parameters must be defined. Here, the speed of sound is given as:

$$c^2 = (\gamma - 1) c_{f,p}\, T_f \tag{A.26}$$

This equation must be satisfied by the non-dimensional values, and therefore:

$$c_{f,p} = \frac{1}{(\gamma - 1) Ma^2} \tag{A.27}$$

The Reynolds number in the case is defined as:

$$Re = \frac{\rho_r u_r L_r}{\mu_f} \tag{A.28}$$

where ρ_f, u_f and L_r are set to unity for the jet. Thus, the viscosity is:

$$\mu_f = \frac{1}{Re} \tag{A.29}$$

The value of the κ is set assuming Pr is constant, and therefore:

$$\kappa = \frac{\mu_f \, c_{f,p}}{Pr} = \frac{1}{PrRe(\gamma - 1)Ma^2} \tag{A.30}$$

Now, the entropy equation is defined as:

$$\frac{\partial s_f}{\partial t} = -\mathbf{u}_f \cdot \nabla s_f + \frac{1}{\rho_f T_f} RHS \tag{A.31}$$

where entropy is expressed as $s_f = \ln T_f$. Thus, Equation (A.31) can be expressed as:

$$\frac{\partial \ln T_f}{\partial t} = -\mathbf{u}_f \cdot \nabla \ln T_f + \frac{1}{\rho_f c_{f,v} \, T_f} \text{RHS} - (\gamma - 1) \, \nabla \cdot \mathbf{u}_f \tag{A.32}$$

here the RHS corresponds to:

$$\text{RHS} = \nabla \cdot (\kappa_f \nabla T_f) + 2\rho_f \nu_f \mathbf{S} \otimes \mathbf{S} + \xi \rho_f (\nabla \cdot \mathbf{u}_f)^2 \tag{A.33}$$

Starting from Equation (A.32), both sides of this equation are multiplied with $\frac{L_r}{u_r}$. It is noted that since $\partial \ln(T_f)/\partial x = 1/T_f \, \partial T_f/\partial x$, the term $\ln(T_f)$, when inside the derivative, is effectively unitless. In other words, $\ln(T_f) = \ln(\tilde{T}_f)$. As a result:

$$\frac{L_r}{u_r} \frac{\partial \ln T}{\partial t} = -\frac{L_r}{u_r} \mathbf{u}_f \cdot \nabla \ln T_f + \frac{L_r}{u_r} \frac{1}{\rho_f c_{f,v} T_f} \, \text{RHS} - \frac{L_r}{u_r} \, (\gamma - 1) \, \nabla \cdot \mathbf{u}_f \tag{A.34}$$

Thus:

$$\frac{\partial \ln \tilde{T}}{\partial \tilde{t}} = -\tilde{\mathbf{u}}_f \cdot \tilde{\nabla} \ln \tilde{T}_f + \frac{L_r}{u_r} \frac{1}{\rho_f c_{f,v} T} \, \text{RHS} - (\gamma - 1) \, \tilde{\nabla} \cdot \tilde{\mathbf{u}}_f \tag{A.35}$$

Now considering the term $\dfrac{L_r}{u_r} \dfrac{\text{RHS}}{\rho_f c_{f,v} T_f}$:

$$\frac{L_r}{u_r} \frac{1}{\rho_f c_{f,v} T_f} \nabla \cdot (\kappa_f \nabla T_f) + \frac{L_r}{u_r} \frac{1}{\rho_f c_{f,v} T_f} 2\rho_f \nu_f \mathbf{S} \otimes \mathbf{S} + \frac{L_r}{u_r} \frac{1}{\rho_f c_{f,v} T_f} \xi \rho_f (\nabla \cdot \mathbf{u})^2 \tag{A.36}$$

By multiplying the first term with T_0/T_0, the temperature can be non-dimensionalized as:

$$\frac{1}{L_r u_r} \frac{1}{\rho_f c_{f,v} \tilde{T}_f} \nabla \cdot \left(\kappa_f \nabla \tilde{T}_f \right) \tag{A.37}$$

Recall that:

$$\frac{\partial \ln \rho}{\partial x} = \frac{1}{\rho}\frac{\partial \rho}{\partial x} \tag{A.38}$$

Since κ_f is constant, it can be expressed as:

$$\frac{1}{L_r u_r}\frac{1}{\rho_f c_{f,v}\tilde{T}}\kappa_f \nabla \cdot \left(\nabla \tilde{T}_f\right) \tag{A.39}$$

Therefore, Equation (A.39) can be written as:

$$\frac{\mu_r}{L_r u_r \rho_r}\frac{1}{Pr}\frac{\gamma}{\tilde{\rho}_f \tilde{T}_f}\nabla \cdot \left(\nabla \tilde{T}_f\right) \tag{A.40}$$

Then:

$$\frac{1}{RePr}\frac{\gamma}{\tilde{\rho}_f \tilde{T}_f}\nabla \cdot \left(\tilde{\nabla} \tilde{T}_f\right) \tag{A.41}$$

Now, considering the second term of Equation (A.36):

$$\frac{L_r}{u_r}\frac{1}{\rho_f c_{f,v} T_f} 2\rho_f \nu_f \mathbf{S} \otimes \mathbf{S} \tag{A.42}$$

The units of $\mathbf{S}$ and ν_f are $1/s$ and m^2/s, respectively. To non-dimensionalize ν_f the above equation is multiplied with L_r/L_r:

$$L_r^2 \frac{1}{c_{f,v} T_f} 2\tilde{\nu}_f \mathbf{S} \otimes \mathbf{S} \tag{A.43}$$

Since $Ma > 1$, u_r is a multiple of the speed of sound c. For simplicity, it is assumed that $u_r \sim c_r$:

$$c_r^2 t_r^2 \frac{1}{c_{f,v} T_f} 2\tilde{\nu}_f \mathbf{S} \otimes \mathbf{S} \tag{A.44}$$

Substituting Equation (A.26) in the above equation:

$$(\gamma - 1) c_{f,p} T_f \frac{1}{c_{f,v} T_f} 2\tilde{\nu}_f \tilde{\mathbf{S}} \otimes \tilde{\mathbf{S}} \tag{A.45}$$

Consequently:

$$2\gamma\tilde{\nu}_f(\gamma - 1)\tilde{\mathbf{S}} \otimes \tilde{\mathbf{S}} \tag{A.46}$$

While in the third term of Equation (A.36), by default in Pencil-Code $\xi = 0$.

A.2.5 Lagrangian Equations

The Lagrangian equations of particle motion are:

$$\frac{dx_p}{dt} = u_p \tag{A.47}$$

$$\frac{du_p}{dt} = \frac{C_D}{\tau_p}\left(u_f(x_p) - u_p\right) \tag{A.48}$$

Multiplying Equation (A.47) with t_r/L_r and Equation (A.48) with t_r/u_r:

$$\frac{t_r}{L_r}\frac{dx_p}{dt} = \frac{t_r}{L_r}u_p \tag{A.49}$$

$$\frac{t_r}{u_r}\frac{du_p}{dt} = \frac{t_r}{u_r}\frac{C_D}{\tau_p}\left(u_f - u_p\right) \tag{A.50}$$

By using Table A.1, the above equations can be written in the non-dimensional form as:

$$\frac{d\tilde{x}_p}{d\tilde{t}} = \tilde{u}_p \tag{A.51}$$

$$\frac{d\tilde{u}_p}{d\tilde{t}} = \frac{C_D}{\tilde{\tau}_p}\left(\tilde{u}_f(x_p) - \tilde{u}_p\right) \tag{A.52}$$